The Ultraviolet Spectra of Active Galactic Nuclei: Intrinsic Properties and Intervening Material

by

Evan M. Tilton

B.S., University of Florida, Physics & Astronomy, 2010

M.S., University of Colorado, Astrophysical & Planetary Sciences, 2013

A thesis submitted to the

Faculty of the Graduate School of the

University of Colorado in partial fulfillment

of the requirements for the degree of

Doctor of Philosophy

Department of Astrophysical & Planetary Sciences

2017

This thesis entitled:
The Ultraviolet Spectra of Active Galactic Nuclei: Intrinsic Properties and Intervening Material
written by Evan M. Tilton
has been approved for the Department of Astrophysical & Planetary Sciences

Prof. J. Michael Shull

Prof. Paul D. Beale

Prof. Julia M. Comerford

Prof. Kevin France

Prof. James C. Green

Date

The final copy of this thesis has been examined by the signatories, and we find that both the content and the form meet acceptable presentation standards of scholarly work in the above mentioned discipline.

Tilton, Evan M. (Ph.D., Astrophysical & Planetary Sciences)

The Ultraviolet Spectra of Active Galactic Nuclei: Intrinsic Properties and Intervening Material

Thesis directed by Prof. J. Michael Shull

The spectra of active galactic nuclei (AGNs) are important probes of astrophysical phenomena on many scales. At the smallest scales, AGN spectra probe the accretion processes that control the growth of super massive black holes (SMBHs) and provide diagnostics of black hole masses. On galactic scales, AGNs play an important role in regulating star formation and controlling the coevolution of galaxies and their central SMBHs. On cosmological scales, AGN spectra, acting as backlights, provide a means for studying via absorption the diffuse gas of the intergalactic medium (IGM), the primary reservoir of baryons in the universe whose ionization state is largely controlled by ionizing flux from AGNs. A comprehensive understanding of the diverse, complex spectra of AGN is necessary to understand any of these phenomena, and because key atomic transitions and absorption edges lie in the ultraviolet (UV), many of these processes are best studied in the UV with space telescopes. In this thesis, I address the nature of several of these physical environments using UV spectra obtained with the Cosmic Origins Spectrograph (COS).

Using a large database of IGM absorption lines, I constrain the metal abundance of the IGM by comparing numerical photoionization models to the observed abundances of ions of carbon, sillicon, and oxygen. This work suggests an enhancement of alpha-process elements relative to solar abundances, and it also tests predictions of the metagalactic ionizing UV background spectrum (UVB).

By combining new and archival spectra of AGNs at redshifts $1.45 \leq z_{\rm AGN} \leq 2.14$, I construct composite spectra that constrain the typical extreme-UV AGN spectrum, a key input for models of the UVB. I measure a typical EUV slope in frequency space of $F_\nu \propto \nu^{-0.72\pm0.26}$ and limit the intrinsic He I 504 Å photoelectric absorption edge opacity to $\tau_{\rm HeI} < 0.047$ while also tentatively identifying numerous emission lines.

I also present preliminary results from a large, homogeneous catalog of absorption systems associated with AGNs that presumably trace gas outflows. This work represents the first step toward the largest sample of such absorbers in the low-redshift universe to date, and will enable a more comprehensive understanding of the physical nature of these absorbers and how they relate to their host galaxies.

Acknowledgements

I acknowledge support from NASA Earth and Space Science Fellowship grant NNX14-AO18H. Chapter 2 was supported in part by Space Telescope Science Institute (STScI) COS grant NNX08-AC14G. Chapter 3 uses data from program number HST-GO-13302.01 with support provided by NASA through a grant from STScI. Portions of this thesis are based on observations made with the NASA/ESA *Hubble Space Telescope*, obtained from the data archive at STScI. STScI is operated by the Association of Universities for Research in Astronomy, Inc., under NASA contract NAS5-26555.

Contents

Chapter

1 Introduction **1**

1.1 AGNs: A Diversity of Complex Spectra 2

1.1.1 Whence come AGNs, and whither go AGNs? 2

1.1.2 An AGN Taxonomy 4

1.2 The IGM: A Great Reservoir of Intervening Material 9

1.3 Thesis Outline 12

2 Modeling the Photoionization State of the Intergalactic Medium with Cloudy: Ionization Fractions and Mass Densities for Metal Species **13**

2.1 Chapter Preface 13

2.2 Chapter Abstract 13

2.3 Introduction 14

2.4 Observational Data and Results 17

2.5 Photoionization Models 20

2.5.1 Metagalactic Ionizing Background Spectrum Inputs 21

2.6 Results 24

2.6.1 The Photoionized Species: Carbon and Silicon 24

2.6.2 UVB Redshift Evolution within the Observed Absorber-Redshift Range . . . 30

2.6.3 The Extent of Photoionization of O VI 30

2.6.4 The Total Metal Abundance 31
2.7 Discussion and Conclusion 33

3 *HST*-COS Observations of AGNs. III. Spectral Constraints in the Lyman Continuum from Composite COS/G140L Data **36**
3.1 Chapter Preface 36
3.2 Chapter Abstract 36
3.3 Introduction 37
3.4 Methodology 40
3.4.1 Sample, Data Acquisition, and Processing 40
3.4.2 Composite Construction 48
3.5 Discussion 53
3.5.1 The EUV Slope from 450 to 770 Å 53
3.5.2 Emission Lines 61
3.5.3 The He I 504 Å Absorption Edge 64
3.6 Summary and Conclusions 65

4 The Associated Absorbers of the HST/COS Archive of Observations of AGNs: Preliminary Results **68**
4.1 Introduction 68
4.2 Catalog Construction and Methodology 71
4.2.1 Sample, Data Acquisition, and Processing 71
4.2.2 Associated Absorber Identification 78
4.3 Absorber Measurements 80
4.4 Discussion 132
4.4.1 Detection Rates and the Global Covering Fraction 132
4.4.2 Trends with Luminosity 134
4.4.3 Possible Strong Covering-Fraction Velocity Dependence in a Single Transition 136

4.5 Summary and Conculsions 137

5 Summary and Future Work **140**

5.1 Summary 140

5.2 Future Work 142

5.2.1 IGM Absorption Lines 142

5.2.2 The EUV spectra of AGNs. 145

5.2.3 The UVB. 145

5.2.4 Associated Absorbers 146

Bibliography **150**

Appendix

A Notes on Individual Sightlines **165**

A.1 H 1118-429 165

A.2 HE 0429-5343 165

A.3 HE 1228+0131 165

A.4 HE 2332-3556 166

A.5 IRAS 23443-4502 166

A.6 IRASF22456-5125 166

A.7 Kaz 238 166

A.8 MR 2251-178 167

A.9 Mrk 279 167

A.10 Mrk 304 168

A.11 Mrk 478 168

A.12 Mrk 486 168

A.13 Mrk 509 168

A.14 Mrk 841 168
A.15 Mrk 876 169
A.16 Mrk 1513 169
A.17 NGC 985 169
A.18 PG0804+761 169
A.19 PG0844+349 169
A.20 PG1126-041 170
A.21 PG1351+640 170
A.22 PG1411+442 170
A.23 PG1626+554 170
A.24 QSO 0045+3926 170
A.25 RBS542 171
A.26 RBS1763 172
A.27 RBS2055 172
A.28 SDSS J091728.56+271951.0 172
A.29 SDSS J135712.61+170444.1 172
A.30 VPC 0798 173

Tables

Table

2.1 Absorption-Line Data 18

2.2 Summary of Metal-Ion Densities 18

3.1 *HST*/COS Observation Details 41

3.2 AGN Properties[a]. 42

3.3 Identified pLLS (56) and LLS (2) Absorption Systems 46

3.3 Identified pLLS (56) and LLS (2) Absorption Systems 47

3.4 Equivalent Widths of Spectral Regions of Emission 64

4.1 Observational Data and AGN Properties 74

4.1 Observational Data and AGN Properties 75

4.1 Observational Data and AGN Properties 76

4.2 References for AGN Systemic Redshifts 77

4.3 Basic HI Line Measurements 90

4.3 Basic HI Line Measurements 91

4.3 Basic HI Line Measurements 92

4.3 Basic HI Line Measurements 93

4.3 Basic HI Line Measurements 94

4.3 Basic HI Line Measurements 95

4.4 Basic CIV Line Measurements 96

4.4 Basic CIV Line Measurements 97
4.4 Basic CIV Line Measurements 98
4.4 Basic CIV Line Measurements 99
4.4 Basic CIV Line Measurements 100
4.5 Basic OVI Line Measurements 100
4.5 Basic OVI Line Measurements 101
4.5 Basic OVI Line Measurements 102
4.6 HI Line Fits 103
4.6 HI Line Fits 104
4.6 HI Line Fits 105
4.6 HI Line Fits 106
4.6 HI Line Fits 107
4.6 HI Line Fits 108
4.6 HI Line Fits 109
4.6 HI Line Fits 110
4.6 HI Line Fits 111
4.6 HI Line Fits 112
4.6 HI Line Fits 113
4.7 CIV Line Fits 113
4.7 CIV Line Fits 114
4.7 CIV Line Fits 115
4.8 OVI Line Fits 116
4.8 OVI Line Fits 117
4.9 Power-Law Inhomogeneous HI Line Measurements 117
4.9 Power-Law Inhomogeneous HI Line Measurements 118
4.9 Power-Law Inhomogeneous HI Line Measurements 119
4.9 Power-Law Inhomogeneous HI Line Measurements 120

4.9 Power-Law Inhomogeneous HI Line Measurements 121
4.9 Power-Law Inhomogeneous HI Line Measurements 122
4.9 Power-Law Inhomogeneous HI Line Measurements 123
4.9 Power-Law Inhomogeneous HI Line Measurements 124
4.9 Power-Law Inhomogeneous HI Line Measurements 125
4.9 Power-Law Inhomogeneous HI Line Measurements 126
4.10 Power-Law Inhomogeneous CIV Line Measurements 127
4.10 Power-Law Inhomogeneous CIV Line Measurements 128
4.10 Power-Law Inhomogeneous CIV Line Measurements 129
4.11 Power-Law Inhomogeneous OVI Line Measurements 130
4.11 Power-Law Inhomogeneous OVI Line Measurements 131
4.12 Detection Frequencies by AGN Type 132

Figures

Figure

1.1 Optical spectrum of 3C 273 5

1.2 FUV spectrum of 3C 273 8

1.3 Schematic of AGN Unified model 10

1.4 H I absorber frequency distribution 12

2.1 Several UVB spectral energy distributions 23

2.2 Ionization ratios for carbon and silicon as a function of baryon overdensity 25

2.3 Ionization correction factors for carbon and silicon as a function of baryon overdensity 27

2.4 Ratio of the silicon and carbon ionization correction factors 29

2.5 Ionization fraction of O VI 32

3.1 AGN spectra observed with COS/G140L 49

3.2 Further AGN spectra observed with COS/G140L 50

3.3 Composite spectra for the full sample of 20 AGN 54

3.4 Number of AGN spectra contributing to the composite spectra as a function of rest-frame wavelength 55

3.5 Results of the Monte-Carlo realizations for the power-law parameters 57

3.6 Rest-frame FUV spectrum of SBS1010+535 59

3.7 Composite spectra excluding SBS1010+535 60

3.8 Emission-line equivalent width for the sample of targets as a function of AGN rest-frame wavelength 63

3.9 Subsample composite of 5 AGN illustrating non-detection of edge-like spectral breaks due to He I absorption in the region around rest-frame 504 Å 66

4.1 Sample Voigt profiles under different covering model assumptions 85

4.2 Sample absorption and emission fit 86

4.3 Sample probability distributions for MCMC parameters 87

4.4 Maximum blueshift velocity versus UV luminosity 135

4.5 CIV equivalent widths versus UV luminosity 136

4.6 Lyα absorption toward RBS542 and IRAS F22456-5125 138

Chapter 1

Introduction

The spectra of active galactic nuclei (AGNs) are of exceptional astrophysical importance. Observations of AGNs probe the growth of supermassive black holes (SMBHs; e.g., Marconi et al., 2004; Fabian, 2004; Vestergaard & Peterson, 2006; Comerford & Greene, 2014), the structure of accretion disks (e.g., Hubeny & Hubeny, 1997; Done et al., 2012; Slone & Netzer, 2012; Laor & Davis, 2014; Castelló-Mor et al., 2017; Fabian et al., 2017), and the connection between SMBHs and their host galaxies (e.g., Renzini & Daddi, 2008; Canalizo & Stockton, 2001; Heckman & Best, 2014; Davies et al., 2017). They offer the most detailed ways of studying high-velocity outflows from the AGNs (e.g., Muzahid et al., 2013; Arav et al., 2015) as well as the diffuse gas of the intergalactic medium (IGM; e.g., Tilton et al., 2012; Danforth et al., 2016) and circumgalactic medium (CGM; e.g., Tumlinson et al., 2011; Stocke et al., 2014). These absorption features are observed against the AGN backlight. AGN spectra are a major and often dominant component of the metagalactic ultraviolet background (UVB), which controls the ionization state of the IGM and CGM (e.g., Haardt & Madau, 2012; Madau & Haardt, 2015).

The ultraviolet (UV) portion of AGN spectra, in particular, offers a wealth of diagnostics of these diverse physical environments. The baryonic matter in these environments is typically partially-ionized gas with numerous strong atomic transitions in the far-UV (FUV) and extreme-UV (EUV). However, because these wavelengths are unobservable from the ground, space telescopes are required if we are to study this spectral regime in the low-redshift universe.

In this thesis, I will use spectra of AGNs obtained by the Cosmic Origins Spectrograph (COS)

on board the *Hubble Space Telescope*, as well as results obtained with other FUV instruments, to study several of these astrophysical phenomena. I will explore the metal content of the IGM and use it to test our knowledge of the spectral properties of the UVB (Chapter 2). I will measure the typical EUV spectrum of AGNs, and use it to produce constraints on accretion disk models and its contribution to the UVB (Chapter 3). I will identify and analyze a large catalog of absorption lines that likely trace outflows from AGNs (Chapter 4). First, however, I will introduce in this Chapter the basic properties of AGNs (Section 1.1) and the IGM (Section 1.2) to help orient the reader.

1.1 AGNs: A Diversity of Complex Spectra

1.1.1 Whence come AGNs, and whither go AGNs?

As early as the 1940s, there were remarkable hints that at least some of the radio brightness in the sky might have something to do with extragalactic objects. For the first time, it was becoming possible to identify distinct, discrete radio sources. Finally, the so-called "radio-stars," which so many had supposed *must* give rise to the diffuse Galactic radio noise identified years earlier, were being discovered. In 1947 alone, John G. Bolton found three of these new objects (Bolton, 1948). But that was insufficient: they were discrete sources, yes, but their positions were only known to within several degrees. If these objects were to be understood, they would need to be located much more precisely. Their locations would need to be refined to better than degree precision, so that the great optical telescopes of the day could be pointed at them. With that in mind, Bolton and his collaborators set out to New Zealand to find a good cliff (Bolton, 1982).

An antenna on a cliff overlooking the sea gets to see a radio source twice: once directly from the radio source and once from the radio source bounced off of the water. The latter path is slightly longer, so the two waves create an interference pattern at the antenna that depends on the height of the source above the horizon. Bolton et al. (1949), with the help of some astronomically-minded cliffs, were able to locate the optical counterparts for three radio sources. Taurus A, Virgo A, and Centaurus A were located near the Crab Nebula and the galaxies M87 and NGC 5128. Though no

one was sure at the time, the suggestion of incredibly luminous and distant extragalactic sources was planted (Kellermann, 2013).

More than a decade later, many more radio sources were known, but still few had accurate positions. Indeed, only a handful of the hundreds of sources in the vast 3rd Cambridge (3C) survey (Edge et al., 1959) had known counterparts,[1] and many of the brightest sources in the catalog, including the variable 3C 273 that had been known since the 1880s, were not among them. New methods were needed if more optical counterparts were to be found – which is where the Moon came into play. If one were to observe the precise moment of a lunar occultation of a radio source, Hazard (1962) pointed out, then one could deduce the position of the source to great accuracy. In August, 1962, Hazard et al. (1963) seized just such an opportunity to observe the occultation of 3C 273 with the 210-foot Parkes radio telescope in New South Wales, Australia. They had determined 3C 273's position to less than a tenth of an arcsecond.[2]

Shortly after the occultation measurements, John Bolton wrote to Maarten Schmidt of the California Institute of Technology to discuss the optical observations of radio sources; included in the letter were the coordinates for 3C 273 (Kellermann, 2013). Several months later in December, once 3C 273 moved further from the Sun in the sky, Schmidt obtained two optical spectra of the bright, apparently stellar, object at the 3C 273 location using the Palomar 200-inch telescope. Two months after that, in February, 1963, Schmidt recognized the familiar pattern of the Balmer series of hydrogen in his spectra – they were shifted by 15.8% to longer wavelengths, implying a redshift factor $z = 0.158$ (Schmidt, 1963). One of the brightest "stars" and one of the brightest radio sources were one and the same, and its redshift suggested such a great distance as to imply a previously unimaginable luminosity. The observation was rapidly confirmed with near-infrared observations (Oke, 1963), and, in hardly any time at all, other star-like radio sources at vast distances were being identified (Greenstein, 1963).[3] The quasi-stellar objects, soon shortened to

[1] However, by this time, several of these objects were beginning to be recognized as nebulous "radio galaxies" that were probably extragalactic (e.g., Baade & Minkowski, 1954; Minkowski, 1960).

[2] Or, rather, they would have measured the position to less than a tenth of an arcsecond, if the initial calculations had not had a fifteen-arcsecond mistake in the calculations (Kellermann, 2013).

[3] The radio source discussed by Greenstein (1963), 3C 48, had its optical counterpart identified as an apparently

the more-pronounceable name "quasars," were born, and soon they would be recognized as merely a sliver of the great diversity of AGNs, the broader class of objects to which the quasars belong. It is to this diversity that we now turn.

1.1.2 An AGN Taxonomy

Unlike 3C 273, most quasars, and AGNs in general, are not even radio-loud. Though nearly all AGNs produce some degree of radio flux, only $\sim$ 10% of AGNs have large ratios of radio flux (typically reckoned near 5 GHz) to optical flux (Kellermann et al., 1989; White et al., 2000; Cirasuolo et al., 2003). These radio-loud AGNs typically display highly-collimated, synchrotron-emitting jets, though their properties in spectral regimes outside of the radio wavelengths can be diverse. In this section, we will focus primarily on the classification and theoretical unification of AGNs by spectral properties in the UV and optical regimes. The question of how those properties relate to radio-loudness, if at all, remains a topic of debate. Rather than digress into that rich field of research, I refer the reader to more comprehensive treatments (e.g., Ho, 2008; Heckman & Best, 2014).

Maarten Schmidt's first optical spectrum of 3C 273 (Figure 1.1) already shows many of the hallmark characteristics of AGN spectra, which have led to physical models that address the nature of AGNs and how they can produce such diverse, complex spectra. Perhaps the most defining feature is their enormous bolometric luminosity, which spans decades of frequency from γ-rays to radio waves. In the case of 3C 273, assuming isotropic emission, the bolometric luminosity is $L_{\rm bol} \sim 10^{47}$ erg s^{-1} (Türler et al., 1999). Owing to their distinct discoveries throught history, all quasars are AGNs, but not all AGNs are quasars.[4] By convention, the luminosity is the defining characteristic of the quasars. Quasars are defined to be the highly-luminous end of the distribution of AGNs, with nuclear bolometric luminosities $L_{\rm bol} \gtrsim 10^{46}$ erg s^{-1} such that they greatly outshine

stellar object and had a publicized optical spectrum much earlier than 3C 273. However, until the identification of the redshift of 3C 273, there was "general agreement" that 3C 48 was a "relatively nearby star," despite "a remote possibility that it may be a very distant galaxy" (Matthews et al., 1960; Federer, 1960). A similar discovery history occured for 3C 196 and 3C 286 (Matthews & Sandage, 1963).

[4] Except that this rule isn't always followed; many authors sometimes use "quasar" as a convenient shorthand for AGN, so the reader must beware.

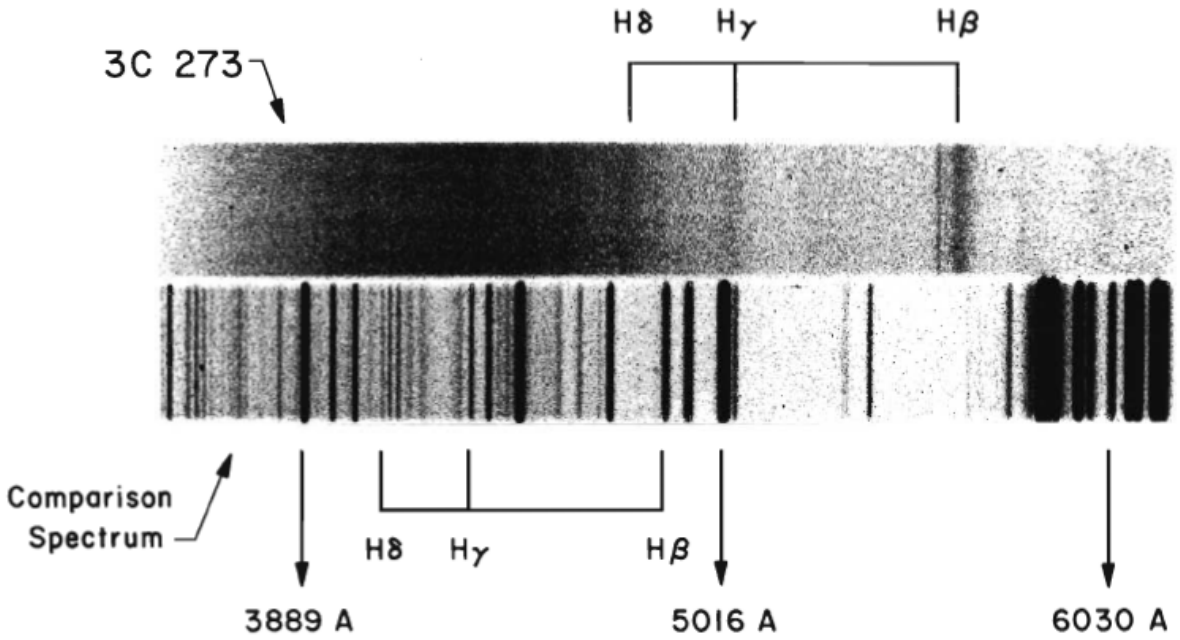

Figure 1.1 Reproduced from Schmidt (2013):[5] Maarten Schmidt's 1963 optical, photographic plate spectrum of 3C 273 (top) along with the comparison spectrum (bottom) used to determine the cosmological redshift of the source. Note also that the Balmer lines in 3C 273 are quite broad; the Hβ line has a full width at half maximum of $\Delta v_{\rm FWHM} \approx 3650$ km s^{-1} (Marziani et al., 1996).

their host galaxies' stars (e.g., Peterson, 1997).

However, the majority of AGNs, especially those at low redshift, tend to be less luminous. Perhaps the most relevant class for the purposes of this thesis are the Seyfert galaxies. In a sense, the Seyferts were the first AGNs discovered, with their emission lines being identified as early as 1908 (Fath, 1909; Slipher, 1917). Early spectra of NGC 1068, NGC 4151, and NGC 3516 revealed emission lines that were thousands of km s^{-1} wide (Seyfert, 1941), and this class of objects with "nuclear emission in spiral nebulae" was defined by their namesake in 1943 (Seyfert, 1943, 1946). Unlike 3C 273, however, no one at the time recognized their true distances or luminosities. These objects are the nearby and fainter siblings of the quasars, with typical nuclear bolometric luminosities $L_{\rm bol} \sim 10^{41} - 10^{45}$ erg s^{-1}, and they typically reside in spiral galaxies (e.g., Peterson, 1997).

[5] Every effort has been made to comply with fair use as well as the guidelines of the Visual Resources Association (Wagner & Kohl, 2012) in the necessary reproduction of visual images for scholarly, illustrative purposes within this thesis.

These huge luminosities naturally lead to, and begin to answer, the question of what powers an AGN. Assuming spherical symmetry, it is straightforward to derive a quantity, the Eddington luminosity, that represents the maximum luminosity that a self-gravitating object can achieve when there is a balance of gravitational and radiation pressure forces. The gravitational force at distance R due to a body of mass M on a mass m is

$$F_g = \frac{GMm}{R^2}. \tag{1.1}$$

The radiation pressure for luminosity L is

$$P_r = \frac{L}{c4\pi R^2}, \tag{1.2}$$

which can be written as a force by assuming an opacity κ:

$$F_r = P_r \kappa m. \tag{1.3}$$

The opacity can be simplified by assuming that the scattering gas is predominantly ionized hydrogen. In this case, the opacity is approximately that due to Thomson scattering on electrons, $\kappa = \sigma_{\rm T}/m_{\rm p}$, where $\sigma_{\rm T}$ is the Thomson cross section and $m_{\rm p}$ is the proton mass. Setting Equations 1.1 and 1.3 equal yields the Eddington luminosity limit,

$$L_{\rm Edd}(M) = \frac{4\pi GMc}{\kappa} \approx \frac{4\pi GMcm_{\rm p}}{\sigma_{\rm T}}. \tag{1.4}$$

Solving for $M(L)$ yields the Eddington mass limit,

$$M_{\rm Edd}(L) = \left(\frac{\sigma_{\rm T}}{4\pi G m_{\rm p} c}\right) L \approx 10^5 \left(\frac{L}{10^{43}\ {\rm erg\ s^{-1}}}\right)\ {\rm M_\odot}. \tag{1.5}$$

This simple argument provides a rough lower limit to the masses of AGN central engines. This vast mass must all reside within the central few parsecs in the host galaxy, a limit set by the spatial resolution of observations and causality arguments arising from the often rapid variability of AGN spectra. Coupled with the need for more efficent radiation than fusion over long periods of time, as well as consistency with many spectral features, these properties have led to the conclusion that the central engines of AGNs are supermassive black holes (SMBHs) with associated accretion disks.

In addition to overall luminosity, the other measurable information in Schmidt's 3C 273 spectrum (Figure 1.1) comes from the emission lines. We have already noted that the spectrum displays strong H I[6] Balmer lines which are redshifted, indicating cosmological distance. The emission lines show great variety in relative strengths and widths among AGNs, and they form the basis for another aspect of AGN classification. All of the permitted emission lines of 3C 273, which often come from highly ionized species, have very broad components with widths of thousands of km s^{-1}, and both forbidden and permitted lines show narrower components hundreds of km s^{-1}. These widths are perhaps easier seen in a more modern, one-dimensional FUV spectrum (Figure 1.2), which clearly shows the full extent of the H I Lyα emission line, as well as lines from highly ionized species like O VI. Qualitatively speaking, these sorts of emission properties, along with the higher flux in the roughly power-law-shaped continuum, define Type I AGNs. In contrast, Type II AGN lack broad emission lines (except in polarized light) and have lower power-law continuum fluxes. This basic classification scheme (Khachikian & Weedman, 1971; Khachikian & Weedman, 1974; Urry & Padovani, 1995) is sometimes supplemented by intermediate classes (e.g., Seyfert 1.5) based on line widths, as described by Osterbrock (1989).

This spectral diversity can be at least partially explained by a simplified unification model. This model incorporates the SMBH and accretion disk central engine and combines it with variations in AGN inclination relative to the observer's line of sight. This picture, first proposed by Antonucci & Miller (1985) and described in more detail by Urry & Padovani (1995), still has multiple hypothetical elements and fails to explain some AGN phenomena, but it successfully predicts many basic features of AGN spectra. We refer the reader to a recent review by Netzer (2015) for the modern nuances, and only present a simplified description here of the classic model to familiarize the reader with the basic picture. If we suppose that the central engine is a SMBH with a surrounding accretion disk, then the accretion disk should produce radially-dependent thermal radiation (roughly $T(r) \propto r^{-3/4}$). The spectrum of this radiation should be smooth and, when

[6] Throughout this thesis we will refer to atomic species with this notation, common in many subfields of physics and astronomy. H I refers to the first ion state, neutral hydrogen, and H II is ionized hydrogen, and so forth. For example, O VI is five-times ionized oxygen.

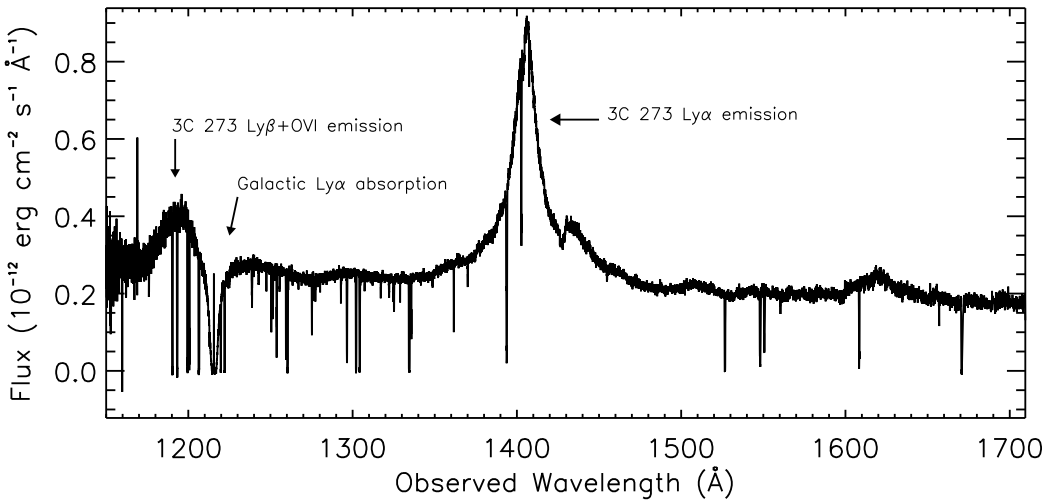

Figure 1.2 A portion of the UV spectrum of 3C 273, obtained with HST/STIS. The data plotted are from the reduction and coaddition used in Tilton et al. (2012).

viewed in localized soft X-ray, UV, and optical wavelength regimes, can approximately account for the power-law continua such as in Figure 1.2 (e.g., Shakura, 1973; Shakura & Sunyaev, 1973; Shakura et al., 1978; Pringle, 1981).

Beyond the accretion disk lies the gas responsible for the broad emission lines, which is known as the broad-line region (BLR or sometimes BELR; see Peterson, 2006, for a more detailed summary of BLR properties). Though this gas is often referred to as broad emission-line "clouds," that terminology is likely misleading on some level, as it is difficult to produce the extraordinarily smooth observed line profiles with an ensemble of truly discrete clouds (Arav et al., 1997) in the very small BLR (on the scale of light-days or tens of light-days). More likely, the BLR gas consists of some sort of supersonic flow or disk wind. This gas lies within the SMBH gravitational sphere of influence, and its motion thus directly probes that potential. The Doppler shifts of this motion give rise to the large emission line widths (and this also provides a means for measuring the SMBH mass; see, e.g., Peterson et al., 2004; Vestergaard & Peterson, 2006; Tilton & Shull, 2013). The gas is relatively dense ($n_e > 10^9$ cm^{-3}) and of high temperature ($T \gtrsim 10^4$ K) (Netzer, 1990; Peterson, 1997; Moloney & Shull, 2014).

Surrounding the SMBH, accretion disk, and the BLR is a dusty, axisymmetric, torus-like gas

structure. The inner radius, which likely corresponds to the outer radius of the BLR, may be set by the dust sublimation radius (Netzer & Laor, 1993). Still farther out is the narrow line region (NLR), whose clouds have sufficient density to produce emission from forbidden lines in addition to the permitted transitions. The torus creates the inclination-dependent spectral variations that give rise to Type I and Type II spectra (see Figure 1.3 for a schematic illustration). Equatorial lines of sight allow the torus to obscure the continuum and BLR but not the NLR, giving rise to Type II spectra. When observed in polarized light, Type II spectra reveal broad emission lines, presumably scattered off electrons in the NLR; it was this observation in NGC 1068 (Antonucci & Miller, 1985) that motivated the unified model. Type I spectra, on the other hand, are presumed to arise from lines of sight further from equatorial, such that the observer sees radiation beyond the torus and receives flux from the continuum, NLR, and BLR.

There are a number of less common classes of AGN that are beyond the scope of this introduction. The BL Lacertae objects (BL Lacs), however, will be mentioned at several points in this thesis, so it is worth defining the class. BL Lacs are a subclass of the blazars that was first identified as extragalactic by Oke & Gunn (1974). Their flux is highly variable and polarized, and their spectra are smooth and non-thermal power laws over all portions of the spectrum, with no obvious line-emission features. In the context of unification models, they are thought to be the same intrinsic objects as Fanaroff-Riley class I (Fanaroff & Riley, 1974) radio galaxies, except that they are viewed from an angle very closely aligned with the axial jet, creating a relativistic beaming effect (Urry & Padovani, 1995; Urry, 1999; Falomo et al., 2014).

1.2 The IGM: A Great Reservoir of Intervening Material

One cannot study the UV spectra of AGN without encountering the IGM. In addition to the emission-line and continuum features described in Section 1.1.2, a great many absorption features complicate the spectrum of 3C 273 (Figure 1.2) and all AGNs. Some of these absorption lines originate in the interstellar medium (ISM) of our own galaxy and some are intrinsic to the AGN (as discussed in Chapter 4), but many of them are cosmologically intervening absorbers from the

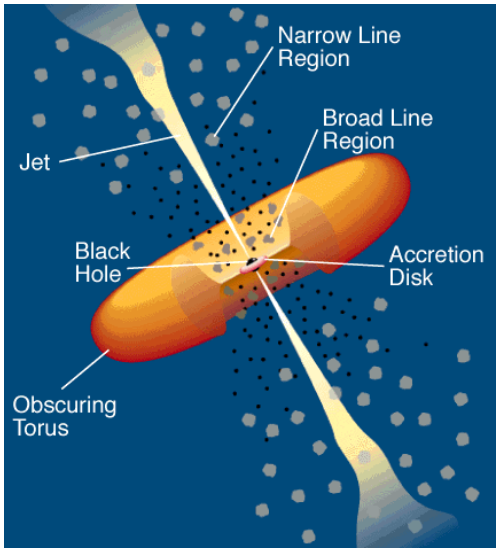

Figure 1.3 Reproduced from Urry & Padovani (1995): A schematic representation of the unified picture of AGNs.

IGM and CGM. Even before the discovery of the extragalactic nature of quasars, it was known that UV spectroscopy was of crucial importance to the understanding of the diffuse gases that make of galaxies and their surroundings (Spitzer, 1956). With the quasar discovery, speculation as to the possible detection of intergalactic gas immediately ensued (Gunn & Peterson, 1965; Bahcall & Spitzer, 1969). If continuum or line absorption was to be discovered, it would likely lie in the rest-frame UV, where the strongest atomic resonance line transitions and absorption edges occur. Thus, intergalactic absorption would either have to be studied at high redshift, where the rest-frame UV could be observed in the optical from the ground,[7] or it would have to wait for UV spectroscopy from space.

Lynds (1971) achieved the former goal. In 1970, Lynds identified numerous absorption lines, mostly from the Lyman series of H I, toward the $z_{\rm AGN} = 2.877$ quasar 4C 05.34. Though there was initially debate as to whether the lines were associated with the quasar itself or of cosmological origin, Bahcall & Goldsmith (1971) persuasively argued for the cosmological interpretation. The "Lyman-α forest," as Lynds later called it, had been discovered.

In recent decades, progress in studies of the IGM have been driven by improved optical and

[7] For example, H I Lyα redshifts to observed wavelengths $\lambda > 3600$ Å for absorber redshifts $z_{\rm abs} > 1.96$, C IV λ1551 does so for $z_{\rm abs} > 1.32$, and O VI λ1038 does so for $z_{\rm abs} > 2.47$.

UV observatories and instruments and by advances in numerical, hydrodynamical, cosmological simulations. In the interim, observations of the cosmic microwave background (CMB) radiation (Planck Collaboration et al., 2016) as well as predictions from Big Bang nucleosynthesis (primarily of D/H) have constrained the cosmic baryon budget with great precision. At low-redshift, however, much of this matter is not directly observed, which has been dubbed by some, "the missing bayon problem" (e.g. Fukugita et al., 1998; Shull, 2003; Bregman, 2007; Shull et al., 2012a). The cosmological simulations have provided part of the solution. They suggested that by $z = 0$ about 30% of the cosmic baryon budget resides in the photoionized Lyα forest, while much of the remainder resides in a much hotter ($T \sim 10^5 - 10^7$ K) phase called the warm-hot intergalactic medium (WHIM; Cen & Ostriker, 1999; Davé et al., 1999, 2001; Oppenheimer & Davé, 2008; Smith et al., 2011). Studies of UV absorption lines with space telescopes (e.g., Danforth & Shull, 2005; Danforth et al., 2006; Danforth & Shull, 2008; Lehner et al., 2007; Thom & Chen, 2008; Tripp et al., 2008; Tilton et al., 2012; Danforth et al., 2016) have now characterized the low-redshift UV absorber distribution in great detail (Figure 1.4), accounting for $\sim 50\%$ of the cosmic baryons, but as much as a third is still unobserved, likely in WHIM-like phases that are too highly ionized to easily detect in UV absorption (Shull et al., 2012a).

In recent years, as the increased sensitivity of *HST*/COS has allowed many more AGN sightlines to be observed with medium-resolution spectroscopy, studies of intervening absorbers have gained a new focus. In conjunction with imaging surveys, absorption-line observations have begun to constrain the properties of the extended gaseous galaxy halos known as the circumgalactic medium (CGM; e.g., Tumlinson et al., 2011, 2013; Werk et al., 2013, 2014; Stocke et al., 2013, 2017). These studies have shown that many of the intervening absorbers trace the CGM, and that the CGM is intimately related to galaxy evolution. The mass of baryons and heavy elements in the CGM of a galaxy seems to be comparable to those in disk gas and stars. Not only are these investigations steps toward resolving the missing baryons problem, but they also provide a means to explain ongoing high rates of star formation in star forming galaxies.

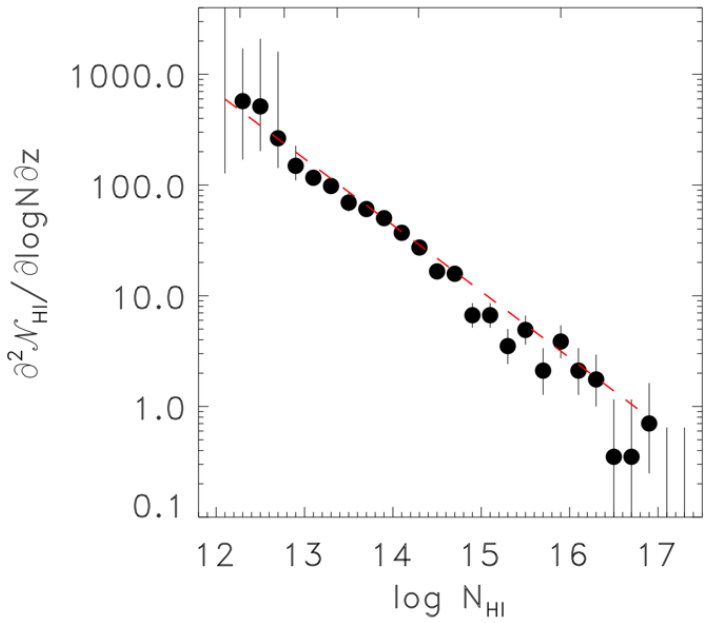

Figure 1.4 Reproduced from Danforth et al. (2016), showing the differential H I IGM absorber frequency distribution. The data shows the number of H I absorbers per unit redshift per unit logarithmic H I column density $\log N_{\rm HI}$.

1.3 Thesis Outline

The subsequent chapters will address several outstanding issues in studies of AGN and the IGM. Each makes use of data from the Cosmic Origins Spectrograph (COS) on board the *HST* (Green et al., 2012). The order-of-magnitude increase in sensitivity of COS compared to previous FUV spectrographs has enabled research that was previously completely impractical. In Chapter 2, I use the vast statistical database of IGM absorbers found in numerous AGN sightlines to constrain the metal evolution of the IGM by comparing observations to numerical photoionization models. That work highlights the uncertainties in current predictions of the UVB, a key motivating factor for Chapter 3. Chapter 3 uses COS to obtain and combine spectra of AGNs at $1.45 \leq z_{\rm AGN} \leq 2.14$, which allows us to constrain the typical rest-frame EUV spectrum of AGNs, a key input into models of the UVB as well as an important constraint for models of AGN accretion disks. In Chapter 4, I present preliminary results from a large survey of absorption lines associated with AGNs, rather than the IGM. Many of these absorbers likely trace energetic outflows. Finally, in Chapter 5, I summarize the results and suggest future work that can build on what is presented here.

Chapter 2

Modeling the Photoionization State of the Intergalactic Medium with Cloudy: Ionization Fractions and Mass Densities for Metal Species

2.1 Chapter Preface

This chapter is based upon Shull et al. (2014), which includes the author of this thesis as a coauthor and was published in The Astrophysical Journal in 2014. For the purposes of this thesis chapter, it has been partially reframed to focus more specifically on the portions of the article to which the author of this thesis made the most major contributions, most notably the numerical photoionization modeling. This chapter compares photoionization models to intergalactic absorber statistics so as to address problems relevant to constraining the ultraviolet metagalactic background spectrum, the total mass of metal species in the intergalactic and circumgalactic media, and the typical baryon overdensities in which intergalactic gas resides. Note that this study was conducted using the absorber statistics from Danforth et al. (2014), an early preprint version of Danforth et al. (2016). The latter publication made several improvements to its analysis and sample size, but this study was not updated to incorporate the improved absorber database. The changes are not expected to have a significant impact on the results of this study.

2.2 Chapter Abstract

We present a study of the metal abundances for five ions (C III, C IV, Si III, Si IV, and O VI) in the low-redshift ($z < 0.75$) intergalactic medium (IGM) using the comprehensive databases of absorption lines detected with the *Far Ultraviolet Spectroscopic Explorer* (*FUSE*)

and the Space Telescope Imaging Spectrograph (STIS) and Cosmic Origins Spectrograph (COS) onboard the *Hubble Space Telescope* that have been presented in Tilton et al. (2012) and Danforth et al. (2014). We express the ion mass densities of these species relative to the critical density as $\Omega_{\rm ion} \equiv \rho_{\rm ion}/\rho_{\rm crit}$, and we use there ratios of the abundances of adjacent ionization states $\frac{\Omega_{\rm CIII}}{\Omega_{\rm CIV}} = 0.70^{+0.43}_{-0.20}$ and $\frac{\Omega_{\rm SiIII}}{\Omega_{\rm SiIV}} = 0.67^{+0.35}_{-0.19}$, to constrain numerical photoionization models. The combination of these observational results and the photoionization models suggests an ionization parameter $\log U \approx -1.5 \pm 0.4$, baryon overdensities $\Delta_b \approx 200 \pm 50$, and Si/C enhanced to approximately three times solar abundances. These results also constrain the shape and strength of the ionizing ultraviolet metagalactic background (UVB) spectral energy distribution. In agreement with several recent investigations (Kollmeier et al., 2014; Shull et al., 2015), we find that the recent calculation of the UVB by Haardt & Madau (2012) underpredicts ionizing photons, and we further find that all published UVB SED shapes struggle to acommodate all observational constraints if a single metallicity is required. Finally, we use our photoionization models to derive correction factors that allow us to convert the metal abundances from observed ionization states to total mass densities for the element. The elemental mass densities are then used to estimate the total metal inventory of the low-redshift IGM, which accounts for $\sim 10 \pm 5\%$ of the cosmic metal abundance.

2.3 Introduction

A complete understanding of cosmology and galaxy evolution requires a detailed understanding of the diffuse gas that lies outside of galaxies, collectively known as the intergalactic medium (IGM) and the circumgalactic medium (CGM). Simulations (e.g., Cen & Ostriker, 1999; Davé et al., 2001; Oppenheimer & Davé, 2008; Smith et al., 2011) predict that most of the universe's baryonic mass at all redshifts resides in the non-luminous, mostly unvirialized IGM and CGM in the form of primordial gas and gas processed by galaxies. Observations confirm these predictions, suggesting that $\sim 80\%$ of baryonic matter resides in these diffuse phases (Shull et al., 2012a).

At high-redshift, a photoionized phase of the IGM, commonly known as the Lyα forest, accounts for nearly all of this baryonic matter; this fraction reduces to $\sim 30\%$ by $z \sim 0$ (e.g.,

Penton et al., 2000; Davé et al., 2001; Danforth et al., 2016). The remainder of the gas resides in hotter gas phases, perhaps shocked during gravitational infall, cloud-cloud collisions, and/or by galaxy winds (e.g, Cen & Fang, 2006). Owing to its diffuse, non-luminous nature, the IGM is most readily observed in absorption against a background continuum source such as an active galactic nucleus (AGN), often using strong, far-ultraviolet (FUV) transitions such as Lyman series H I lines as well as ionized metal species such as C III, C IV, Si III, Si IV, and O VI. Recent low redshift ($z \lesssim 0.4$) studies (e.g., Danforth & Shull, 2005; Danforth et al., 2006; Danforth & Shull, 2008; Lehner et al., 2007; Thom & Chen, 2008; Tripp et al., 2008; Tilton et al., 2012; Danforth et al., 2014, 2016) of these species have focused on observations with the *Far Ultraviolet Spectroscopic Explorer* (*FUSE*) and the Space Telescope Imaging Spectrograph (STIS) and Cosmic Origins Spectrograph (COS) onboard the *Hubble Space Telescope* (*HST*). COS in particular has enormously enhanced our understanding of the IGM and CGM, owing to its order-of-magnitude sensitivity improvement (Green et al., 2012) over previous UV missions, which has allowed the detection of thousands of intergalactic absorption features (e.g., Tumlinson et al., 2011; Danforth et al., 2016). Together, these studies have characterized the bivariate distribution of absorbers in redshift and column density in great detail for many ionic species.

Despite these advances, perhaps as much as $\sim 30\%$ of the universe's baryonic content is undetected or suffers from systematic uncertainties (Shull et al., 2012a). These uncertainties arise from a variety of observational limitations, such as difficulties associated with detecting the hottest gas, which may only display detectable transitions in the x-ray wavelength regime. Further, though metal species do not dominate the cosmological mass inventory of baryons, these species are important tracers of metallicity, ionization state, enrichment history, and interactions with galaxies. In particular, a detailed accounting of cosmological metal production is an important test of our understanding of galaxy evolution and star formation histories, and authors have gone as far as to ask if a "missing metals" problem (Pettini, 1999) may exist if there is a mismatch between observed galaxy metallicities (e.g. Madau & Dickinson, 2014) and absorption line metallicities from systems such as damped Lyα absorbers (e.g. Wolfe et al., 2003) or Lyman-break galaxies (e.g. Steidel et al.,

1999), presumed to trace reservoirs of these metals. However, recent studies of intergalactic gas, especially the CGM, have suggested that this diffuse gas may also be an important reservoir of these metal species (Tumlinson et al., 2011).

Unfortunately, for most sightlnes in the COS archive of observations, one cannot detect all ionization states of an element for a single absorber, owing to practical limitations of the wavelength band-passes of the instrument. For example, one can only observe the primary diagnostic line(s) for a single ionization state of carbon for a particular absorber at a particular redshift with the COS medium-resolution gratings, while absorbers at other redshifts may only offer access to diagnostic line(s) for a single, different ionization state. This limitation introduces a severe uncertainty in any accounting of the mass density of metals in the IGM and CGM: most observed absorption lines probe gas of an unknown, not-directly-observable ionization fraction.

This issue is compounded by uncertainties in the ionizing metagalactic ultraviolet background spectrum (UVB). There have been numerous determinations of the expected UVB, which typically take the form of radiative transfer calculations performed for a grid of redshifts using observational quantities related to AGN, IGM, and galaxy populations as inputs (see Haardt & Madau, 2012, and references therein). However, recently several authors have have questioned the ability of these theoretical spectra to match observations and simulations (Kollmeier et al., 2014; Shull et al., 2015; Khaire & Srianand, 2015). Because many of the ionic species of the IGM and CGM are expected to be photoionized by the UVB, uncertainty in the UVB's spectral shape introduces uncertainty in the baryon census and the ionization fractions necessary to trace the cosmic evolution of metals.

In this chapter, we will address these issues with a suite of photoionization models which we will compare with observed IGM absorber distributions. Though the individual absorbers in these observational databases do not usually contain sufficient diversity of atomic transitions to compare to such photoionization models, the ensemble of absorbers in the database does, enabling us to treat these problems in a statistical sense. In combination with the photoionization models, we will use lines from adjacent ionic species of carbon (C III $\lambda977$ and C IV $\lambda\lambda1548, 1551$) and silicon (Si III $\lambda1206$ and Si IV $\lambda\lambda1393, 1403$) to determine the mean ionization fractions of these

species and thus the cosmic mass density of carbon and silicon, including unseen ion states. We will explore how these results depend on assumptions about the shape of the UVB, and we will test whether the higher ionization species O VI ($\lambda\lambda 1032, 1038$) is sensitive to photoionization from these spectra. We will also discuss the implications of our results for abundance ratios in the IGM.

2.4 Observational Data and Results

We focus our investigation on five metal ion species (C III, C IV, Si III, Si IV, and O VI) with strong transitions in the FUV; Table 2.1 provides the atomic data for these absorption lines along with the redshift ranges and minimum column densities probed by this study. In particular, we draw from two observational surveys of low-z IGM absorption lines (Tilton et al., 2012; Danforth et al., 2014). Unlike high-redshift surveys, Lyα forest line blanketing has negligible effect on the detection and measurement of absorption lines in these surveys. We primarily compare with the results of Danforth et al. (2014)[1] , who used the *HST*/COS medium-resolution ($R \sim 18,000$) gratings, G130M and G160M, to identify IGM absorption systems in the $1135 - 1796$ Å coverage provided by those gratings. The survey identified 2508 H I systems toward 75 AGN at $z_{\rm abs} < 0.75$. A summary of the absorbers used from the Danforth et al. (2014) survey is given in Columns (1)−(3) of Table 2.2.

Owing to the wavelength coverage of the COS gratings, C III (observable at $0.16 < z_{\rm abs} < 0.84$) and C IV (observable at $0.00 < z_{\rm abs} < 0.16$) are never accessible in the same absorber and therefore never probe the same gas clouds. Similarly, Si III (observable at $0.00 < z_{\rm abs} < 0.49$) and Si IV (observable at $0.00 < z_{\rm abs} < 0.29$) are unobservable in the same absorption system for more than a third of our sample. For these reasons, we also check our results against the Tilton et al. (2012) survey, which used both *FUSE* ($905 - 1187$ Å; $R \sim 20,000$) and *HST*/STIS E140M ($1162 - 1729$ Å; $R \sim 45,800$). Though this is a much smaller survey, detecting 746 H I absorption

[1] Danforth et al. (2014) is an early preprint version of Danforth et al. (2016). The latter publication made several improvements to its analysis and sample size, but this study was not updated to incorporate the improved absorber database. The changes are not expected to have a significant impact on the results of this study. See Danforth et al. (2016) for a more detailed description of the differences between these two survey versions.

Table 2.1. Absorption-Line Data

Ion[a]	λ_0[a] (Å)	f[a]	z Range[a] $z_{\rm min} - z_{\rm max}$	$\log N_{\rm min}$[a] (N in cm^{-2})
C III	977.020	0.757	$0.16 - 0.84$	12.67
C IV	1550.781	0.09475	$0.00 - 0.16$	13.17
	1548.204	0.1899	$0.00 - 0.16$	12.87
O VI	1037.6167	0.06580	$0.09 - 0.73$	13.68
	1031.9261	0.1325	$0.10 - 0.74$	13.38
Si III	1206.500	1.63	$0.00 - 0.49$	12.15
Si IV	1402.7729	0.254	$0.00 - 0.28$	12.83
	1393.7602	0.513	$0.00 - 0.29$	12.53

[a]Column (1) lists the observed ion, Column (2) lists the vacuum rest wavelength (λ_0), Column (3) lists the oscillator strength (f), Column (4) lists the redshift range observable with the COS medium-resolution gratings over $1135 - 1796$ Å, and Column (5) lists the approximate minimum column density considered in this study, corresponding to an equivalent width of 30 mÅ. All atomic parameters taken from Morton (2003).

Table 2.2. Summary of Metal-Ion Densities

Ion[a]	$N_{\rm abs}$[a]	Range in $(\log N)$[a] (N in cm^{-2})	$\Omega_{\rm ion}$(STIS)[a] (in $10^{-8} h_{70}^{-1}$)	$\Omega_{\rm ion}$(COS)[a] (in $10^{-8} h_{70}^{-1}$)
C III	77	$12.67 - 14.19$	$4.6^{+1.8}_{-0.8}$	$7.1^{+1.9}_{-1.2}$
C IV	49	$12.87 - 14.87$	$8.1^{+4.6}_{-1.7}$	$10.1^{+5.6}_{-2.4}$
O VI	212	$13.38 - 14.83$	$33.9^{+9.3}_{-4.1}$	$38.6^{+4.8}_{-3.2}$
Si III	87	$12.15 - 13.44$	$1.1^{+0.8}_{-0.3}$	$1.4^{+0.3}_{-0.2}$
Si IV	31	$12.53 - 13.94$	$4.5^{+3.0}_{-1.2}$	$2.1^{+1.0}_{-0.5}$

[a]Column (1) lists the observed ion species, Column (2) lists the number of absorbers from the COS survey (Danforth et al., 2014), Column (3) lists the range of column densities sampled by those absorbers, and Columns (4) and (5) list the IGM mass densities of the different ionic species given as a fractional contribution to closure density ($\Omega_{\rm ion} \equiv \rho_{\rm ion}/\rho_{\rm crit}$) for the *FUSE*+*HST*/STIS survey (Tilton et al., 2012, revised as described in the text) and the *HST*/COS survey (Danforth et al., 2014), respectively.

lines toward 44 AGN, the expanded wavelength coverage of this survey often allows sensitivity to all transitions we consider within the same absorption system. However, we revised the absorber statistics of Tilton et al. (2012) to match the column density ranges of Table 2.2 and the grouping of absorption systems used in Danforth et al. (2014). For more details on revisions to Tilton et al. (2012), see the discussion in Danforth et al. (2016). Also note that these two surveys are not strictly independent of each other; the two surveys overlap in the absorption systems included and the AGN sightlines analyzed.

We express all metal ion mass densities as a fractional contribution to closure density, $\Omega_{\rm ion} \equiv \rho_{\rm ion}/\rho_{\rm crit}$. Here,

$$\rho_{\rm crit} \equiv \frac{3H_0^2}{8\pi G} = 9.205 \times 10^{-30} h_{70}^2 \text{ g cm}^{-3}, \tag{2.1}$$

where the Hubble constant is parameterized $H_0 = (70 \text{ km s}^{-1} \text{ Mpc}^{-1}) h_{70}$. To obtain an ion mass density, an integral is performed over the column-density distribution function of absorbers for a given ion species. This distribution function is typically parameterized as a power law,

$$f(N,z) \equiv (\partial^2 \mathcal{N}/\partial N \partial z) \propto N^{-\beta}, \tag{2.2}$$

with β on the order of 2 for surveys of most ions. The contribution to the critical density by the IGM mass of an ion, given and described in more detail in Tilton et al. (2012), is then calculated as

$$\begin{aligned} \Omega_{\rm ion} &= \frac{H_0 m_{\rm ion}}{c\rho_{\rm cr}} \int_{N_{\rm min}}^{N_{\rm max}} f(N,z) N d(N) \\ &= (1.365 \times 10^{-23} \text{cm}^2) h_{70}^{-1} \, (m_{\rm ion}/\text{amu}) \int_{N_{\rm min}}^{N_{\rm max}} f(N,z) N d(N), \end{aligned} \tag{2.3}$$

where $m_{\rm ion}$ is the ion mass and the integration is over column density (cm^{-2}). We report the uncertainty in $\Omega_{\rm ion}$ as the asymmetric Poisson uncertainty (Gehrels, 1986) in $d\mathcal{N}$, and, in practice, the mass density and its uncertainty is calculated as a sum in logarithmic bins, $\Delta \log N \approx 0.2$. Our lower integration limit ($N_{\rm min}$) is fixed at the column density corresponding to a 30 mÅ equivalent width, set to ensure even and reliable line detections throughout the surveys of interest. The

upper limit, $N_{\rm max}$, is set ion-by-ion according to where the absorber distribution function becomes uncertain, as summarized in Table 2.2. The resultant $\Omega_{\rm ion}$ values for both the *FUSE*+*HST*/STIS and the *HST*/COS surveys are given in Columns (4) and (5) in Table 2.2.

2.5 Photoionization Models

To address the ionization states of the gas hosting the detections of silicon, carbon, and oxygen as well as their dependence on assumptions about the spectral shape of the UVB, we calculate grids of numerical photoionization models from which we identify the ionization conditions consistent with the observations. These numerical models are computed using version 13.03 of the photoionization code Cloudy, last described by Ferland et al. (2013). Our basic approach will be to illuminate slabs of gas with various assumed UVB spectra, and to do this for a variety of gas densities. It is often convenient to instead express this density as a baryon overdensity, Δ_b, which can be related to the hydrogen number density, $n_{\rm H}$, via

$$\Delta_b = (5.26 \times 10^5 \text{ cm}^3) n_{\rm H} (1+z)^{-3}, \tag{2.4}$$

which we will use for most plots of density throughout this chapter. All of our photoionization models will be conducted with solar elemental abundance ratios, though we will discuss the issue of possible enhancements to some abundances later in this chapter.

In describing our photoionization models, it is important to carefully define the intensity and flux quantities to which we will be referring, as there has been some inconsistency in the literature, especially in discussions of photoionization models conducted with Cloudy. In particular, we note that the hydrogen photoionization rate $\Gamma_{\rm H}$ can be related to the specific intensity of the incident spectrum I_ν and its value at the Lyman limit (912 Å), I_0, or to the one-sided unidirectional flux of ionizing photons, Φ_0. Here, we are considering absorbers distant from an isotropic ionizing background spectrum, rather than gas clouds close to a ionizing source, such as a galaxy or star, that iluminates the cloud from one side. In quantifying the unidirectional flux of ionizing photons for input into our photoionization models, the isotropic case of interest here differs from the local-source

case by a factor of 1/4, owing to the illumination of both the forward and backward hemispheres as well as the angluar dependence of that incident light, which introduces a factor of $\langle \cos\theta \rangle = 1/2$. Therefore, the unidirectional ionizing flux for a number density of ionizing photons, n_γ, and a local source can be written as $\Phi_0 = n_\gamma c$, while the corresponding unidirectional flux for an isotropic background is $\Phi_0 = n_\gamma c/4$. This relatively small difference could substantially alter our interpretation of ionization fractions in our models, as well as determinations of the photoionization parameter, $U \equiv n_\gamma / n_{\rm H}$.

2.5.1 Metagalactic Ionizing Background Spectrum Inputs

There is substantial disagreement in the literature over both the strength and shape of the UVB, the primary input to our photoionization models. Here, our approach will be to choose a fixed hydrogen-ionizing background flux Φ_0 ($\rm cm^{-2}\ s^{-1}$) to which we will normalize a variety of commonly-used UVB input spectra of different spectral shapes. For convenience, we label the various spectral energy distributions (SEDs) that we will consider as HM01, HM05, HM12, FG11, and PL. The various HM SEDs are all different versions of the same style of radiative transfer calculation conducted by the same research group with incremental changes among them. HM01 refers to the spectrum provided by Haardt & Madau (2001), which has been included in tabluated form and freqently used with the hydrodynamical grid-code, Enzo (Bryan et al., 2014). HM05, included in tabulated form with Cloudy, is the unpublished 2005 August update to the galaxies+quasars spectrum described in Haardt & Madau (2001). As there are only minor differences between HM01 and HM05, we will only calculate photoionization models for the latter spectrum. HM12, described in Haardt & Madau (2012), is the most recent full version of this lineage of the UVB spectra (but see also Madau & Haardt, 2015, for a partial update). HM01, HM05, and HM12 differ from other calculations of the UVB in their inclusion of the $10 - 100$ keV hard X-ray background, but this portion of the spectrum is not expected to have a substantial effect on the ionization states of the elements considered here.

The other two UVB spectra, FG11 ("Faucher-Giguère 2011") and PL ("power law"), do

not derive from the research group or methodology of the various HM spectra. FG11, a radiative transfer calculation similar in concept to the HM SEDs, refers to the 2011 December update[2] of the spectrum from Faucher-Giguère et al. (2009). The PL spectrum is a broken power-law spectrum that we have constructed for the purposes of these photoionization models, though it is similar in concept to the spectrum in Mathews & Ferland (1987). It connects the $F_\nu \propto \nu^{-1.41}$ composite AGN spectrum of Shull et al. (2012b) (see also Stevans et al., 2014; Tilton et al., 2016, for updated versions of this spectrum) with the soft X-ray observations of AGNs detected in the Lockman Hole (Hasinger, 1994), using a total of four power-law pieces with power-law indices $\alpha_\nu = (2.40, 0.96, 2.58, 1.41)$. All of the UVB spectra used in our photoionization models are plotted in Figure 2.1.

Though it represents the most recent detailed calculation of the UVB, HM12's hydrogen ionizing flux $\Phi_0 \approx 2630$ cm^{-2} s^{-1} has been shown to be inconsistent with the Danforth et al. (2014) observations by Kollmeier et al. (2014), who argue for a factor of five increase based on cosmological simulations using a variant of the GADGET2.0 smooth-particle hydrodynamical code (Springel, 2005; Oppenheimer & Davé, 2008). Though there is general agreement that the HM12 values underpredict the ionizing flux, other authors who have carried out simulations with ENZO have argued for a smaller shortfall of perhaps a factor of two, possibly due to incorrect UV photon escape fractions from galaxies or insufficient quasar emissivities (Shull et al., 2015; Khaire & Srianand, 2015). In general, older, higher values for the hydrogen ionizing flux (e.g., Shull et al., 1999; Haardt & Madau, 2001) seem to have more success reproducing observations of the absorber column-density distribution in cosmological simulations. We therefore normalize all UVBs in our photoionization models to a unidirectional hydrogen ionizing flux $\Phi_0 = 10^4$ cm^{-2} s^{-1}, corresponding to specific intensity $I_0 \approx 3 \times 10^{-23}$ erg cm^{-2} s^{-1} Hz^{-1} sr^{-1} at the 912 Å Lyman edge and hydrogen photoionization rate $\Gamma_{\rm H} \approx 8 \times 10^{-14}$ s^{-1}. Though this value may differ from the actual value to some degree, it is chosen to be broadly consistent with the variety of results in the literature, including recent results from Gaikwad et al. (2017a) and Fumagalli et al. (2017). Small differences in Φ_0

[2] Retreived from `http://galaxies.northwestern.edu/uvb/`.

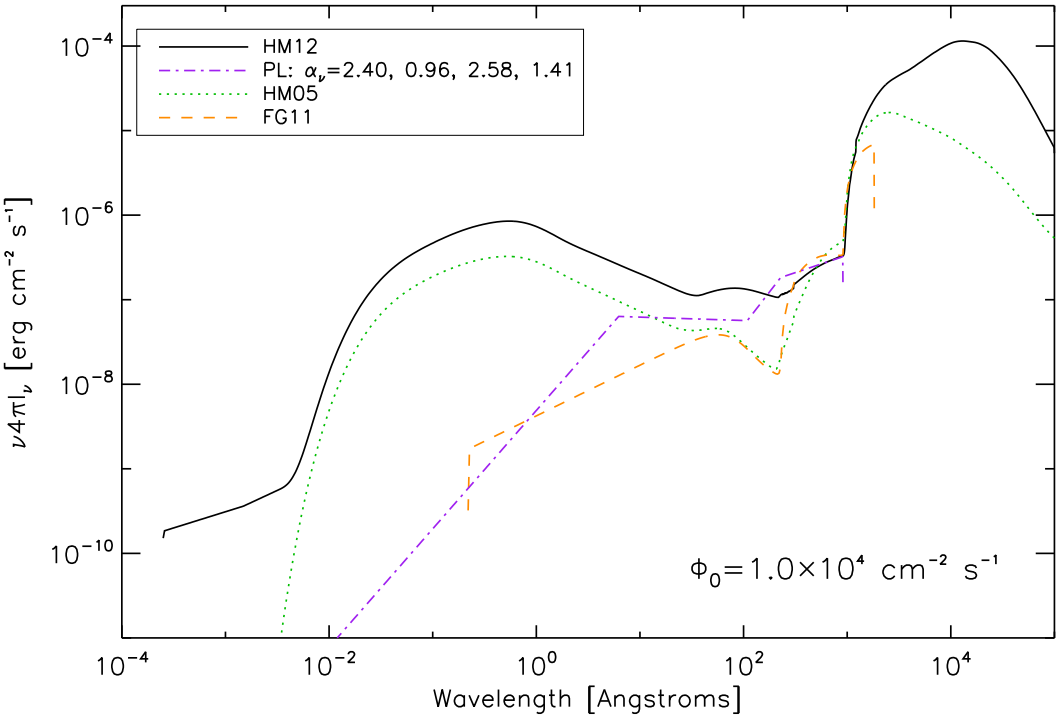

Figure 2.1 Several UVB spectral energy distributions (SEDs) used in our photoionization models. The monochromatic flux, $\nu F_\nu \equiv 4\pi\nu I_\nu$, is plotted for the HM12 (Haardt & Madau, 2012), broken power-law, HM05 (the 2005 update to Haardt & Madau, 2001), and FG11 (the 2001 update to Faucher-Giguère et al., 2009). Each SED is normalized to a unidirectional hydrogen ionizing flux $\Phi_0 = 10^4$ cm^{-2} s^{-1}.

will have little effect on the qualitative results of this chapter except for causing a shift in the preferred values for the baryon overdensity Δ_b in our models. In particular, the photoionization parameter, unidirectional ionizing flux, and baryon overdensity can be related using Equation 2.4 and the definitions given in Section 2.5 as

$$U \equiv \frac{4\Phi_0}{n_{\rm H} c} = (7.02 \times 10^{-8})\Phi_0 \Delta_b^{-1}. \tag{2.5}$$

Baryon densities can thus be easily rescaled to be compatible with different values of Φ_0.

2.6 Results

2.6.1 The Photoionized Species: Carbon and Silicon

The ratios of the adjacent ionization states for carbon and silicon provide a constraint on the appropriate UVB SED shape and the typical baryon overdensity, through the photoionization parameter, $U = n_\gamma / n_{\rm H}$. The numerical Cloudy photoionization models provide the ionization ratios, C III/C IV and Si III/Si IV, for each input UVB SED as a function of baryon overdensity, Δ_b; these values are plotted in Figure 2.2. These curves can be compared against the mean observed values for these ratios in the ensemble of absorbers of the Danforth et al. (2014) COS survey:

$$\frac{\Omega_{\rm CIII}}{\Omega_{\rm CIV}} = 0.70^{+0.43}_{-0.20}, \tag{2.6}$$

$$\frac{\Omega_{\rm SiIII}}{\Omega_{\rm SiIV}} = 0.67^{+0.35}_{-0.19}. \tag{2.7}$$

Comparison against the photoionization model results of Figure 2.2 reveals that the HM05 and FG11 input SEDs cannot reproduce ionization ratios consistent with the observations; they under-produce the doubly ionized states relative to the triply ionized states for all baryon overdensities. The HM12 and PL SEDs, however, produce consistent observationally-consistent ionization ratios for a wide range of overdensities ($\Delta_b \sim 70 - 230$), roughly consistent with photoionization parameters $\log U \approx -1.5 \pm 0.4$

Ultimately, however, we would like to constrain the total mass densities of all ionization states of carbon and silicon. These total mass densities can be expressed in terms of the two ionization

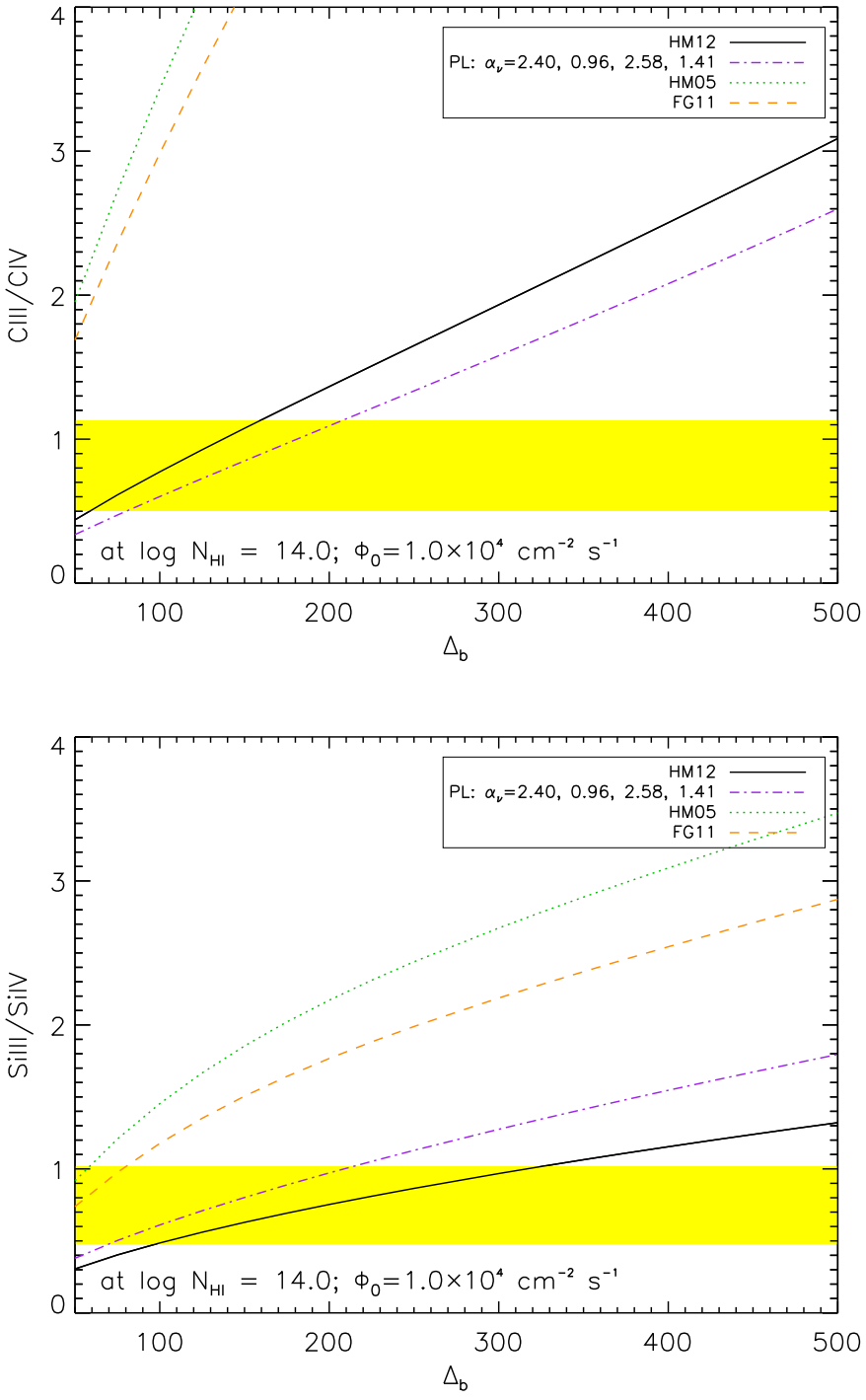

Figure 2.2 Ion abundance ratios for C III/C IV (top) and Si III/Si IV (bottom) as a function of baryon overdensity, Δ_b, for five ionizing SEDs, labeled in the legend. The mean observed ratios from Danforth et al. (2014) are given by the yellow bands. The top two curves, HM05 and FG11, give higher ratios that are inconsistent with observations, while the HM12 and PL SEDs are consistent with observations.

states for which we have observations as

$$\Omega_{\rm C} = (\Omega_{\rm CIII} + \Omega_{\rm CIV}) \left(\frac{\rm C_{total}}{\rm CIII + CIV} \right), \tag{2.8}$$

$$\Omega_{\rm Si} = (\Omega_{\rm SiIII} + \Omega_{\rm SiIV}) \left(\frac{\rm Si_{total}}{\rm SiIII + SiIV} \right). \tag{2.9}$$

The first parenthetical term in each of these expressions is simply the sum of the mass densities for the two observed ioization states. The second terms, which hereafter we refer to as $\rm CF_C$ and $\rm CF_{Si}$ respectively, are the ionization correction factors that express the relationship between the total of all ionization states for the element to the portion in the two observed states. These correction factors are not observables, but, rather, they are quantities that we can determine from the photoionization models. Figure 2.3 presents these theoretical correction factors as a function of baryon overdensity for the various ionizing SEDs in a manner similar to Figure 2.2. From Figure 2.3, we can see that the correction factors become implausibly large for $\Delta_b < 100$, especially for silicon, perhaps suggesting that the metal absorption systems tend to reside in fairly high-density systems relative to the weakest Lyα forest absorbers. The correction factors for the SEDs and baryon overdensities allowed by the ionization ratios discussed above are seemingly

$$\rm CF_C \equiv \frac{\Omega_C}{\Omega_{CIII} + \Omega_{CIV}} \sim 2.0^{+1.0}_{-0.5}, \tag{2.10}$$

$$\rm CF_{Si} \equiv \frac{\Omega_{Si}}{\Omega_{SiIII} + \Omega_{SiIV}} \sim 6^{+4}_{-3}. \tag{2.11}$$

In principle, we can further constrain these results by considering the relative abundances of carbon and silicon. Not only must our results be consistent with plausible overdensities and the observed ionization ratios, but the metallicities implied by the correction factors must also be consistent with the relative abundances of carbon and silicon by mass. From the measured mass densities from the COS survey in Table 2.2, we know that

$$\Omega_{\rm CIII} + \Omega_{\rm CIV} = 17.2^{+5.9}_{-2.7}\ (10^{-8}\ h_{70}^{-1}), \tag{2.12}$$

$$\Omega_{\rm SiIII} + \Omega_{\rm SiIV} = 3.5^{+1.0}_{-0.5}\ (10^{-8}\ h_{70}^{-1}). \tag{2.13}$$

We can therefore express the ratio of the correction factors in terms of the Si/C abundance ratio

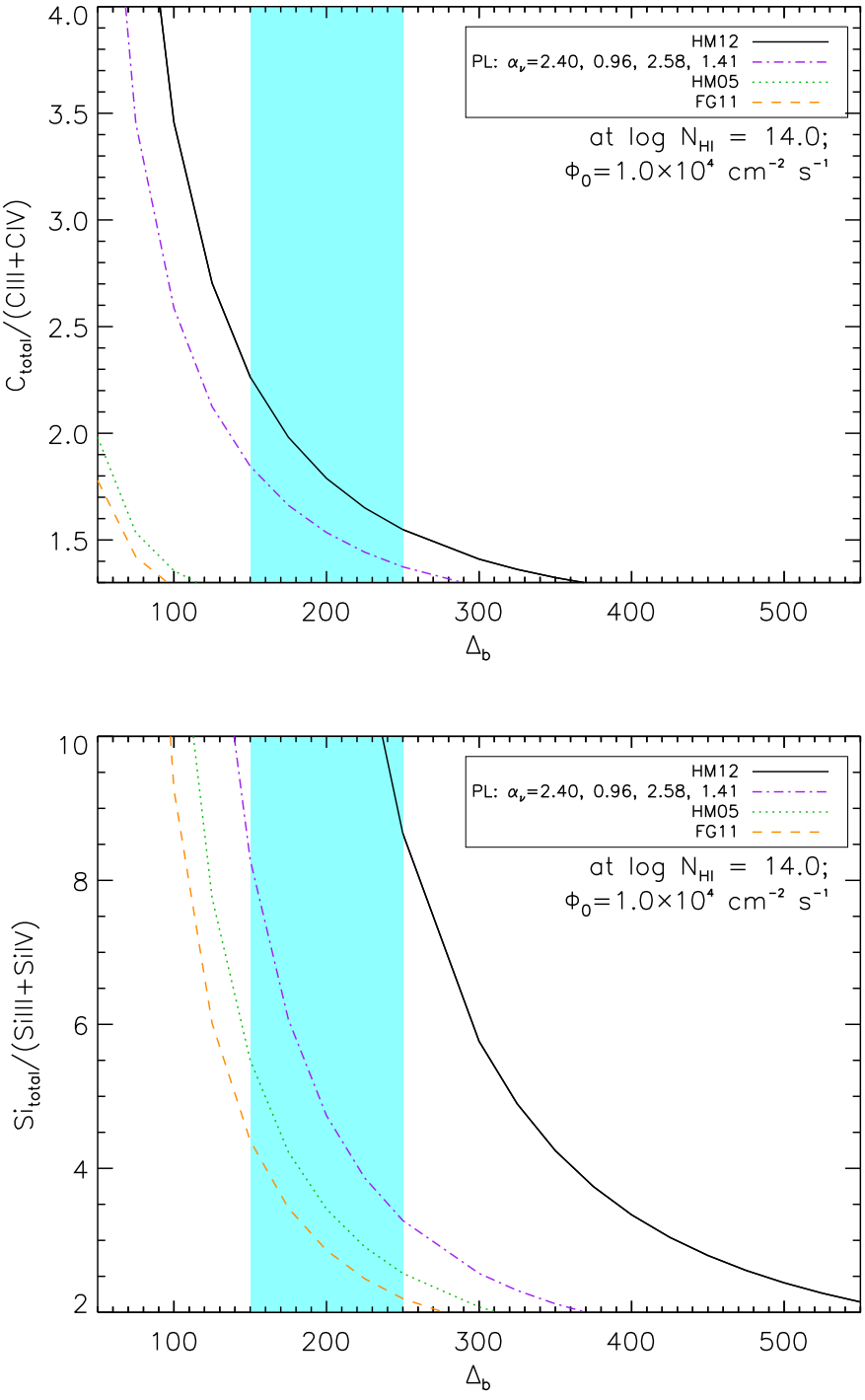

Figure 2.3 Ionization correction factors for total carbon (top) and silicon (bottom) relative to the two observed ionization states as a function of baryon overdensity, Δ_b, for five ionizing SEDs, labeled in the legend. Vertical blue bands mark $\Delta_b = 200 \pm 50$, roughly the values that provide consistent ionization corrections and metallicities with enhanced Si/C.

by mass, $\rho_{\rm Si}/\rho_{\rm C}$, as

$$\frac{{\rm CF_{Si}}}{{\rm CF_C}} = \left(\frac{\rho_{\rm Si}}{\rho_{\rm C}}\right) \frac{\Omega_{\rm CIII} + \Omega_{\rm CIV}}{\Omega_{\rm SiIII} + \Omega_{\rm SiIV}} = \left(1.17^{+0.52}_{-0.25}\right) \left[\frac{\rho_{\rm Si}/\rho_{\rm C}}{0.238}\right]. \tag{2.14}$$

In the final step, we have substituted the expressions from Equations 2.12 and 2.13 and written the expression in terms of the solar abundance ratio, $\rho_{\rm Si}/\rho_{\rm C} = 0.238$. We plot this ratio in Figure 2.4, again for all SEDs and as a function of baryon overdensity. The yellow band in Figure 2.4 indicates the values allowed under the assumption of solar abundances. However, the high baryon overdensities allowed under this assumption, $\Delta_b > 310$, are inconsistent with our previous constraints on overdensity, suggesting that silicon must be enhanced relative to carbon above solar abundances. Evidently, to maintain consistency the the constraints discussed previously, we require an enhancement of Si/C to approximately three times that of solar abundances, as indicated by the blue band in Figure 2.4. This could be due to enhancements from alpha-process nucleosynthesis, similar to ratios that have long been known to occur in metal-poor stars (e.g., Wallerstein, 1962; Akerman et al., 2004) and some damped Lyα absorbers (Pettini et al., 2008).

The ensemble of constraints from Figures 2.2 through 2.4 suggests baryon overdensities $\Delta_b \sim 200 \pm 50$ for $\Phi_0 = 10^4$ cm^{-2} s^{-1}. Lower values of Φ_0, such as those suggested by Haardt & Madau (2012), would require baryon overdensities so low that they would imply unrealistic ionization ratios and correction factors. These photoionization models thus further confirm the uncertainty in UVB strength noted by other authors, suggesting that the recent calculations of Haardt & Madau (2012) are insufficient to account for the ionization state of the IGM. Uncertainty regarding the UVB also extends to the shape of the SED, however. A close examination of Figures 2.2 through 2.4 reveals that no one SED can match all of the aformentioned constraints without tension. Somewhat surprisingly, our simplistic PL SED seems to do the best job at matching the constraints, suggesting that substantial work is still required to correctly reproduce the UVB in radiative transfer calculations. Some of this uncertainty may arise due to uncertainties in the mean contributions of AGNs and galaxies in the extreme-UV and soft X-ray regimes; some constraints for the extreme-UV spectra of AGNs are suggested by the work presented in Chapter 3.

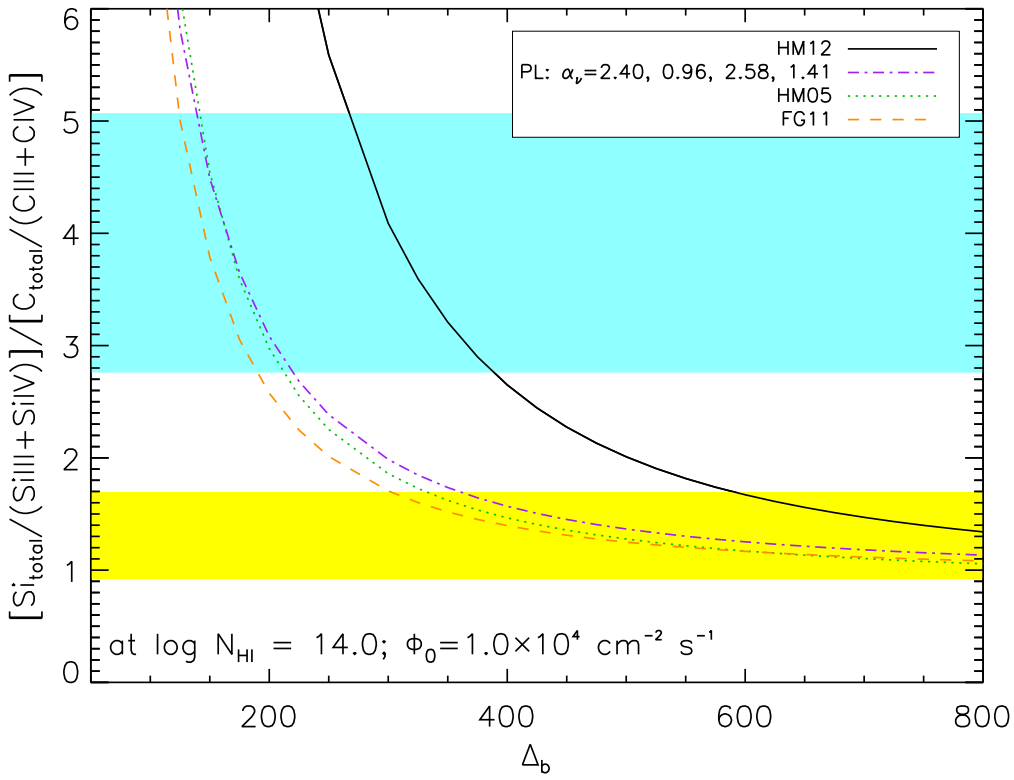

Figure 2.4 Ratio of the silicon and carbon ionization correction factors for several SEDs as a function of baryon overdensity. The yellow band shows the region allowed by solar abundance ratios for Si/C, while the blue band shows the allowed region when Si/C is enhanced to three-times solar ratios.

2.6.2 UVB Redshift Evolution within the Observed Absorber-Redshift Range

A potential limitation of the analysis so far is the evolution of the UVB with redshift among the absorbers probed by the observational surveys. Shull et al. (2012a) parameterized the the UVB redshift evolution given in Haardt & Madau (2012) as $\Gamma_{\rm H} \propto (1+z)^{4.4}$ which, after accounting for the factor of $n_{\rm H} \propto (1+z)^3$, corresponds to a photoionization parameter evolution of $U \propto (1+z)^{1.4}$. In particular, we might therefore expect to see redshift evolution in the carbon absorbers of the Danforth et al. (2014) survey, which have mean redshifts of $\langle z_{\rm CIII} \rangle = 0.35$ and $\langle z_{\rm CIV} \rangle = 0.06$. If the Haardt & Madau (2012) parameterization is correct, then we might expect that the C IV absorbers probe gas with a photoionization parameter that is on average only 70% that of the gas probed by C III.

To test this evolution effect, we consider the *FUSE*+*HST*/STIS survey of Tilton et al. (2012), which has wider wavelength coverage and can probe both ions in the same gas. In those 28 absorbers, we find no significant difference in the C III/C IV ratios compared to the COS survey. We therefore make no attempt to correct for this redshift evoution in the remainder of this study, as the effect is evidently smaller than our other uncertainties.

2.6.3 The Extent of Photoionization of O VI

The highly-ionized species O VI is one of the most common diagnostics of IGM gas (e.g., Savage et al., 2014) and the only commonly observable species of oxygen for UV and optical studies. Owing to its higher ionization state and ionization energy, O VI likely traces gas of different thermal conditions and ionization state than the photoionized carbon and silicon species that we have discussed so far. If we wish to constrain the total mass density of metals in the IGM, it is crucial to constrain the ionization state of the gas traced by O VI, as the mass density traced by O VI is additive with that traced by the silicon and carbon species. However, many cosmological simulations (e.g., Oppenheimer & Davé, 2009) have suggested that O VI can be produced through both photoionization and collisional ionization processes and can exist in complicated multiphase

gas structures. If we wish to use the O VI mass densities in an additive fashion with the photoionized carbon and silicon species, it is therefore worth asking if a substantial amount of detected O VI is likely to arise in gas at the overdensities probed by the aforementioned photoionized species.

Figure 2.5 plots the ionization fraction of O VI for each ionizing SED as a function of baryon overdensity. For all SEDs at the preferred baryon overdensities, $\Delta_b \sim 200 \pm 50$, the O VI fraction remains below 10%, and for all SEDs other than HM12 it remains far below that. These results strongly suggest that the O VI detections are indeed tracing gas that is distinct from that probed by C III, C IV, Si III, and Si IV.

2.6.4 The Total Metal Abundance

Ultimately, we would like to calculate the total mass density of metals in the IGM, $\Omega_{\rm Z}$, combining our results for the photoionized species of carbon and silicon and the higher ionization state of oxygen, O VI. We can calculate this value by determining the individual mass densities of carbon, silicon, and oxygen using the measurements of the detected species and the results of our photoionization modeling. We can then divide those values by the mass fractions of those elements relative to all heavy elements. Finally, we can combine the results for the gas traced by the photoionized species and that traced by O VI to obtain a total IGM mass density of metals.

Caffau et al. (2011) provide solar abundances of 18.2%, 4.34%, and 44.0% for carbon, silicon, and oxygen, respectively, as well as for all other elements. If we enhance all alpha-process elements (those with even atomic numbers from oxygen through calcium) by a factor of three as we argued above, then these mass fractions become 7.95%, 5.70%, and 58.0%. These values yield $\Omega_{\rm Z} = 4.3 \times 10^{-6}$ from carbon and $\Omega_{\rm Z} = 3.7 \times 10^{-6}$ from silicon, for a combined value of $\Omega_{\rm Z} = (4.0 \pm 0.5) \times 10^{-6}$ for the photoionized gas.

As our photoionization models do not constrain the ionization fraction of the gas traced by O VI, we follow the approach taken in several IGM surveys (Danforth & Shull, 2008; Shull et al., 2012a; Tilton et al., 2012; Danforth et al., 2016) and adopt an ionization fraction $f_{\rm OVI} = 0.1$, though we note that some cosmological hydrodynamic simulations find ionization fractions as high

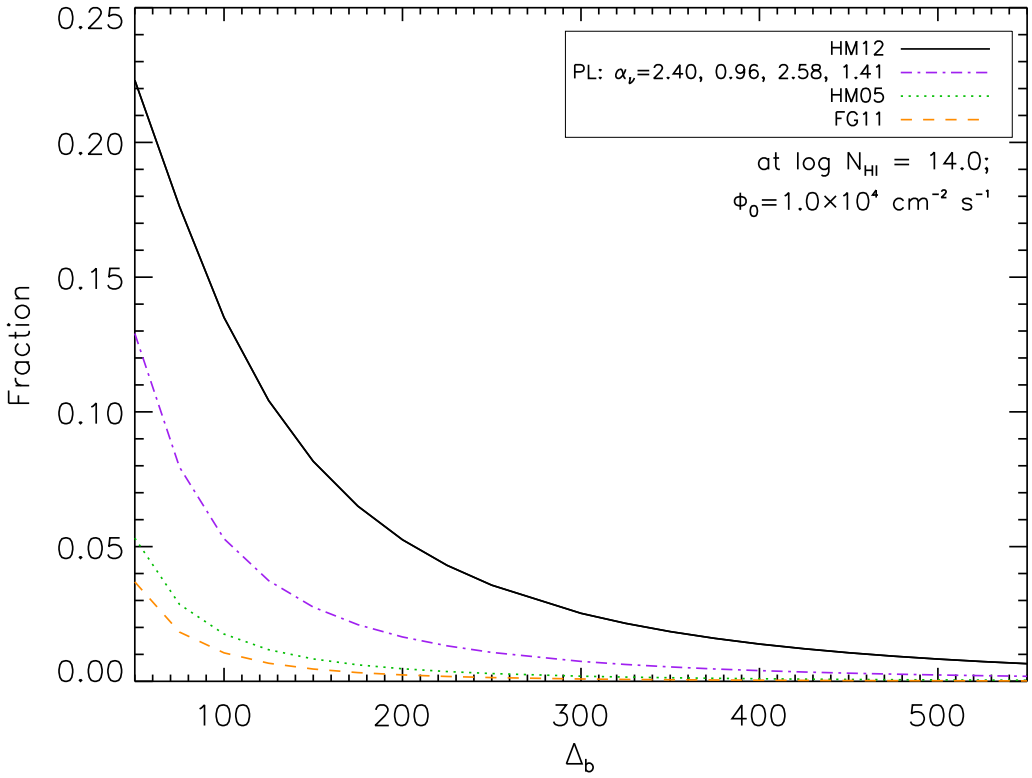

Figure 2.5 Ionization fraction of O VI for several ionizing SEDs as a function of baryon overdensity.

as $f_{\rm OVI} = 0.2$ (e.g., Smith et al., 2011). Combined with the oxygen-to-metals mass fraction (50%), this yields $\Omega_{\rm Z} = (6.7 \pm 0.8) \times 10^{-6}$.

The combined, total IGM metal density for both the photoionized gas traced by silicon and carbon and the hotter phase traced by O VI is thus $\Omega_{\rm Z} \sim 10^{-5}$ and a mass density of $\rho_{\rm Z} = (1.45 \pm 0.92) \times 10^6$ M$_\odot$ Mpc^{-3}.

2.7 Discussion and Conclusion

The combination of our *FUSE*+*HST*/STIS (Tilton et al., 2012) and *HST*/COS (Danforth et al., 2014, 2016) IGM surveys, the largest such catalogs to date, with suites of photoionization models conducted with Cloudy is a powerful tool for constraining the metal content of the IGM and CGM. We have shown that the ratios of adjacent ionization states of carbon and silicon (C III, C IV, Si III, and Si IV) can constrain the shape of the UVB SED and the typical IGM baryon overdensity. We have calculated ionization correction factors, $\mathrm{CF_C} \equiv \Omega_{\rm C}/(\Omega_{\rm CIII} + \Omega_{\rm CIV}) \sim 2.0^{+1.0}_{-0.5}$ and $\mathrm{CF_{Si}} \equiv \Omega_{\rm Si}/(\Omega_{\rm SiIII} + \Omega_{\rm SiIV}) \sim 6^{+4}_{-3}$. Interestingly, the combined constraints of the observations and these photoionization models suggest that abundances of alpha-process elements are enhanced relative to solar abundances in the low-z IGM. Perhaps the bulk of these metals are injected into the IGM by massive stars in young stellar populations.

Using these results, we have shown that the photoionized phase of the IGM contains a metal abundance $\Omega_{\rm Z} = (4.0 \pm 0.5) \times 10^{-6}$, while the hotter phase traced by O VI contains metal abundance $\Omega_{\rm Z} = (6.7 \pm 0.8) \times 10^{-6}$, for a combined mass density in both phases of $\rho_{\rm Z} = (1.45 \pm 0.9) \times 10^6$ M$_\odot$ Mpc^{-3}. Considering a typical integrated star formation rate density, $\rho_* = (6 \pm 2) \times 10^8$ M$_\odot$ Mpc^{-3} (Gallazzi et al., 2008; Bouwens et al., 2011; Madau & Dickinson, 2014), with a typical metal yield $y_m = 0.025 \pm 0.010$, the expected cosmic density of heavy elements is $(1.5 \pm 0.8) \times 10^7$ M$_\odot$ Mpc^{-3}. Our accounting of IGM metals therefore accounts for approximately 10 ± 5% of the expected cosmic heavy elements, with the remainder presumably residing in the halos of galaxies and in phases of the IGM and CGM that are not effectively probed by the transitions discussed in this study. Further progress toward a comprehensive account of IGM metals will likely require

further, carefully targeted UV and X-ray observations that identify multiphase gas around galaxies in a variety of absorption lines. Similar accountings to those presented in this chapter could be undertaken with many more ionized species, should the statistics for the absorber column-density distributions of those species become robust enough in the future.

In summary, the primary conclusions of this chapter are:

- The mean mass densities of adjacent ionization states of carbon and silicon from the Danforth et al. (2014, 2016) survey allows us to statistically calculate the mean mass abundance ratios of these species, C III/C IV$= 0.70^{+0.43}_{-0.20}$ and Si III/Si IV$= 0.67^{+0.35}_{-0.19}$. Combined with photoionization modeling, these values imply correction factors for the unseen ionization states and also imply an enhancement to Si/C abundance to approximately three times the solar ratios.

- This photoionized gas accounts for a total metal abundance of $\Omega_{\rm Z} = (4.0 \pm 0.5) \times 10^{-6}$, while the more highly ionized gas traced by O VI accounts for $\Omega_{\rm Z} = (6.7 \pm 0.8) \times 10^{-6}$. Combined, this represents $\sim 10 \pm 5\%$ of the expected cosmic heavy elements, or a mass density of $\rho_{\rm Z} = (1.45 \pm 0.92) \times 10^6$ M$_\odot$ Mpc^{-3}.

- Our photoionization models are roughly consistent with a UVB with a unidirectional hydrogen ionizing flux of $\Phi_0 = 10^4$ cm^{-2} s^{-1}, a value higher than that recommended by the recent study of the UVB by Haardt & Madau (2012). This value is consistent with other values in the literature (Shull et al., 1999; Haardt & Madau, 2001; Kollmeier et al., 2014; Shull et al., 2015; Khaire & Srianand, 2015). However, all of the UVB SEDs investigated show some tension with the observational constraints, suggesting that substantially more work is required if calculations of the UVB are to fully match observations.

- The combination of observations and photoionization models requires an ionization parameter $\log U \approx -1.5 \pm 0.4$, baryon overdensities $\Delta_b \approx 200 \pm 50$, and Si/C enhanced to approximately three times solar abundances. At the mean redshift of the observations,

$\langle z_{\rm abs} \rangle = 0.14$, the overdansity corresponds to a hydrogen density typical of extended halo gas, $n_{\rm H} \approx 10^{-4.25 \pm 0.10}$ cm^{-3}.

Chapter 3

HST-COS Observations of AGNs. III. Spectral Constraints in the Lyman Continuum from Composite COS/G140L Data

3.1 Chapter Preface

This chapter originally appeared as Tilton et al. (2016), published in The Astrophysical Journal, Volume 817, article 56, in 2016. It addresses the typical extreme-ultraviolet AGN spectrum, its contribution to the ultraviolet mategalactic background spectrum, and the contraints implied for accretion disk atmospheres. It builds upon two preceding papers which addressed related issues, Shull et al. (2012b) and Stevans et al. (2014), the latter of which included the author of this thesis as a coauthor.

3.2 Chapter Abstract

The rest-frame ultraviolet (UV) spectra of active galactic nuclei (AGNs) are important diagnostics of both accretion disk physics and their contribution to the metagalactic ionizing UV background. Though the mean AGN spectrum is well characterized with composite spectra at wavelengths greater than 912 Å, the shorter-wavelength extreme-UV (EUV) remains poorly studied. In this third paper in a series on the spectra of AGNs, we combine 11 new spectra taken with the Cosmic Origins Spectrograph on the *Hubble Space Telescope* with archival spectra to characterize the typical EUV spectral slope of AGNs from $\lambda_{\rm rest} \sim 850$ Å down to $\lambda_{\rm rest} \sim 425$ Å. Parameterizing this slope as a power law, we obtain $F_\nu \propto \nu^{-0.72\pm0.26}$, but we also discuss the limitations and systematic uncertainties of this model. We identify broad emission features in this

spectral region, including emission due to ions of O, Ne, Mg, and other species, and we limit the intrinsic He I 504 Å photoelectric absorption edge opacity to $\tau_{\rm HeI} < 0.047$.

3.3 Introduction

Active galactic nuclei (AGNs) represent the phase of rapid gas accretion and the associated high-energy emission around the supermassive black holes at the centers of their host galaxies. Their spectral properties in the ultraviolet and optical wavelength regimes are complex and diverse. Most commonly, their extreme-UV (EUV; $\lambda < 912$ Å) and far-UV (FUV; 1000 Å $< \lambda <$ 2000 Å) spectra consist of broad (>1000 km s^{-1}) and narrow emission lines superimposed on top of a roughly power-law continuum spectrum thought to arise in the AGN's accretion disk (e.g., Krolik, 1999). As some of the most luminous objects in the universe, AGNs are important to a wide array of astrophysical phenomena at all scales. Understanding their spectra is therefore crucial to understanding a variety of processes.

At the smallest scales, AGN spectra probe the structure of the accretion processes that produce the continuum flux and ultimately control the flow of gas onto the black hole. This flux in turn regulates the ionization conditions of the gas that forms the broad emission lines. The kinematics and geometry of the broad emission line region itself remain poorly understood (e.g., Gaskell, 2009, for a review), but the spectral properties of these lines serve as the primary diagnostics of the masses of the AGN black holes (e.g., Peterson, 1993; Vestergaard & Peterson, 2006; Tilton & Shull, 2013). At galactic scales, we are just beginning to understand the broader role of AGN mechanical and radiative luminosity in regulating processes such as star formation in their host galaxies (e.g., Hopkins et al., 2009; Silk & Norman, 2009; Arav et al., 2013, and references therein).

On the largest cosmological scales, radiation from AGNs governs much of the evolution of the intergalactic medium (IGM), the primary reservoir of baryons at all redshifts. Because galactic stellar populations cannot produce sufficient radiation to reionize He II, AGNs are thought to be the primary cause of He II reionization at $z \approx 3$ (e.g., Shull et al., 2004). At lower redshifts ($z < 3$),

AGNs dominate the UV metagalactic ionizing background radiation (UVB; Haardt & Madau, 2012, and references therein), which largely controls the ionization and thermal state of the IGM. Low-redshift UV surveys of IGM absorption lines (e.g., Danforth & Shull, 2008; Tripp et al., 2008; Thom & Chen, 2008; Tilton et al., 2012; Danforth et al., 2016) have now characterized the distribution of H I and metal absorbers. However, the IGM baryon census remains incomplete (Shull et al., 2012a) and sensitive to assumptions about the metagalactic ionizing background, which in turn depends on an understanding of the mean properties of the UV spectra of AGNs. Recently, there have been doubts raised in the literature (Kollmeier et al., 2014; Shull et al., 2015; Khaire & Srianand, 2015) about the ability of current estimates of the UVB to match observational results in the low-redshift Lyα forest of H I absorbers.

A common technique for constraining the average behavior of AGN spectra is the construction of composite spectra from individual spectra of different AGNs. Though such a technique cannot address the dramatic variations among AGN spectra, it can constrain the consistent mean behavior of their spectral energy distributions while also allowing the detection of spectral features that may be too weak to detect in any one observation, such as faint emission lines or absorption edges. The rest-frame FUV continuum has been well-studied in composites that draw from samples of moderate-to-high redshift AGNs, where their rest-frame UV is accessible to ground-based telescopes (Francis et al., 1991; Carballo et al., 1999; Brotherton et al., 2001; Vanden Berk et al., 2001; Xie et al., 2015; Selsing et al., 2015). Probing deeper into the rest-frame EUV from the ground, however, is complicated by the increased density of IGM absorbers at higher redshifts. Further, the EUV and FUV spectra of low-redshift AGNs are entirely inaccessible from ground-based facilities.

For these reasons, the best probes of the rest-frame EUV and FUV continua come from space-based observations in the UV. Various authors have constructed EUV and FUV composites using the Faint Object Spectrograph (FOS), the Goddard High-Resolution Spectrograph (GHRS), the Space Telescope Imaging Spectrograph (STIS), and the Wide Field Camera 3 (WFC3) UVIS grism onboard the *Hubble Space Telescope* (*HST*) (Zheng et al., 1997; Telfer et al., 2002; Lusso et al., 2015), and others have used the *Far-Ultraviolet Spectroscopic Explorer* (*FUSE*; Scott et al., 2004a).

Parameterizing the EUV continua as power laws, $F_\lambda \propto \lambda^{\alpha_\lambda}$ and $F_\nu \propto \nu^{\alpha_\nu}$ with $\alpha_\nu = -(2 + \alpha_\lambda)$, these authors arrived at spectral indices that differed owing to systematic differences in target selection, composite construction, and the separation of continuum and emission-line flux, which can be complicated by broad emission lines such as Ne VIII $\lambda\lambda 770, 780$. In particular, Scott et al. (2004a) obtained a substantially harder EUV spectrum, $\alpha_\nu = -0.56^{+0.38}_{-0.28}$, than Telfer et al. (2002), who obtained $\alpha_\nu = -1.57 \pm 0.17$ in a radio-quiet subsample, or Lusso et al. (2015), who obtained $\alpha_\nu = -1.70 \pm 0.61$.

This paper is the third in a series that use the Cosmic Origins Spectrograph (COS) on *HST* to constrain the EUV and FUV spectra of AGN through composite spectra. The improved sensitivity of COS compared to past UV spectrographs makes it an ideal instrument for studying a large sample of AGN at high signal-to-noise ratios (S/N). In Shull et al. (2012b) we presented a pilot study of composite spectrum construction using 22 AGNs observed with the medium-resolution grating modes of COS (G130M and G160M). Stevans et al. (2014) extended this work, constructing a medium-resolution COS composite spectrum of the rest-frame FUV and EUV from 159 AGNs at redshifts $0.001 < z_{\rm AGN} < 1.476$. This study obtained an EUV slope $\alpha_\nu = -1.41 \pm 0.15$, consistent with values in Shull et al. (2012b), Telfer et al. (2002), and Lusso et al. (2015). Unfortunately, the COS archive of spectra from which Stevans et al. (2014) drew had fewer than 10 AGNs sampling rest-frame wavelengths $\lambda < 600$ Å and none at $\lambda < 480$ Å.

In this paper, we present 11 new, low-resolution COS/G140L spectra of AGNs at $1.45 \leq z_{\rm AGN} \leq 2.14$ from *HST* Cycle 21 observations (PID 13302, Shull P.I.). We combine them with existing medium-resolution data to construct composite spectra that extend to shorter rest-frame wavelengths, 400 Å $< \lambda <$ 850 Å, more robustly than our previous COS composites. This paper updates the work presented in Shull et al. (2012b) and Stevans et al. (2014) and improves the constraints and statistical bounds on the spectral behavior of the shortest wavelengths probed by Stevans et al. (2014). In Section 3.4 we describe the sample, data processing, and composite contruction techniques. In Section 3.5, we discuss our results for the typical EUV slope, limits on the He I 504 Å photoelectric edge, applications to accretion disk models, and the broad emission

lines observed in the composite. Finally, in Section 3.6 we summarize our results.

3.4 Methodology

At a general level, our analysis is similar to the methods described in Stevans et al. (2014). However, a number of small differences arise, owing to our use of lower resolution COS/G140L data and our focus on a smaller EUV wavelength range. We therefore describe our methodology in this section. Throughout this chapter we adopt atomic transition wavelengths and other atomic properties from Morton (2003). When that catalog does not contain the line of interest, we use the NIST Atomic Spectra Database.[1] Where necessary, we adopt a flat ΛCDM cosmology with $H_0 = 71$ km s^{-1} Mpc^{-1}, $\Omega_m = 0.27$, and $\Omega_\Lambda = 0.73$. All neutral hydrogen column densities $N_{\rm HI}$ are expressed in units of cm^{-2}.

3.4.1 Sample, Data Acquisition, and Processing

We observed 11 AGNs at $1.45 \leq z_{\rm AGN} \leq 2.14$ with COS/G140L. The COS/G140L grating provides a resolving power of 1500 to 4000 over a waveband of approximately 1100 Å to 2150 Å with the 1105 Å central wavelength setting used for all exposures. These targets were selected on the basis of their high *GALEX* fluxes (Bianchi et al., 2014), so the sample likely probes the high end of the AGN UV luminosity function. It is not a complete or unbiased sample, except in the sense that these targets represent the best COS observations of known bright AGNs in this redshift regime and were chosen without prior knowledge of their EUV spectral shapes. One other target in the redshift range of interest, Ton 34, has existing high-S/N observations with COS/G140L and other UV instruments available in the HST archives. We exclude this target from our analysis because it was observed owing to its position as an extreme outlier in the distribution of EUV slopes as well as its prominent broad absorption lines (Binette & Krongold, 2008a,b; Krongold et al., 2010). It would therefore strongly bias the slope of our composite spectrum. In addition to the COS/G140L data, we also use almost all (9 of 10) medium-resolution targets from Stevans et al. (2014) with

[1] `http://www.nist.gov/pml/data/asd.cfm`

Table 3.1. *HST*/COS Observation Details

Target	Right Ascension (J2000)	Declination (J2000)	Grating	Exp. Time (s)	Obs. Date (GMT)	Program ID
			COS/G140L			
HS1803+5425	18 04 37.478	+54 25 40.65	G140L	5460.736	2014-02-26	13302
HE1120+0154	11 23 20.720	+01 37 47.56	G140L	4992.768	2014-06-19	13302
SBS1010+535	10 13 30.165	+53 15 59.71	G140L	10921.440	2014-01-30, 2013-10-01	13302
HE0248-3628	02 50 55.326	-36 16 35.76	G140L	9597.568	2014-06-28, 2014-12-06	13302
US2504	11 29 50.178	+26 52 53.97	G140L	5040.704	2015-02-15	13302
SDSSJ125140.83+080718.4	12 51 40.810	+08 07 18.19	G140L	5000.800	2014-06-19	13302
SDSSJ083850.15+261105.4	08 38 50.153	+26 11 05.26	G140L	5040.672	2013-12-01	13302
SDSSJ094209.14+520714.5	09 42 09.163	+52 07 14.54	G140L	5460.704	2013-10-06	13302
PG1115+080A1	11 18 16.930	+07 45 58.52	G140L	5000.704	2014-02-12	13302
HB89-1621+392	16 23 07.665	+39 09 32.18	G140L	5108.800	2013-10-11	13302
SBS1307+462	13 10 11.620	+46 01 24.50	G140L	5270.720	2013-11-17	13302
			COS/G130M and COS/G160M			
SDSSJ084349.49+411741.6	08 43 49.476	+41 17 41.64	G130M	4361.408	2011-05-11	12248
			G160M	7010.368	2011-05-11	12248
HE0439-5254	04 40 11.900	-52 48 18.00	G130M	8402.944	2010-06-10	11520
			G160M	8936.064	2010-06-10	11520
SDSSJ100535.24+013445.7	10 05 35.257	+01 34 45.60	G130M	11251.740	2011-03-13	12264
			G160M	22413.152	2011-03-13	12264
PG1206+459	12 08 58.011	+45 40 35.48	G130M	17361.120	2010-01-04	11741
			G160M	36093.824	2010-01-04	11741
PG1338+416	13 41 00.780	+41 23 14.10	G130M	22743.488	2010-05-30, 2010-05-24	11741
			G160M	35013.312	2010-05-24, 2010-05-25, 2010-05-27	11741
LBQS1435-0134	14 37 48.284	-01 47 10.78	G130M	22347.52	2010-08-08, 2010-08-18	11741
			G160M	34165.984	2010-08-18, 2010-08-17, 2010-08-22	11741
PG1522+101	15 24 24.580	+09 58 29.70	G130M	16401.184	2010-09-12, 2010-09-14	11741
			G160M	23026.304	2010-09-14, 2010-09-07	11741
Q0232-042	02 35 07.385	-04 02 05.67	G130M	16019.104	2010-02-16, 2010-02-20	11741
			G160M	22840.192	2010-02-20, 2010-01-09	11741
PG1630+377	16 32 01.120	+37 37 50.00	G130M	22988.992	2009-12-13, 2010-11-25	11741
			G160M	14304.032	2010-08-01, 2010-11-26	11741

$z_{\rm AGN} > 0.98$, the redshift threshold above which all of our targets can be normalized to the same continuum window. The one exception is FIRST J020930.7-043826 ($z_{\rm AGN} = 1.131$), which we exclude because H I continuum absorption at $z_{\rm LLS} = 0.39035$ makes most of the short-wavelength end of the spectrum unusable. All observations are summarized in Table 3.1. Table 3.2 lists basic physical parameters of the targets, including redshifts retrieved from the literature and measured monochromatic luminosities at rest-frame 573 Å (a wavelength region for which all targets have useable coverage). For redshifts without a reported formal uncertainty, we conservatively assume $\sigma_{z_{\rm AGN}} = 0.01$. All luminosity measurements are taken from spline fits and include corrections for Galactic extinction, identified H I absorption, and resolution effects (see below). They do not account for errors due to unidentified H I absorption from intervening absorbers that are redshifted out of the observational band or the absolute flux calibration of the instrument.

All calibrated exposures for each target were coadded using CoAdd_X1D version 3.3 from

Table 3.2. AGN Properties[a]

Target	Redshift ($z_{\rm AGN}$)	$z_{\rm AGN}$ Reference	α_λ	F_0	$\log\left[\frac{\lambda L_\lambda(573\ \text{Å})}{\text{erg s}^{-1}}\right]$
		COS/G140L			
HS1803+5425	1.448	Engels et al. (1998)	-0.12 ± 0.03	1.9642 ± 0.0555	46.329 ± 0.019
HE1120+0154	1.471700 ± 0.000438	Hewett & Wild (2010)	-1.24 ± 0.05	1.1386 ± 0.0241	46.499 ± 0.021
SBS1010+535	1.515848 ± 0.000444	Hewett & Wild (2010)	-4.17 ± 0.01	0.0911 ± 0.0005	46.280 ± 0.004
HE0248-3628	1.536	Wisotzki et al. (2000)	-1.54 ± 0.07	2.2393 ± 0.0602	46.773 ± 0.010
US2504	1.542621 ± 0.000499	Hewett & Wild (2010)	-1.88 ± 0.02	0.6622 ± 0.0104	46.421 ± 0.011
SDSSJ125140.83+080718.4	1.596100 ± 0.005000	Schneider et al. (2010)	-1.40 ± 0.03	0.7683 ± 0.0139	46.397 ± 0.016
SDSSJ083850.15+261105.4	1.618279 ± 0.000438	Hewett & Wild (2010)	-1.80 ± 0.07	0.6582 ± 0.0185	46.458 ± 0.026
SDSSJ094209.14+520714.5	1.652971 ± 0.000493	Hewett & Wild (2010)	-2.53 ± 0.03	0.2592 ± 0.0033	46.298 ± 0.024
PG1115+080A1	1.735512 ± 0.000439	Hewett & Wild (2010)	-1.11 ± 0.07	0.6563 ± 0.0201	46.442 ± 0.021
HB89-1621+392	1.981361 ± 0.000450	Hewett & Wild (2010)	-1.52 ± 0.01	0.3133 ± 0.0022	46.274 ± 0.010
SBS1307+462	2.142306 ± 0.000247	Hewett & Wild (2010)	-2.25 ± 0.07	0.3204 ± 0.0139	46.565 ± 0.008
		COS/G130M and COS/G160M			
SDSSJ084349.49+411741.6	0.990788 ± 0.000450	Hewett & Wild (2010)	-1.54 ± 0.07	0.8770 ± 0.0245	45.875 ± 0.033
HE0439-5254	1.053	Wisotzki et al. (2000)	-1.34 ± 0.02	2.0865 ± 0.0205	46.239 ± 0.008
SDSSJ100535.24+013445.7	1.080900 ± 0.000379	Hewett & Wild (2010)	-1.61 ± 0.20	1.5900 ± 0.0757	46.228 ± 0.060
PG1206+459	1.164941 ± 0.000436	Hewett & Wild (2010)	-0.84 ± 0.28	3.3995 ± 0.7101	46.518 ± 0.057
PG1338+416	1.217076 ± 0.000445	Hewett & Wild (2010)	-2.07 ± 0.03	0.5149 ± 0.0059	46.095 ± 0.007
LBQS1435-0134	1.310790 ± 0.000437	Hewett & Wild (2010)	-0.67 ± 0.06	4.2471 ± 0.0975	46.678 ± 0.028
PG1522+101	1.328005 ± 0.000445	Hewett & Wild (2010)	-0.66 ± 0.07	4.1178 ± 0.1478	46.673 ± 0.029
Q0232-042	1.437368 ± 0.000183	Hewett & Wild (2010)	-0.95 ± 0.09	1.5086 ± 0.0715	46.423 ± 0.084
PG1630+377	1.478949 ± 0.000439	Hewett & Wild (2010)	-1.69 ± 0.09	2.4274 ± 0.1901	46.836 ± 0.045

[a]Power-law parameters are fit to the form $F_\lambda = F_0(\lambda/1100\ \text{Å})^{\alpha_\lambda}$ in the rest frame. Fluxes are in units of 10^{-15} erg cm^{-2} s^{-1} Å^{-1}. Monochromatic luminosities, λL_λ, are measured from luminosity distances and the spline fit at rest-frame 573 Å (the normalization window used for the composite). Power-law parameters and luminosities include corrections for identified HI absorption, Galactic extinction, and resolution effects, as described in Section 2.1.

the COS Tools website,[2] described in detail by Danforth et al. (2010) and Keeney et al. (2012). This version of the software implements several minor changes, such as improved exposure cross-correlation and scaling between gratings, compared to the version used in Stevans et al. (2014). Because the COS detector oversamples the line-spread function by ~ 6 pixels, the spectra were binned by three pixels during the coaddition process to improve the S/N per bin without degrading the resolution of the spectra.

We fit each spectrum with a combination of splines and polynomials using the same procedure as in Shull et al. (2012b) and Stevans et al. (2014). This process allows us to smooth and reconstruct the shape of the intrinsic AGN spectrum, removing intervening absorption lines from the IGM and interstellar medium (ISM) by interpolating over them, in contrast to other composites (e.g., Telfer et al., 2002; Lusso et al., 2015) that apply statistical corrections for such absorption. However, the reduced resolving power of the G140L grating compared to the medium-resolution COS gratings leads to many absorption features being marginally resolved or under-resolved, especially at the weak end of the absorber distribution. We therefore expect the spline fit to be systematically low

[2] `http://casa.colorado.edu/~danforth/science/cos/costools.html`

compared to higher resolution data and to evolve with wavelength as the density of intervening Lyα lines increases with redshift. To quantify and correct for this effect, we degraded our medium-resolution data to the typical resolution and S/N of the G140L data and repeated the spline fits on the degraded data. The typical ratio of the degraded-to-original spline as a function of wavelength can then serve as a correction factor for the G140L splines. Blueward of the Galactic Lyα absorption feature, we assume that the correction factor is a constant, $C = 0.970 \pm 0.002$. Redward of the Galactic Lyα absorption feature, we parameterize the correction function by fitting the median correction factor at each wavelength to a power law, $C = (0.961 \pm 0.001) \left(\frac{\lambda}{1215.67} - 1\right)^{-(0.0045 \pm 0.0005)}$ over roughly 1216 Å $< \lambda <$ 1800 Å. We match these two functions near Galactic Lyα by requiring continuity. This small (2% to 5%) effect has little impact on the broader conclusions of this paper and suggests that our G140L spline fits are robust for the purposes of determining the large-scale spectral properties of AGNs.

In addition to correcting for the effects of IGM and ISM absorption, the spline fits almost always interpolate successfully over absorbers intrinsic to the background AGN. In particular, at least five of our medium-resolution targets that we have retained from Stevans et al. (2014) (PG 1206+459, PG 1228+416, LBQS 1435+0134, Q0232-042, PG 1630+377) have known intrinsic absorbers (Muzahid et al., 2013, 2016). These absorbers are well-resolved in the COS/G130M and COS/G160M data and are narrower than the broad undulations in the local AGN continuum, so we do not expect that they introduce any substantial error to the quantities discussed in this study. However, two of the new COS/G140L targets (PG 1115+080A1 and HE 1120+0154) feature more severe and more poorly resolved intrinsic absorption. These absorbed regions required additional manual adjustment to ensure that the semi-automated spline fitting was adequately rejecting the absorbed regions of the spectra. Though it appears that the spline fits adequately capture the behavior of the underlying AGN continua, these two targets may suffer additional systematic error that is not present in the rest of our sample. We further discuss the potential effect of such error on our measured power-law indices in Section 3.5.1.

Prominent geocoronal emission lines of H I, O I, and N I were masked from the spectra. We

excluded 2 Å on either side of N I λ1200 in both the flux array and the spline fit. We mask 9 Å in the G140L flux arrays and 5 Å in the G130M/G160M flux arrays on either side of O I λ1304, but we allow the spline interpolation through this region to contribute to the composite. We also mask 14 Å around the Galactic Lyα absorption feature. In the G140L data, all observed wavelengths greater than 2000 Å were masked because the sensitivity of the COS detector declines rapidly in this region, leading to low S/N and complicated systematic effects. Finally, we discard any bins with S/N < 0.5, which in practice extends the long-wavelength masking slightly below 2000 Å in some targets.

Each spectrum and its associated spline fit were corrected for Galactic extinction assuming a Fitzpatrick (1999) reddening law with values derived from the Schlafly & Finkbeiner (2011) recalibration of the Schlegel et al. (1998) dust maps. We follow Schlegel et al. (1998) and adopt 1σ uncertainties of 16% in the selective extinction, $E(B-V)$. We assume a mean value $R_V = 3.13$ for the ratio of total-to-selective extinction and adopt a 1σ uncertainty of 0.52, following the distribution of Galactic sightlines from Geminale & Popowski (2004). We do not attempt to measure or correct for extinction intrinsic to the AGN.

Where possible, we correct the spectra for continuum H I absorption due to Lyman limit systems (LLSs; $\log N_{\rm HI} \geq 17.2$) and partial-LLSs (pLLSs; $15.0 \leq \log N_{\rm HI} < 17.2$). We do not attempt to identify or correct H I continuum absorption for systems with $\log N_{\rm HI} < 15.0$ because these systems have a negligible effect on the spectrum, as discussed in Stevans et al. (2014). In the G140L targets, we identify these absorption systems by calculating the effective equivalent width (EW) at each pixel location by summing the contributions of spline-normalized surrounding pixels weighted by the convolution of the COS/G140L linespread function and a Voigt profile with a Doppler parameter $b = 20$ km s^{-1}. This yields an EW array as a function of wavelength, which we search for correlated EWs at the separations of the Lyman series lines at a significance level greater than 2σ per line. We confirm these candidate H I systems visually. In the medium-resolution data, we adopt the list of H I systems reported in Stevans et al. (2014), although we make new column density determinations from the new coadditions of the data. We measure the EWs of the

individual absorption lines and fit them to a curve of growth to determine the column density of the system and the associated uncertainty. The column density measurement is then used to correct for the H I opacity shortward of the Lyman limit. We mask the region immediately surrounding the Lyman break, discarding absorber rest-frame wavelengths 911.253 Å to 916.249 Å for absorbers with $\log N_{\rm HI} < 15.9$ and 911.253 Å to 920.963 Å for absorbers with $\log N_{\rm HI} \geq 15.9$. We mask all flux at $\lambda < 1161$ Å in the observed frame for the target HE1120+0154 because a particularly strong LLS at $z = 0.273$ renders the S/N in this region too low for continuum recovery.

Five targets (PG1206+459, LBQS1435-0134, PG1522+101, Q0232-042, PG1630+377) have also been observed in the near-UV (NUV) with STIS/E230M, allowing the identification via Lyα (and occasionally Lyβ) of H I systems that are redshifted out of the COS band. For these systems, column densities were determined directly from Voigt profile fitting to the Lyα feature in the coadded data. These column density determinations are more uncertain than those measured in the COS data because Lyα is on the flat part of the curve of growth at these column densities and higher order Lyman lines are unavailable.[3] The 58 identified LLS and pLLS absorption systems are listed in Table 3.3.

[3] The one exception is the system at $z = 0.9532$ in the PG1630+377 sightline, for which we were able to simultaneously fit the STIS/E230M Lyα feature and higher-order lines at the longest-wavelength end of the COS/G160M data. Though the COS data are noisy and contaminated by other absorption lines, they constrain the fit to a much lower value ($\log N_{\rm HI} = 16.10 \pm 0.15$) than previously reported in the literature. Janknecht et al. (2006a,b) previously reported $\log N_{\rm HI} = 18.484 \pm 1.483$ for this system.

Table 3.3. Identified pLLS (56) and LLS (2) Absorption Systems

Target	z_{abs}	$\log N_{\rm HI}({\rm cm}^{-2})$
SDSSJ084349.49+411741.6	0.5326	16.71 ± 0.08
SDSSJ084349.49+411741.6	0.5335	16.38 ± 0.07
SDSSJ084349.49+411741.6	0.5411	15.47 ± 0.04
SDSSJ084349.49+411741.6	0.5437	15.61 ± 0.07
HE0439-5254	0.3280	15.70 ± 0.02
HE0439-5254	0.6152	16.31 ± 0.02
HE0439-5254	0.8653	15.57 ± 0.07
SDSSJ100535.24+013445.7	0.4185	17.00 ± 0.10
SDSSJ100535.24+013445.7	0.4197	15.71 ± 0.03
SDSSJ100535.24+013445.7	0.8372	16.90 ± 0.04
SDSSJ100535.24+013445.7	0.8394	16.28 ± 0.04
PG1206+459	0.4081	15.75 ± 0.03
PG1206+459	0.4141	15.47 ± 0.04
PG1206+459	0.9277	17.20 ± 0.10
PG1206+459[a]	1.1387	16.42 ± 0.99
PG1338+416	0.3488	16.46 ± 0.02
PG1338+416	0.4636	15.37 ± 0.03
PG1338+416	0.6211	16.17 ± 0.02
PG1338+416	0.6862	16.49 ± 0.04
LBQS1435-0134	0.2990	15.33 ± 0.02
LBQS1435-0134	0.6119	15.00 ± 0.04
LBQS1435-0134	0.6128	15.34 ± 0.02
LBQS1435-0134	0.6812	15.52 ± 0.02
PG1522+101	0.5184	16.24 ± 0.03
PG1522+101	0.5719	15.85 ± 0.02
PG1522+101	0.6750	15.88 ± 0.02
PG1522+101	0.7284	16.60 ± 0.10
PG1522+101[a]	0.9448	15.25 ± 0.21
PG1522+101[a]	1.0447	15.59 ± 0.27
PG1522+101[a]	1.1659	15.41 ± 0.17
Q0232-042	0.3225	16.14 ± 0.10
Q0232-042	0.7390	16.75 ± 0.10
Q0232-042	0.8078	15.74 ± 0.04
Q0232-042[a]	0.9632	15.60 ± 1.25
Q0232-042[a]	1.0888	15.55 ± 1.45
HE1120+0154	0.2558	> 18.0
HE1120+0154	0.5771	15.71 ± 0.13
PG1630+377	0.2741	17.05 ± 0.10
PG1630+377	0.2782	15.09 ± 0.05
PG1630+377	0.4177	15.71 ± 0.02
PG1630+377	0.8110	15.64 ± 0.03
PG1630+377	0.9145	15.94 ± 0.06
PG1630+377[a]	0.9532	16.10 ± 0.15
PG1630+377[a]	0.9596	15.77 ± 0.30

Table 3.3 (cont'd)

Target	z_{abs}	$\log N_{\rm HI}(\rm cm^{-2})$
PG1630+377[a]	1.0961	16.12 ± 0.58
PG1630+377[a]	1.1608	15.30 ± 0.41
PG1630+377[a]	1.4333	15.27 ± 0.23
HE0248-3628	0.5346	16.61 ± 0.10
HE0248-3628	0.5443	15.65 ± 0.04
HE0248-3628	0.5704	15.43 ± 0.06
US2504	0.3498	15.58 ± 0.13
SDSSJ125140.83+080718.4	0.4412	15.60 ± 0.16
SDSSJ125140.83+080718.4	0.7329	16.03 ± 0.14
SDSSJ094209.14+520714.5	0.7411	16.25 ± 0.18
PG1115+080A1	0.5964	15.27 ± 0.16
SBS1307+462	0.3679	15.45 ± 0.30
SBS1307+462	0.4601	15.52 ± 0.27
SBS1307+462	0.5176	16.31 ± 0.53

[a]Measurement made using STIS/E230M data.

We characterize the local continuum of each spectrum as a power law,

$$F_\lambda = F_0 \left(\frac{\lambda}{1100 \text{ Å}} \right)^{\alpha_\lambda}, \tag{3.1}$$

where the observed flux distribution, F_λ, is a function of the rest-frame wavelength λ and has two free parameters: the normalization, F_0, and the power-law index, α_λ. The index can be converted to the equivalent flux distribution in frequency space, $F_\nu \propto \nu^{\alpha_\nu}$, via $\alpha_\nu = -(2 + \alpha_\lambda)$. The best-fitting power law passes through two spline points such that all other possible power laws through other spline-point combinations lie above the best-fit power law. We determine the probability distribution of the best-fit power law via 15,000 Monte Carlo realizations of the spectrum-correction process that account for the aforementioned uncertainties. In each realization, the parameters are calculated iteratively and analytically, enforcing the additional constraints that the two points must be separated by at least 50 Å and lie more than 5 Å from the edge of the spectrum to avoid effects from the spline ends. The best-fit parameters and 1σ marginalized uncertainties are determined from this distribution. These uncertainties are dominated by the extinction correction and LLS/pLLS measurements. We emphasize that this parameterization represents only the local behavior of the spectrum, and it may not represent exclusively continuum flux if the broad emission lines overlap such that there are no pure-continuum windows in the spectrum. We also note that these power-law fits do not account for the possibility of unidentified H I continuum absorption from LLSs whose Lyman breaks are redshifted out of the COS observational bands (approximately $\lambda_{\rm obs} > 2000$ Å for G140L and $\lambda_{\rm obs} > 1800$ Å for G160M) but are not observed with any NUV

data. Though we correct for these effects statistically in our composite spectrum, such corrections to individual objects are not particularly useful, owing to the stochasticity of such H I systems. As a result, each of these power-law slopes should be treated as a lower limit to the true slope until near-UV observations of these objects become available. The best-fit power-law parameters are given in Table 3.2.

The eleven G140L spectra are plotted in Figures 3.1 and 3.2. The light-gray line is the observed flux, and the overplotted black line is the flux corrected for Galactic extinction, H I absorption, and geocoronal emission. This corrected flux is used to construct our composite spectrum. The solid red line is the associated spline fit corrected for the measured resolution and wavelength-dependent systematic error, while the solid blue line is a power-law fit to the continuum underlying the spline fit.

3.4.2 Composite Construction

In order to construct a composite spectrum, the spectra and their associated spline fits must first be resampled onto uniform wavelength grids. As in Shull et al. (2012b) and Stevans et al. (2014), we adopt the method formalized in Equations 2 and 3 of Telfer et al. (2002) and resample onto 0.61 Å bins. Because we are focused on a more limited wavelength regime in this study compared to Stevans et al. (2014), the composite construction process can be simplified. Instead of the bootstrap-normalization process, we normalize the resampled spectra to their median flux values in a single window of overlap, 575 Å $< \lambda <$ 610 Å, without any apparent strong emission lines. We construct two styles of composite spectra. The first style is calculated as the geometric mean of the contributing flux bins and is used for slope determinations because it preserves power-law shapes. The second style uses the median of the contributing flux bins to better preserve the relative strengths of the emission lines.

In both cases, in a method analogous to that used for the individual target spectra, we construct 15,000 Monte Carlo realizations of mock composites to determine the probability distributions of measured quantities. Unlike the realizations used for the determination of power-law

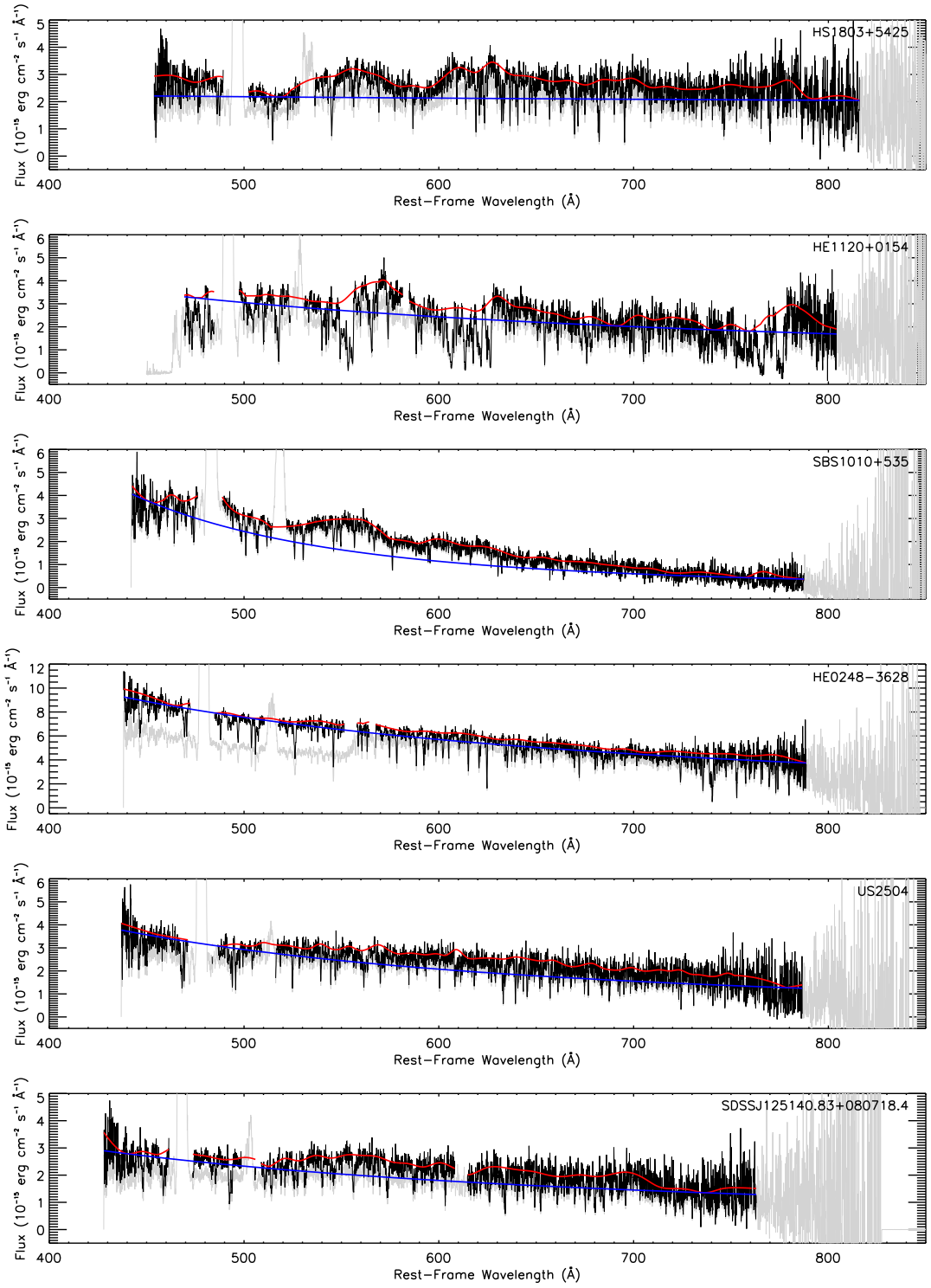

Figure 3.1 AGN spectra observed with COS/G140L. The light-gray line is the uncorrected flux, while the black line is corrected for Galactic extinction, intervening H I absorption, and geocoronal emission as described in Section 3.4.1. The red line is the spline fit, and the blue line is a power-law fit to the underlying continuum.

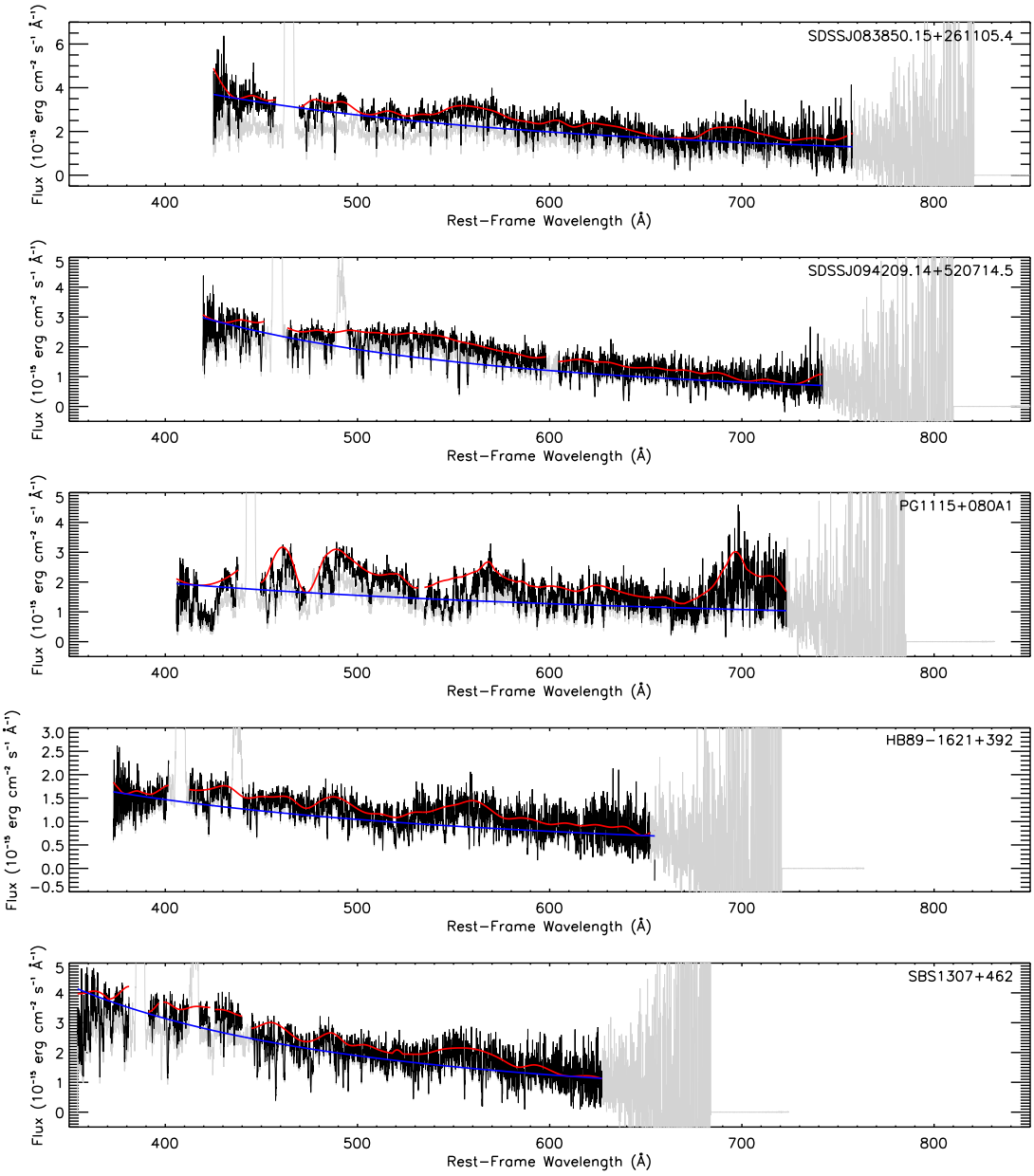

Figure 3.2 Same as Figure 3.1.

parameters for the individual targets, we statistically account for the effects of unidentified LLSs and pLLSs whose 912 Å Lyman edges are redshifted out of the observational band. To do so, however, we must adopt a functional form for the evolution of the distribution of absorbers in both column density and redshift. Following the usual notation in the literature, we parameterize this frequency distribution as a power law,

$$f(N_{\rm HI}, z) = A \left(\frac{N_{\rm HI}}{\rm cm^{-2}} \right)^{-\beta} (1+z)^{\gamma}, \tag{3.2}$$

over the ranges $10^{15} < N_{\rm HI} < 10^{18}$ cm^{-2} and $1.19 < z < 2.14$. Mock absorbers are drawn from this distribution according to Poisson statistics over the unobserved redshift range in which they could have occurred. The modeled effects of their continuum opacity are then injected into each mock composite realization.

Such an absorber distribution is well-characterized at both low-redshifts (e.g., Tilton et al., 2012; Danforth et al., 2016) and high-redshifts (e.g., Rudie et al., 2013) where extensive FUV and optical observations probe the Lyα forest. However, results for the intermediate redshifts of relevance here, best studied in the NUV, are substantially more uncertain. The few studies that have been conducted neither arrive at consistent results nor conduct thorough, multivariate analyses, making the optimal choices for (A, β, γ) unclear. Further, no one study has covered the entirety of the relevant range of both column densities and redshifts, forcing us to attempt to match disparate distributions of absorbers from different methodologies. Our general approach is to choose values for these parameters based on measurements from the literature and allow them to vary in the Monte-Carlo realizations of the composite spectrum to account for their uncertainties.

The slope of the column-density distribution is perhaps the most secure of the three parameters, as it remains fairly constant near $\beta \approx 1.6$ over a wide variety of redshifts and column density ranges (Kim et al., 2002; Janknecht et al., 2006a; Tilton et al., 2012; Rudie et al., 2013; Danforth et al., 2016). We therefore adopt $\beta = 1.6 \pm 0.1$ in our absorber distribution. The overall normalization of the distribution and its redshift evolution remain far more uncertain. Early surveys (Storrie-Lombardi et al., 1994; Stengler-Larrea et al., 1995) used combinations of *International*

Ultraviolet Explorer and *HST* data to characterize the LLS absorber distribution as a function of redshift alone, obtaining $\gamma = 1.5 \pm 0.39$ for $\log N_{\rm HI} \geq 17.2$ over $0.32 \leq z_{\rm LLS} \leq 4.11$. More recently, Kim et al. (2002) combined ground-based data and *HST* surveys to obtain $\gamma = 3.11 \pm 0.42$ for $14.5 < \log N_{\rm HI} < 17$ over $1.5 < z_{\rm abs} < 4$. We attempt to accommodate the range of results in the literature by adopting $\gamma = 2 \pm 1$. The overall normalization for this distribution is constrained by the expectation that the density of absorbers should increase with redshift; the low-redshift and high-redshift surveys thus bound the normalization. We therefore set the value of A by requiring that the integrated quantity $f(N_{\rm HI}, z) = 5.3 \pm 0.25$ over $10^{15} < N_{\rm HI} < 10^{18}$ cm^{-2} and $1.19 < z < 2.14$, in approximate agreement with the Stengler-Larrea et al. (1995) and Kim et al. (2002) integrated distributions and the bounds set by Danforth et al. (2016) and Rudie et al. (2013). Though none of these studies investigates the joint-probability distribution for these three parameters, the normalizations of their fits to the redshift distribution of absorbers imply an additional constraint on the integrated column-density distribution, which we implement by requiring that

$$0.2 < A \int_{10^{15}}^{10^{18}} N_{\rm HI}^{-\beta} dN_{\rm HI} < 9. \tag{3.3}$$

Finally, we require that no realization yields an H I opacity that implies an intrinsic AGN spectral slope of $\alpha_\nu > +1.15$, roughly $\Delta\alpha_\nu = 0.9$ greater than the maximum slope we observed at lower redshifts in Stevans et al. (2014).

The Monte Carlo experiment implements a bootstrap-with-replacement technique to quantify the effects of cosmic variance among our targets. Each realization is composed of a randomly selected set of available targets. Because of the small number of spectra contributing at some wavelengths, a few combinations lead to composite spectra that lack data at wavelengths of interest; these realizations are rejected. The final composite spectrum is determined from the median flux in each wavelength bin of the Monte Carlo realizations. Measured quantities such as the power-law parameters are determined directly from the ensemble of realizations in the same manner as for the individual targets.

Our full-sample composite (geometric-mean and median) spectra are presented in Figure 3.3

along with the best-fit power law, $\alpha_\nu = -0.72 \pm 0.26$, as determined from the Monte-Carlo realizations. The solid red line is the composite spline spectrum that best represents the intrinsic AGN spectrum shape, while the black line is the composite flux spectrum, produced directly from the corrected flux of the individual targets. Potential identifications of the major emission lines are labeled in the plot. Figure 3.4 shows the number of AGNs contributing to the composite spectra as a function of wavelength. Because the number of contributing spectra fall off rapidly below 450 Å and above 770 Å, we restrict all power-law measurements to this wavelength range. The long wavelength fall off is due to our sample selection and our redshift threshold that allows all targets to be normalized to the same continuum window (575 Å $< \lambda <$ 610 Å). The short wavelength fall off, on the other hand, represents a true paucity of COS observations of AGNs that probe this wavelength regime.

3.5 Discussion

3.5.1 The EUV Slope from 450 to 770 Å

One of the goals of this study is the determination of the typical slope of AGN spectra in the EUV wavelength regime for input to radiative transfer calculations of quantities such as the UVB or photoionization models of the IGM and gas around active galaxies. As mentioned in Section 3.4.2, our full-sample composite spectrum leads to a power-law index of $\alpha_\nu = -0.72 \pm 0.26$. This value is substantially harder than EUV spectral slopes reported from most other composites, including Shull et al. (2012b) ($\alpha_\nu = -1.41 \pm 0.20$), Stevans et al. (2014) ($\alpha_\nu = -1.41 \pm 0.15$), Telfer et al. (2002) with $\alpha_\nu = -1.57 \pm 0.17$ in the radio-quiet subsample, and Lusso et al. (2015) with $\alpha_\nu = -1.70 \pm 0.61$. The harder Scott et al. (2004a) slope, $\alpha_\nu = -0.56^{+0.38}_{-0.28}$, is in better agreement with this study's result, although their *FUSE* composite only extends down to 630 $\mathring{A}$. In Stevans et al. (2014), we explained the discrepant Scott et al. (2004a) slope as a result of their choice of continuum windows and their fitting the power law over the tops of unidentified emission lines in their shortest-wavelength fitting window (630 − 750 Å). This resulted in an artificial hardening

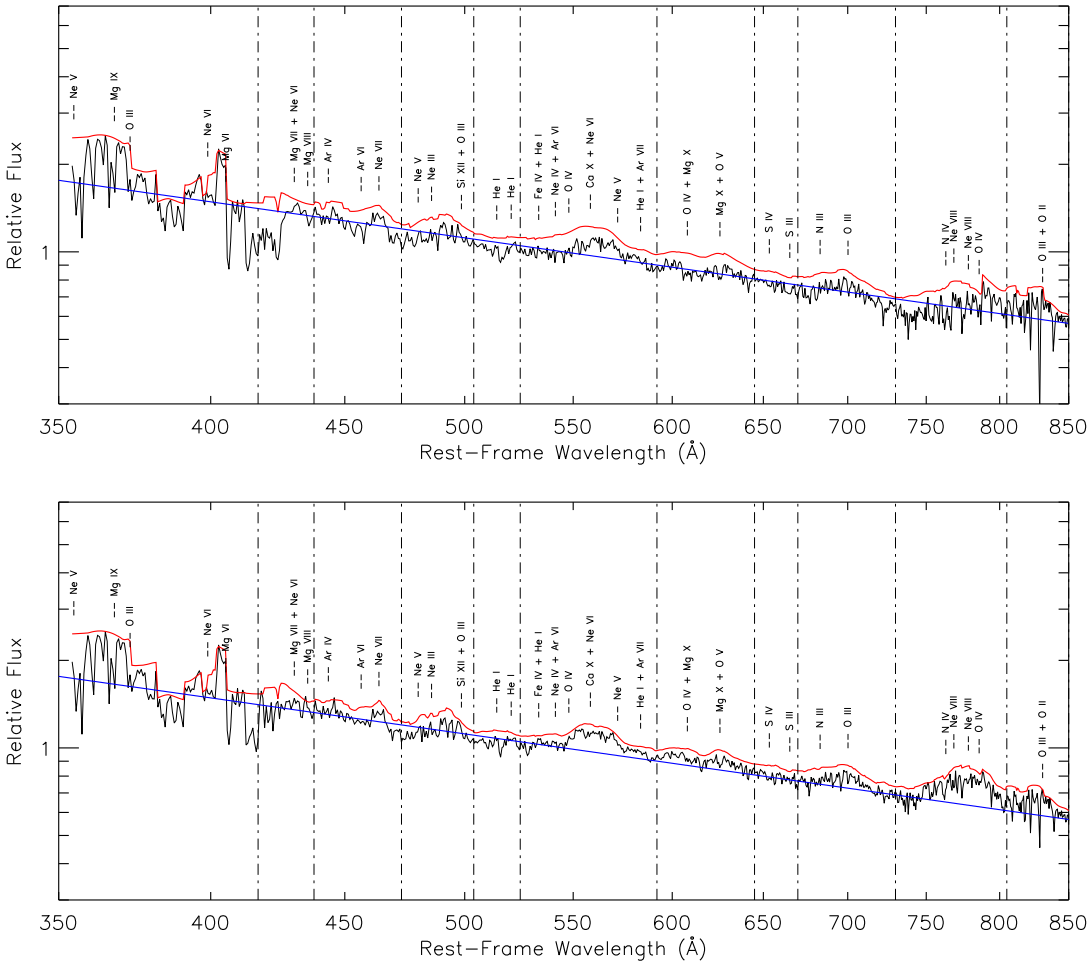

Figure 3.3 Composite spectra for the full sample of 20 AGN. The top panel is the geometric-mean composite, and the bottom panel is the median composite. Black lines show the composite flux, and red lines show the composite spline, which lies above the black line owing to intervening absorption. Possible emission-line identifications are labeled. The best-fit continuum power law ($\alpha_\nu = -0.72 \pm 0.26$) is shown in blue. Vertical dot-dashed lines indicate the divisions used for emission-line EW measurements in Section 3.5.2.

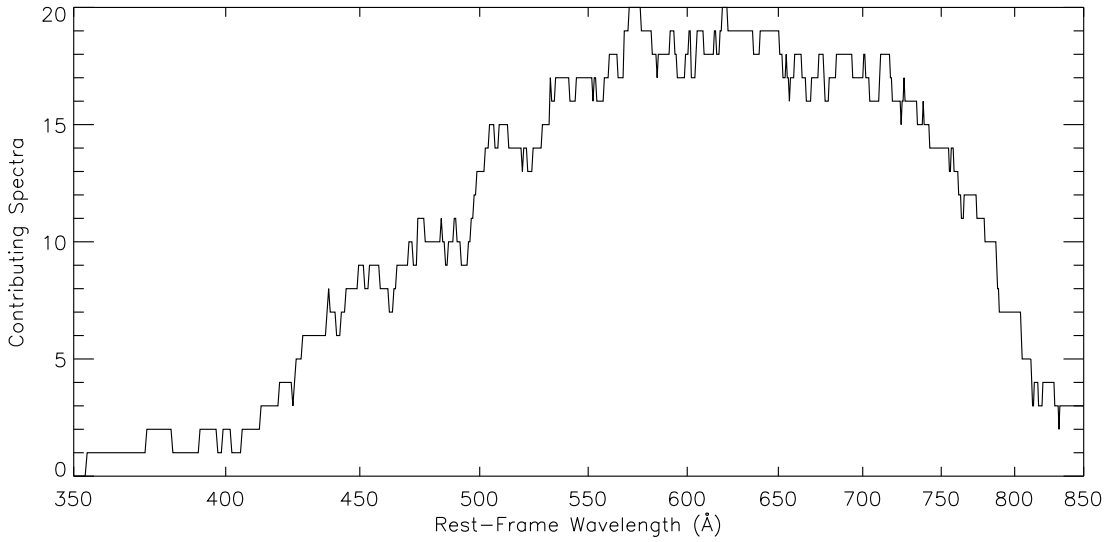

Figure 3.4 The number of AGN spectra contributing to the composite spectra as a function of rest-frame wavelength.

of the spectrum and incorrect separation of the power-law continuum and the broad emission-line flux.

The apparent tension between our present result and the slopes of other composites can be explained several ways. It is important to note that, while all of these composite spectra probe the EUV, their wavelength coverage is not completely equivalent, and the windows used to determine the power-law slope differ among surveys. For example, the Telfer et al. (2002) EUV power law is a fit to many flux bins that range from 350 Å to 1150 Å with varying degrees of contamination from broad emission lines, but it is dominated by the higher-S/N bins at the longer-wavelength end of this range. The authors noted that the spectral slope hardened substantially below $\sim$ 500 Å, but they ascribed little significance to the change, owing to the small number of spectra contributing at those wavelengths. Scott et al. (2004a) used the same fitting windows as Telfer et al. (2002), but enhanced emission-line flux in some of their targets may have led to a harder slope, as we discussed in Stevans et al. (2014). Lusso et al. (2015) adopt the fitting windows initially defined by Telfer et al. (2002), but they note that the fit is complicated by the the high density of emission lines in the region, rendering the power-law model an insufficient description of the spectrum. They explain their softer slope compared to Scott et al. (2004a) in terms of improvements to their statistical IGM

absorption corrections. Finally, the Stevans et al. (2014) power law is determined by connecting two continuum-like windows centered on 724.5 Å and 859 Å, chosen to avoid the locations of expected strong emission lines. Therefore, it does not constrain the slope at wavelengths below $\sim$ 724 Å, a region that can be seen to harden in their Figure 5, much like the Telfer et al. (2002) composite.

The power law described by our current study therefore probes a different spectral region than in Stevans et al. (2014). This region (450 Å $< \lambda <$ 770 Å) exhibits a spectral hardening seen in several previous studies, which also might be expected from the need for the spectrum to match up with soft X-ray observations with $F_\nu \propto \nu^{-1}$ (e.g., Hasinger, 1996). The power-law determination in this study further differs from the others because it does not specify any continuum windows *a priori* and thus avoids the need to explain the unidentified and seemingly unphysical "absorption" features that arise in the Telfer et al. (2002), Scott et al. (2004a), and Lusso et al. (2015) composites. In general, the determination of the underlying continuum in this region is complicated by a number of emission features, including a significant bump around 700 Å due to O IIII λ702 and N III λ686 as well as features due to Ne VIII ($\lambda\lambda 770, 780$), O IV (λ554, λ608, λ788), and O IV (λ630).

It might also be possible to explain the hardening of the spectral slope through errors in our corrections for Galactic extinction or H I absorption, either from the measured column densities or the statistical correction for unidentified systems. Our Monte Carlo experiments, however, attempt to account for these uncertainties. The two-dimensional joint-probability distribution for the full suite of power-law realizations is shown in Figure 3.5, along with the marginalized distributions for F_0 and α_ν. Though these correlated variables show a low-probability tail toward softer spectra caused by the unidentified H I systems, a steady or softening slope compared to the EUV slope of Stevans et al. (2014) is excluded at 99.6% confidence. The hardening of the EUV slope observed in our composite is too large to be explained by uncertainties in Galactic extinction or H I absorption alone.

As mentioned in Section 3.4.1, two of the targets (PG 1115+080A1 and HE 1120+0154) could potentially introduce systematic error to our measurements because of the presence of absorption associated with the AGN. The bootstrap-with-replacement procedure included in our Monte Carlo

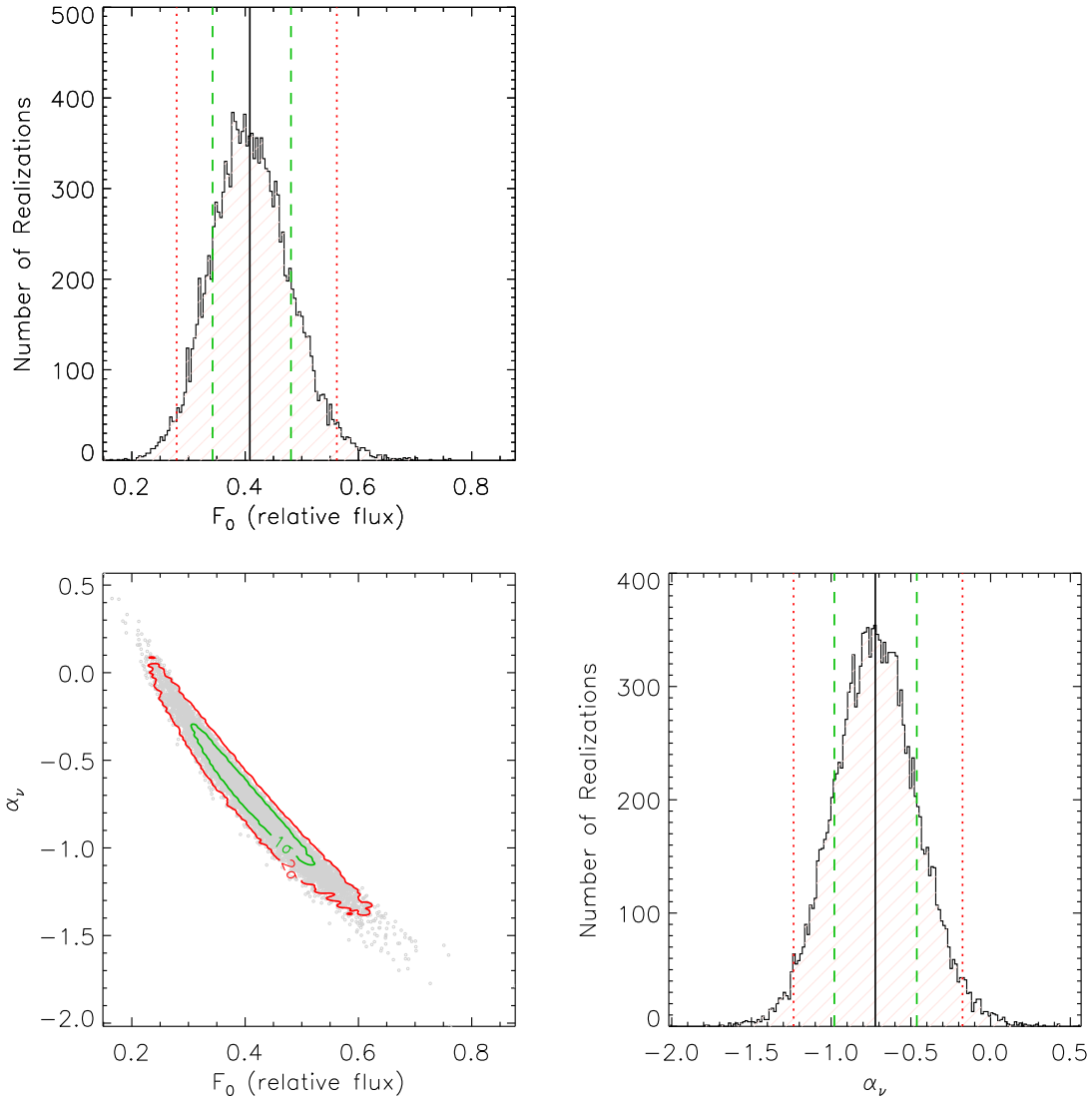

Figure 3.5 The results of the Monte-Carlo realizations for the power-law parameters. The lower-left panel plots the 2D joint-probability distribution for the power-law index, α_ν, and the normalization, F_0, with approximate 1σ and 2σ contours in green and red, respectively. The other panels show the marginalized distributions for these parameters, with the median value ($\alpha_\nu = -0.72 \pm 0.26$) marked with a solid black line and the 1σ and 2σ bounds marked with green dashed lines and red dotted lines, respectively.

experiments naturally includes in the error analysis any additional variance carried by these two targets. However, as an additional check to ensure that the inclusion of these targets is not artificially hardening the power-law slope, we repeated the Monte Carlo calculations with these two targets removed. This procedure results in a slightly harder EUV slope, $\alpha_\nu = -0.66 \pm 0.29$, consistent with the full-sample results.

At least one of our targets, SBS1010+535, exhibits a very hard, inverted slope, $\alpha_\nu = +2.17 \pm 0.01$, that warrants further discussion. The most obvious explanation for such an anomolous slope is the potential presence of an extremely strong, undetected H I system at wavelengths longward of our observational band. Because this AGN ($z_{\rm AGN} = 1.515848$) has never been observed in the near-UV, we cannot directly investigate the H I systems in the relevant redshift range. However, the object has publicly-available optical spectra from the Sloan Digital Sky Survey (SDSS; for the most recent data release see Alam et al., 2015) which gives some indications about the intrinsic spectral slope at longer, rest-frame FUV wavelengths and could potentially reveal the redshifts of intervening H I absorption systems via the Mg II $\lambda\lambda 2796, 2804$ feature. This spectrum is shown in Figure 3.6. Even in the FUV, the spectrum is anomalously hard, exceeding all but one of the slopes discussed in Stevans et al. (2014). At rest wavelengths $\lambda_{\rm rest} > 2000$ Å, the slope is $\alpha_\nu \approx -0.45$, but it rapidly hardens at shorter wavelengths to $\alpha_\nu \approx +0.29$. No detectable (EW > 0.3 Å) Mg II absorbers are apparent in the expected range (6130 Å $< \lambda_{\rm obs} <$ 7041 Å), suggesting that if a LLS is present, it must be part of a low-metallicity population. Previous surveys (Lehner et al., 2013) have identified a population of LLS absorbers with $\sim 2.5\%$ solar metallicity. When combined with our Mg II non-detection, such a metallicity would imply a maximum H I column density of $\log N_{\rm HI} \sim 18.67$. Therefore, a low-metallicity LLS with sufficient column density to account for the anomalous EUV slope may be present despite our non-detection of Mg II absorbers. Further, the longest wavelength ($\sim$ 1800 Å) fluxes from the COS/G140L data are a factor of ~ 4 lower than at the shortest wavelength ($\sim$ 3800 Å) covered by the SDSS data, perhaps suggesting the effects of a LLS between the two regions (however, target variability may also contribute, as these observations were not simultaneous). The most likely explanation for the observed inverted EUV

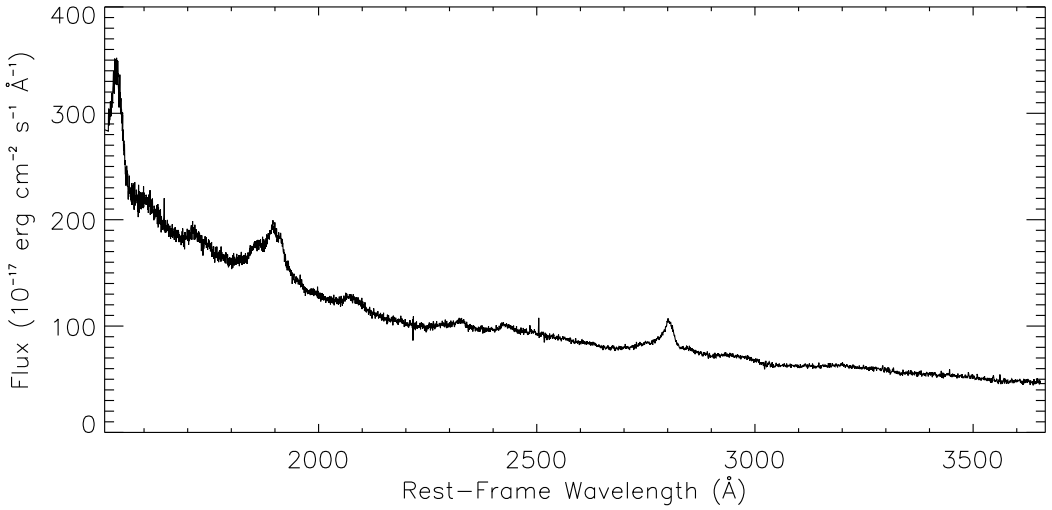

Figure 3.6 Rest-frame FUV spectrum of SBS1010+535 ($z_{\rm AGN} = 1.515848$) from the Sloan Digital Sky Survey. Note the rapidly hardening slope and the absence of any strong, intervening Mg II absorbers shortward of 2800 Å in the range $1.190 < z < 1.516$.

slope of SBS1010+535 seems to be a combination of its position as one of the hardest slopes in the AGN slope distribution and additional hardening from one or more intervening H I absorbers in the range $1.190 < z < 1.516$. To test the effect of including this object in our sample, Figure 3.7 shows a version of the composite with its spectrum removed, which leads to a slope $\alpha_\nu = -0.89 \pm 0.22$ using the same methodology as above. Although this softens the composite slope somewhat, it is still significantly harder than the EUV slopes from Telfer et al. (2002) or Stevans et al. (2014). The inclusion of the outlier SBS1010+535 in our sample is thus insufficient to explain the observed spectral hardening of the composite.

If the fast-rising composite flux at short wavelengths is not an artifact of a systematic uncertainty associated with foreground corrections, then we must understand it in terms of flux from the AGN itself. It is plausible that the power-law slope represents a true hardening of the accretion disk continuum spectrum in the EUV. This EUV-rise has been predicted by some models, such as those that include reprocessing of the disk continuum by cold, optically thick clouds (Lawrence, 2012). However, more standard alpha-disk and wind models (e.g., Slone & Netzer, 2012; Laor & Davis, 2014, and references therein) tend to predict EUV spectral turnovers that depend on the

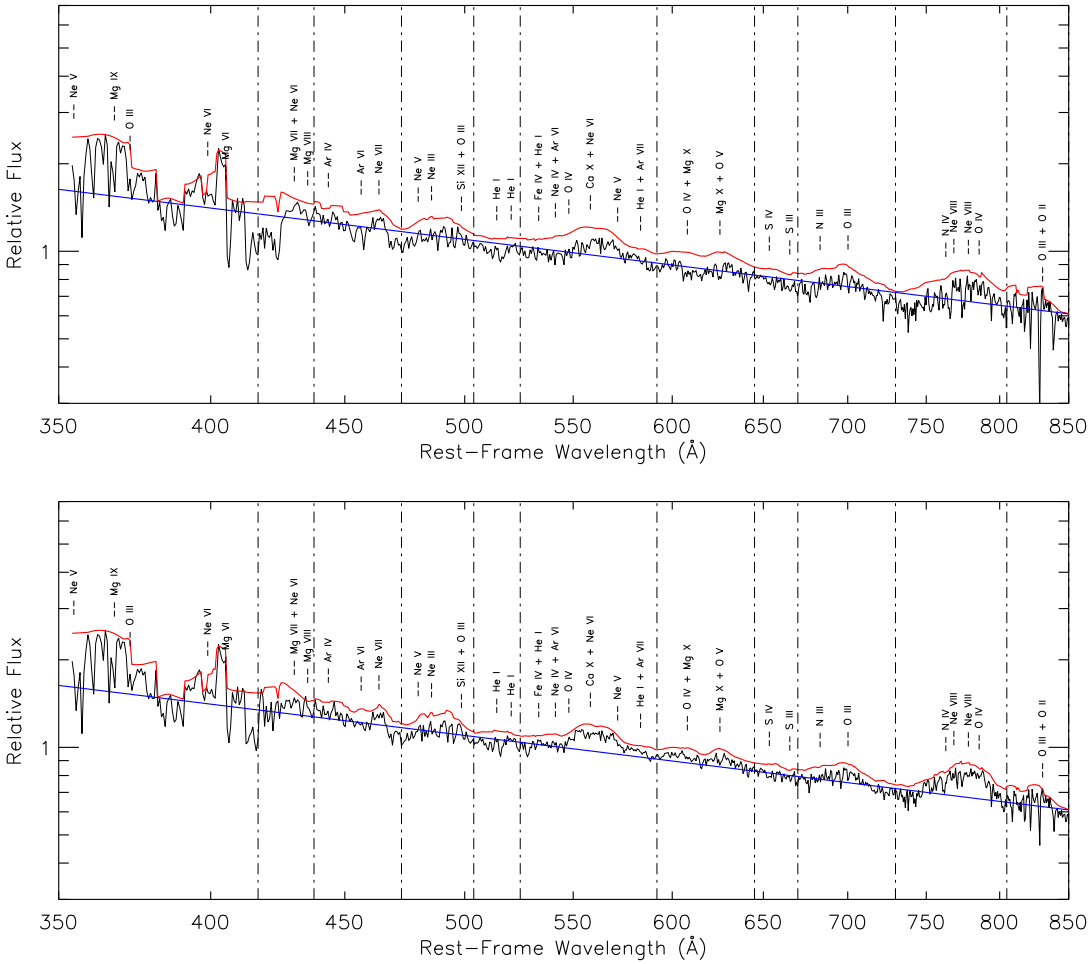

Figure 3.7 Same as Figure 3.3, but with the outlier SBS1010+535 removed from the sample. The resulting power-law index is $\alpha_\nu = -0.89 \pm 0.22$, slightly steeper than the full sample.

innermost edge of the disk, determined by black hole mass and spin, and on the radial profile of the mass accretion rate. These sorts of models are difficult to simultaneously reconcile with our observed hardening EUV slope and with the shorter-wavelength EUV and FUV slopes seen by Stevans et al. (2014).

Perhaps the simplest explanation for the hardening spectral index is the large number of highly blended broad emission lines in the spectral region between 400 Å and 800 Å. Far more than in the optical, near-UV, or FUV, these overlapping emission lines create a pseudo-continuum, leaving no spectral region free of emission-line flux. As noted by Lusso et al. (2015), the simple power-law model that has often been used may be insufficient to determine the behavior of the underlying continuum separately from the broad emission-line flux. This pseudo-continuum limits the utility of EUV power-law fits to composite spectra for the purpose of understanding the generation of continuum flux within accretion disk models, but it is not particularly problematic from the standpoint of determining inputs to photoionization modeling or calculations of the UVB. Such calculations are concerned only with the average contribution of photons from AGN to the background at each wavelength. An ideal determination of the UVB would include all the photons, whether they originate in the accretion disk or the broad-line region. However, if the power-law parameterization is substantially contaminated with emission-line flux, caution must be exercised in extrapolating the continuum slope beyond the observational window.

3.5.2 Emission Lines

The large number and diverse strengths of the emission lines in the EUV has been apparent in all composite spectra that cover this spectral region. Unfortunately, perhaps owing to the difficulties associated with measuring the individual line fluxes, there have been few attempts to understand and disentangle this complicated ensemble of lines. Though there have been some attempts to reproduce EUV emission lines at $\lambda \geq 765$ Å (e.g., N IV λ765, N III λ991, O IV λ788, O III λ834, O II λ833, Ne VIII $\lambda\lambda 770, 780$) via photoionization modeling (e.g., Moloney & Shull, 2014), there has been no detailed effort to do so at shorter wavelengths. It is therefore difficult to uniquely

identify the emission lines that dominate our composite spectra without a detailed photoionization study beyond the scope of this paper (but see the list of expected EUV lines in Table 4 of Shull et al., 2012b). Instead, we have labeled Figures 3.3 and 3.7 with possible line identifications. These identifications are based on the strongest lines in each spectral region as estimated from the CLOUDY (last described by Ferland et al., 2013) models used by Moloney & Shull (2014) using their default "local optimally emitting cloud" model (see Baldwin et al., 1995) with a 40% covering factor, five-times solar metallicity, and 250 km s^{-1} turbulence. While these models reproduce the emission lines at slightly longer wavelengths, their behavior has not been explored in detail at the shorter wavelengths discussed here. The models likely suffer from inaccuracies due to high densities, ionizing fluxes, and temperatures in the emitting gas. These line identifications thus serve only as a guide until more extensive photoionization modeling is undertaken. In particular, some of the features correspond to lower-abundance elements such as argon, calcium, and sulfur which are unlikely to be strong.

Because all of the emission lines are highly blended, there is no straightforward way to isolate them and measure their strengths. Instead, Table 3.4 lists the emission EWs determined from the spline-fit Monte Carlo realizations for different regions of the composite spectra chosen to roughly separate the most prominent features. These divisions are plotted in Figures 3.3 and 3.7 as vertical dot-dashed lines. The reliability of these measurements is limited by the power-law continuum fit against which they are referenced. Therefore, most of the EWs likely underestimate the true emission flux if the power law is artificially high due to a pseudo-continuum of emission lines. Future studies may be able to more robustly separate and measure these emission lines by targeting AGNs with narrow emission lines (e.g., narrow-line Seyfert 1 galaxies), but all targets in our sample exhibit broad lines. The emission line strengths of the targets that contribute to the composites vary widely, as can be seen in the G140L spectra plotted in Figures 3.1 and 3.2. Some targets have nearly blazar-like continua with extremely weak emission features, while others have strong, prominent emission lines. This variation is illustrated in Figure 3.8, which divides into quartiles the sample of EWs for the contributing targets to each composite wavelength.

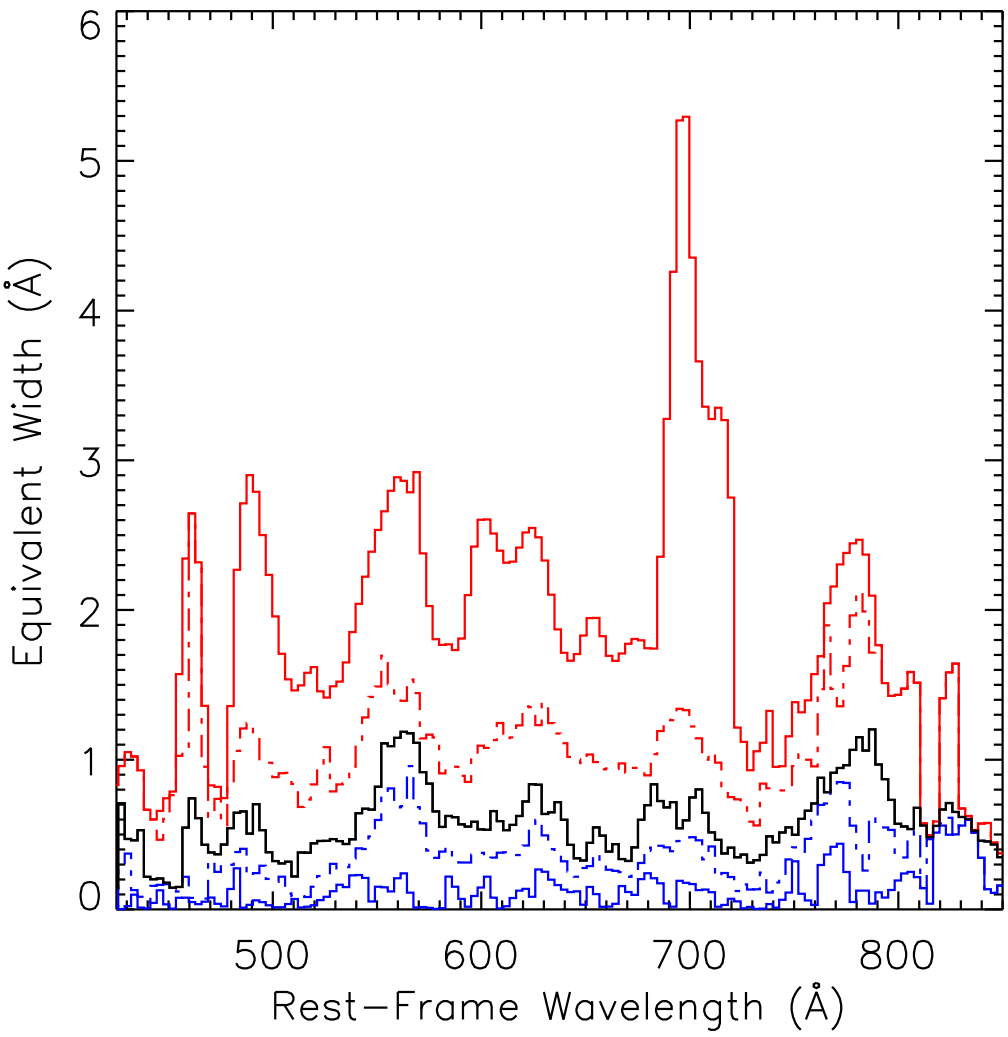

Figure 3.8 Emission-line equivalent width for the sample of targets as a function of AGN rest-frame wavelength, illustrating the diversity of emission line strengths among these targets. The lines separate the contributing AGNs into quartiles at each wavelength, from bottom to top: bottom (blue) solid line plots the minimum values; bottom (blue) dot-dashed line plots the 25th percentile; middle (black) solid line plots the median values; top (red) dot-dashed line plots the 75th percentile; and top (red) solid line plots the maximum values. Bins ($\sim$ 3 Å) are five times the width of the bins used in the composite spectrum.

Table 3.4. Equivalent Widths of Spectral Regions of Emission

Possible Contributing Ions	Wavelength Range (Å)	EW (Å)	EW (Å) (no SBS1010+535)
Mg VII, Ne VI, Mg VIII	417 − 438	2.2 ± 1.1	3.5 ± 1.1
Ar IV, Ar VI, Ne VII	438 − 473	2.6 ± 0.9	3.5 ± 1.0
Ne V, Na III, Si XII, O III	473 − 504	2.3 ± 0.5	3.0 ± 0.6
He I	504 − 525	0.6 ± 0.4	0.9 ± 0.4
Fe IV, He I, Ne IV, Ar VI, O IV, Ca X, Ne VI, Ar VII	525 − 592	7.9 ± 0.9	8.1 ± 1.1
O IV, Mg X, O V	592 − 645	5.9 ± 0.8	5.2 ± 0.9
S IV, S III	645 − 670	2.0 ± 0.4	1.4 ± 0.4
N III, O III	670 − 730	7.2 ± 1.0	5.2 ± 0.9
N IV, Ne VIII, O IV	730 − 805	16.4 ± 2.2	12.8 ± 2.0
O III, O II	805 − 850	7.9 ± 2.5	4.3 ± 2.3

3.5.3 The He I 504 Å Absorption Edge

A number of accretion disk atmosphere models have predicted the presence of absorption edges due to hydrogen, helium, and/or metal species in the spectra of AGN (e.g., Kolykhalov & Sunyaev, 1984; Sincell & Krolik, 1997; Koratkar & Blaes, 1999; Done & Davis, 2008; Davis & Laor, 2011; Done et al., 2012; Laor & Davis, 2014). Often, these models use atmospheres and winds analogous to those of hot stars, applying stellar atmospheres codes such as TLUSTY (Hubeny & Lanz, 1995, 2011) to generate spectra. The relative strengths and shapes of these edges vary greatly, ranging from broad spectral depressions to more distinctly edge-like features, depending on the details of the accretion disk models, such as the temperature profile of the disk atmosphere and the viewing angle of the observer. Shull et al. (2012b) and Stevans et al. (2014) searched for and set upper limits on the continuum optical depth beyond the H I 912 Å edge ($\tau_{\rm HI} < 0.01$) and the He I 504 Å edge ($\tau_{\rm HeI} < 0.1$). Our EUV sample does not probe any significant H I or metal absorption edges likely to be present in an AGN spectrum, but the He I 504 Å edge lies near the center of our wavelength coverage.

To test for absorption edges in the region of 504 Å, we constructed a composite spectrum from a subsample of five targets that have completely continuous, useable coverage with no masking in the $\sim$ 20 Å region surrounding the edge. We normalized this composite by the best-fit power law to remove the global slope. The flux in this spectra region is plotted in Figure 3.9. We set an optical depth limit by fitting the stacked flux to a model of pure He I continuum opacity using empirical photoionization cross-sections (Marr & West, 1976). This procedure yields a 2σ upper

limit to the optical depth just beyond the edge, $\tau_{\rm HeI} < 0.047$, corresponding to a column density of $N_{\rm HeI} < 10^{15.8}$ cm^{-2}.

Despite the non-detection of a He I edge, there is weak evidence for He I emission longward of the edge, as shown by the measurements discussed in Section 3.5.2. This detection is at less than the 2σ level, however, and it may be contaminated by other emission lines or by improper identification of the continuum flux with the power-law fit. If the He I edge is substantially smeared out or broadened, whether by inclination, disk atmospheric effects, or uncertainties in the redshifts used in our composite, the absorption would be difficult to identify amidst the numerous emission lines in this region. Nonetheless, there does not appear to be any region in which the He I optical depth could plausibly exceed $\tau_{\rm HeI} \approx 0.08$, corresponding to $N_{\rm HeI} < 10^{16}$ cm^{-2}. It seems unlikely that He I opacity plays a significant role in the structure of AGN spectra.

3.6 Summary and Conclusions

In this paper, we have continued and updated our investigation of the mean AGN spectrum that we began in Shull et al. (2012b) and Stevans et al. (2014). We obtained 11 new COS/G140L spectra of AGNs at redshifts $1.45 \leq z_{\rm AGN} \leq 2.14$ and combined their UV spectra with 9 existing medium-resolution COS spectra of AGNs to better characterize the typical spectral properties of AGNs in the rest-frame EUV. Using these data, we constructed composite spectra to aid in the determination of the typical spectral slope, the identification of the major emission lines, and the search for absorption edges predicted by some accretion disk models.

The major findings of this study are:

- Compared to 700 Å $< \lambda <$ 900 Å, the 450 Å $< \lambda <$ 770 Å region of AGN spectra exhibits a hardening spectral slope, $F_\nu \propto \nu^{-0.72\pm0.26}$. Similar hardening can be seen in the composites from Telfer et al. (2002) and Stevans et al. (2014). Though this hardening may represent curvature of the continuum slope, it could represent a failure of the power-law model to separate continuum from a pseudo-continuum of emission-line flux.

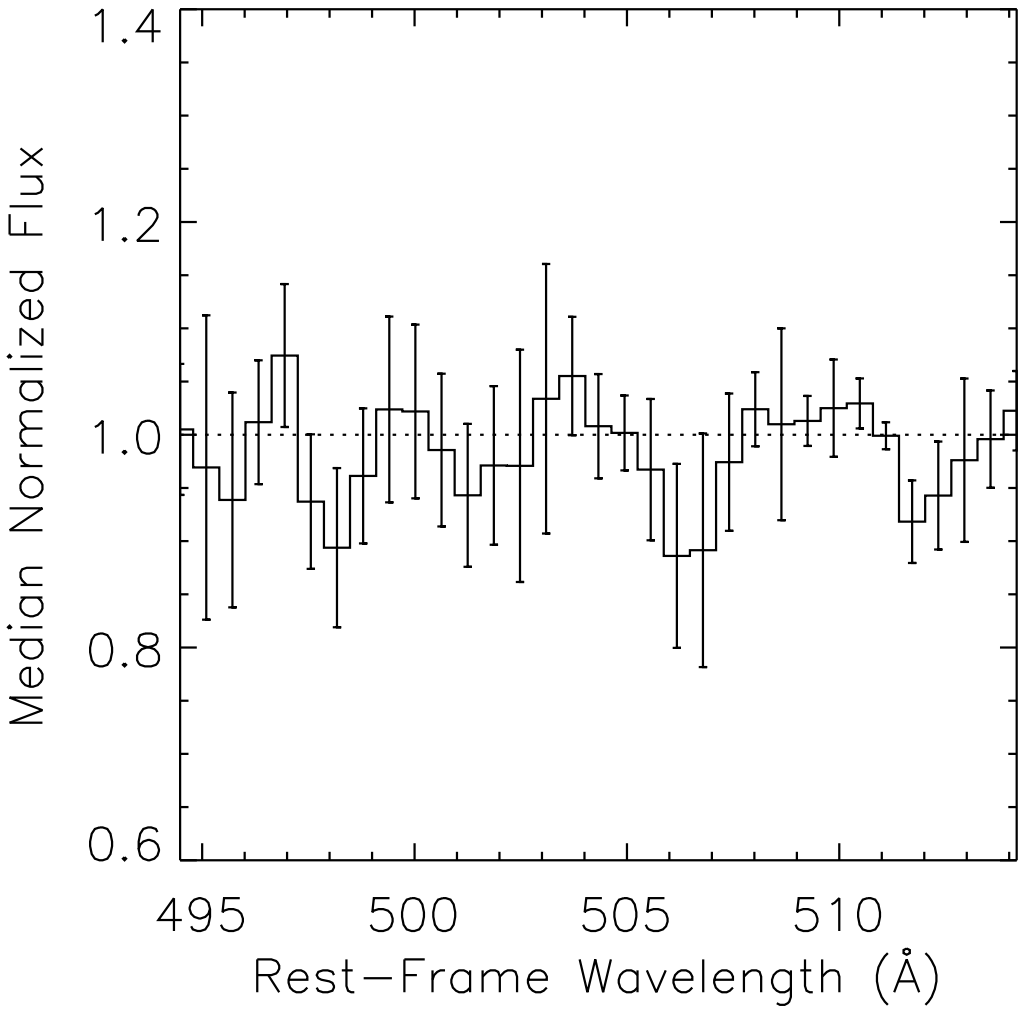

Figure 3.9 A subsample composite of 5 AGN illustrating the non-detection ($\tau_{\rm HeI} < 0.047$) of any edge-like spectral breaks due to He I absorption in the region around rest-frame 504 Å.

- The EUV spectral band contains a variety of prominent broad emission lines from ions of O, Ne, Mg, and other elements that are difficult to disentangle and identify. Possible identifications based upon the CLOUDY models of Moloney & Shull (2014) were presented in Section 3.5.2 along with measurements of the strength of emission in different spectral regions. More detailed photoionization modeling and observations targeting AGNs with narrower emission lines are required to fully understand these features.

- The He I 504 Å absorption edge predicted by some accretion disk models is not detected. Our composite spectra limit the typical He I optical depth just below the edge to $\tau_{\rm HeI} < 0.047$ ($N_{\rm HeI} < 10^{15.8}$ cm^{-2}).

The sample of targets observed at high-S/N with EUV coverage below 500 Å in the rest frame remains extremely small and is biased toward the most luminous sources. Nevertheless, COS offers the opportunity to expand this sample with AGNs at $z_{\rm AGN} \simeq 1.9 - 2.4$. It would also be useful to obtain NUV spectra necessary to characterize the intervening H I absorption that introduces systematic error to measurements of AGN spectral features. This resource should be exploited while it is available, and it should be combined with photoionization modeling to understand the numerous emission features that complicate the interpretation of these spectra. Such studies are necessary steps toward understanding the processes that govern AGN as well as their effects on the IGM through their contributions to the UVB.

Chapter 4

The Associated Absorbers of the HST/COS Archive of Observations of AGNs: Preliminary Results

4.1 Introduction

The UV spectra of active galactic nuclei (AGNs) host numerous absorption lines from neutral and partially-ionized atomic species. The majority of these features are either interstellar absorption lines local to the Milky Way or cosmologically intervening absorbers from IGM gas, such as those absorbers discussed in Chapter 2, Tilton et al. (2012), and Danforth et al. (2016), among others. However, it has been known since at least the 1960s (Anderson & Kraft, 1969) that some absorption features appear to be associated with the AGNs or their host galaxies. These associated absorbers (also sometimes called intrinsic absorbers, when definitively linked to AGN outflow) are often blueshifted at hundreds to thousands of km s^{-1} (or, rarely, tens of thousands of km s^{-1}) relative to the rest-frame of the AGN (e.g., Hamann, 1997) and are thus presumed to trace mass outflows. Though the precise launching mechanism of these winds remains a subject of debate, the most prominent candidates are radiation pressure, some variant of magnetocentrifugal forces, or a combination of the two (see Crenshaw et al., 2003; Proga, 2007, for a review).

In addition to their proximity to the AGN in redshift space, these absorbers often, but not always, have a number of other properties that distinguish them from intervening absorption lines. In contrast to the low-metallicity intervening absorbers, the associated absorbers often have high metallicities on the order of solar abundances (e.g., Hamann, 1997; Arav et al., 2007). They additionally may be time-variable (e.g., Barlow et al., 1989; Arav et al., 2015), probably owing

to changes in ionization state in response to AGN luminosity variability but also plausibly due to transverse motion of the absorbing gas in some cases. Based on photoionization modeling, the photoionization parameter $U \equiv n_\gamma n_{\rm H}$ is also often much higher than that of interveninig absorbers, and the associated absorbers sometimes show absorption from metastable fine-structure levels that suggest higher densities than is typical of the diffuse IGM or CGM (e.g., Srianand & Petitjean, 2000; Arav et al., 2013).

However, one of the most obvious properties of these associated absorbers is the unusual relative strengths of absorption from different transitions of the same atomic species. In particular, aborption line strengths in multiplets, especially the Li-like doublets from species like C IV, often deviate dramatically from the ratios expected from atomic paramters, shifting closer to 1:1 ratios among the lines. This deviation is usually interpreted as partial or inhomogeneous covering of the background light source by the absorbing gas (see Arav, 1997; Arav et al., 1999; Barlow et al., 1997; Telfer et al., 1998; de Kool et al., 2001, for early discussions of these properties), which from geometric considerations strongly implies that the gas is relatively close to the AGN compared to the cosmological distances of the intervening absorbers. These complications make column density determination sensitive to model assumptions, and they make the usual Voigt-profile fitting or apparent optical depth (AOD; Savage & Sembach, 1991) methods insufficient.

Associated absorption systems are often further classified into broad absorption lines (BALs) and narrow absorption lines (NALs) according to the total velocity width of the absorption trough, with many authors defining NALs as those with full width at half maximum (FWHM) less than 500 km s^{-1} and BALs consisting of everything wider (e.g. Edmonds et al., 2011). However, the distribution of absorption system widths is continuous, so there is no unambiguous distinguishing observational or physical feature that divides these populations. Further, though the UV hosts the most easily studied atomic transitions, associated absorbers can also be identified via optical (e.g., Hutchings et al., 2002; Aoki et al., 2006; Hall, 2007) and soft X-ray (e.g. Chartas et al., 2003) absorption lines.

An understanding of these absorbers is necessary for any comprehensive model of AGN

central engines. If these absorbers reside or originate in the nuclear regions of their host galaxies, they offer probes of galactic nuclear evolution and metallicity. Further, the mass flux and kinetic luminosity of these outflows may contribute to AGN feedback (Elvis, 2006; Dunn et al., 2010), which is frequently invoked to explain a wide array of galactic evolutionary processes, including supermassive black hole evolution (Silk & Rees, 1998; Murray et al., 2005), the quasar luminosity function (Hopkins et al., 2005b), and many other aspects of galaxy evolution (e.g., Hopkins et al., 2006, 2008). However, placing associated absorbers in context with these astrophysical phenomena requires a systematic and comprehensive catalog of associated UV absorbers that can be compared against associated absorption in other wavebands as well as AGN properties such as luminosity, type, emission-line widths, and inclination. Such a catalog can then be placed in geometric and kinematic context to the host galaxies with constraints on variability and comparison to photoionization modeling. There have been numerous past attempts to construct such a catalog. Early work with instruments such as the *International Ultraviolet Explorer* (*IUE*) and the Faint Object Spectrograph (FOS) and Space Telescope Imaging Spectrograph (STIS) onboard the *Hubble Space Telescope* (*HST*) were limited by spectral resolution and/or sensitivity (e.g., Ulrich & Boisson, 1983; Laor & Brandt, 2002; Ganguly et al., 2007), while more recent work with *Far Ultraviolet Spectroscopic Explorer* (*FUSE*) was limited to studying the O VI doublet and Lyman β (e.g., Dunn et al., 2007, 2008). Further, none of these surveys attempted robust determination of absorber column density, owing to the aforementioned complications from partial coverage of the background illumination by the absorbing material. This complication makes the usual measurement techniques unreliable (see, e.g., Arav et al., 2008).

Until now, work with the Cosmic Origins Spectrograph (COS) (Green et al., 2012) onboard *HST* has been limited to small surveys of a few objects (e.g., Muzahid et al., 2013) or detailed studies of single absorption complexes (e.g. Borguet et al., 2012; Arav et al., 2015, among many others). In this chapter, we present preliminary results from a comprehensive survey of associated absorbers covering numerous ionic species in the archive of $\sim$ 200 deep, medium-resolution ($R \sim 18,000$), *HST*/COS AGN spectra. Here, in this preliminary accounting, we report the identified systems

towards 76 AGNs in 93 observational epochs, representing all available COS data for AGN at redshifts $0.03 < z_{\rm AGN} < 0.16$. These absorbers include many outflows not previously discussed in the literature. Though our initial focus is on the NALs in this redshift range, we also identify and report all BALs. For all NAL systems and some BAL systems we have measured or limited physical parameters such as absorber column density and multiple models for the partial coverage of the backlight for our primary identification species of H I, C IV, and O VI. The forthcoming full catalog will extend this redshift range to over 300 sightlines at $z_{\rm AGN} \sim 2$ and report on additional ionic species.

4.2 Catalog Construction and Methodology

In this section, we describe the methodology used to select and process the observational data as well as the measurement techniques employed. Throughout this chapter we adopt atomic transition wavelengths and other atomic properties from Morton (2003). All absorber velocity offsets are defined relativistically relative to the restframe of the systemic redshift of the AGN $z_{\rm AGN}$, unless otherwise noted, i.e., an absorber detected at observed wavelength $\lambda_{\rm obs}$ has a reported velocity position $v_{\rm abs}$ defined by

$$\lambda_{\rm obs} = \lambda_0 \sqrt{\frac{1 + v_{\rm abs}/c}{1 - v_{\rm abs}/c}} \, (1 + z_{\rm AGN}) \, . \tag{4.1}$$

Where necessary, we adopt a flat ΛCDM cosmology with $H_0 = 71$ km s^{-1} Mpc^{-1}, $\Omega_m = 0.27$, and $\Omega_\Lambda = 0.73$. All column densities N are expressed in units of cm^{-2}.

4.2.1 Sample, Data Acquisition, and Processing

More than 600 AGNs have been observed to date with *HST*/COS. As our primary goal is the construction of a comprehensive catalog of associated absorbers in the COS archive of observations, we take an inclusive approach to our sample selection. We limit our sample to targets that have been observed with one or both of the COS medium-resolution gratings, G130M and G160M, as their resolving powers ($R = \lambda/\Delta\lambda \sim 16,000 - 21,000$) are generally sufficient to resolve the absorption

line profiles; the data obtained with the low-resolution grating, G140L ($R \sim 1500 - 4000$), is not considered. The G130M grating provides wavelength coverage over approximately $1135 - 1450$ Å and the G160M grating covers approximately $1405 - 1775$ Å, though both ranges vary slightly depending on the particular central wavelength setting used for a given observation. We select only targets at $z_{\rm AGN} \geq 0.03$ to ensure that most associated H I absorbers are well-separated in wavelength from the Galactic damped Lyα feature. For the purposes of these preliminary results, we further restrict our discussion to the absorbers at $0.03 \leq z_{\rm AGN} \leq 0.16$, roughly the range that allows for C IV detection. Finally, we include only targets with a median signal-to-noise ratio (S/N) per resolution element (resel) S/N ≥ 5 as reported in the HST Spectroscopic Legacy Archive.[1]

These selection criteria result in 76 AGNs observed in 93 distinct observational epochs. For the purposes of our analysis, we define an observational epoch as all exposures taken within less than a two-week period. In practice, exposures from a given observing campaign of a target in our sample are often spread over hours or days, but they can be unambiguously grouped by this criterion. It is unlikely but possible that non-negligible variation could have occured within some of these epochs, but further subdivision is not practical owing to S/N concerns. Twelve targets in the sample have multiple epochs of observations; each epoch is processed and analyzed in isolation so that variability might be detected. This is in contrast, for example, to the approach usually used in IGM surveys such as Tilton et al. (2012) and Danforth et al. (2016), which coadd all available exposures of a target to maximize S/N.

The full sample of targets is given in Table 4.1, along with basic target information such as the AGN activity type and right ascension (R.A.) and declination as given by NASA/IPAC Extragalactic Database (2017) and systemic AGN redshifts $z_{\rm AGN}$ taken from the references given in Table 4.2. We do not use systemic redshifts measured from the prominent high-ionization emission lines present in the FUV COS spectra because these are typically blueshifted relative to the systemic redshift (Gaskell, 1982). Instead, where possible, we adopt redshifts from the literature with robust error determinations and derived from multiple optical emission lines. In some cases we

[1] `https://archive.stsci.edu/missions/hst/spectral_legacy/welcome.html`

adopt redshifts based on radio observations or, in the case of some BL Lacertae-type objects, based on absorption lines. When no error measurement is reported for the available systemic redshift, we conservatively assume $\sigma_{z_{AGN}} = 0.01$. Observational dates and gratings, common target names, and short names used in subsequent tables are also given in Table 4.1.

Table 4.1. Observational Data and AGN Properties

Target[a]	Short Name	RA & Dec.[a] (J2000)	Redshift (z_{AGN})[b]	Ref.[b]	Chan.[c]	Obs. Start[c] (GMT)	Type[a]
MRK0421	mrk421b	11 04 27.3 +38 12 32	0.030021 ± 0.000080	9	2	2012-11-09	BLLac
MRK0421	mrk421a	11 04 27.3 +38 12 32	0.030021 ± 0.000080	9	6	2009-12-24	BLLac
MRK 0279	mrk279a	13 53 03.4 +69 18 30	0.030451 ± 0.000083	0	6	2011-06-27	Sy1.0
IRAS 23443-4502	i23443a	23 47 00.7 -44 45 43	0.030491 ± 0.000183	1	6	2012-07-17	AGN
MRK0817	mrk817b	14 36 22.1 +58 47 39	0.031328 ± 0.000103	9	6	2009-12-28	Sy1.5
MRK0817	mrk817a	14 36 22.1 +58 47 39	0.031328 ± 0.000103	9	6	2009-08-04	Sy1.5
HE 0003-5023	he0003a	00 05 43.1 -50 06 55	0.033446 ± 0.000150	22	6	2012-11-07	Sy1
MRK0509	mrk509c	20 44 09.7 -10 43 25	0.034397 ± 0.000040	23	6	2012-10-11	Sy1.5
MRK0509	mrk509b	20 44 09.7 -10 43 25	0.034397 ± 0.000040	23	6	2012-09-03	Sy1.5
MRK0509	mrk509a	20 44 09.7 -10 43 25	0.034397 ± 0.000040	23	6	2009-12-10	Sy1.5
MRK0504	mrk504a	17 01 07.7 +29 24 25	0.035788 ± 0.000177	9	2	2011-07-18	NLSy1
MRK1392	mrk1392a	15 05 56.5 +03 42 26	0.036135 ± 0.000157	9	6	2014-08-29	Sy1.8
MRK0841	mrk841a	15 04 01.2 +10 26 16	0.036422 ± 0.000120	24	6	2014-07-06	Sy1.5
IRAS 19169-5845	i19169a	19 21 14.1 -58 40 13	0.037109 ± 0.000150	1	6	2012-11-20	Sy1.2
MRK0486	mrk486a	15 36 38.3 +54 33 33	0.038934 ± 0.000093	9	2	2011-12-18	Sy1.0
RBS2055	rbs2055a	23 51 52.8 +26 19 33	0.040000	25	6	2015-10-02	Sy1
HE 0429-5343	he0429a	04 30 40.0 -53 36 56	0.040008 ± 0.000150	22	2	2011-08-19	NLSy1
MRK0231	mrk231a	12 56 14.2 +56 52 25	0.042170 ± 0.000015	26	2	2011-10-15	Sy1
KAZ 238	kaz238a	00 00 58.1 +33 20 38	0.043100 ± 0.000100	27	6	2015-09-29	Sy2
NGC 0985	ngc985b	02 34 37.8 -08 47 15	0.043127 ± 0.000100	9	6	2015-01-14	Sy1.5
NGC 0985	ngc985a	02 34 37.8 -08 47 15	0.043127 ± 0.000100	9	6	2013-08-12	Sy1.5
FAIRALL 0009	fair9a	01 23 45.8 -58 48 21	0.047016 ± 0.000067	28	6	2012-07-18	Sy1.2
MRK1253	mrk1253a	10 19 32.9 -03 20 14	0.049000 ± 0.000297	29	6	2014-06-08	Sy1
H 1118-429	h1118a	11 20 48.0 -43 15 50	0.056576 ± 0.000150	1	2	2010-11-05	Sy1.5
PG1011-040	pg1011a	10 14 20.7 -04 18 40	0.058314 ± 0.000150	1	6	2010-03-26	Sy1.2
RBS1763	rbs1763a	21 36 23.1 -62 24 01	0.058561 ± 0.000150	1	6	2013-04-28	Sy1.5
I Zw 001	izw1b	00 53 34.9 +12 41 36	0.060725 ± 0.000083	9	6	2015-01-20	Sy1
I Zw 001	izw1a	00 53 34.9 +12 41 36	0.060725 ± 0.000083	9	2	2012-11-01	Sy1
PG 1126-041	pg1126d	11 29 16.6 -04 24 08	0.061960 ± 0.000150	1	6	2015-06-14	Sy1.0
PG 1126-041	pg1126c	11 29 16.6 -04 24 08	0.061960 ± 0.000150	1	6	2014-06-28	Sy1.0
PG 1126-041	pg1126b	11 29 16.6 -04 24 08	0.061960 ± 0.000150	1	6	2014-06-01	Sy1.0
PG 1126-041	pg1126a	11 29 16.6 -04 24 08	0.061960 ± 0.000150	1	2	2012-04-15	Sy1.0
RBS144	rbs144a	01 00 27.1 -51 13 54	0.062817 ± 0.000150	1	6	2012-04-10	Sy1
MRK1513	mrk1513a	21 32 27.8 +10 08 19	0.062977 ± 0.000100	2	6	2010-10-28	Sy1.5
PG1229+204	pg1229a	12 32 03.6 +20 09 29	0.063010 ± 0.000153	3	2	2012-04-26	Sy1.0
MR2251-178	mr2251a	22 54 05.8 -17 34 55	0.063777 ± 0.000150	1	6	2011-09-29	Sy1.5
RX J0503.1-6634	rxj0503a	05 03 04.0 -66 33 46	0.064000	6	6	2010-09-22	Sy1
PG0844+349	pg0844a	08 47 42.4 +34 45 04	0.064300	5	2	2012-03-06	Sy1.0
SDSS J145108.76+270926.9	pg1448a	14 51 08.7 +27 09 27	0.064500 ± 0.005000	30	6	2011-06-18	NLSy1
1H 1613-097	1h1613a	16 15 19.1 -09 36 13	0.064962 ± 0.000150	1	6	2014-09-03	Sy1
MRK0304	mrk304b	22 17 12.2 +14 14 21	0.065762 ± 0.000027	9	2	2011-11-08	Sy1.0
MRK0304	mrk304a	22 17 12.2 +14 14 21	0.065762 ± 0.000027	9	6	2012-09-21	Sy1.0
SBS 1624+575	sbs1624a	16 25 26.5 +57 27 28	0.067000	31	2	2011-10-17	Sy1

Table 4.1 (cont'd)

Target[a]	Short Name	RA & Dec.[a] (J2000)	Redshift (z_{AGN})[b]	Ref.[b]	Chan.[c]	Obs. Start[c] (GMT)	Type[a]
RBS0563	rbs563a	04 38 29.2 -61 47 59	0.069000	32	6	2010-07-31	Sy1.5
PKS2005-489	pks2005a	20 09 25.4 -48 49 54	0.071000	7	6	2009-09-21	BLLac
SBS 1537+577	sbs1537a	15 38 10.0 +57 36 13	0.073424 ± 0.001252	33	2	2011-10-19	Sy1
SDSS J091728.56+271951.0	s091728b	09 17 28.6 +27 19 51	0.075634 ± 0.001288	33	2	2016-02-06	Sy1
KAZ 447	kaz447a	17 03 29.0 +61 41 10	0.077319 ± 0.001194	33	2	2011-10-05	Sy1
RBS1483	rbs1483a	15 19 21.6 +59 08 24	0.078005 ± 0.000351	8	2	2011-06-25	Sy1.0
MRK478	mrk478a	14 42 07.4 +35 26 23	0.079055 ± 0.000264	9	2	2012-01-26	NLSy1
TON1187	ton1187a	10 13 03.2 +35 51 24	0.079097 ± 0.000351	8	2	2011-01-31	Sy1.2
RBS1666	rbs1666a	20 05 53.0 -41 34 42	0.079632 ± 0.000150	1	6	2014-09-06	Sy1
RBS0390	rbs390a	03 10 27.8 -00 49 51	0.080139 ± 0.000150	1	6	2011-12-04	Sy1.0
SDSS J121930.87+064334.4	s121930a	12 19 30.9 +06 43 34	0.080395 ± 0.001440	33	2	2014-05-21	Sy1
SDSS J123235.82+060310.0	s123235a	12 32 35.8 +06 03 10	0.083807 ± 0.001261	33	4	2014-05-31	Sy1
SDSS J123235.82+060310.0	s123235b	12 32 35.8 +06 03 10	0.083807 ± 0.001261	33	6	2014-07-11	Sy1
PG 1351+640	pg1351a	13 53 15.8 +63 45 46	0.088200 ± 0.000100	34	2	2011-10-21	Sy1.5
MRK1501	mrk1501a	00 10 31.0 +10 58 30	0.089425 ± 0.000093	9	2	2011-12-14	Sy1.2
PG 1411+442	pg1411c	14 13 48.3 +44 00 14	0.089600 ± 0.000500	34	6	2016-04-16	Sy1.0
PG 1411+442	pg1411b	14 13 48.3 +44 00 14	0.089600 ± 0.000500	34	6	2015-02-12	Sy1.0
PG 1411+442	pg1411a	14 13 48.3 +44 00 14	0.089600 ± 0.000500	34	2	2011-10-23	Sy1.0
RBS2023	rbs2023a	23 34 52.4 -35 38 43	0.098000	35	2	2014-07-13	Sy1
RBS1503	rbs1503a	15 29 07.4 +56 16 07	0.099800	30	2	2010-11-26	Sy1.5
PG0804+761	pg0804a	08 10 58.6 +76 02 43	0.100000	11	6	2010-06-12	Sy1.0
UKS0242-724	uks0242a	02 43 09.6 -72 16 48	0.101800	12	6	2011-06-29	Sy1.2
IRASF22456-5125	i22456a	22 48 41.1 -51 09 53	0.102000	10	6	2010-06-17	Sy1.5
RBS542	rbs542a	04 26 00.7 -57 12 01	0.104000	10	6	2010-06-01	Sy1.5
HE 2332-3556	he2332a	23 34 44.3 -35 39 48	0.110000 ± 0.001000	4	2	2014-07-04	Sy1
MRK0877	mrk877a	16 20 11.3 +17 24 28	0.112438 ± 0.000334	36	2	2012-06-16	Sy1.0
2MASX J15031625+6810067	rxj1503a	15 03 16.3 +68 10 06	0.114000	38	2	2010-12-31	Sy1
TONS210	tons210a	01 21 51.5 -28 20 57	0.116000 ± 0.001000	4	6	2011-06-23	Sy1.0
PKS2155-304	pks2155a	21 58 52.0 -30 13 32	0.116000 ± 0.002000	13	2	2012-07-28	BLLac
VPC 0798	vpc0798a	12 31 13.1 +12 03 07	0.116116 ± 0.000942	37	2	2016-01-24	NLSy1
HE 1228+0131	q1230a	12 30 50.0 +01 15 23	0.118300 ± 0.000500	14	6	2010-07-07	NLSy1
HS 0033+4300	hs0033a	00 36 22.9 +43 16 40	0.120000	39	6	2009-10-06	Sy1
MRK106	mrk106a	09 19 55.4 +55 21 37	0.123366 ± 0.000351	8	6	2011-05-12	Sy1.0
IRAS-L 06229-6434	i06229a	06 23 07.7 -64 36 20	0.128889 ± 0.000100	16	6	2010-09-15	Sy1
IRAS-L 06229-6434	i06229b	06 23 07.7 -64 36 20	0.128889 ± 0.000100	16	6	2009-12-17	Sy1
PG1435-067	pg1435a	14 38 16.1 -06 58 20	0.129000	15	2	2012-02-29	Sy1.0
PG1435-067	pg1435b	14 38 16.1 -06 58 20	0.129000	15	4	2014-08-06	Sy1.0
MRK876	mrk876a	16 13 57.2 +65 43 10	0.129000	17	6	2010-04-08	Sy1.0
PG0838+770	pg0838a	08 44 45.3 +76 53 10	0.131000 ± 0.000670	17	6	2009-09-24	Sy1.0
PG1626+554	pg1626a	16 27 56.1 +55 22 32	0.131700	5	6	2011-06-15	Sy1.0
QSO0045+3926	q0045a	00 48 18.9 +39 41 11	0.134000	18	4	2010-09-07	Sy1
QSO0045+3926	q0045b	00 48 18.9 +39 41 11	0.134000	18	2	2010-10-19	Sy1
QSO0045+3926	q0045c	00 48 18.9 +39 41 11	0.134000	18	6	2009-10-06	Sy1

Table 4.1 (cont'd)

Target[a]	Short Name	RA & Dec.[a] (J2000)	Redshift (z_{AGN})[b]	Ref.[b]	Chan.[c]	Obs. Start[c] (GMT)	Type[a]
PKS0558-504	pks0558a	05 59 47.4 -50 26 52	0.137200 ± 0.001000	19	6	2010-05-26	NLSy1
RBS0799	rbs799a	09 47 33.2 +10 05 09	0.139540 ± 0.000351	8	6	2011-03-30	Sy1.5
HE 2258-5524	he2258a	23 01 52.0 -55 08 31	0.141000 ± 0.001000	4	2	2014-03-22	NLSy1
PG0026+129	pg0026a	00 29 13.7 +13 16 04	0.145000	20	2	2011-10-25	Sy1.2
SDSS J135341.03+361947.9	s135341a	13 53 41.0 +36 19 48	0.146589 ± 0.001752	40	2	2014-06-14	Sy1
RX J0053.7+2232	rxj0053a	00 53 46.1 +22 32 22	0.148000	41	6	2016-02-02	Sy1
SDSS J135712.61+170444.1	s135712a	13 57 12.6 +17 04 44	0.150500	21	6	2011-06-10	AGN

[a]Columns (1), (3), and (8) give the common name, right ascension and declination, and AGN activity type, as given in the NASA/IPAC Extragalactic Database (2017).

[b]Column (4) gives the AGN systemic redshift and, if available, the uncertainty in the redshift, while Column (5) gives the number of the source of the redshift measurement as listed in Table 4.2.

[c]Column (6) gives the available COS data channels for the target, represented as bit flags with 2 representing COS/G130M and 4 representing COS/G160M, and Column (7) gives the starting date of the observation, both retreived from the Mikulski Archive for Space Telescopes (2017).

All exposures were retreived from Mikulski Archive for Space Telescopes (2017) and reduced to one-dimensional calibrated spectra using the standard `CALCOS` version 3.1 calibration pipeline.[2]

All exposures from each observational epoch were then coadded using a modified version of `Coadd_X1D` version 3.3 from the COS Tools website.[3] The original version of this coaddition routine was described in detail by Danforth et al. (2010), with subsequent major updates detailed in Keeney et al. (2012) and Danforth et al. (2016), the latter of which also includes comparisons to similar coaddition routines. In general, we perform the coaddition in the same manner as Danforth et al. (2016), with several important differences. The `Coadd_X1D` coaddition software was modified to also track the contributions of different central wavelength settings on a pixel-by-pixel basis allowing more careful treatment of the COS line spread function (LSF; see Section 4.2.2) during line measurements. Further, in contrast to the analysis described in Danforth et al. (2016), relative flux scaling among exposures was disabled because we do not expect substantial AGN flux variation within a single observational epoch and the spectra are not further binned prior to coaddition. Finally, it is worth pointing out that, as with most COS reductions, the absolute wavelength solution may be unreliable at the ~ 15 km s^{-1} level (Fox et al., 2017); this systematic uncertainty is not included in any of our further error determinations for redshifts, velocities, and wavelengths.

[2] `http://www.stsci.edu/hst/cos/pipeline/`

[3] `http://casa.colorado.edu/~danforth/science/cos/costools.html`

Table 4.2. References for AGN Systemic Redshifts

Ref. Number[a]	Reference[a]	Ref. Number[a]	Reference[a]
0	Strauss & Huchra (1988)	21	Schneider et al. (2010)
1	Jones et al. (2009)	22	Dressler & Shectman (1988)
2	Huchra et al. (1999)	23	Huchra et al. (1993)
3	Falco et al. (1999)	24	Falco et al. (1999)
4	Wisotzki et al. (2000)	25	Wei et al. (1999)
5	Tang et al. (2012)	26	Carilli et al. (1998)
6	Cowley et al. (1984)	27	Kazarian (1987)
7	Falomo et al. (1987)	28	Lauberts & Valentijn (1989)
8	Hewett & Wild (2010)	29	Colless et al. (2003)
9	Corwin et al. (1994)	30	Schneider et al. (2010)
10	Grupe et al. (1999)	31	Véron-Cetty & Véron (2001)
11	Schmidt & Green (1983)	32	Grupe et al. (1998)
12	Allen et al. (1978)	33	Abazajian et al. (2004)
13	Falomo et al. (1993)	34	Marziani et al. (1996)
14	Bachev et al. (2008)	35	Schwope et al. (2000)
15	Boroson & Green (1992)	36	Tarenghi et al. (1994)
16	Pietsch et al. (1998)	37	Adelman-McCarthy et al. (2006)
17	Alloin et al. (1992)	38	Bade et al. (1995)
18	Liu et al. (1999)	39	Hagen et al. (1999)
19	Remillard et al. (1986)	40	Adelman-McCarthy et al. (2007)
20	Wilkes et al. (1999)	41	Grazian et al. (2000)

[a]Columns (1) and (3) list the reference numbers used in Table 4.1. Columns (2) and (4) list the corresponding references, respectively.

4.2.2 Associated Absorber Identification

In order to identify and measure absorption features, it is first necessary to characterize the unabsorbed continuum flux. Here, in contrast to the usage in Chapter 3, we use the term "continuum" to refer to the entire unabsorbed background AGN spectrum, i.e., the combined flux from the power-law component and all of the emission lines rather than the power-law continuum alone. In a method inspired by Pieri et al. (2014) and similar to that used in several of our previous studies (Shull et al., 2012b; Stevans et al., 2014; Danforth et al., 2016; Tilton et al., 2016), we apply a mostly-automated method for fitting a combination of splines and piecewise-continuous Legendre polynomials. In brief, the spectrum is divided into several-Ångstrom bins. Sigma-clipping rejects pixels that deviate substantially in flux or error (e.g., pixels with absorption present) from the median, and a spline is fitted to the resultant points. This process generally produces an acceptable model over most spectra, but the model generally fails to converge close to the Galactic damped Lyα feature, strong geocoronal emission features (Lyα, O I λ1304, and N I λ1200), and the cusps of the strongest AGN emission lines (Lyα, O VI $\lambda\lambda 1032, 1038$, C IV $\lambda\lambda 1548, 1551$). In these regions, we manually force the use of piecewise-continuous Legendre polynomials with the order of the polynomial determined via an F-test with a critical probability value of 0.05.

We next determine the "crude significance level" (CSL; Danforth et al., 2016; Gaikwad et al., 2017b) at each pixel location in the spectrum. The CSL is defined as

$$CSL = \frac{W(\lambda)}{\bar{\sigma}(\lambda)}, \tag{4.2}$$

where wavelength-dependent equivalent-width (EW) vector $W(\lambda)$ and the "line-less error vector" are determined by convolving a line profile with the continuum-normalized flux of the spectrum and the interpolation of the continuum error vector through regions of non-continuum, respectively. For the line profile, we adopt a Voigt profile with Doppler parameter $b = 25$ km s^{-1} convolved with the COS LSF. The precise choice of b for line detection purposes does not substantially impact detection results, as shown in Danforth et al. (2016). For a Gaussian width σ and Lorentzian scale

parameter γ, the Voigt profile is the convolution of Gaussian and Lorentzian profiles,

$$V(x;\sigma,\gamma) = \Re\left[e^{-z^2}\mathrm{erfc}(-iz)\right]\left(\sigma\sqrt{2\pi}\right)^{-1} \tag{4.3}$$

where $z = (x+iy)/(\sigma\sqrt{2\pi})$ (Armstrong, 1967). The COS LSFs for different COS lifetime positions and central wavelength settings are retrieved in tabulated form from the STScI website[4] (Ghavamian et al., 2009; Kriss, 2011; Fox et al., 2017). For all LSF calculations in this chapter, the LSF for a given pixel location in a coadded spectrum is calculated as a linear combination of the LSFs appropriate different central wavelength settings of the exposures that contribute to that spectrum location. However, the tabulated LSFs for the 1055 central wavelength setting do not qualitatively reproduce the data, so as a makeshift solution, all instances of this LSF are replaced by the Kriss (2011) LSF, which qualitatively better matches observed absorption lines.

Associated absorber candidates are identified by searching for significance spikes such that $CSL > 4$. In the redshift range represented by our AGN sample, the primary absorption system identification lines are H I Lyα, O VI $\lambda\lambda1032, 1038$, and C IV $\lambda\lambda1548, 1551$, for which we search over the range $-15,000 < v_{\rm abs} < 1500$ km s^{-1}. Each candidate absorber is visually inspected and measured (see Section 4.3). However, unless additional evidence of AGN association is detected (e.g., partial covering, variability, lines suggesting high metallicity), all lines at $v_{\rm abs} < -1500$ km s^{-1} are ignored. All lines at $-1500 < v_{\rm abs} < 1500$ km s^{-1} are retained and assumed to be associated with AGN, though all systems that show no evidence for association other than their velocity offset are flagged in our tables. We discuss the likely extent of IGM contamination to our catalog that results from these cutoffs in Section 4.4. Our adoption of a velocity cutoff of $-1500 < v_{\rm abs} < 1500$ km s^{-1} makes this catalog complementary to the assumption made in the Danforth et al. (2016) IGM survey; that study discards all absorbers at $v_{\rm abs} > -1500$ km s^{-1} under the assumption that they are associated (though there is a slight difference in the velocity definition, $v_{\rm abs} = (cz_{\rm AGN} - cz_{\rm abs}) \,/\, (1+z_{\rm AGN})$, used in that catalog).

[4] `http://www.stsci.edu/hst/cos/performance/spectral_resolution/`

4.3 Absorber Measurements

As mentioned in Section 4.1, the determination of column densities in associated absorbers is often complicated by partial or inhomogeneous coverage of the background light source (i.e., the AGN continuum or emission-line flux sources) by the absorbing gas. Our approach is to uniformly apply six common methods of column density determination so that once the full catalog is constructed we can compare among them. The simplest of these models are those that make no attempt to account for partial or inhomogeneous coverage and are commonly used in studies of IGM absorption lines (e.g., Tilton et al., 2012; Danforth et al., 2016). Such absorption models serve as firm lower limits on the mean optical depth, and thus column density, of the absorber in question, as any partial covering causes an underestimate of the maximum optical depth in the line of sight. For each absorber we measure two such "full-coverage" column densities: one from the apparent optical depth of each line and one from Voigt-profile component fitting. The latter also provides measures of the Doppler b parameters of the components assuming that all sub-components are correctly identified and separated.

To implement absorption models that account for partial or inhomogeneous coverage of the background source it is necessary to define the surface brightness distribution of the background light source, $S(x, y, \lambda)$, and the optical-depth distribution, $\tau(x, y, \lambda)$, in front of that source, where (x, y) is a spatial coordinate. Using the notiation and simplifications outlined in de Kool et al. (2002) and Arav et al. (2005), we can express the flux at a wavelength λ as

$$F(\lambda) = \int\int S(x, y, \lambda)\ e^{-\tau(x,y,\lambda)}\ dxdy. \tag{4.4}$$

Though Equation 4.4 is completely general, it is not practically applicable to spectra, as both $S(x, y, \lambda)$ and $\tau(x, y, \lambda)$ have unknown forms and multiple degrees of freedom. Again following Arav et al. (2005), we make the assumption that our normalized spectra have $S(x, y, \lambda) = 1$. This assumption is unlikely to be strictly true as the accretion disk that generates the AGN continuum flux has a vastly different physical scale than the gas that creates the broad and narrow emission lines. However, it is a better approximation in cases where the absorption system does not lie on

a portion of the spectrum with a rapidly varying ratio of emission line to continuum flux, and it is a necessary approximation for the practical construction of a large survey-oriented catalog such as this one. We do, however, discuss some possibiities toward the determination of differential covering of the broad emission line region and the continuum source in Section 4.4. We further assume that $\tau(x, y, \lambda) = \tau(x, \lambda)$ and use x-coordinates $0 \leq x \leq 1$ normalized to the spatial extent of the line of sight. This simplification is unlikely to significantly affect the generality of our models as we are not interested in the precise two-dimensional position of the the various optical depths within the line of sight.

The most significant assumption is the adoption of a functional form for $\tau(x, \lambda)$. In principle, this function could take any form. In practice, we are only able to substantially constrain models with two or fewer model parameters because we rarely have flux data points from more than two transitions of an atomic species (although line profile shape also might constrain the model, it is a very weak constraint in practice). Though various authors have considered an assortment of covering models, such as Gaussian fall-offs and others, two models are used by most authors and are well-suited to the survey nature of this work: a power-law distribution of optical depths and step-function partial covering. Expressed mathematically, the power-law model can be written with power-law index $a \geq 0$ and maximum optical depth within the line of sight $\tau_{\max}$ as

$$\tau(x, \lambda) = \tau_{\max}(\lambda) x^{a(\lambda)}. \tag{4.5}$$

Similarly, we consider a simple discontinuous step function in which a portion $(1 - C)$ of the background light is unattenuated and a fraction C of the background light is covered by optical depth $\tau_{\max}$. This model can be written as

$$\tau(x, \lambda) = \tau_{\max}(\lambda)\ H\left(C\left(\lambda\right) - x\right), \tag{4.6}$$

where $H(x)$ is the Heaviside step function. The normalized residual flux in an absorption line after making these simplifications is then

$$F\left(\lambda\right) = \int_0^1 e^{-\tau(x,\lambda)}\ dx. \tag{4.7}$$

Each of these absorption models is dependent on wavelength (or, equivalently, velocity) and has two free parameters that must be measured from the data. In a method analogous to the (one-parameter) AOD method, in which the optical depth τ is measured at each normalized flux bin in an absorption line, these functions can be evaluated for each velocity location in an absorption system. However, because it has two free parameters, absorption in at least two transitions from the same species with known strength ratios from atomic paramters (e.g., the 2:1 ratio of O VI or C IV doublets, or both Lyα and Lyβ from H I) must be present to determine both parameters. We perform this velocity-dependent determination in each identified associated absorber for which we have two or more transitions of the species in question. Each transition is resampled onto uniform ~ 20 km s^{-1} velocity bins, and the two parameters, $\tau_{\rm max}$ and a or C, are calculated bin by bin.

Ultimately, we wish to turn these optical-depth models into physical column densities for future comparison against photoionization models. To do so, we follow Equation 3 from Edmonds et al. (2011) in adapting the AOD relationship from Savage & Sembach (1991) into a spatially averaged, velocity-dependent column density,

$$N_{\rm ion}\left(v\right) = \frac{3.8 \times 10^{14}}{f_j \lambda_j} \langle \tau_j \left(v\right) \rangle \ \left({\rm cm}^{-2} \ {\rm km}^{-1} \ {\rm s} \right), \tag{4.8}$$

where f_j, λ_j, and $\langle \tau_j \left(v\right) \rangle$ are the oscilator strength, wavelength, and spatially-averaged optical depth, respectively, for absorption line j of an atomic species. The spatially-averaged optical depth is easily calculated for the power-law model as

$$\langle \tau_j \left(v\right) \rangle = \frac{\tau_{{\rm max},j} \left(v\right)}{a\left(v\right) + 1}, \tag{4.9}$$

and for the step-function partial covering models as,

$$\langle \tau_j \left(v\right) \rangle = C\left(v\right) \ \tau_{{\rm max},j} \left(v\right). \tag{4.10}$$

We report this velocity-summed column density for each absorber with two or more transitions.

This velocity-dependent, integrated column density approach is inapplicable in many situations. Many absorbers, especially those that are only detected via H I, do not have two measurable transitions from the same species. Further, the bin-by-bin solutions often fail, giving unphysical

solutions or huge uncertainties, in weak detections in which the noise is comparable to the flux difference between the transitions or in bins in which $\tau_{\max}$ is a highly saurated optical depth that provides no flux contrast between the solutions. Finally, if there is any degree of BAL-style overlapping of multiple transitions in wavelength space, then the method cannot be applied. As the majority of associated absorbers suffer from one or more of these complications, it is worth devising an approximate means of determining these column densities for the entire sample, even if it sacrifices some model detail. To do so, we abandon the velocity-dependence of the formalism, instead assuming a single average C or a for the absorption species, and we construct modified Voigt line profiles that can be fit to the spectrum (a similar approach was also used in Muzahid et al., 2013, for the step-function model only). This approach has the advantage of leveraging line profile shape in the constraint of the model; for example, a non-black but clearly flat-bottomed absorber still strongly constrains C, even if only one transition is present.

For the step-function partial covering model, this line profile is relatively straightforward to construct. First, the opitcal depth profile, $\tau_{\max}(v)$ is calculated for a sum of standard Voigt profile components, in the same manner as it is in our standard, full-coverage Voigt profile model, each component of which has three free parameters: the velocity offset, the Doppler b parameter, and the column density $N_{\max}$. The residual flux in a normalized spectrum with mean covering factor C is then simply given by,

$$F(v) = (1 - C) + Ce^{-\tau_{\max}(v)}, \tag{4.11}$$

which reduces to the full-coverage case if $C = 1$. The effects of the step function partial coverage on this profile can be visualized in the simulated profiles in Figure 4.1, in which the top-left panel shows Voigt profiles with saturated $N_{\max}$ and the top-right panel shows the profiles for an opitcally thin $N_{\max}$, each for several values of C. To calculate the component profiles in the power law inhomogeneous absorption case, we directly numerically evaluate Equation 4.7 for the $\tau_{\max}(v)$ defined by a given Voigt profile and power-law index a. This model reduces to the full-coverage case for $a = 0$. For all component fit methods (standard Voigt profiles, partial covering, and power-

law inhomogeneous covering), the final step in calculating the line profile is a convolution with the appropriate COS LSF, determined as described in Section 4.2.2.

In most cases, all of the aforementioned column density determinations are performed using the spectrum's continuum-normalized flux. Usually, the absorption lines are isolated and located in regions of smoothly varying continuum that is well-separated from the cusps of major AGN emission lines. In these cases, as in Danforth et al. (2016), we first normalize the spectrum using the continuum determination described in Section 4.2.2, before performing the measurements of the absorption system. In this case, fits are performed using the `MPFIT` implementation of the computationally-inexpensive Levenberg-Marquardt technique (Moré, 1978; Markwardt, 2009). However, in cases where the absorption system overlaps the cusp of a major emission line, the continuum determination can be degenerate with the absorption strength determination. In these cases, we instead fit a sum of Gaussian emission components to the emission lines. The absorption component fits are performed simultaneously with the Gaussian emission fits. Because each fit usually requires several Gaussian components and several absorption components, representing more than 20 free parameters per fit, as well as, in some cases, numerical integrals in the fitting functions, this is a computationally expensive optimization problem. For this reason, we optimize the likelihood function and determine the best-fit parameters by sampling the posterior probability distribution with version 2.1.0 of `emcee` (Foreman-Mackey et al., 2013), which implements the affine-invariant Markov-Chain Monte Carlo (MCMC) ensemble sampler from Goodman & Weare (2010). We adopt uniform priors on all parameters. We initialize at least 600 walkers randomly over the domain, allowing each to take a minimum of 375 steps, and we discard steps prior to parameter stability as a burn-in period. Parameters and their uncertainties are determined as the median and 1σ quantile values, respectively, in the marginalized posterior probability distributions.

When we must fit the unabsorbed AGN emission lines with a sum of Gaussians, the number of Gaussian components is determined by performing successive fits with additional components until the fit with the minimum Akaike information criterion (AIC) (Akaike, 1974; Burnham & Anderson, 2003) is acheived and chosen. In contrast, we choose the number of absorption components using a

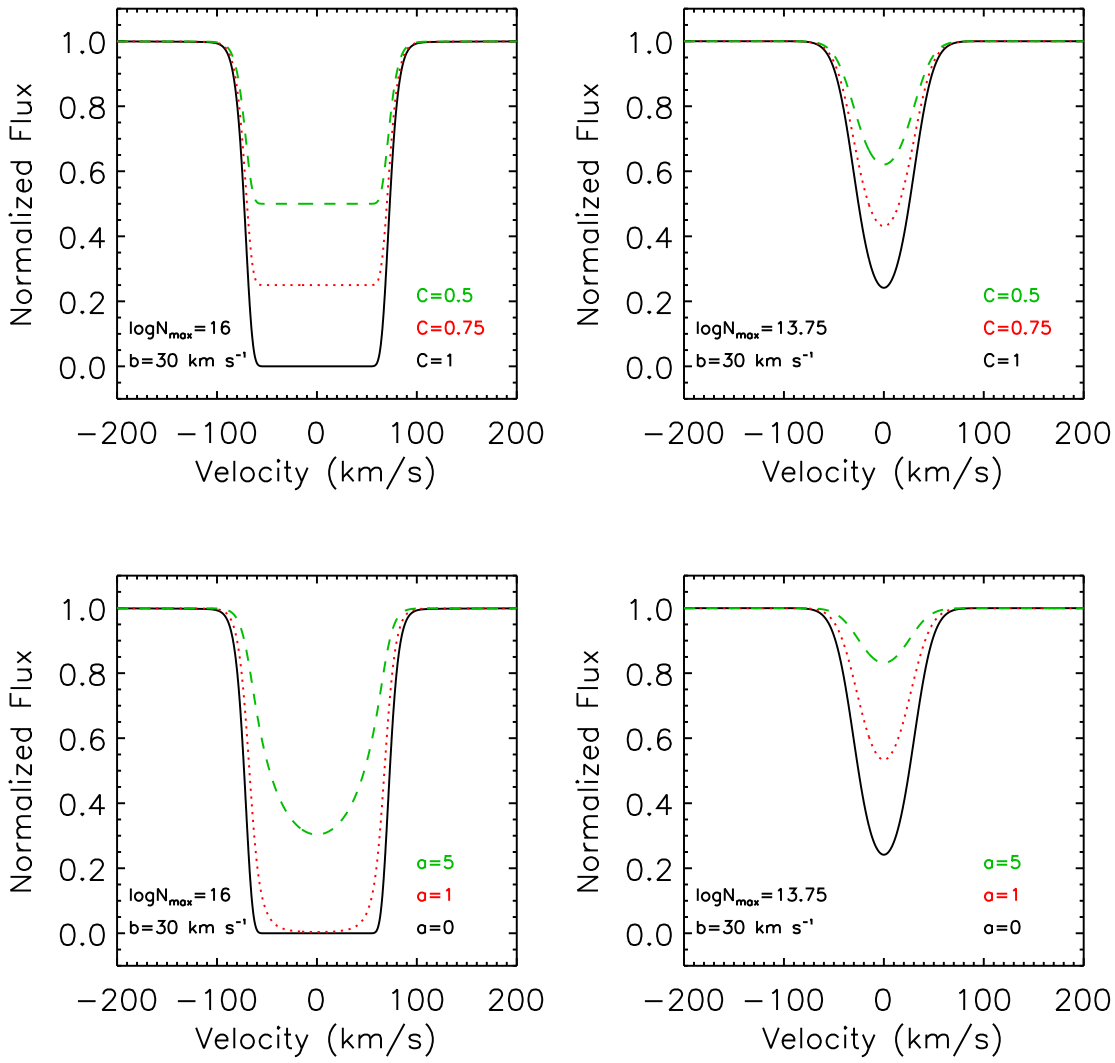

Figure 4.1 Sample line profiles computed under different assumptions about the covering of the background light source. The top row uses the step function partial coverage model, and the bottom row uses the power law inhomogeneous absorption model. The left column shows cases in which the maximum column density in the line of sight is saturated, and the right column shows purely optically thin cases.

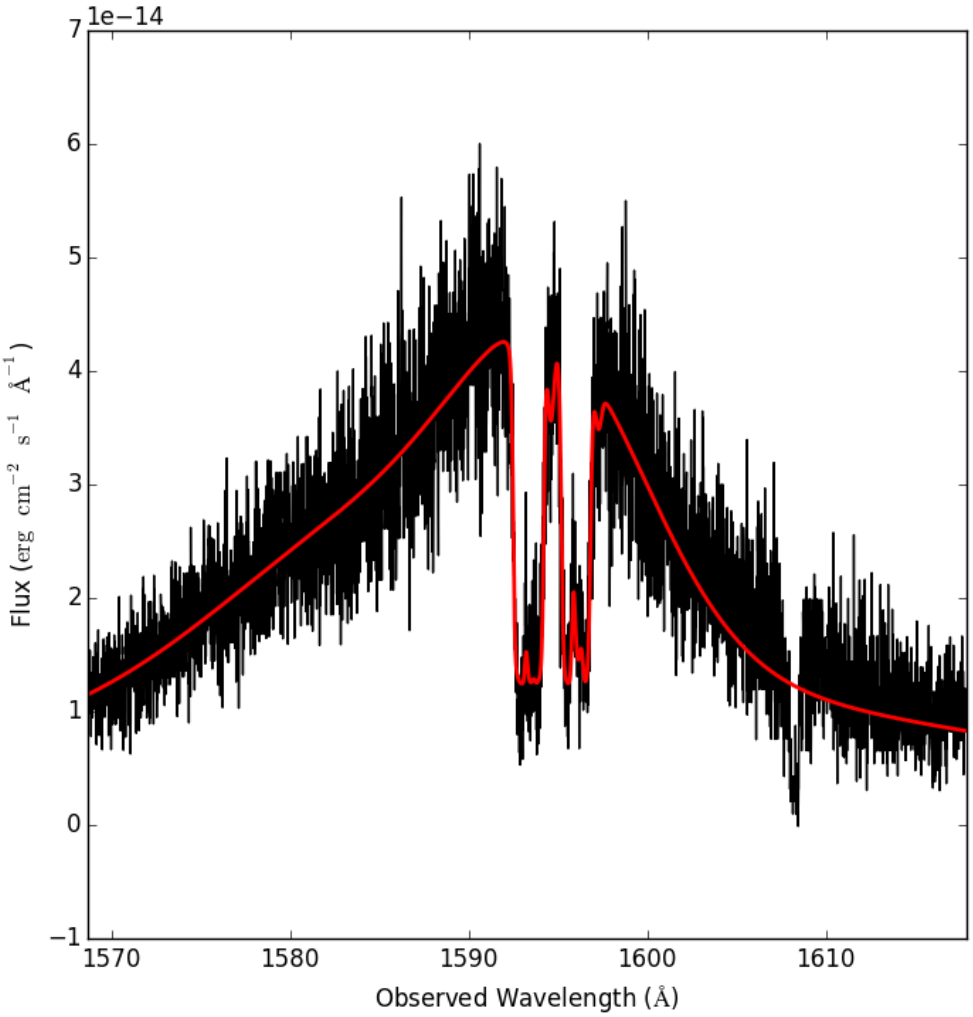

Figure 4.2 Sample MCMC fit to four emission components and four absorption components using the step function partial covering method for the C IV emission and absorption system toward Mrk 279. The black line is the coadded COS data, and the red line is the best fit model.

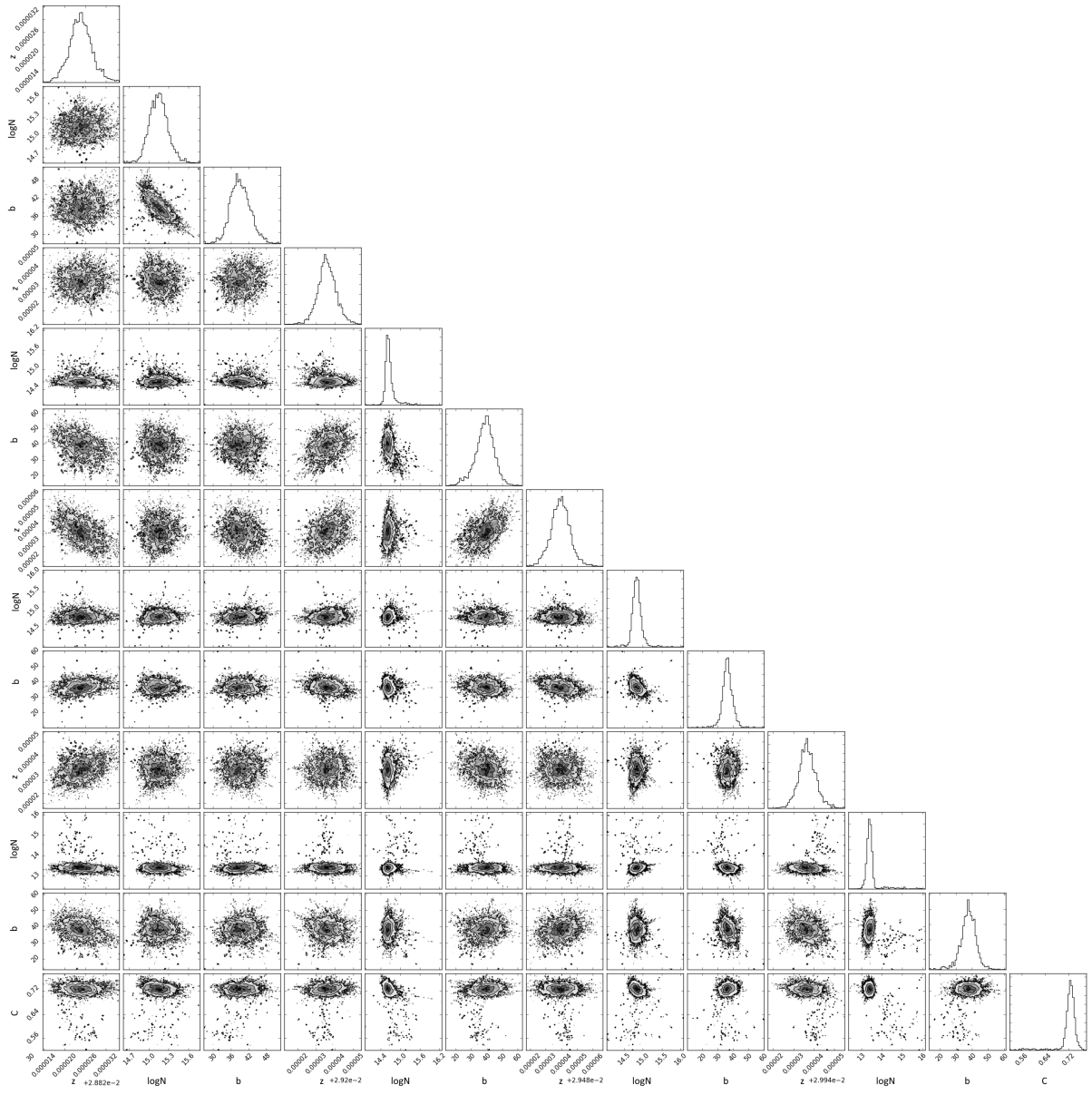

Figure 4.3 Sample probability distributions for the four absorption components plotted in Figure 4.2 from the C IV absorption system toward Mrk 279. These distributions marginalize over the distributions of the twelve parameters of the emission compoenents, which are not shown.

similar procedure with the Bayesian information criterion (BIC) (Schwarz, 1978). A full discussion of the differences among model selection statistics is beyond the scope of this chapte. In general, the AIC less severely penalizes the addition of model parameters compared to the BIC, so the latter will systematically choose models with fewer paramters than the former for the same model types and data sets. In qualitative terms, the assumptions underlying the AIC are concerned with reproducing the data regardless of any underlying truth of the model, while the BIC makes firmer assumptions about the physical meaning of the models being compared (see, e.g., Burnham & Anderson, 2004; Liddle, 2007). We apply the AIC to the unabsorbed spectrum because we are primarily concernd with reproducing the spectral shape in an information theoretic sense rather than deriving physical meaning from the parameters, while the BIC is more appropriate for assigning physical meaning to absorption component parameters. The BIC further performs more accurately in tests of the recovery of the correct number of simulated absorption components in artificial, noisy data sets.

Once each absorber identified via the CSL has been measured, we make a more careful determination of the significance level of its EW using the method described by Equations 4-10 of Keeney et al. (2012) for determining the minimum detectable EW at a given signifcance level within COS medium-resolution data. All features with a significance level less than 3σ are set to upper limits.

Finally, we flag some absorbers as BALs. Instead of applying a strict velocity-width cutoff to match a particular subset of the literature that uses that same definition, we instead take a purely procedural approach to this flagging. BALs typically require a fundamentally different approach to determining their physical parameters than NALs do. Continuum determination is complicated because large swaths of the spectrum are obscured by the absorption, and the overlapping of absorption from different transitions makes determining the equivalent widths or column densities of individual absorption lines require specialized approaches. Therefore, for the purposes of this catalog, we define any absorption system that displays overlap of multiple transitions in the metal doublets to be a BAL. This leads to a broader definition than used by most studies, including some absorbers with widths near or slightly below the common 500 km s^{-1} boundary that would normally

be classified as "mini-BALs" or just NALs. When we can adequately identify the continuum, we still attempt to measure parameters for these absorbers, but all such measurements, with the exception of the velocity extent of the absorber, should be treated as potentially unreliable due to unstudied systematic effects.

We report our column density measurements for all absorbers in several tables. For convenience, each absorption system is assigned a system ID number within its sightline, which identifies the absorber among the various data tables. Columns (1) and (2) in all measurement tables give the short name of the target sightline and the system ID number. Tables 4.3, 4.4, and 4.5 report basic, integrated, velocity-dependent quantities for H I, C IV, and O VI, respectively. Column (3) gives the velocity range over which the the subsequent quantities were determined. Columns (4)−(6) give the EW, AOD column density, and integrated velocity-dependent step function partial coverage column density, respectively. Tables 4.6, 4.7, and 4.8 give the full-coverage and partial-coverage component fit parameters for all detections. Finally, Tables 4.9, 4.10, and 4.11 give the integrated column densities and component-fit parameters for the power-law models. Some of these fits suffer from additional complications or have features of interest not captured by the data tables alone. To address this, Appendix A contains additional notes on several sightlines.

Table 4.3. Basic HI Line Measurements

Target[a]	Sys.	Velocity (km s^{-1})	EW (mÅ)	AOD ($\log N$ [cm^{-2}])	$\log N$ (PC) ($\log N$ [cm^{-2}])
1h1613a	0	$-708, -466$	384.7 ± 7.0	14.14 ± 0.00	14.96 ± 0.04
1h1613a	1	$-285, -83$	230.3 ± 5.3	13.81 ± 0.00	14.88 ± 0.04
1h1613a	2	$-12, 35$	< 17.7	< 12.64	
fair9a	0	$-292, 20$	55.1 ± 1.9	13.03 ± 0.00	15.07 ± 0.05
h1118a	0	$-907, -706$	47.3 ± 5.3	12.97 ± 0.00	14.88 ± 0.05
h1118a	1	$-704, -493$	62.9 ± 4.9	13.09 ± 0.00	14.90 ± 0.05
h1118a	2	$-497, -182$	508.3 ± 5.1	14.21 ± 0.00	15.07 ± 0.04
h1118a	3	$-77, 271$	470.7 ± 5.0	14.24 ± 0.00	15.12 ± 0.04
he0003a	0	$-929, -721$	34.6 ± 3.3	12.82 ± 0.00	14.89 ± 0.05
he0003a	1[b]	$-356, 263$	804.5 ± 3.7	14.34 ± 0.00	15.37 ± 0.04
he0429a	0	$-689, -529$	126.6 ± 5.9	13.49 ± 0.00	14.78 ± 0.05
he0429a	1	$-287, 317$	1427.0 ± 4.8	14.86 ± 0.00	15.36 ± 0.04
he0429a	2	$417, 857$	904.0 ± 5.8	14.91 ± 0.00	15.22 ± 0.04
he2258a	0	$-3231, -2990$	322.4 ± 7.7	13.99 ± 0.11	15.27 ± 0.26
			93.0 ± 14.7	14.21 ± 0.11	
he2258a	1	$-1901, -1767$	71.7 ± 6.6	13.17 ± 0.15	15.21 ± 0.30
			12.2 ± 10.7	13.44 ± 0.15	
he2258a	2	$-883, -341$	1181.2 ± 7.7	14.73 ± 0.38	16.58 ± 0.42
			760.6 ± 17.2	15.49 ± 0.38	
he2332a	0	$-2161, -1302$	1252.2 ± 12.9	14.52 ± 0.00	15.51 ± 0.04
he2332a	1	$-560, -444$	18.0 ± 2.9	12.54 ± 0.01	14.64 ± 0.05
he2332a	2	$-190, 101$	452.2 ± 2.9	14.19 ± 0.00	15.04 ± 0.04
hs0033a	0[b]	$-61, 713$	2119.8 ± 15.5	14.94 ± 0.66	$\sim NaN$
			1547.8 ± 36.1	16.25 ± 0.66	
i06229a	0	$-729, -531$	59.0 ± 3.6	13.07 ± 0.10	~ 15.05
			9.3 ± 9.4	13.24 ± 0.10	
i06229a	1	$1469, 1493$	< 19.2	< 12.67	
			< 24.0	< 13.64	
i06229b	0	$-1518, -1380$	< 18.7	< 12.66	
			< 43.1	< 13.89	
i06229b	1	$-770, -565$	57.0 ± 4.7	13.06 ± 0.17	14.94 ± 0.36
			10.1 ± 17.6	13.37 ± 0.17	
i06229b	2	$-162, -138$	< 17.1	< 12.62	
			< 34.1	< 13.79	
i06229b	3	$1007, 1019$	< 18.4	< 12.65	
			< 27.1	< 13.69	
i06229b	4	$1223, 1229$	< 21.5	< 12.72	
			< 26.9	< 13.69	
i06229b	5	$1361, 1385$	< 20.7	< 12.71	
			< 27.9	< 13.70	
i19169a	0	$-774, -523$	347.5 ± 2.3	14.12 ± 0.00	14.97 ± 0.04
i22456a	0	$-1758, -1579$	262.0 ± 1.7	13.97 ± 0.00	14.83 ± 0.04
i22456a	1	$-992, -13$	2660.0 ± 1.9	15.09 ± 0.00	15.57 ± 0.04

Table 4.3 (cont'd)

Target[a]	Sys.	Velocity (km s^{-1})	EW (mÅ)	AOD (log N [cm^{-2}])	log N (PC) (log N [cm^{-2}])
i23443a	0[b]	$-2335, 1493$			
izw1a	0	$-2089, -1653$	255.4 ± 10.9	13.74 ± 0.00	15.21 ± 0.04
izw1a	1	$-1200, -1152$	< 20.6	< 12.70	
izw1a	2	$-301, -120$	28.8 ± 4.4	12.76 ± 0.01	14.83 ± 0.05
izw1a	3	$41, 95$	< 18.5	< 12.66	
izw1a	4	$156, 345$	55.4 ± 7.7	13.05 ± 0.01	14.85 ± 0.05
izw1b	0	$-2092, -1649$	259.7 ± 6.2	13.74 ± 0.00	15.22 ± 0.04
izw1b	1	$-1262, -1099$	40.4 ± 3.0	12.90 ± 0.00	14.79 ± 0.05
izw1b	2	$-321, -112$	68.5 ± 2.0	13.12 ± 0.00	14.90 ± 0.04
izw1b	3	$-15, 122$	18.5 ± 1.9	12.55 ± 0.01	14.71 ± 0.05
izw1b	4	$125, 349$	69.4 ± 3.1	13.14 ± 0.00	14.93 ± 0.05
kaz238a	0[b]	$-657, 405$	2347.1 ± 28.4	15.51 ± 0.00	15.60 ± 0.04
mr2251a	0	$-810, 281$	1911.6 ± 3.1	14.76 ± 0.00	15.61 ± 0.04
mr2251a	1	$400, 772$	103.6 ± 2.3	13.31 ± 0.00	15.15 ± 0.04
mrk106a	0	$-1489, -1459$	< 15.4	< 12.58	
			< 51.1	< 13.97	
mrk106a	1	$-1381, -1357$	< 16.4	< 12.60	
			< 44.8	< 13.91	
mrk106a	2	$-1225, -1207$	< 20.9	< 12.71	
			< 42.1	< 13.88	
mrk106a	3	$-1143, -996$	30.5 ± 3.5	12.78 ± 0.37	15.28 ± 0.47
			16.9 ± 11.9	13.49 ± 0.37	
mrk106a	4	$791, 821$	< 12.5	< 12.49	
			< 33.2	< 13.78	
mrk1253a	0	$-320, 116$	804.5 ± 6.3	14.50 ± 0.00	15.21 ± 0.04
mrk1392a	0	$-525, -146$	551.0 ± 3.0	14.35 ± 0.00	15.15 ± 0.04
mrk1392a	1	$-16, 117$	211.4 ± 1.6	13.70 ± 0.00	14.70 ± 0.04
mrk1501a	0	$-511, -200$	751.6 ± 23.0	14.92 ± 0.00	15.07 ± 0.04
mrk1501a	1	$-115, 11$	269.5 ± 8.0	13.97 ± 0.00	14.68 ± 0.04
mrk1513a	0	$-1667, -1345$	505.0 ± 4.1	14.19 ± 0.00	15.08 ± 0.04
mrk1513a	1	$-1245, -988$	< 13.8	< 12.53	
mrk1513a	2	$-895, -691$	28.1 ± 2.7	12.73 ± 0.00	14.88 ± 0.05
mrk1513a	3	$-684, -361$	71.1 ± 3.1	13.14 ± 0.00	15.08 ± 0.05
mrk1513a	4	$-371, -162$	14.5 ± 2.1	12.44 ± 0.01	14.90 ± 0.05
mrk1513a	5	$-136, 218$	334.0 ± 2.5	13.92 ± 0.00	15.13 ± 0.04
mrk279a	0	$-727, -72$	1014.7 ± 8.4	14.52 ± 0.00	15.39 ± 0.04
mrk279a	1	$-34, 324$	650.0 ± 5.2	14.32 ± 0.00	15.13 ± 0.04
mrk304a	0[b]	$-1597, -294$			
mrk304a	1	$-260, -68$	371.6 ± 4.3	14.14 ± 0.00	14.86 ± 0.04
mrk304a	2	$227, 455$	< 18.8	< 12.66	
mrk304b	0[b]	$-1801, -444$			
mrk304b	1	$-244, 25$	395.7 ± 5.1	14.16 ± 0.00	15.01 ± 0.04
mrk304b	2	$196, 382$	83.9 ± 7.1	13.24 ± 0.00	14.84 ± 0.05

Table 4.3 (cont'd)

Target[a]	Sys.	Velocity (km s^{-1})	EW (mÅ)	AOD ($\log N$ [cm^{-2}])	$\log N$ (PC) ($\log N$ [cm^{-2}])
mrk421a	0	$-1461, -1318$	21.0 ± 3.4	12.61 ± 0.01	14.73 ± 0.05
mrk421b	0	$-1470, -1364$	21.5 ± 3.1	12.62 ± 0.01	14.60 ± 0.06
mrk478a	0	$-2881, -2596$	191.4 ± 8.7	13.65 ± 0.00	15.03 ± 0.05
mrk478a	1	$-2330, -2154$	199.9 ± 5.3	13.67 ± 0.00	14.82 ± 0.04
mrk478a	2	$-1176, -963$	82.3 ± 4.3	13.21 ± 0.00	14.90 ± 0.05
mrk478a	3	$-463, -242$	170.1 ± 4.9	13.68 ± 0.00	14.92 ± 0.04
mrk478a	4	$-166, 142$	39.3 ± 6.5	12.91 ± 0.01	15.07 ± 0.05
mrk486a	0[b]	$-1373, 989$	6704.0 ± 20.7	16.09 ± 0.00	15.95 ± 0.04
mrk504a	0	$-1146, -891$	325.9 ± 8.0	14.05 ± 0.00	14.98 ± 0.04
mrk504a	1	$-843, -623$	57.6 ± 8.5	13.08 ± 0.01	14.92 ± 0.05
mrk504a	2	$-575, -313$	195.8 ± 6.8	13.74 ± 0.00	14.99 ± 0.04
mrk504a	3	$-244, -37$	258.4 ± 4.7	13.92 ± 0.00	14.89 ± 0.04
mrk509a	0[b]	$-510, 338$	2067.3 ± 1.1	14.94 ± 0.00	15.50 ± 0.04
mrk509b	0[b]	$-520, 338$	2043.9 ± 2.9	14.92 ± 0.00	15.51 ± 0.04
mrk509c	0[b]	$-491, 345$	2095.5 ± 2.8	14.93 ± 0.00	15.50 ± 0.04
mrk817a	0	$-1190, -867$	94.2 ± 3.2	13.27 ± 0.00	15.08 ± 0.04
mrk817a	1	$-612, 89$	< 10.3	< 12.40	
mrk817b	0	$-1105, -920$	53.3 ± 3.4	13.02 ± 0.00	14.84 ± 0.05
mrk817b	1	$-553, -435$	18.7 ± 2.8	12.57 ± 0.01	14.65 ± 0.05
mrk841a	0	$-1832, -1584$	427.7 ± 5.0	14.23 ± 0.00	14.97 ± 0.04
mrk841a	1	$-1173, -917$	227.1 ± 4.9	13.72 ± 0.00	14.98 ± 0.04
mrk841a	2	$-888, -399$	703.0 ± 5.7	14.41 ± 0.00	15.26 ± 0.04
mrk841a	3	$219, 323$	52.6 ± 2.6	13.06 ± 0.00	14.59 ± 0.05
mrk876a	0	$-3883, -3355$	100.5 ± 1.8	13.31 ± 0.19	15.21 ± 0.24
			31.9 ± 6.5	13.69 ± 0.19	
mrk876a	1	$-1606, -1170$	87.3 ± 2.9	13.23 ± 0.00	15.21 ± 0.04
mrk876a	2	$-591, -499$	64.9 ± 1.1	13.13 ± 0.05	13.47 ± 0.17
			11.3 ± 2.2	13.21 ± 0.05	
mrk876a	3	$485, 533$	< 7.6	< 12.27	
			< 10.9	< 13.30	
mrk877a	0	$-827, -409$	665.6 ± 5.1	14.73 ± 0.62	16.46 ± 0.66
			601.3 ± 18.2	15.97 ± 0.62	
ngc985a	0[b]	$-996, 184$	2169.8 ± 9.9	14.84 ± 0.00	15.65 ± 0.04
ngc985b	0[b]	$-1048, 213$	1858.3 ± 4.5	14.72 ± 0.00	15.68 ± 0.04
pg0804a	0	$99, 285$	< 7.6	< 12.27	
pg0804a	1	$489, 690$	399.5 ± 1.2	14.20 ± 0.00	14.88 ± 0.04
pg0804a	2	$1343, 1367$	< 8.2	< 12.30	
pg0838a	0	$11, 59$	< 13.1	< 12.51	
			< 23.6	< 13.63	
pg0838a	1	$335, 576$	120.8 ± 4.6	13.39 ± 0.03	15.08 ± 0.14
			15.7 ± 7.8	13.44 ± 0.03	
pg0844a	0	$-1642, -1314$	116.7 ± 6.1	13.36 ± 0.00	15.09 ± 0.05
pg0844a	1	$-1315, -812$	230.2 ± 7.2	13.74 ± 0.00	15.28 ± 0.04

Table 4.3 (cont'd)

Target[a]	Sys.	Velocity (km s^{-1})	EW (mÅ)	AOD ($\log N$ [cm^{-2}])	$\log N$ (PC) ($\log N$ [cm^{-2}])
pg0844a	2	$-205, 398$	724.4 ± 6.0	14.58 ± 0.00	15.36 ± 0.04
pg1011a	0	$-1078, -663$	70.5 ± 6.6	13.15 ± 0.00	15.19 ± 0.05
pg1011a	1	$-604, -478$	< 15.7	< 12.59	
pg1011a	2	$-322, -286$	< 16.1	< 12.59	
pg1011a	3	$-12, 169$	41.4 ± 3.8	12.93 ± 0.00	14.84 ± 0.05
pg1126a	0	$-5433, -4075$	1393.1 ± 26.8	14.56 ± 0.00	15.71 ± 0.04
pg1126a	1	$-3634, -3126$	1120.1 ± 11.0	14.58 ± 0.00	15.28 ± 0.04
pg1126a	2	$-3091, -2026$	2165.3 ± 14.7	15.02 ± 0.00	15.60 ± 0.04
pg1126a	3	$-1967, -1249$	1049.0 ± 10.0	14.51 ± 0.00	15.43 ± 0.04
pg1126a	4	$-1066, -876$	304.5 ± 3.4	14.02 ± 0.00	14.85 ± 0.04
pg1126a	5	$-795, -319$	651.5 ± 5.7	14.32 ± 0.00	15.25 ± 0.04
pg1126b	0	$-5120, -4261$	1108.9 ± 16.6	14.44 ± 0.00	15.51 ± 0.04
pg1126b	1	$-3701, -3136$	1095.0 ± 10.5	14.54 ± 0.00	15.33 ± 0.04
pg1126b	2	$-3067, -2059$	2136.2 ± 10.6	14.94 ± 0.00	15.58 ± 0.04
pg1126b	3	$-1914, -1255$	962.7 ± 8.0	14.45 ± 0.00	15.39 ± 0.04
pg1126b	4	$-1085, -876$	306.4 ± 3.1	14.02 ± 0.00	14.90 ± 0.04
pg1126b	5	$-852, -292$	671.2 ± 4.9	14.34 ± 0.00	15.32 ± 0.04
pg1126c	0	$-5099, -4344$	1086.5 ± 22.7	14.44 ± 0.00	15.45 ± 0.04
pg1126c	1	$-3782, -3119$	1245.4 ± 16.1	14.61 ± 0.00	15.40 ± 0.04
pg1126c	2	$-3071, -2038$	2226.9 ± 15.4	15.03 ± 0.00	15.59 ± 0.04
pg1126c	3	$-1928, -1310$	1008.2 ± 10.7	14.48 ± 0.00	15.37 ± 0.04
pg1126c	4	$-1142, -868$	327.0 ± 5.8	14.05 ± 0.00	15.01 ± 0.04
pg1126c	5	$-785, -288$	606.2 ± 6.4	14.30 ± 0.00	15.27 ± 0.04
pg1126d	0	$-5150, -4171$	1003.4 ± 28.2	14.41 ± 0.00	15.57 ± 0.04
pg1126d	1[b]	$-3770, -3123$	1111.2 ± 17.3	14.54 ± 0.00	15.39 ± 0.04
pg1126d	2	$-3032, -2063$	2042.1 ± 15.3	14.92 ± 0.00	15.56 ± 0.04
pg1126d	3	$-1898, -1295$	892.9 ± 11.3	14.41 ± 0.00	15.36 ± 0.04
pg1126d	4	$-1082, -904$	291.7 ± 4.0	14.01 ± 0.00	14.83 ± 0.04
pg1126d	5	$-781, -312$	671.8 ± 6.3	14.35 ± 0.00	15.25 ± 0.04
pg1229a	0	$-717, -587$	56.9 ± 4.2	13.08 ± 0.00	14.69 ± 0.05
pg1229a	1	$-436, -412$	< 18.2	< 12.65	
pg1351a	0[b]	$-2264, -397$	3868.2 ± 16.0	15.09 ± 0.00	15.85 ± 0.04
pg1351a	1	$-1, 125$	38.7 ± 3.8	12.90 ± 0.01	14.68 ± 0.05
pg1411a	0[b]	$-2683, -564$			
pg1411a	1	$-219, 221$	849.5 ± 5.8	14.58 ± 0.00	15.22 ± 0.04
pg1411b	0[b]	$-3277, -505$			
pg1411b	1	$-265, 268$	862.1 ± 5.4	14.58 ± 0.00	15.30 ± 0.04
pg1411c	0[b]	$-3067, -258$			
pg1411c	1	$-280, 288$	854.1 ± 5.4	14.60 ± 0.00	15.33 ± 0.04
pg1435a	0	$-801, -561$	137.7 ± 7.1	13.46 ± 0.10	14.95 ± 0.29
			-0.1 ± 15.3	13.21 ± 0.16	
pg1448a	0	$-1050, -906$	< 41.8	< 13.01	
pg1448a	1	$-428, 315$	2166.5 ± 11.9	15.17 ± 0.00	15.45 ± 0.04

Table 4.3 (cont'd)

Target[a]	Sys.	Velocity (km s^{-1})	EW (mÅ)	AOD ($\log N$ [cm^{-2}])	$\log N$ (PC) ($\log N$ [cm^{-2}])
pg1626a	0	$-543, -124$	831.7 ± 4.3	14.51 ± 0.07	15.15 ± 0.15
			268.1 ± 9.6	14.65 ± 0.07	
pg1626a	1	$1487, 1493$	< 14.9	< 12.56	
			< 18.5	< 13.52	
pks2155a	0	$449, 485$	< 16.4	< 12.60	
			< 35.3	< 13.81	
pks2155a	1	$671, 785$	< 16.0	< 12.59	
			< 30.2	< 13.74	
pks2155a	2	$857, 875$	< 15.0	< 12.56	
			< 28.4	< 13.71	
q0045b	0	$9, 445$	313.6 ± 3.5	14.08 ± 0.20	15.51 ± 0.25
			163.6 ± 7.3	14.47 ± 0.20	
q0045c	0	$239, 436$	339.0 ± 5.5	14.10 ± 0.17	14.70 ± 0.45
			144.0 ± 12.0	14.45 ± 0.17	
q1230a	0[b]	$-3702, -2061$	1364.9 ± 6.7	14.52 ± 0.00	15.79 ± 0.04
q1230a	1	$-620, -518$	38.9 ± 1.3	12.88 ± 0.00	14.58 ± 0.05
q1230a	2	$-520, 6$	458.6 ± 2.5	14.02 ± 0.00	15.30 ± 0.04
rbs144a	0	$-831, -586$	49.2 ± 6.8	13.00 ± 0.01	14.96 ± 0.05
rbs144a	1	$-521, -143$	98.7 ± 7.8	13.30 ± 0.00	15.15 ± 0.05
rbs144a	2	$-100, 44$	64.5 ± 3.6	13.12 ± 0.00	14.74 ± 0.05
rbs144a	3	$151, 211$	< 16.6	< 12.61	
rbs1483a	0	$-129, 32$	166.8 ± 4.2	13.63 ± 0.00	14.78 ± 0.04
rbs1503a	0	$-83, 104$	121.4 ± 4.2	13.47 ± 0.00	14.85 ± 0.05
rbs1666a	0	$41, 89$	< 11.1	< 12.44	
rbs1763a	0	$-382, -65$	368.9 ± 2.3	14.19 ± 0.00	15.08 ± 0.04
rbs2023a	0	$-969, -352$	826.7 ± 11.1	14.46 ± 0.00	15.37 ± 0.04
rbs2023a	1	$-272, -148$	238.1 ± 3.7	13.91 ± 0.00	14.67 ± 0.04
rbs2055a	0	$-1404, -1226$	155.5 ± 3.1	13.58 ± 0.00	14.83 ± 0.04
rbs2055a	1	$-778, -554$	77.4 ± 2.4	13.19 ± 0.00	14.93 ± 0.04
rbs390a	0	$-395, -167$	193.8 ± 7.2	13.71 ± 0.00	14.93 ± 0.04
rbs390a	1	$-184, 34$	190.0 ± 6.4	13.67 ± 0.00	14.91 ± 0.04
rbs542a	0	$-677, -410$	159.7 ± 1.0	13.52 ± 0.00	15.00 ± 0.04
rbs542a	1	$-349, 87$	1142.0 ± 0.7	14.73 ± 0.00	15.22 ± 0.04
rbs563a	0	$-666, -648$	< 18.7	< 12.66	
rbs563a	1	$-540, -432$	< 12.3	< 12.48	
rbs563a	2	$-296, -198$	17.7 ± 2.5	12.54 ± 0.01	14.57 ± 0.06
rbs563a	3	$-183, -65$	24.1 ± 3.4	12.67 ± 0.00	14.65 ± 0.05
rbs799a	0	$-1590, -1282$	154.8 ± 9.7	13.54 ± 0.34	15.44 ± 0.62
			97.7 ± 18.1	14.21 ± 0.34	
rxj0053a	0	$94, 353$	375.7 ± 7.0	14.06 ± 0.28	$\sim NaN$
			224.0 ± 13.0	14.63 ± 0.28	
rxj0503a	0	$-603, -482$	65.9 ± 4.8	13.13 ± 0.00	14.66 ± 0.05
rxj0503a	1	$413, 449$	< 26.8	< 12.82	

Table 4.3 (cont'd)

Target[a]	Sys.	Velocity (km s^{-1})	EW (mÅ)	AOD ($\log N$ [cm^{-2}])	$\log N$ (PC) ($\log N$ [cm^{-2}])
rxj1503a	0	$-1920, -1462$	1233.9 ± 8.0	15.37 ± 0.48	16.77 ± 0.52
			896.0 ± 23.2	16.33 ± 0.48	
rxj1503a	1	$-1223, -1038$	145.9 ± 9.5	13.53 ± 0.12	15.28 ± 0.33
			-23.1 ± 40.9	13.09 ± 0.40	
rxj1503a	2	$-673, -473$	67.0 ± 7.5	13.14 ± 0.39	15.56 ± 0.48
			28.6 ± 21.8	13.90 ± 0.39	
rxj1503a	3	$-242, 57$	454.4 ± 6.6	14.26 ± 0.00	15.05 ± 0.04
rxj1503a	4	$1013, 1055$	< 31.8	< 12.89	
			< 62.2	< 14.05	
s091728b	0	$-341, -166$	188.8 ± 6.6	13.70 ± 0.00	14.82 ± 0.04
s091728b	1	$-121, 228$	849.8 ± 7.2	14.77 ± 0.00	15.12 ± 0.04
s121930a	0	$-646, -507$	30.7 ± 5.1	12.80 ± 0.01	14.72 ± 0.05
s121930a	1	$-346, -78$	159.0 ± 7.2	13.55 ± 0.00	15.00 ± 0.05
s121930a	2	$23, 59$	< 20.2	< 12.69	
s121930a	3	$299, 323$	< 24.0	< 12.77	
s135712a	0	$-1004, -755$	374.1 ± 4.5	13.97 ± 0.09	14.94 ± 0.17
			83.9 ± 13.1	14.14 ± 0.09	
sbs1624a	0	$-1532, -1277$	103.5 ± 9.4	13.34 ± 0.00	14.98 ± 0.05
ton1187a	0	$-558, 150$	73.1 ± 9.8	13.18 ± 0.00	15.43 ± 0.05
tons210a	0	$-1553, -1359$	65.2 ± 2.5	13.11 ± 0.27	15.35 ± 0.50
			25.6 ± 8.8	13.63 ± 0.27	
uks0242a	0	$-518, -304$	37.8 ± 7.0	12.88 ± 0.01	14.90 ± 0.05
vpc0798a	0	$-752, -501$	156.3 ± 8.4	13.54 ± 0.00	14.98 ± 0.05
vpc0798a	1	$-290, 51$	918.9 ± 5.2	14.90 ± 0.00	15.11 ± 0.04

[a]Column (1) gives the short target name from Table 4.1, Column (2) gives the absorption system ID number, Column (3) gives the velocity range in the restframe of the AGN over-which the absorption was integrated, Column (4) gives the absorber equivalent width in the restframe of the absorber, and Columns (5) and (6) give the column density as measured with the apparent optical depth method and the velocity dependent partial covering method, respectively.

[b]This absorber is a BAL, as defined in the text, and all measurements should be treated as unreliable.

Table 4.4. Basic CIV Line Measurements

Target[a]	Sys.	Velocity (km s^{-1})	EW (mÅ)	AOD ($\log N$ [cm^{-2}])	$\log N$ (PC) ($\log N$ [cm^{-2}])
1h1613a	0	$-661, -547$	81.7 ± 9.4	13.39 ± 0.04	~ 14.93
			49.9 ± 8.9	13.45 ± 0.04	
1h1613a	1	$-354, -84$	< 36.6	< 13.08	
			< 32.1	< 13.33	
1h1613a	2	$-12, 35$	< 34.2	< 13.05	
			< 35.9	< 13.38	
fair9a	0	$-258, -12$	< 14.9	< 12.69	
			< 15.6	< 13.01	
he0003a	0	$-870, -732$	< 43.6	< 13.16	
			< 33.2	< 13.34	
he0003a	1	$-348, 275$	< 33.3	< 13.04	
			< 34.3	< 13.36	
hs0033a	0[b]	$-204, 725$	2669.6 ± 32.1	15.21 ± 0.13	16.67 ± 0.17
			2699.5 ± 29.6	15.47 ± 0.13	
i06229a	0	$-715, -390$	< 52.9	< 13.24	
			< 44.8	< 13.47	
i06229a	1	$1469, 1493$	< 81.9	< 13.43	
			< 90.2	< 13.78	
i06229b	0	$-1518, -1380$	< 64.2	< 13.33	
			< 67.0	< 13.65	
i06229b	1	$-798, -432$	< 59.1	< 13.29	
			< 54.6	< 13.56	
i06229b	2	$-162, -138$	< 56.4	< 13.27	
i19169a	0	$-768, -510$	< 25.1	< 12.92	
			< 25.8	< 13.23	
i22456a	0	$-1724, -1634$	117.6 ± 4.3	13.60 ± 0.09	14.95 ± 0.14
			98.2 ± 3.9	13.78 ± 0.09	
i22456a	1	$-1006, -82$	2016.1 ± 10.2	15.00 ± 0.16	16.78 ± 0.21
			2071.6 ± 9.2	15.33 ± 0.16	
i23443a	0[b]	$-2335, 1493$			
kaz238a	0[b]	$-176, 152$	836.3 ± 115.5	15.76 ± 5.22	16.27 ± 5.30
			630.2 ± 92.6	~ 15.80	
mr2251a	0	$-448, 48$	685.2 ± 5.5	14.34 ± 0.03	14.75 ± 0.09
			441.4 ± 5.6	14.40 ± 0.03	
mr2251a	1	$355, 895$	< 16.6	< 12.74	
			< 18.7	< 13.09	
mrk106a	0	$-1489, -1459$	< 39.8	< 13.12	
			< 40.0	< 13.42	
mrk106a	1	$-1381, -1357$	< 41.5	< 13.14	
			< 40.4	< 13.43	
mrk106a	2	$-1225, -1207$	< 39.5	< 13.12	
			< 37.8	< 13.40	
mrk106a	3	$-1123, -744$	< 40.2	< 13.12	

Table 4.4 (cont'd)

Target[a]	Sys.	Velocity (km s^{-1})	EW (mÅ)	AOD (log N [cm^{-2}])	log N (PC) (log N [cm^{-2}])
			< 37.2	< 13.39	
mrk106a	4	791, 821	< 42.5	< 13.15	
			< 40.2	< 13.42	
mrk1253a	0	−236, 102	532.4 ± 19.9	14.38 ± 0.02	15.02 ± 0.16
			321.3 ± 21.5	14.42 ± 0.02	
mrk1392a	0	−455, −247	446.4 ± 9.5	14.28 ± 0.06	15.01 ± 0.18
			326.7 ± 8.9	14.39 ± 0.06	
mrk1392a	1	−126, 311	< 36.3	< 13.08	
			< 34.9	< 13.36	
mrk1513a	0	−1675, −1328	452.3 ± 10.6	14.22 ± 0.05	15.36 ± 0.11
			326.0 ± 10.0	14.33 ± 0.05	
mrk1513a	1	−1245, −988	< 28.1	< 12.97	
			< 28.1	< 13.27	
mrk1513a	2	−874, −736	< 26.8	< 12.95	
			< 26.0	< 13.23	
mrk1513a	3	−658, −364	< 28.3	< 12.97	
			< 25.1	< 13.22	
mrk1513a	4	−340, −208	< 25.4	< 12.92	
			< 23.5	< 13.19	
mrk1513a	5	−146, 166	59.6 ± 8.3	13.23 ± 0.32	14.99 ± 0.43
			2.9 ± 8.8	12.54 ± 0.37	
mrk279a	0	−622, −71	1241.8 ± 20.5	14.71 ± 0.09	15.39 ± 0.15
			1005.2 ± 23.3	14.88 ± 0.09	
mrk304a	0[b]	−1597, −294			
mrk304a	1	−264, 41	< 35.1	< 13.37	
mrk304a	2	227, 455	< 39.8	< 13.42	
mrk421a	0	−1429, −1345	< 36.3	< 13.08	
			< 40.9	< 13.43	
mrk509a	0[b]	−454, 240	1472.5 ± 2.4	14.76 ± 0.05	16.17 ± 0.09
			1012.2 ± 2.5	14.85 ± 0.05	
mrk509b	0[b]	−439, 171	1144.0 ± 6.5	14.63 ± 0.06	16.09 ± 0.11
			844.9 ± 7.0	14.76 ± 0.06	
mrk509c	0[b]	−474, 169	1157.1 ± 7.1	14.64 ± 0.08	16.28 ± 0.13
			923.3 ± 7.4	14.81 ± 0.08	
mrk817a	0	−1110, −708	< 36.9	< 13.09	
			< 36.8	< 13.39	
mrk817a	1	−612, 89	< 38.3	< 13.10	
			< 35.9	< 13.38	
mrk817b	0	−1080, −948	< 32.6	< 13.03	
			< 40.5	< 13.43	
mrk817b	1	−528, −240	< 39.8	< 13.12	
			< 37.2	< 13.39	
mrk841a	0	−1795, −1411	< 73.7	< 13.69	

Table 4.4 (cont'd)

Target[a]	Sys.	Velocity (km s^{-1})	EW (mÅ)	AOD ($\log N$ [cm^{-2}])	$\log N$ (PC) ($\log N$ [cm^{-2}])
mrk841a	1	$-1218, -930$	< 73.8	< 13.39	
			< 64.4	< 13.63	
mrk841a	2	$-713, -590$	178.0 ± 16.1	13.78 ± 0.01	15.17 ± 0.08
			103.8 ± 9.1	13.79 ± 0.01	
mrk841a	3	$205, 341$	< 36.6	< 13.08	
			< 33.2	< 13.34	
mrk876a	0	$-3936, -3611$	87.1 ± 8.8	13.38 ± 0.12	15.39 ± 0.17
			75.9 ± 7.7	13.61 ± 0.12	
mrk876a	1	$-1927, -997$	< 22.5	< 12.87	
			< 22.0	< 13.16	
mrk876a	2	$-721, -487$	< 21.1	< 12.84	
			< 21.6	< 13.15	
mrk876a	3	$485, 533$	< 23.5	< 12.89	
			< 21.8	< 13.16	
ngc985a	0[b]	$-723, 211$	2289.5 ± 15.6	14.91 ± 0.02	16.28 ± 0.07
			1358.2 ± 18.0	14.96 ± 0.02	
ngc985b	0[b]	$-852, 385$	815.1 ± 14.2	14.38 ± 0.11	16.37 ± 0.16
			668.4 ± 14.2	14.60 ± 0.11	
pg0804a	0	$99, 285$	< 16.7	< 12.74	
			< 17.3	< 13.06	
pg0804a	1	$497, 697$	195.1 ± 3.5	13.83 ± 0.09	15.19 ± 0.14
			163.6 ± 3.9	14.01 ± 0.09	
pg0804a	2	$1343, 1367$	< 20.5	< 12.83	
			< 27.0	< 13.25	
pg0838a	0	$11, 59$	< 49.3	< 13.21	
			< 52.4	< 13.54	
pg0838a	1	$341, 557$	< 49.3	< 13.21	
			< 56.8	< 13.57	
pg1011a	0	$-1048, -706$	< 46.2	< 13.18	
			< 41.7	< 13.44	
pg1011a	1	$-604, -478$	< 42.1	< 13.14	
			< 36.5	< 13.38	
pg1011a	2	$-322, -286$	< 40.0	< 13.12	
			< 32.9	< 13.34	
pg1011a	3	$25, 139$	< 34.0	< 13.05	
			< 40.2	< 13.42	
pg1448a	0	$-1050, -906$	< 69.9	< 13.36	
			< 63.8	< 13.63	
pg1448a	1	$-427, 316$	2602.8 ± 24.2	15.35 ± 0.03	16.66 ± 0.07
			2041.9 ± 27.6	15.41 ± 0.03	
pg1626a	0	$-949, -120$	< 41.8	< 13.14	
			< 38.6	< 13.41	
pg1626a	1	$1487, 1493$	< 49.9	< 13.22	

Table 4.4 (cont'd)

Target[a]	Sys.	Velocity (km s^{-1})	EW (mÅ)	AOD ($\log N$ [cm^{-2}])	$\log N$ (PC) ($\log N$ [cm^{-2}])
			< 51.6	< 13.53	
q0045a	0	210, 408	280.5 ± 8.0	14.09 ± 0.09	15.21 ± 0.17
			241.4 ± 9.7	14.27 ± 0.09	
q1230a	0[b]	−3602, −2061	1841.1 ± 18.5	14.77 ± 0.05	16.27 ± 0.09
			1218.4 ± 18.5	14.86 ± 0.05	
q1230a	1	−642, −528	< 23.5	< 12.89	
			< 28.4	< 13.27	
q1230a	2	−417, −102	426.8 ± 6.8	14.13 ± 0.02	14.73 ± 0.10
			255.7 ± 8.3	14.17 ± 0.02	
rbs144a	0	−862, −628	< 44.4	< 13.17	
			< 39.7	< 13.42	
rbs144a	1	−478, −208	< 43.5	< 13.16	
			< 44.4	< 13.47	
rbs144a	2	−76, 49	< 43.0	< 13.15	
			< 42.3	< 13.45	
rbs144a	3	151, 211	< 44.5	< 13.17	
			< 46.2	< 13.49	
rbs1666a	0	41, 89	< 28.9	< 12.98	
			< 27.0	< 13.25	
rbs1763a	0	−283, −124	289.4 ± 4.4	14.11 ± 0.07	15.20 ± 0.12
			234.5 ± 4.5	14.25 ± 0.07	
rbs390a	0	−372, −185	< 60.5	< 13.30	
			< 63.3	< 13.62	
rbs390a	1	−175, 17	< 54.9	< 13.26	
			< 55.9	< 13.57	
rbs542a	0	−1763, −385	< 16.4	< 12.73	
			< 15.1	< 13.00	
rbs542a	1	−335, 23	829.8 ± 3.1	14.61 ± 0.08	15.70 ± 0.12
			720.2 ± 3.0	14.77 ± 0.08	
rbs563a	0	−666, −648	< 46.3	< 13.19	
			< 28.3	< 13.27	
rbs563a	1	−540, −432	< 38.4	< 13.10	
			< 29.2	< 13.29	
rbs563a	2	−270, −216	< 30.6	< 13.01	
			< 37.1	< 13.39	
rbs563a	3	−168, −55	< 25.4	< 12.93	
			< 33.0	< 13.34	
rbs799a	0	−1530, −1140	< 98.8	< 13.51	
			< 94.3	< 13.79	
rxj0053a	0	150, 321	166.9 ± 38.2	13.89 ± 0.30	15.82 ± 0.40
			174.6 ± 38.0	14.48 ± 0.30	
rxj0503a	0	−612, −498	< 51.8	< 13.23	
			< 54.0	< 13.55	

Table 4.4 (cont'd)

Target[a]	Sys.	Velocity (km s^{-1})	EW (mÅ)	AOD (log N [cm^{-2}])	log N (PC) (log N [cm^{-2}])
rxj0503a	1	413, 449	< 64.2	< 13.33	
			< 64.8	< 13.63	
s135712a	0	$-1182, -750$	< 118.1	< 13.59	
			< 103.1	< 13.83	
tons210a	0	$-1555, -1357$	< 31.3	< 13.02	
			< 28.9	< 13.28	
uks0242a	0	$-486, -402$	< 56.7	< 13.27	
			< 56.5	< 13.57	

[a]Column (1) gives the short target name from Table 4.1, Column (2) gives the absorption system ID number, Column (3) gives the velocity range in the restframe of the AGN overwhich the absorption was integrated, Column (4) gives the absorber equivalent width in the restframe of the absorber, and Columns (5) and (6) give the column density as measured with the apparent optical depth method and the velocity dependent partial covering method, respectively.

[b]This absorber is a BAL, as defined in the text, and all measurements should be treated as unreliable.

Table 4.5. Basic OVI Line Measurements

Target[a]	Sys.	Velocity (km s^{-1})	EW (mÅ)	AOD (log N [cm^{-2}])	log N (PC) (log N [cm^{-2}])
he2258a	0	$-3108, -2799$	206.1 ± 15.8	14.32 ± 0.02	15.64 ± 0.11
			117.3 ± 12.4	14.34 ± 0.02	
he2258a	1	$-1929, -1769$	90.2 ± 9.6	13.97 ± 0.13	15.91 ± 0.20
			86.8 ± 9.4	14.23 ± 0.13	
he2258a	2	$-772, -349$	1096.3 ± 6.5	15.55 ± 0.07	16.77 ± 0.11
			980.2 ± 8.5	15.69 ± 0.07	
he2332a	0	$-1954, -1383$	< 155.2	< 14.22	
			< 70.7	< 14.18	
he2332a	1	$-524, -464$	< 74.8	< 13.90	
			< 68.0	< 14.16	
he2332a	2	$-103, 19$	78.8 ± 13.1	13.92 ± 0.08	15.55 ± 0.27
			50.7 ± 16.1	14.05 ± 0.08	
hs0033a	0[b]	$-92, 666$	2077.2 ± 31.0	16.16 ± 0.13	17.20 ± 0.17
			1906.2 ± 27.5	16.42 ± 0.13	
i06229a	0	$-715, -390$	< 22.7	< 13.38	
			< 22.2	< 13.67	
i06229a	1	$1469, 1493$	< 22.1	< 13.37	
			< 26.8	< 13.76	
i06229b	0	$-1518, -1380$	< 31.2	< 13.52	
			< 25.4	< 13.73	
i06229b	1	$-798, -432$	< 27.5	< 13.47	
			< 26.5	< 13.75	
i06229b	2	$-162, -138$	< 24.8	< 13.42	
			< 28.5	< 13.78	
i06229b	3	$1007, 1019$	< 27.6	< 13.47	
			< 31.3	< 13.82	
i06229b	4	$1223, 1229$	< 25.5	< 13.44	
			< 30.2	< 13.81	
i06229b	5	$1361, 1385$	< 27.3	< 13.46	
			< 30.6	< 13.81	
i22456a	0[b]	$-1739, -1624$	42.8 ± 3.0	13.89 ± 0.00	15.51 ± 0.05
i22456a	1[b]	$-1395, -33$			
mrk106a	0	$-1489, -1459$	< 41.5	< 13.65	
			< 26.6	< 13.75	
mrk106a	1	$-1381, -1357$	< 38.9	< 13.62	
			< 27.3	< 13.76	
mrk106a	2	$-1225, -1207$	< 36.0	< 13.58	
			< 28.4	< 13.78	
mrk106a	3	$-1123, -744$	< 32.8	< 13.54	
			< 28.7	< 13.79	
mrk106a	4	$791, 821$	< 26.6	< 13.45	
			< 24.5	< 13.72	
mrk876a	0	$-3865, -3398$	358.5 ± 5.7	14.57 ± 0.09	16.12 ± 0.13

Table 4.5 (cont'd)

Target[a]	Sys.	Velocity (km s^{-1})	EW (mÅ)	AOD ($\log N$ [cm^{-2}])	$\log N$ (PC) ($\log N$ [cm^{-2}])
			297.7 ± 5.0	14.75 ± 0.09	
mrk876a	1	$-1927, -997$	< 11.8	< 13.10	
			< 11.5	< 13.39	
mrk876a	2	$-721, -487$	< 11.1	< 13.07	
			< 10.3	< 13.34	
mrk876a	3	$485, 533$	< 9.8	< 13.02	
			< 10.8	< 13.36	
mrk877a	0	$-682, -475$	407.6 ± 12.8	14.75 ± 0.16	14.62 ± 0.21
			124.3 ± 12.2	14.42 ± 0.17	
pg0804a	0	$99, 285$	< 29.6	< 13.50	
			< 26.6	< 13.75	
pg0804a	1	$524, 632$	107.8 ± 3.4	14.02 ± 0.10	15.89 ± 0.14
			88.0 ± 4.0	14.21 ± 0.10	
pg0804a	2	$1343, 1367$	< 23.2	< 13.39	
			< 20.4	< 13.64	
pg0838a	0	$11, 59$	< 18.8	< 13.30	
			< 20.6	< 13.64	
pg0838a	1	$341, 557$	< 20.1	< 13.33	
			< 20.9	< 13.65	
pg1435a	0	$-756, -480$	< 34.1	< 13.56	
			< 31.0	< 13.82	
pg1626a	0	$-949, -120$	< 20.4	< 13.34	
			< 19.7	< 13.62	
pg1626a	1	$1487, 1493$	< 19.3	< 13.31	
			< 22.5	< 13.68	
pks2155a	0	$449, 485$	< 22.0	< 13.37	
			< 19.9	< 13.63	
pks2155a	1	$671, 785$	< 22.1	< 13.37	
			< 19.2	< 13.61	
pks2155a	2	$857, 875$	< 21.2	< 13.35	
			< 18.3	< 13.59	
q0045b	0	$221, 390$	309.1 ± 3.1	14.70 ± 0.10	15.49 ± 0.14
			268.8 ± 3.5	14.89 ± 0.10	
q0045c	0	$202, 396$	333.9 ± 8.4	14.75 ± 0.09	15.74 ± 0.17
			292.2 ± 9.5	14.93 ± 0.09	
q1230a	0	$-3695, -2111$	3323.5 ± 12.4	15.78 ± 0.06	16.63 ± 0.11
			2854.3 ± 9.0	15.91 ± 0.06	
q1230a	1	$-642, -528$	< 12.3	< 13.42	
q1230a	2	$-436, -28$	1035.5 ± 3.0	15.33 ± 0.06	15.60 ± 0.11
			896.9 ± 3.0	15.46 ± 0.06	
rbs1503a	0	$-144, 89$	< 59.2	< 14.10	
rbs2023a	0	$-963, -416$	704.4 ± 29.9	15.38 ± 0.00	16.18 ± 0.04
rbs2023a	1	$-288, 245$	< 109.8	< 14.07	

Table 4.5 (cont'd)

Target[a]	Sys.	Velocity (km s^{-1})	EW (mÅ)	AOD ($\log N$ [cm^{-2}])	$\log N$ (PC) ($\log N$ [cm^{-2}])
			< 61.7	< 14.12	
rbs542a	0	$-1763, -385$	< 15.7	< 13.22	
			< 11.6	< 13.39	
rbs542a	1	$-339, 6$	904.6 ± 1.6	15.27 ± 0.12	16.82 ± 0.17
			838.3 ± 1.7	15.52 ± 0.12	
rbs799a	0	$-1584, -1309$	96.4 ± 14.5	13.99 ± 0.22	16.25 ± 0.26
			133.2 ± 12.2	14.41 ± 0.22	
rxj0053a	0	$106, 338$	187.8 ± 11.9	14.26 ± 0.08	15.94 ± 0.13
			137.6 ± 11.8	14.42 ± 0.08	
rxj1503a	0	$-1934, -1603$	221.4 ± 21.2	14.81 ± 0.00	15.97 ± 0.05
rxj1503a	1	$-1200, -1068$	< 69.7	< 13.87	
			< 72.7	< 14.19	
rxj1503a	2	$-630, -480$	< 59.7	< 13.80	
			< 57.3	< 14.09	
rxj1503a	3	$-216, 47$	< 63.6	< 14.13	
rxj1503a	4	$1013, 1055$	< 58.2	< 13.79	
			< 68.9	< 14.17	
s135712a	0	$-1065, -765$	287.9 ± 12.4	14.50 ± 0.00	15.62 ± 0.04
tons210a	0	$-1555, -1357$	< 22.0	< 13.37	
			< 18.4	< 13.59	
uks0242a	0	$-486, -402$	< 40.2	< 13.93	

[a]Column (1) gives the short target name from Table 4.1, Column (2) gives the absorption system ID number, Column (3) gives the velocity range in the restframe of the AGN over-which the absorption was integrated, Column (4) gives the absorber equivalent width in the restframe of the absorber, and Columns (5) and (6) give the column density as measured with the apparent optical depth method and the velocity dependent partial covering method, respectively.

[b]This absorber is a BAL, as defined in the text, and all measurements should be treated as unreliable.

Table 4.6. HI Line Fits

Target[a]	Sys.	Vel. (Full Cov.) (km s^{-1})	b (Full Cov.) (km s^{-1})	log N (Full Cov.) (log N [cm^{-2}])	Vel. (PC) (km s^{-1})	b (PC) (km s^{-1})	log $N_{\rm max}$ (PC) (log N [cm^{-2}])	C (PC)
1h1613a	0[c]	-630.9 ± 2.9	25.4 ± 2.7	14.35 ± 0.09	-630.9 ± 1.6	22.9 ± 3.4	14.56 ± 0.23	0.98 ± 0.01
		-578.8 ± 40.1	~ 38.6	13.36 ± 0.63	-577.6 ± 5.8	~ 36.2	13.36 ± 0.56	
		-520.3 ± 2.5	~ 6.9	12.83 ± 0.19	-520.4 ± 1.6	~ 7.1	12.85 ± 0.17	
1h1613a	1[cd]	-191.7 ± 0.6	32.1 ± 0.9	13.88 ± 0.01	-191.7 ± 0.8	32.1 ± 0.9	13.88 ± 0.01	~ 1.00
fair9a	0[cd]	-228.9 ± 1.9	6.5 ± 5.2	12.07 ± 0.10	-229.2 ± 1.5	~ 4.5	14.02 ± 7.60	0.12 ± 0.01
		-168.2 ± 2.0	45.7 ± 3.2	12.93 ± 0.02	-167.3 ± 1.5	31.5 ± 5.6	14.32 ± 0.24	
		-39.3 ± 1.7	13.7 ± 3.0	12.33 ± 0.04	-39.3 ± 1.3	12.0 ± 3.0	13.50 ± 0.12	
h1118a	0[cd]	-817.6 ± 8.3	76.5 ± 14.1	13.03 ± 0.06	-814.5 ± 2.4	~ 28.0	16.66 ± 12.29	0.08 ± 0.01
h1118a	1[cd]	-585.4 ± 8.4	98.2 ± 16.4	13.18 ± 0.05	-600.4 ± 2.1	~ 30.6	16.92 ± 15.03	0.10 ± 0.01
h1118a	2[cd]	-398.4 ± 169.5	~ 90.2	13.18 ± 1.12	-398.4 ± 13.0	~ 90.2	13.18 ± 1.12	~ 1.00
		-352.7 ± 1.6	7.2 ± 5.0	13.70 ± 0.63	-352.7 ± 1.3	7.2 ± 5.0	13.70 ± 0.63	
		-324.7 ± 4.6	50.6 ± 8.1	14.11 ± 0.14	-324.7 ± 2.2	50.6 ± 8.1	14.11 ± 0.14	
		-259.6 ± 4.8	22.1 ± 6.5	13.25 ± 0.24	-259.6 ± 2.2	22.1 ± 6.5	13.25 ± 0.24	
h1118a	3[cd]	26.2 ± 0.4	14.4 ± 0.7	13.74 ± 0.02	26.2 ± 0.6	14.4 ± 0.7	13.74 ± 0.02	~ 1.00
		159.7 ± 0.3	21.7 ± 1.3	14.99 ± 0.17	159.7 ± 0.5	21.7 ± 1.3	14.99 ± 0.17	
he0003a	0[cd]	-808.1 ± 4.3	51.7 ± 6.5	12.84 ± 0.04	-809.4 ± 1.0	~ 4.8	17.54 ± 0.15	0.11 ± 0.03
he0003a	1[bc]	-297.4 ± 13.3	23.2 ± 18.3	12.72 ± 1.02	-302.8 ± 3.1	~ 18.3	12.59 ± 1.00	0.94 ± 0.01
		-236.5 ± 67.0	~ 44.8	13.51 ± 1.25	-259.2 ± 3.8	36.7 ± 35.3	13.21 ± 0.67	
		-181.4 ± 33.9	39.6 ± 19.1	13.65 ± 0.81	-192.6 ± 2.9	48.6 ± 15.3	13.83 ± 0.29	
		-97.4 ± 4.9	36.9 ± 5.1	13.25 ± 0.08	-96.4 ± 1.4	17.6 ± 5.6	12.86 ± 0.21	
		61.3 ± 2.3	81.8 ± 5.1	13.46 ± 0.02	-82.5 ± 11.4	~ 112.4	13.37 ± 0.75	
		148.7 ± 7.2	8.4 ± 6.0	13.65 ± 0.71	39.5 ± 1.1	20.2 ± 3.5	12.99 ± 0.11	
		172.2 ± 5.7	~ 16.4	13.82 ± 0.83	95.0 ± 1.0	16.4 ± 2.5	12.95 ± 0.08	
		197.1 ± 8.1	9.9 ± 4.7	13.59 ± 0.70	172.3 ± 0.4	16.8 ± 1.3	15.30 ± 0.29	
he0429a	0[cd]	-634.2 ± 0.8	6.2 ± 3.0	13.76 ± 0.63	-634.2 ± 0.9	6.2 ± 3.0	13.76 ± 0.63	~ 1.00
		-599.0 ± 1.4	10.6 ± 2.6	13.14 ± 0.04	-599.0 ± 1.2	10.6 ± 2.6	13.14 ± 0.04	
he0429a	1[cd]	-188.8 ± 0.6	21.9 ± 1.0	14.17 ± 0.03	-188.8 ± 0.8	21.9 ± 1.0	14.17 ± 0.03	~ 1.00
		-99.2 ± 0.5	32.8 ± 1.0	14.79 ± 0.05	-99.2 ± 0.7	32.8 ± 1.0	14.79 ± 0.05	
		149.8 ± 1.4	34.7 ± 1.8	15.98 ± 0.20	149.8 ± 1.2	34.7 ± 1.8	15.98 ± 0.20	
		233.2 ± 22.3	37.0 ± 12.9	13.47 ± 0.35	233.2 ± 4.7	37.0 ± 12.9	13.47 ± 0.35	
he0429a	2[cd]	647.2 ± 0.4	37.2 ± 1.0	17.32 ± 0.16	647.2 ± 0.6	37.2 ± 1.0	17.32 ± 0.16	~ 1.00
he2258a	0[d]	-3097.0 ± 2.5	25.3 ± 0.4	13.28 ± 0.04	-3099.3 ± 1.8	~ 31.9	13.32 ± 0.04	0.94 ± 0.01
		-3032.3 ± 0.8	26.2 ± 0.3	14.03 ± 0.02	-3032.8 ± 0.9	26.9 ± 0.4	14.10 ± 0.03	
he2258a	1[d]	-1836.9 ± 8.6	103.8 ± 1.5	13.41 ± 0.04	-1834.8 ± 1.7	~ 33.0	13.19 ± 0.03	0.97 ± 0.02
he2258a	2	-661.0 ± 0.4	24.1 ± 0.2	17.07 ± 0.05	-802.7 ± 1.9	30.5 ± 2.4	12.75 ± 0.06	0.97 ± 0.01
		-478.9 ± 0.7	27.2 ± 0.2	15.84 ± 0.06	-661.1 ± 0.7	32.8 ± 0.2	15.71 ± 0.04	
		-426.0 ± 2.4	22.1 ± 0.4	13.59 ± 0.10	-474.7 ± 0.6	35.9 ± 0.2	15.27 ± 0.02	
he2332a	0[cd]	-2071.8 ± 15.8	33.6 ± 27.1	12.50 ± 0.29	-2061.1 ± 3.6	47.4 ± 20.2	12.95 ± 0.14	0.72 ± 0.04
		-1841.1 ± 5.3	141.8 ± 8.0	14.29 ± 0.02	-1835.9 ± 2.1	~ 125.0	14.56 ± 0.07	
		-1643.5 ± 5.7	73.4 ± 8.4	13.94 ± 0.10	-1647.2 ± 1.8	55.8 ± 7.8	14.21 ± 0.10	
		-1505.7 ± 24.7	107.5 ± 20.4	13.73 ± 0.12	-1538.8 ± 3.2	~ 125.0	14.05 ± 0.06	
he2332a	1[cd]	-498.9 ± 5.5	36.2 ± 9.0	12.59 ± 0.07	-498.5 ± 2.2	~ 15.6	~ 15.99	0.06 ± 0.01

Table 4.6 (cont'd)

Target[a]	Sys.	Vel. (Full Cov.) (km s^{-1})	b (Full Cov.) (km s^{-1})	log N (Full Cov.) (log N [cm^{-2}])	Vel. (PC) (km s^{-1})	b (PC) (km s^{-1})	log $N_{\rm max}$ (PC) (log N [cm^{-2}])	C (PC)
he2332a	2[cd]	-86.3 ± 1.3	32.3 ± 1.5	13.66 ± 0.02	-86.3 ± 1.2	32.3 ± 1.5	13.66 ± 0.02	1.00 ± 0.01
		-18.7 ± 0.5	28.2 ± 0.6	14.20 ± 0.01	-18.7 ± 0.7	28.1 ± 1.0	14.20 ± 0.04	
hs0033a	0[b]	-13.7 ± 0.1	~ 28.9	12.26 ± 0.30	-15.2 ± 0.1	43.1 ± 1.6	13.14 ± 0.09	0.89 ± 0.01
		155.7 ± 1.4	26.2 ± 0.5	18.54 ± 0.03	181.3 ± 1.3	49.9 ± 0.6	~ 18.00	
		308.8 ± 2.1	26.9 ± 0.8	17.11 ± 0.23	436.2 ± 1.8	43.4 ± 0.7	17.96 ± 0.15	
		481.9 ± 1.1	22.0 ± 0.4	18.39 ± 0.03	626.4 ± 1.7	39.6 ± 1.1	13.62 ± 0.04	
i06229a	0[d]	-649.2 ± 3.9	59.3 ± 6.1	13.12 ± 0.03	-646.6 ± 1.9	44.1 ± 8.2	14.25 ± 0.29	0.15 ± 0.03
i06229b	1[d]	-654.9 ± 3.9	56.9 ± 5.6	13.10 ± 0.03	-655.3 ± 2.0	47.0 ± 10.4	14.12 ± 0.43	0.16 ± 0.07
i19169a	0[c]	-671.2 ± 63.0	37.9 ± 34.4	12.90 ± 0.99	-678.0 ± 5.5	30.8 ± 19.7	12.85 ± 0.55	0.99 ± 0.01
		-632.6 ± 0.8	23.7 ± 1.1	14.58 ± 0.05	-632.4 ± 0.9	21.3 ± 1.2	14.84 ± 0.12	
i22456a	0[c]	-1669.7 ± 0.1	20.2 ± 0.4	14.37 ± 0.03	-1669.7 ± 0.4	20.1 ± 0.5	14.38 ± 0.05	1.00 ± 0.01
i22456a	1[c]	-910.1 ± 0.4	44.5 ± 0.6	13.89 ± 0.00	-911.1 ± 0.5	39.5 ± 0.4	13.82 ± 0.00	0.99 ± 0.01
		-821.4 ± 1.8	26.6 ± 2.5	13.28 ± 0.04	-722.6 ± 0.9	15.4 ± 0.3	18.25 ± 0.01	
		-728.0 ± 0.8	39.0 ± 1.8	14.73 ± 0.03	-652.6 ± 1.0	13.7 ± 1.3	13.77 ± 0.04	
		-656.8 ± 0.9	20.3 ± 0.9	13.96 ± 0.03	-561.3 ± 0.4	36.6 ± 0.5	14.65 ± 0.02	
		-563.5 ± 0.2	40.6 ± 0.5	14.55 ± 0.01	-441.8 ± 0.6	39.7 ± 0.7	13.93 ± 0.01	
		-438.3 ± 0.3	49.2 ± 0.5	14.01 ± 0.00	-269.0 ± 2.8	112.9 ± 7.8	13.95 ± 0.05	
		-255.1 ± 0.4	52.0 ± 0.4	14.65 ± 0.00	-252.9 ± 0.6	32.2 ± 1.3	15.34 ± 0.09	
		-159.5 ± 0.5	35.8 ± 0.4	14.13 ± 0.01	-159.0 ± 0.7	31.5 ± 0.5	14.13 ± 0.01	
i23443a	0[b]	$-2335, 1493$						
izw1a	0[c]	-1954.7 ± 10.2	57.1 ± 13.7	13.17 ± 0.10	-1954.7 ± 3.2	57.1 ± 13.7	13.17 ± 0.10	~ 1.00
		-1816.2 ± 5.0	70.6 ± 6.9	13.62 ± 0.04	-1816.2 ± 2.2	70.6 ± 6.9	13.62 ± 0.04	
izw1a	2[c]	-245.9 ± 3.8	22.0 ± 6.4	12.60 ± 0.07	-246.0 ± 2.0	21.7 ± 7.0	12.86 ± 1.08	~ 0.57
		-154.7 ± 1.9	~ 2.0	12.75 ± 0.11	-154.9 ± 1.0	~ 2.6	14.72 ± 7.93	
izw1a	4[cd]	233.4 ± 5.7	47.1 ± 8.8	13.05 ± 0.06	233.3 ± 2.2	27.6 ± 16.9	14.59 ± 1.30	0.15 ± 0.02
izw1b	0[c]	-1965.8 ± 8.8	60.3 ± 10.3	13.13 ± 0.08	-1962.5 ± 3.1	54.7 ± 10.3	13.76 ± 0.09	0.31 ± 0.01
		-1825.6 ± 4.1	80.0 ± 5.0	13.64 ± 0.03	-1824.8 ± 1.9	58.3 ± 5.9	14.55 ± 0.13	
izw1b	1[cd]	-1180.0 ± 2.5	37.3 ± 3.9	12.92 ± 0.03	-1180.0 ± 1.6	37.3 ± 3.9	12.92 ± 0.03	~ 1.00
izw1b	2[cd]	-239.4 ± 1.9	45.4 ± 3.2	13.02 ± 0.02	-239.5 ± 1.4	36.3 ± 6.9	14.04 ± 0.33	0.17 ± 0.05
		-155.5 ± 2.0	19.3 ± 3.3	12.56 ± 0.05	-156.3 ± 1.5	17.2 ± 3.4	13.56 ± 0.27	
izw1b	3[cd]	26.7 ± 5.8	23.7 ± 9.8	12.34 ± 0.11	12.4 ± 1.7	~ 4.5	12.83 ± 2.65	~ 0.25
		65.5 ± 4.5	~ 2.0	12.38 ± 0.24	65.3 ± 1.6	20.5 ± 12.2	13.31 ± 2.29	
		78.2 ± 16.6	~ 2.0	11.76 ± 0.51	108.6 ± 0.4	2.5 ± 0.6	15.02 ± 1.75	
izw1b	4[cd]	233.1 ± 1.9	50.6 ± 2.9	13.15 ± 0.02	233.4 ± 1.4	46.8 ± 8.0	13.76 ± 0.65	~ 0.31
kaz238a	0[bc]	-331.1 ± 28.9	146.1 ± 21.8	14.41 ± 0.11	-352.2 ± 2.7	~ 125.0	14.33 ± 0.03	1.00 ± 0.01
		-62.2 ± 82.4	125.9 ± 67.3	14.81 ± 0.43	-105.5 ± 4.5	~ 125.0	14.66 ± 0.09	
		75.9 ± 32.8	79.7 ± 17.6	14.97 ± 0.40	48.3 ± 3.4	88.8 ± 5.4	15.25 ± 0.14	
mr2251a	0[c]	-696.3 ± 3.3	67.0 ± 4.0	13.30 ± 0.02	-696.6 ± 1.9	66.4 ± 4.1	13.38 ± 0.03	0.85 ± 0.01
		-608.3 ± 2.4	31.3 ± 3.8	13.04 ± 0.08	-602.4 ± 1.8	35.0 ± 4.5	13.26 ± 0.08	
		-528.8 ± 0.7	48.8 ± 1.4	13.89 ± 0.01	-528.9 ± 1.0	41.7 ± 1.6	13.98 ± 0.02	
		-419.5 ± 1.6	40.9 ± 3.8	13.23 ± 0.07	-371.8 ± 4.0	87.1 ± 13.6	14.10 ± 0.12	
		-293.0 ± 3.5	104.3 ± 5.8	14.19 ± 0.06	-241.8 ± 1.4	66.9 ± 6.6	14.82 ± 0.03	

Table 4.6 (cont'd)

Target[a]	Sys.	Vel. (Full Cov.) (km s^{-1})	b (Full Cov.) (km s^{-1})	log N (Full Cov.) (log N [cm^{-2}])	Vel. (PC) (km s^{-1})	b (PC) (km s^{-1})	log $N_{\rm max}$ (PC) (log N [cm^{-2}])	C (PC)
		-163.7 ± 7.7	~ 150.0	14.43 ± 0.03	-117.6 ± 2.4	59.1 ± 7.4	14.11 ± 0.10	
		20.2 ± 1.2	54.5 ± 2.8	13.48 ± 0.04	-1.7 ± 2.2	73.6 ± 5.2	13.99 ± 0.04	
		120.2 ± 2.2	28.1 ± 2.9	12.85 ± 0.03	122.8 ± 1.5	27.2 ± 3.3	12.92 ± 0.06	
		230.9 ± 2.3	17.6 ± 3.7	12.36 ± 0.05	229.8 ± 1.5	18.9 ± 3.7	12.46 ± 0.05	
mr2251a	1[c]	443.6 ± 1.7	14.0 ± 3.1	12.34 ± 0.04	444.7 ± 1.3	14.5 ± 3.1	13.09 ± 0.06	0.23 ± 0.01
		527.9 ± 0.8	35.5 ± 1.3	13.12 ± 0.01	527.3 ± 0.9	25.6 ± 2.7	14.17 ± 0.17	
		628.0 ± 1.8	19.9 ± 3.1	12.48 ± 0.04	627.2 ± 1.4	19.9 ± 3.0	13.22 ± 0.05	
		725.0 ± 1.1	14.3 ± 2.0	12.57 ± 0.03	725.0 ± 1.1	12.9 ± 2.0	13.37 ± 0.06	
mrk106a	3	-1077.2 ± 2.8	29.7 ± 4.2	12.80 ± 0.04	-1079.5 ± 1.8	7.8 ± 2.0	17.00 ± 0.29	0.13 ± 0.01
mrk1253a	0[c]	-219.8 ± 0.6	16.8 ± 1.0	13.60 ± 0.02	-219.8 ± 0.8	16.7 ± 1.0	13.61 ± 0.02	0.99 ± 0.01
		-146.1 ± 0.5	25.6 ± 0.9	13.85 ± 0.01	-146.0 ± 0.7	25.7 ± 0.9	13.87 ± 0.01	
		-20.8 ± 0.4	33.1 ± 1.3	14.86 ± 0.07	-20.8 ± 0.6	31.5 ± 1.5	14.99 ± 0.11	
mrk1392a	0[c]	-342.5 ± 1.8	37.3 ± 1.3	14.24 ± 0.02	-442.1 ± 1.8	26.4 ± 5.4	12.63 ± 0.05	0.96 ± 0.01
		-287.6 ± 1.8	27.6 ± 1.2	14.00 ± 0.04	-321.8 ± 0.5	39.0 ± 0.7	14.84 ± 0.03	
		169.3 ± 0.1	~ 2.0	17.80 ± 0.16	-196.0 ± 2.2	~ 5.2	11.87 ± 0.16	
mrk1392a	1[c]	19.7 ± 0.9	43.0 ± 1.8	13.55 ± 0.01	19.3 ± 1.0	37.4 ± 2.4	13.59 ± 0.04	0.97 ± 0.07
		154.0 ± 41.7	~ 2.0	16.92 ± 3.69	92.3 ± 0.9	~ 3.4	15.69 ± 1.01	
mrk1501a	0[cd]	-409.9 ± 3.6	35.8 ± 5.6	14.84 ± 0.24	-409.9 ± 1.9	35.8 ± 5.6	14.84 ± 0.24	~ 1.00
		-310.6 ± 6.5	39.4 ± 7.5	14.17 ± 0.06	-310.6 ± 2.5	39.4 ± 7.5	14.17 ± 0.06	
mrk1501a	1[c]	-47.7 ± 1.1	31.9 ± 1.8	14.10 ± 0.03	-47.3 ± 1.0	16.1 ± 14.8	16.04 ± 4.61	0.87 ± 0.02
mrk1513a	0[c]	-1519.2 ± 0.6	61.9 ± 0.9	14.22 ± 0.00	-1520.5 ± 0.8	53.6 ± 1.7	14.42 ± 0.04	0.87 ± 0.01
		-1413.3 ± 3.8	17.3 ± 6.5	12.53 ± 0.11	-1416.0 ± 1.8	20.2 ± 4.8	12.83 ± 0.09	
mrk1513a	2[c]	-785.3 ± 6.0	67.7 ± 9.7	12.78 ± 0.04	-789.5 ± 2.0	~ 24.3	16.54 ± 7.46	0.06 ± 0.01
mrk1513a	3[c]	-646.6 ± 3.0	17.6 ± 5.0	12.37 ± 0.06	-646.6 ± 1.7	16.9 ± 5.7	12.97 ± 1.56	~ 0.28
		-559.2 ± 3.6	~ 10.0	12.12 ± 0.10	-559.2 ± 1.9	~ 10.0	12.72 ± 1.60	
		-479.2 ± 5.9	43.8 ± 10.2	12.78 ± 0.07	-479.5 ± 2.4	41.8 ± 13.2	13.38 ± 1.57	
		-411.0 ± 2.4	20.5 ± 3.5	12.72 ± 0.07	-411.5 ± 1.7	19.2 ± 9.9	13.40 ± 2.03	
mrk1513a	4[cd]	-254.6 ± 3.1	30.4 ± 4.8	12.49 ± 0.04	-253.8 ± 1.7	9.6 ± 2.5	16.65 ± 0.73	0.06 ± 0.01
mrk1513a	5[c]	-22.4 ± 0.5	33.7 ± 0.8	13.81 ± 0.01	-100.8 ± 1.7	~ 3.2	11.93 ± 0.11	~ 1.00
		28.9 ± 6.7	93.5 ± 6.0	13.36 ± 0.04	-21.5 ± 0.7	36.1 ± 0.7	13.87 ± 0.01	
		56.0 ± 7.6	~ 2.0	11.54 ± 0.47	66.3 ± 2.0	45.6 ± 6.3	13.03 ± 0.05	
		174.2 ± 1.5	21.4 ± 2.6	12.74 ± 0.04	171.4 ± 1.3	26.4 ± 2.6	12.83 ± 0.03	
mrk279a	0[c]	-537.3 ± 3.1	31.5 ± 4.6	13.68 ± 0.08	-535.2 ± 2.4	32.5 ± 5.0	13.76 ± 0.21	0.95 ± 0.15
		-473.6 ± 2.5	23.2 ± 3.8	13.63 ± 0.06	-473.9 ± 1.9	17.4 ± 14.8	13.80 ± 1.00	
		-427.9 ± 4.5	103.5 ± 4.2	14.33 ± 0.02	-444.7 ± 3.1	~ 2.0	12.73 ± 1.55	
		-255.7 ± 5.8	~ 2.0	12.25 ± 0.36	-429.7 ± 2.8	100.3 ± 7.3	14.38 ± 0.17	
		-236.6 ± 3.9	47.4 ± 4.6	13.37 ± 0.05	-240.3 ± 2.0	47.8 ± 4.5	13.45 ± 0.13	
mrk279a	1[c]	102.4 ± 0.4	46.3 ± 0.7	14.28 ± 0.01	101.9 ± 0.6	37.1 ± 1.3	14.61 ± 0.05	0.92 ± 0.01
mrk304a	0[b]	$-1597, -294$						
mrk304a	1[cd]	-168.1 ± 10.4	51.5 ± 5.4	13.63 ± 0.13	-168.1 ± 3.2	51.5 ± 5.4	13.63 ± 0.13	~ 1.00
		-134.8 ± 0.7	21.5 ± 2.7	14.41 ± 0.12	-134.8 ± 0.9	21.5 ± 2.7	14.41 ± 0.12	
mrk304b	0[b]	$-1801, -444$						

Table 4.6 (cont'd)

Target[a]	Sys.	Vel. (Full Cov.) (km s^{-1})	b (Full Cov.) (km s^{-1})	$\log N$ (Full Cov.) ($\log N$ [cm^{-2}])	Vel. (PC) (km s^{-1})	b (PC) (km s^{-1})	$\log N_{\rm max}$ (PC) ($\log N$ [cm^{-2}])	C (PC)
mrk304b	1[cd]	-131.8 ± 1.4	52.9 ± 3.2	13.94 ± 0.06	-131.6 ± 1.2	52.7 ± 3.1	13.95 ± 0.06	0.99 ± 0.01
		-125.0 ± 0.8	19.4 ± 3.4	14.43 ± 0.22	-125.0 ± 0.9	18.1 ± 4.3	14.57 ± 0.44	
mrk304b	2[cd]	279.1 ± 3.4	43.0 ± 4.9	13.26 ± 0.04	280.4 ± 1.8	5.1 ± 1.5	17.36 ± 0.12	0.31 ± 0.04
mrk421a	0[cd]	-1388.3 ± 8.3	52.8 ± 14.1	12.66 ± 0.08	-1391.3 ± 2.6	~ 20.3	~ 16.45	0.05 ± 0.01
mrk421b	0[cd]	-1411.6 ± 4.5	29.0 ± 7.1	12.63 ± 0.07	-1411.4 ± 0.2	4.1 ± 0.2	16.96 ± 0.23	0.16 ± 0.07
mrk478a	0[c]	-2770.9 ± 10.7	36.6 ± 12.5	13.53 ± 0.58	-2762.4 ± 1.3	35.1 ± 5.5	14.22 ± 0.23	0.52 ± 0.06
		-2721.3 ± 119.2	~ 55.5	13.18 ± 1.28	-2675.5 ± 2.1	10.7 ± 8.0	12.92 ± 0.16	
mrk478a	1[c]	-2274.0 ± 2.8	20.1 ± 3.6	13.32 ± 0.11	-2245.4 ± 1.1	39.0 ± 4.2	14.13 ± 0.22	0.65 ± 0.13
		-2223.7 ± 7.0	39.0 ± 7.1	13.46 ± 0.09	-2237.2 ± 0.5	3.3 ± 0.1	15.93 ± 0.86	
mrk478a	2[cd]	-1120.1 ± 26.2	54.9 ± 39.7	12.79 ± 0.30	-1069.6 ± 3.9	94.6 ± 16.4	13.67 ± 0.16	0.33 ± 0.06
		-1034.6 ± 8.7	39.1 ± 8.5	13.05 ± 0.14	-1038.5 ± 1.3	4.4 ± 2.7	16.23 ± 1.52	
mrk478a	3[cd]	-402.5 ± 0.4	17.7 ± 0.7	13.85 ± 0.02	-402.4 ± 0.6	14.7 ± 1.7	14.18 ± 0.22	0.90 ± 0.02
		-278.5 ± 2.4	~ 2.0	12.53 ± 0.14	-278.8 ± 1.7	~ 2.0	12.59 ± 0.16	
mrk478a	4[c]	-89.4 ± 3.1	30.1 ± 4.8	12.91 ± 0.04	-89.4 ± 1.8	30.1 ± 4.8	12.91 ± 0.04	~ 1.00
mrk486a	0[bc]	-1054.8 ± 5.1	114.3 ± 5.6	14.23 ± 0.02	-1054.9 ± 2.3	113.8 ± 6.3	14.23 ± 0.03	1.00 ± 0.01
		-663.5 ± 10.4	186.6 ± 11.0	15.12 ± 0.03	-651.9 ± 3.0	191.4 ± 10.7	15.16 ± 0.02	
		-214.5 ± 18.9	~ 200.0	15.56 ± 0.09	-191.0 ± 4.8	103.2 ± 37.7	18.01 ± 2.43	
		206.0 ± 11.8	~ 200.0	15.18 ± 0.04	201.8 ± 3.8	~ 200.0	15.20 ± 0.05	
		547.6 ± 12.1	~ 200.0	14.24 ± 0.04	545.7 ± 3.8	~ 200.0	14.25 ± 0.04	
mrk504a	0[cd]	-1053.7 ± 33.8	58.5 ± 34.4	13.16 ± 0.29	-1052.1 ± 6.0	59.7 ± 34.8	13.18 ± 0.31	0.99 ± 0.01
		-990.1 ± 0.8	20.6 ± 2.7	14.50 ± 0.18	-990.1 ± 0.9	19.6 ± 3.5	14.62 ± 0.33	
mrk504a	1[cd]	-731.2 ± 4.8	42.6 ± 7.0	13.13 ± 0.05	-726.2 ± 2.0	~ 18.9	16.22 ± 7.19	0.17 ± 0.02
mrk504a	2[cd]	-432.7 ± 0.6	24.2 ± 0.9	13.86 ± 0.01	-432.7 ± 0.8	24.2 ± 0.9	13.86 ± 0.01	~ 1.00
mrk504a	3[cd]	-161.0 ± 66.4	47.2 ± 42.7	12.86 ± 0.78	-146.0 ± 5.0	43.1 ± 11.0	13.12 ± 0.41	0.96 ± 0.02
		-121.8 ± 0.6	22.3 ± 1.9	14.09 ± 0.04	-121.2 ± 0.9	19.2 ± 3.1	14.27 ± 0.17	
mrk509a	0[bc]	-398.7 ± 0.8	33.9 ± 0.6	13.57 ± 0.01	-381.2 ± 0.9	43.8 ± 0.7	13.87 ± 0.01	0.93 ± 0.01
		-312.8 ± 0.5	47.1 ± 1.0	14.31 ± 0.01	-309.4 ± 0.6	22.0 ± 1.2	15.28 ± 0.16	
		-241.4 ± 1.0	36.1 ± 0.6	13.83 ± 0.02	-249.0 ± 1.0	38.0 ± 0.6	14.05 ± 0.01	
		-68.4 ± 0.4	27.6 ± 0.5	13.91 ± 0.02	-16.3 ± 0.7	40.0 ± 0.4	15.50 ± 0.03	
		-1.1 ± 0.8	56.9 ± 1.6	14.30 ± 0.02	111.8 ± 0.9	52.0 ± 2.6	14.50 ± 0.02	
		119.8 ± 0.9	78.3 ± 2.2	14.43 ± 0.01	203.8 ± 1.4	40.8 ± 1.0	14.24 ± 0.02	
		216.5 ± 0.4	35.6 ± 0.6	13.96 ± 0.02	237.3 ± 1.2	13.2 ± 2.1	13.12 ± 0.10	
mrk509b	0[bc]	-404.2 ± 1.8	34.6 ± 1.6	13.53 ± 0.03	-386.4 ± 1.5	44.6 ± 1.8	13.85 ± 0.02	0.92 ± 0.01
		-308.4 ± 1.0	53.9 ± 2.4	14.32 ± 0.02	-308.7 ± 1.0	26.6 ± 2.6	14.85 ± 0.15	
		-232.2 ± 2.1	31.5 ± 1.7	13.61 ± 0.06	-243.3 ± 1.6	35.7 ± 1.8	13.94 ± 0.04	
		-65.0 ± 1.1	31.0 ± 1.7	13.92 ± 0.06	-15.0 ± 1.5	41.7 ± 1.5	15.42 ± 0.09	
		5.5 ± 2.5	61.4 ± 5.0	14.30 ± 0.05	120.4 ± 1.6	69.1 ± 10.0	14.62 ± 0.05	
		127.2 ± 2.6	76.5 ± 5.3	14.39 ± 0.03	148.6 ± 1120.0	~ 137.2	~ 9.00	
		219.6 ± 0.8	34.5 ± 1.5	13.93 ± 0.04	217.4 ± 1.4	32.1 ± 2.1	14.16 ± 0.07	
mrk509c	0[bc]	-426.2 ± 3.6	15.5 ± 3.0	13.06 ± 0.12	-426.3 ± 1.9	15.8 ± 4.4	13.05 ± 0.26	0.92 ± 0.01
		-392.7 ± 3.0	19.5 ± 5.6	13.24 ± 0.15	-378.2 ± 2.4	33.2 ± 13.1	13.77 ± 0.17	
		-312.2 ± 2.2	54.9 ± 3.9	14.32 ± 0.03	-308.1 ± 1.3	25.9 ± 5.9	14.91 ± 0.34	

Table 4.6 (cont'd)

Target[a]	Sys.	Vel. (Full Cov.) (km s^{-1})	b (Full Cov.) (km s^{-1})	$\log N$ (Full Cov.) ($\log N$ [cm^{-2}])	Vel. (PC) (km s^{-1})	b (PC) (km s^{-1})	$\log N_{\rm max}$ (PC) ($\log N$ [cm^{-2}])	C (PC)
		-235.7 ± 4.2	40.7 ± 2.4	13.77 ± 0.09	-246.6 ± 2.1	43.7 ± 2.6	14.05 ± 0.06	
		-70.7 ± 0.8	27.0 ± 1.5	13.80 ± 0.04	-84.0 ± 1.2	11.4 ± 1.9	13.59 ± 0.05	
		-4.5 ± 2.5	62.1 ± 2.8	14.29 ± 0.03	-8.9 ± 1.9	54.2 ± 1.6	14.75 ± 0.05	
		122.6 ± 2.4	84.6 ± 5.9	14.44 ± 0.03	119.5 ± 1.8	72.1 ± 9.8	14.61 ± 0.05	
		137.9 ± 574.4	~ 2.0	~ 10.15	189.7 ± 1.7	13.0 ± 5.0	13.53 ± 0.13	
		221.2 ± 0.9	36.1 ± 1.8	13.92 ± 0.05	228.4 ± 1.5	26.5 ± 2.1	14.00 ± 0.07	
		294.4 ± 672.0	~ 2.0	~ 9.74	290.4 ± 1.4	~ 2.0	12.34 ± 0.12	
mrk817a	0[c]	-1037.6 ± 3.4	41.6 ± 4.0	13.10 ± 0.06	-1036.8 ± 1.7	37.1 ± 7.6	13.85 ± 0.51	0.27 ± 0.17
		-925.2 ± 10.3	73.1 ± 27.0	12.91 ± 0.13	-926.4 ± 3.2	69.4 ± 24.4	13.52 ± 0.36	
mrk817b	0[cd]	-1039.6 ± 2.0	~ 4.8	12.45 ± 0.11	-1039.7 ± 1.7	19.6 ± 4.3	12.85 ± 0.07	~ 1.00
		-1016.6 ± 5.5	50.9 ± 6.2	12.94 ± 0.06	-989.2 ± 2.6	23.8 ± 9.4	12.60 ± 0.13	
mrk817b	1[c]	-510.8 ± 1.9	14.7 ± 3.4	12.64 ± 0.05	-510.7 ± 1.4	~ 10.9	13.97 ± 2.25	0.17 ± 0.07
mrk841a	0[cd]	-1685.3 ± 2.0	42.7 ± 1.2	14.18 ± 0.04	-1685.3 ± 1.4	42.7 ± 1.2	14.18 ± 0.04	~ 1.00
		-1660.7 ± 2.5	18.2 ± 4.0	14.04 ± 0.14	-1660.7 ± 1.6	18.2 ± 4.0	14.04 ± 0.14	
mrk841a	1[cd]	-1053.1 ± 18.0	57.0 ± 12.2	13.47 ± 0.17	-1053.1 ± 4.2	57.0 ± 12.2	13.47 ± 0.17	~ 1.00
		-1003.6 ± 2.4	29.1 ± 5.9	13.40 ± 0.20	-1003.6 ± 1.5	29.1 ± 5.9	13.40 ± 0.20	
mrk841a	2[cd]	-701.0 ± 40.3	79.4 ± 21.5	13.79 ± 0.30	-696.2 ± 6.2	81.8 ± 19.7	13.83 ± 0.28	0.99 ± 0.01
		-684.3 ± 2.0	24.9 ± 4.0	13.73 ± 0.15	-684.2 ± 1.4	24.6 ± 3.8	13.73 ± 0.14	
		-616.9 ± 0.8	22.7 ± 2.3	14.51 ± 0.09	-616.9 ± 0.8	20.8 ± 3.2	14.66 ± 0.22	
		-521.1 ± 8.8	52.1 ± 8.3	13.28 ± 0.09	-521.4 ± 3.4	53.0 ± 10.0	13.28 ± 0.13	
mrk841a	3[cd]	274.3 ± 0.8	~ 3.4	15.71 ± 0.49	274.3 ± 0.9	~ 3.4	15.71 ± 0.49	~ 1.00
		293.8 ± 8.7	~ 3.7	12.38 ± 0.27	293.8 ± 3.0	~ 3.7	12.38 ± 0.27	
mrk876a	0	-3773.9 ± 1.1	61.6 ± 1.6	13.41 ± 0.01	-3773.9 ± 1.1	61.6 ± 1.6	13.41 ± 0.01	~ 1.00
		-3519.3 ± 1.7	61.6 ± 2.7	13.30 ± 0.01	-3519.3 ± 1.3	61.6 ± 2.7	13.30 ± 0.01	
		-3406.5 ± 2.4	27.3 ± 3.8	12.67 ± 0.04	-3406.5 ± 1.6	27.3 ± 3.8	12.67 ± 0.04	
mrk876a	1[cd]	-1554.7 ± 0.9	19.1 ± 1.5	12.85 ± 0.02	-1554.6 ± 0.9	~ 10.0	14.83 ± 0.22	0.20 ± 0.01
		-1451.2 ± 4.1	34.5 ± 6.5	12.44 ± 0.05	-1452.0 ± 2.0	34.6 ± 6.4	13.19 ± 0.06	
		-1311.2 ± 6.7	36.5 ± 11.3	12.31 ± 0.09	-1309.6 ± 2.6	37.2 ± 11.6	13.05 ± 0.09	
		-1225.8 ± 1.7	25.7 ± 2.7	12.79 ± 0.03	-1225.8 ± 1.3	22.1 ± 2.6	13.65 ± 0.06	
mrk876a	2[d]	-591.9 ± 1.4	~ 2.8	11.90 ± 0.09	-561.6 ± 0.8	~ 10.0	13.23 ± 0.25	0.50 ± 0.13
		-564.9 ± 0.9	9.2 ± 2.1	12.69 ± 0.13	-550.1 ± 2.2	53.9 ± 25.1	13.13 ± 0.11	
		-540.6 ± 3.6	23.2 ± 3.2	12.97 ± 0.07	-536.0 ± 1.0	~ 10.0	12.96 ± 0.22	
mrk877a	0	-651.9 ± 1.5	22.8 ± 0.3	15.79 ± 0.13	-707.3 ± 3.2	~ 28.6	12.27 ± 0.18	~ 1.00
		-605.9 ± 3.1	24.5 ± 0.4	15.03 ± 0.19	-633.3 ± 0.8	32.3 ± 0.3	15.70 ± 0.05	
		-527.3 ± 1.0	22.4 ± 0.3	13.67 ± 0.02	-531.7 ± 1.2	33.6 ± 0.5	13.73 ± 0.02	
ngc985a	0[bc]	-734.3 ± 8.6	~ 150.0	14.07 ± 0.03	-724.7 ± 2.9	~ 150.0	14.21 ± 0.03	0.85 ± 0.01
		-672.6 ± 2.7	48.9 ± 4.5	13.80 ± 0.05	-671.3 ± 1.8	43.2 ± 3.9	14.09 ± 0.09	
		-546.3 ± 5.5	65.3 ± 16.3	13.68 ± 0.22	-493.0 ± 1.9	97.9 ± 14.4	14.79 ± 0.06	
		-456.3 ± 11.2	~ 150.0	14.52 ± 0.03	-291.1 ± 4.8	97.5 ± 21.3	14.22 ± 0.13	
		-229.3 ± 3.3	82.2 ± 3.4	13.96 ± 0.03	-196.3 ± 3.1	54.8 ± 15.3	13.63 ± 0.39	
		112.9 ± 0.5	25.3 ± 0.9	13.79 ± 0.01	113.0 ± 0.7	22.7 ± 1.0	13.98 ± 0.04	
ngc985b	0[bc]	-973.5 ± 8.5	50.6 ± 14.0	12.50 ± 0.11	-971.1 ± 2.9	54.2 ± 14.3	12.62 ± 0.10	0.85 ± 0.02

Table 4.6 (cont'd)

Target[a]	Sys.	Vel. (Full Cov.) (km s^{-1})	b (Full Cov.) (km s^{-1})	log N (Full Cov.) (log N [cm^{-2}])	Vel. (PC) (km s^{-1})	b (PC) (km s^{-1})	log $N_{\rm max}$ (PC) (log N [cm^{-2}])	C (PC)
		-751.6 ± 7.0	~ 150.0	13.79 ± 0.02	-743.8 ± 2.6	~ 150.0	13.90 ± 0.02	
		-676.4 ± 0.9	34.1 ± 1.7	13.41 ± 0.03	-675.2 ± 1.0	34.3 ± 1.7	13.60 ± 0.04	
		-503.2 ± 4.5	128.7 ± 7.3	14.36 ± 0.03	-501.9 ± 2.3	115.4 ± 7.0	14.50 ± 0.04	
		-403.4 ± 1.2	43.5 ± 3.5	13.61 ± 0.08	-406.7 ± 1.3	40.7 ± 3.6	13.85 ± 0.09	
		-271.0 ± 3.3	67.3 ± 4.8	13.94 ± 0.04	-270.0 ± 1.6	69.6 ± 4.5	14.11 ± 0.04	
		-182.3 ± 5.6	47.2 ± 4.0	13.34 ± 0.11	-177.1 ± 2.2	43.1 ± 4.2	13.33 ± 0.12	
		56.1 ± 1.5	~ 4.0	12.32 ± 0.07	99.2 ± 2.0	40.4 ± 3.0	13.37 ± 0.14	
		110.9 ± 0.2	26.2 ± 0.4	13.84 ± 0.00	112.6 ± 0.7	19.6 ± 2.0	14.02 ± 0.09	
pg0804a	1[c]	557.8 ± 1.0	16.3 ± 0.8	13.78 ± 0.03	558.3 ± 1.0	16.6 ± 0.8	13.80 ± 0.03	1.00 ± 0.01
		604.9 ± 1.1	17.4 ± 3.3	14.53 ± 0.17	604.7 ± 1.1	14.9 ± 4.4	14.79 ± 0.52	
		639.4 ± 10.9	13.5 ± 6.0	12.93 ± 0.52	637.0 ± 3.4	14.1 ± 6.1	13.08 ± 0.50	
pg0838a	1[d]	400.8 ± 1.8	32.3 ± 2.8	13.16 ± 0.03	400.8 ± 1.3	32.3 ± 2.8	13.16 ± 0.03	~ 1.00
		508.7 ± 3.4	47.0 ± 5.8	13.05 ± 0.04	508.7 ± 1.8	47.0 ± 5.8	13.05 ± 0.04	
pg0844a	0[cd]	-1471.3 ± 8.3	147.9 ± 15.5	13.43 ± 0.03	-1471.3 ± 2.9	147.9 ± 15.5	13.43 ± 0.03	~ 1.00
pg0844a	1[cd]	-1180.0 ± 0.9	51.6 ± 1.4	13.79 ± 0.01	-1180.0 ± 1.0	51.6 ± 1.4	13.79 ± 0.01	~ 1.00
pg0844a	2[c]	-142.1 ± 5.5	21.7 ± 9.0	12.36 ± 0.10	-142.1 ± 2.3	21.7 ± 9.0	12.36 ± 0.10	~ 1.00
		73.6 ± 0.2	40.2 ± 1.0	15.53 ± 0.08	73.6 ± 0.5	40.2 ± 1.0	15.53 ± 0.08	
		305.9 ± 4.9	37.5 ± 7.6	12.74 ± 0.06	305.9 ± 2.2	37.5 ± 7.6	12.74 ± 0.06	
pg1011a	0[cd]	-1033.1 ± 3.8	17.9 ± 6.6	12.53 ± 0.08	-1033.4 ± 1.9	14.5 ± 6.8	13.70 ± 0.27	0.14 ± 0.01
		-864.2 ± 5.9	30.7 ± 9.9	12.57 ± 0.09	-862.6 ± 2.5	29.6 ± 10.4	13.58 ± 0.12	
		-752.1 ± 3.3	39.3 ± 5.5	12.95 ± 0.04	-753.1 ± 1.7	~ 14.4	16.17 ± 6.08	
pg1011a	3[cd]	71.5 ± 1.9	29.1 ± 3.0	13.01 ± 0.03	71.5 ± 1.3	18.8 ± 7.2	14.39 ± 0.79	0.20 ± 0.02
pg1126a	0[c]	-4956.1 ± 7.0	~ 150.0	14.23 ± 0.02	-5052.2 ± 6.0	90.9 ± 24.8	14.07 ± 0.23	0.61 ± 0.01
		-4737.1 ± 5.1	110.2 ± 9.0	14.14 ± 0.03	-4821.5 ± 3.4	117.7 ± 18.4	15.19 ± 0.17	
		-4499.6 ± 5.4	84.0 ± 7.2	13.83 ± 0.03	-4504.1 ± 2.5	81.0 ± 7.8	14.16 ± 0.04	
pg1126a	1[c]	-3464.6 ± 40.2	113.4 ± 25.6	14.16 ± 0.21	-3337.2 ± 1.5	29.4 ± 4.2	13.84 ± 0.06	~ 1.00
		-3239.1 ± 2.1	19.9 ± 4.0	13.52 ± 0.08	-3248.6 ± 1.4	28.2 ± 3.4	13.73 ± 0.05	
pg1126a	2[c]	-2834.7 ± 9.3	41.9 ± 12.5	13.65 ± 0.15	-2751.2 ± 2.1	81.1 ± 10.0	14.80 ± 0.15	0.98 ± 0.01
		-2731.4 ± 2.0	141.6 ± 1.8	14.87 ± 0.01	-2728.9 ± 1.7	~ 150.0	14.79 ± 0.03	
		-2347.8 ± 3.0	50.2 ± 2.9	14.11 ± 0.03	-2348.1 ± 1.7	48.0 ± 2.8	14.12 ± 0.03	
		-2242.8 ± 6.3	64.3 ± 5.9	13.92 ± 0.05	-2244.9 ± 2.5	65.5 ± 6.0	13.95 ± 0.05	
pg1126a	3[c]	-1760.4 ± 0.7	56.4 ± 1.0	14.32 ± 0.01	-1760.7 ± 0.9	51.6 ± 2.2	14.44 ± 0.05	0.94 ± 0.02
		-1631.7 ± 5.1	23.0 ± 8.6	12.72 ± 0.11	-1634.9 ± 2.4	29.5 ± 10.1	12.87 ± 0.12	
		-1483.5 ± 1.1	86.2 ± 1.7	14.17 ± 0.01	-1483.2 ± 1.1	84.2 ± 1.8	14.22 ± 0.02	
pg1126a	4[c]	-985.7 ± 0.3	31.0 ± 0.6	14.16 ± 0.01	-985.8 ± 0.6	25.5 ± 1.1	14.49 ± 0.08	0.92 ± 0.01
pg1126a	5[c]	-687.0 ± 68.1	37.4 ± 32.4	13.20 ± 1.16	-675.5 ± 3.1	40.2 ± 4.7	13.48 ± 0.20	0.93 ± 0.01
		-659.3 ± 1.4	22.9 ± 3.5	13.97 ± 0.18	-659.5 ± 0.9	17.5 ± 2.9	14.29 ± 0.17	
		-559.0 ± 9.4	33.1 ± 17.0	12.51 ± 0.14	-535.1 ± 5.2	56.9 ± 49.8	12.82 ± 0.33	
		-444.0 ± 0.4	38.6 ± 0.7	14.23 ± 0.01	-443.6 ± 0.8	30.7 ± 1.5	14.56 ± 0.06	
pg1126b	0[c]	-4944.6 ± 12.0	72.5 ± 14.1	13.87 ± 0.08	-4949.4 ± 3.3	54.6 ± 14.1	14.20 ± 0.08	0.64 ± 0.02
		-4751.0 ± 7.4	100.9 ± 14.1	14.21 ± 0.04	-4757.2 ± 2.6	63.1 ± 30.2	15.07 ± 0.88	
		-4494.4 ± 7.0	80.3 ± 11.0	13.77 ± 0.04	-4503.1 ± 2.8	85.3 ± 11.3	14.07 ± 0.05	

Table 4.6 (cont'd)

Target[a]	Sys.	Vel. (Full Cov.) (km s^{-1})	b (Full Cov.) (km s^{-1})	$\log N$ (Full Cov.) ($\log N$ [cm^{-2}])	Vel. (PC) (km s^{-1})	b (PC) (km s^{-1})	$\log N_{\rm max}$ (PC) ($\log N$ [cm^{-2}])	C (PC)
pg1126b	1[c]	-3488.3 ± 19.6	113.4 ± 16.8	14.10 ± 0.08	-3488.9 ± 9.6	112.7 ± 64.1	14.10 ± 0.60	~ 1.00
		-3375.4 ± 4.8	~ 23.1	14.90 ± 2.79	-3376.0 ± 7.6	~ 17.3	15.91 ± 14.11	
		-3283.1 ± 3.0	~ 13.5	15.56 ± 9.56	-3283.6 ± 2.3	~ 14.0	15.53 ± 11.43	
		-3190.6 ± 1136.4	~ 3.7	~ 15.72	-3203.7 ± 1.9	~ 6.6	~ 14.52	
pg1126b	2[c]	-2816.8 ± 10.2	76.4 ± 6.5	14.66 ± 0.07	-2954.6 ± 2.6	~ 2.0	13.12 ± 6.02	0.97 ± 0.01
		-2680.5 ± 8.4	~ 20.0	16.00 ± 13.24	-2742.0 ± 1.1	87.8 ± 7.4	15.65 ± 0.22	
		-2634.6 ± 49.6	90.9 ± 25.6	14.34 ± 0.31	-2506.2 ± 1.8	~ 5.6	14.16 ± 12.54	
		-2346.3 ± 2.1	24.2 ± 12.5	15.05 ± 1.42	-2346.2 ± 1.4	22.0 ± 15.0	15.51 ± 2.59	
		-2225.9 ± 2.9	34.4 ± 4.3	13.97 ± 0.04	-2226.1 ± 1.7	35.3 ± 4.4	13.99 ± 0.03	
pg1126b	3[c]	-1759.0 ± 0.6	50.8 ± 1.0	14.26 ± 0.01	-1759.0 ± 0.8	50.5 ± 2.3	14.27 ± 0.05	0.99 ± 0.04
		-1637.7 ± 6.2	33.3 ± 10.7	12.79 ± 0.11	-1638.1 ± 2.6	33.8 ± 11.3	12.80 ± 0.13	
		-1486.6 ± 1.1	86.5 ± 1.7	14.10 ± 0.01	-1486.6 ± 1.1	86.3 ± 1.9	14.11 ± 0.03	
pg1126b	4[c]	-984.8 ± 0.3	29.0 ± 0.6	14.22 ± 0.02	-984.8 ± 0.5	23.5 ± 1.1	14.62 ± 0.10	0.93 ± 0.01
pg1126b	5[c]	-696.6 ± 31.8	55.4 ± 18.7	12.90 ± 0.33	-686.4 ± 3.9	54.4 ± 8.1	13.08 ± 0.19	0.94 ± 0.01
		-656.5 ± 0.4	25.4 ± 1.0	14.07 ± 0.02	-656.3 ± 0.7	22.7 ± 1.2	14.23 ± 0.04	
		-448.0 ± 0.6	39.4 ± 0.5	14.20 ± 0.01	-534.1 ± 1.2	~ 2.0	12.69 ± 0.07	
		-414.3 ± 1.4	5.1 ± 4.2	13.30 ± 0.39	-445.5 ± 0.5	33.3 ± 0.8	14.45 ± 0.03	
pg1126c	0[c]	-4972.5 ± 6.2	8.5 ± 6.4	16.25 ± 3.08	-4972.9 ± 2.4	8.8 ± 7.9	16.29 ± 3.06	0.97 ± 0.26
		-4782.8 ± 7.5	132.2 ± 16.5	14.26 ± 0.04	-4782.9 ± 2.7	131.3 ± 19.5	14.28 ± 0.18	
		-4500.0 ± 8.4	73.7 ± 13.7	13.77 ± 0.05	-4500.2 ± 2.9	73.6 ± 13.7	13.79 ± 0.17	
pg1126c	1[c]	-3492.2 ± 9.4	~ 150.0	14.22 ± 0.03	-3502.8 ± 3.5	~ 150.0	14.20 ± 0.04	~ 1.00
		-3388.7 ± 6.0	~ 18.7	15.18 ± 6.81	-3211.1 ± 2.1	~ 7.3	~ 14.83	
pg1126c	2[c]	-2880.8 ± 8.0	22.5 ± 20.1	14.23 ± 0.86	-2754.6 ± 1.2	107.2 ± 5.5	15.32 ± 0.09	0.98 ± 0.01
		-2738.2 ± 3.2	137.1 ± 2.7	14.93 ± 0.02	-2515.8 ± 2.5	~ 5.2	~ 14.40	
		-2357.6 ± 2.5	~ 19.3	15.90 ± 6.90	-2358.7 ± 1.7	~ 19.7	15.93 ± 6.61	
		-2239.1 ± 3.7	37.4 ± 6.3	14.00 ± 0.04	-2240.0 ± 2.0	38.6 ± 6.6	14.01 ± 0.04	
pg1126c	3[c]	-1770.0 ± 0.8	54.2 ± 1.2	14.28 ± 0.01	-1770.2 ± 0.9	52.2 ± 2.6	14.34 ± 0.06	0.97 ± 0.04
		-1659.6 ± 3.2	8.6 ± 6.9	12.62 ± 0.11	-1660.0 ± 1.8	9.5 ± 6.6	12.68 ± 0.12	
		-1496.1 ± 1.3	89.3 ± 1.8	14.14 ± 0.01	-1496.1 ± 1.1	88.5 ± 2.0	14.17 ± 0.03	
pg1126c	4[c]	-992.3 ± 0.4	29.5 ± 0.8	14.23 ± 0.02	-992.4 ± 0.7	28.5 ± 1.3	14.28 ± 0.07	0.98 ± 0.02
pg1126c	5[c]	-666.3 ± 0.4	25.1 ± 0.6	14.03 ± 0.01	-666.3 ± 0.6	23.2 ± 0.8	14.16 ± 0.04	0.94 ± 0.01
		-453.2 ± 0.4	36.6 ± 0.6	14.25 ± 0.01	-453.4 ± 0.6	31.7 ± 1.1	14.48 ± 0.06	
pg1126d	0[c]	-4902.6 ± 23.2	108.1 ± 21.8	13.96 ± 0.12	-4878.8 ± 4.9	112.4 ± 20.6	14.38 ± 0.10	0.62 ± 0.02
		-4734.0 ± 11.5	89.4 ± 13.1	14.09 ± 0.09	-4735.3 ± 2.6	46.8 ± 12.3	15.06 ± 0.54	
		-4502.6 ± 7.8	91.8 ± 11.2	13.74 ± 0.04	-4513.7 ± 2.7	100.6 ± 10.8	14.06 ± 0.04	
		-4250.7 ± 5.2	15.1 ± 9.1	12.81 ± 0.12	-4250.4 ± 2.3	14.9 ± 9.2	13.04 ± 0.13	
pg1126d	1[bc]	-3716.9 ± 5.8	12.8 ± 10.3	13.01 ± 0.11	-3716.3 ± 2.4	13.0 ± 9.8	13.03 ± 0.11	~ 1.00
		-3448.6 ± 13.0	132.8 ± 12.7	14.30 ± 0.05	-3455.0 ± 2.4	~ 125.0	14.26 ± 0.03	
		-3241.9 ± 1.6	~ 10.6	15.58 ± 7.03	-3241.9 ± 1.3	~ 10.6	15.58 ± 7.24	
pg1126d	2[c]	-2796.7 ± 60.6	99.3 ± 57.6	14.43 ± 1.56	-2745.8 ± 1.4	112.1 ± 4.5	15.01 ± 0.04	0.98 ± 0.01
		-2706.9 ± 147.0	129.8 ± 53.6	14.68 ± 0.87	-2538.4 ± 2.3	26.3 ± 9.2	13.39 ± 0.09	
		-2343.5 ± 3.1	49.0 ± 4.5	14.11 ± 0.02	-2342.9 ± 1.8	52.1 ± 4.3	14.15 ± 0.02	

Table 4.6 (cont'd)

Target[a]	Sys.	Vel. (Full Cov.) (km s^{-1})	b (Full Cov.) (km s^{-1})	$\log N$ (Full Cov.) ($\log N$ [cm^{-2}])	Vel. (PC) (km s^{-1})	b (PC) (km s^{-1})	$\log N_{\rm max}$ (PC) ($\log N$ [cm^{-2}])	C (PC)
		-2228.5 ± 4.3	42.7 ± 5.5	13.87 ± 0.04	-2226.6 ± 2.0	40.5 ± 5.4	13.87 ± 0.04	
pg1126d	3[c]	-1763.1 ± 1.1	42.5 ± 2.4	14.39 ± 0.04	-1763.7 ± 1.2	36.3 ± 5.9	14.67 ± 0.29	0.95 ± 0.02
		-1668.2 ± 27.4	~ 2.2	13.25 ± 8.13	-1663.1 ± 3.0	20.9 ± 14.2	12.91 ± 0.15	
		-1492.3 ± 1.5	78.6 ± 2.4	14.05 ± 0.01	-1491.7 ± 1.2	76.7 ± 2.5	14.09 ± 0.02	
pg1126d	4[c]	-989.5 ± 0.4	27.3 ± 0.7	14.21 ± 0.02	-989.6 ± 0.6	20.9 ± 1.6	14.75 ± 0.19	0.94 ± 0.01
pg1126d	5[c]	-664.1 ± 1.5	37.0 ± 4.2	13.77 ± 0.14	-664.3 ± 1.1	35.7 ± 5.1	13.84 ± 0.09	0.94 ± 0.01
		-660.7 ± 1.1	17.2 ± 3.4	13.92 ± 0.09	-660.5 ± 1.0	~ 10.0	15.50 ± 5.01	
		-461.1 ± 3.5	32.3 ± 2.4	14.10 ± 0.05	-549.6 ± 1.4	~ 2.0	12.41 ± 0.19	
		-418.6 ± 3.4	19.8 ± 2.7	13.69 ± 0.13	-448.8 ± 0.6	33.7 ± 1.1	14.49 ± 0.05	
pg1229a	0[cd]	-660.1 ± 1.5	22.5 ± 2.4	13.13 ± 0.03	-659.9 ± 1.2	16.8 ± 6.2	14.07 ± 0.65	0.32 ± 0.06
pg1351a	0[bc]	-2164.6 ± 16.9	53.8 ± 24.4	12.84 ± 0.26	-2160.9 ± 3.6	58.2 ± 18.9	12.95 ± 0.12	0.90 ± 0.01
		-1946.7 ± 26.6	129.5 ± 29.4	14.06 ± 0.13	-1945.3 ± 2.8	~ 125.0	14.12 ± 0.02	
		-1762.2 ± 8.6	95.0 ± 21.2	14.21 ± 0.14	-1765.7 ± 3.2	89.2 ± 12.2	14.29 ± 0.08	
		-1623.4 ± 8.9	65.1 ± 15.1	13.94 ± 0.23	-1622.3 ± 2.9	70.9 ± 14.7	14.12 ± 0.12	
		-1473.3 ± 20.8	115.2 ± 87.5	13.84 ± 0.36	-1479.5 ± 3.6	68.2 ± 21.1	13.62 ± 0.17	
		-1276.9 ± 12.0	99.1 ± 17.6	14.15 ± 0.12	-1276.2 ± 1.9	123.3 ± 8.2	14.34 ± 0.02	
		-1041.7 ± 8.3	112.7 ± 12.8	14.37 ± 0.08	-947.9 ± 1.9	~ 125.0	15.10 ± 0.03	
		-873.0 ± 15.4	~ 150.0	14.58 ± 0.03	-735.8 ± 3.1	68.5 ± 13.6	13.88 ± 0.15	
		-681.7 ± 17.9	~ 150.0	13.92 ± 0.09	-646.4 ± 4.0	~ 125.0	13.89 ± 0.08	
pg1351a	1[cd]	78.9 ± 2.1	25.8 ± 3.5	12.96 ± 0.03	78.9 ± 1.5	25.8 ± 3.5	12.96 ± 0.03	~ 1.00
pg1411a	0[b]	$-2683, -564$						
pg1411a	1[cd]	-65.2 ± 1.2	30.9 ± 1.9	14.69 ± 0.08	-65.2 ± 1.1	30.9 ± 1.9	14.69 ± 0.08	~ 1.00
		44.5 ± 17.5	60.3 ± 16.7	13.94 ± 0.16	44.5 ± 4.2	60.3 ± 16.7	13.94 ± 0.16	
		67.8 ± 1.6	27.4 ± 3.8	14.34 ± 0.07	67.8 ± 1.3	27.4 ± 3.8	14.34 ± 0.07	
pg1411b	0[b]	$-3277, -505$						
pg1411b	1[cd]	-51.8 ± 0.4	31.9 ± 1.3	14.70 ± 0.06	-51.8 ± 0.6	31.9 ± 1.3	14.70 ± 0.06	~ 1.00
		71.4 ± 0.4	34.6 ± 1.0	14.53 ± 0.03	71.4 ± 0.6	34.6 ± 1.0	14.53 ± 0.03	
pg1411c	0[b]	$-3067, -258$						
pg1411c	1[cd]	-63.4 ± 0.8	20.3 ± 3.8	16.05 ± 0.87	-63.4 ± 0.9	20.3 ± 3.8	16.05 ± 0.87	~ 1.00
		51.0 ± 9.3	47.9 ± 10.5	14.07 ± 0.23	51.0 ± 3.0	47.9 ± 10.5	14.07 ± 0.23	
		68.6 ± 1.7	18.1 ± 7.5	15.66 ± 1.53	68.6 ± 1.3	18.1 ± 7.5	15.66 ± 1.53	
pg1435a	0[d]	-670.0 ± 3.0	67.2 ± 4.3	13.49 ± 0.02	-670.1 ± 0.7	6.1 ± 0.2	17.93 ± 0.07	0.28 ± 0.02
pg1448a	1[c]	-300.3 ± 3.8	45.1 ± 4.0	14.49 ± 0.07	-278.2 ± 2.5	49.8 ± 3.4	15.01 ± 0.14	0.99 ± 0.01
		-188.8 ± 7.2	93.3 ± 7.5	14.70 ± 0.04	-165.5 ± 3.7	79.0 ± 11.7	14.57 ± 0.09	
		-13.8 ± 2.8	27.2 ± 4.5	13.79 ± 0.06	-13.8 ± 1.7	26.9 ± 4.7	13.82 ± 0.06	
		125.1 ± 1.4	59.2 ± 3.2	15.10 ± 0.09	125.3 ± 1.2	56.9 ± 3.4	15.20 ± 0.11	
pg1626a	0[d]	-438.8 ± 0.3	31.3 ± 0.4	14.25 ± 0.01	-439.1 ± 0.6	30.5 ± 0.5	14.27 ± 0.02	1.00 ± 0.01
		-266.8 ± 5.3	42.1 ± 2.9	14.08 ± 0.08	-279.5 ± 1.5	25.9 ± 3.0	13.76 ± 0.09	
		-221.9 ± 1.3	20.4 ± 3.9	14.04 ± 0.20	-257.3 ± 2.2	80.7 ± 15.9	13.62 ± 0.17	
		-199.4 ± 111.4	~ 38.5	13.21 ± 1.85	-225.9 ± 1.1	25.3 ± 1.4	14.18 ± 0.03	
q0045b	0	287.3 ± 1.3	4.2 ± 0.9	14.76 ± 0.53	287.3 ± 1.1	4.1 ± 0.7	14.88 ± 0.49	~ 1.00
		309.6 ± 0.4	26.4 ± 0.4	14.33 ± 0.02	309.5 ± 0.6	26.4 ± 0.4	14.33 ± 0.02	

Table 4.6 (cont'd)

Target[a]	Sys.	Vel. (Full Cov.) (km s^{-1})	b (Full Cov.) (km s^{-1})	$\log N$ (Full Cov.) ($\log N$ [cm^{-2}])	Vel. (PC) (km s^{-1})	b (PC) (km s^{-1})	$\log N_{\rm max}$ (PC) ($\log N$ [cm^{-2}])	C (PC)
q0045c	0	313.8 ± 0.5	25.8 ± 0.7	14.37 ± 0.03	314.1 ± 0.7	25.2 ± 0.7	14.50 ± 0.03	0.95 ± 0.01
		398.8 ± 4.5	26.1 ± 7.8	12.82 ± 0.08	399.6 ± 2.0	24.5 ± 7.1	12.84 ± 0.08	
q1230a	0[bc]	-3554.8 ± 1.1	25.8 ± 2.3	13.25 ± 0.04	-3554.7 ± 1.1	25.8 ± 2.3	13.25 ± 0.04	~ 1.00
		-3467.6 ± 1.5	97.7 ± 1.9	14.17 ± 0.01	-3467.4 ± 1.2	97.8 ± 1.9	14.17 ± 0.01	
		-3279.2 ± 5.3	69.3 ± 10.1	13.39 ± 0.07	-3280.4 ± 2.3	67.0 ± 9.6	13.38 ± 0.07	
		-3166.5 ± 3.2	52.6 ± 3.8	13.46 ± 0.05	-3166.7 ± 1.8	55.5 ± 3.8	13.50 ± 0.04	
		-3055.5 ± 15.8	~ 150.0	13.18 ± 0.04	-3028.6 ± 3.5	~ 125.0	13.08 ± 0.04	
		-2757.8 ± 4.7	29.0 ± 6.9	12.59 ± 0.11	-2758.1 ± 2.2	29.4 ± 6.9	12.60 ± 0.11	
		-2666.3 ± 7.3	61.7 ± 12.6	12.89 ± 0.07	-2666.3 ± 2.7	61.8 ± 12.6	12.90 ± 0.07	
		-2420.9 ± 0.7	27.7 ± 1.6	13.49 ± 0.03	-2420.9 ± 0.8	27.7 ± 1.6	13.49 ± 0.03	
		-2409.9 ± 2.4	109.9 ± 6.2	13.78 ± 0.01	-2409.9 ± 1.6	109.9 ± 6.2	13.78 ± 0.01	
		-2189.6 ± 20.8	79.7 ± 27.4	12.57 ± 0.16	-2189.6 ± 4.6	79.8 ± 27.4	12.57 ± 0.16	
q1230a	1[cd]	-584.0 ± 0.9	17.5 ± 1.5	12.83 ± 0.02	-583.9 ± 1.0	14.7 ± 4.8	13.64 ± 0.68	0.27 ± 0.17
		-544.4 ± 1.9	5.6 ± 5.4	12.14 ± 0.07	-544.6 ± 1.4	~ 5.0	12.84 ± 0.45	
q1230a	2[c]	-467.6 ± 3.5	25.6 ± 5.5	12.42 ± 0.08	-467.6 ± 1.9	25.6 ± 5.5	12.42 ± 0.08	~ 1.00
		-359.9 ± 3.7	60.4 ± 2.8	13.55 ± 0.03	-359.9 ± 1.9	60.4 ± 2.8	13.55 ± 0.03	
		-330.0 ± 0.9	21.7 ± 2.2	13.16 ± 0.07	-330.0 ± 1.0	21.7 ± 2.2	13.16 ± 0.07	
		-241.8 ± 1.6	27.2 ± 3.3	12.99 ± 0.05	-241.8 ± 1.3	27.2 ± 3.3	12.99 ± 0.05	
		-140.5 ± 0.6	27.4 ± 1.2	13.55 ± 0.03	-140.5 ± 0.7	27.4 ± 1.2	13.55 ± 0.03	
		-119.2 ± 10.8	72.5 ± 7.1	13.08 ± 0.10	-119.2 ± 3.3	72.5 ± 7.1	13.08 ± 0.10	
rbs144a	0[cd]	-774.9 ± 4.7	25.2 ± 7.6	12.74 ± 0.08	-774.8 ± 2.0	~ 10.8	~ 15.48	0.13 ± 0.02
		-665.1 ± 3.8	23.5 ± 6.1	12.79 ± 0.07	-660.9 ± 2.0	~ 12.5	~ 15.51	
rbs144a	1[cd]	-447.3 ± 2.9	24.2 ± 4.7	12.91 ± 0.05	-449.7 ± 2.8	7.7 ± 2.9	16.64 ± 0.68	0.19 ± 0.03
		-353.8 ± 2.7	15.6 ± 4.6	12.76 ± 0.06	-352.1 ± 1.7	~ 8.2	~ 14.94	
		-239.5 ± 4.0	30.9 ± 6.0	12.86 ± 0.06	-239.9 ± 2.0	26.1 ± 5.9	13.76 ± 0.15	
rbs144a	2[cd]	-18.5 ± 1.6	29.6 ± 2.5	13.14 ± 0.02	-18.5 ± 1.3	29.6 ± 2.5	13.14 ± 0.02	~ 1.00
rbs1483a	0[cd]	-55.6 ± 7.9	21.0 ± 4.8	13.54 ± 0.24	-49.5 ± 1.1	20.8 ± 3.1	14.10 ± 0.20	0.71 ± 0.04
		-25.1 ± 18.9	21.6 ± 11.4	13.18 ± 0.54	-8.2 ± 0.4	2.2 ± 0.1	14.53 ± 2.56	
rbs1503a	0[cd]	8.4 ± 0.6	20.2 ± 0.9	13.55 ± 0.01	8.4 ± 0.8	20.2 ± 0.9	13.55 ± 0.01	~ 1.00
rbs1763a	0[c]	-214.0 ± 0.1	24.1 ± 0.6	14.96 ± 0.06	-213.9 ± 0.4	22.7 ± 0.7	15.16 ± 0.10	0.99 ± 0.01
rbs2023a	0[c]	-831.6 ± 4.1	28.3 ± 6.9	12.99 ± 0.06	-913.4 ± 6.3	~ 10.8	11.50 ± 3.65	0.96 ± 0.01
		-746.1 ± 1.5	19.2 ± 2.3	13.66 ± 0.03	-747.9 ± 1.1	~ 5.0	13.90 ± 3.76	
		-693.4 ± 1.7	20.7 ± 3.5	13.58 ± 0.05	-667.8 ± 3.6	104.4 ± 9.7	14.18 ± 0.06	
		-599.8 ± 1.2	44.4 ± 2.7	14.35 ± 0.01	-599.7 ± 1.3	15.7 ± 13.4	15.79 ± 3.91	
		-514.5 ± 4.2	24.8 ± 5.0	13.26 ± 0.09	-547.1 ± 4.2	46.5 ± 14.3	13.68 ± 0.25	
rbs2023a	1[c]	-206.9 ± 0.4	23.1 ± 0.8	14.11 ± 0.03	-206.9 ± 0.6	19.7 ± 1.8	14.39 ± 0.17	0.95 ± 0.01
rbs2055a	0[c]	-1342.6 ± 1.1	11.2 ± 2.1	12.86 ± 0.03	-1343.1 ± 1.0	8.9 ± 2.3	12.92 ± 0.04	0.86 ± 0.03
		-1261.3 ± 0.3	13.0 ± 0.6	13.64 ± 0.02	-1260.3 ± 0.4	5.1 ± 0.5	16.44 ± 0.12	
rbs2055a	1[c]	-676.3 ± 1.0	38.9 ± 1.5	13.21 ± 0.01	-676.4 ± 1.0	33.3 ± 3.7	13.93 ± 0.25	0.30 ± 0.08
rbs390a	0[c]	-283.8 ± 0.9	31.3 ± 1.3	13.79 ± 0.01	-283.7 ± 0.9	29.2 ± 3.3	13.95 ± 0.21	0.84 ± 0.16
rbs390a	1[c]	-124.1 ± 4.4	14.5 ± 7.0	12.76 ± 0.14	-123.2 ± 2.2	14.2 ± 7.0	12.99 ± 0.18	0.70 ± 0.10
		-69.8 ± 1.4	28.7 ± 2.1	13.66 ± 0.02	-69.5 ± 1.2	24.1 ± 4.3	14.01 ± 0.24	

Table 4.6 (cont'd)

Target[a]	Sys.	Vel. (Full Cov.) (km s^{-1})	b (Full Cov.) (km s^{-1})	log N (Full Cov.) (log N [cm^{-2}])	Vel. (PC) (km s^{-1})	b (PC) (km s^{-1})	log $N_{\rm max}$ (PC) (log N [cm^{-2}])	C (PC)
rbs542a	0[cd]	-627.1 ± 0.3	3.2 ± 1.1	12.73 ± 0.07	-627.3 ± 1.1	3.4 ± 0.7	14.90 ± 0.85	0.42 ± 0.05
		-571.2 ± 0.4	7.9 ± 1.3	12.70 ± 0.04	-571.0 ± 0.7	7.6 ± 1.0	13.32 ± 0.13	
		-518.2 ± 11.7	40.0 ± 11.6	13.09 ± 0.19	-531.3 ± 2.0	24.0 ± 6.8	13.24 ± 0.11	
		-473.9 ± 3.5	29.2 ± 2.2	13.16 ± 0.15	-481.0 ± 1.4	29.3 ± 1.4	13.85 ± 0.13	
rbs542a	1[c]	-314.6 ± 2.9	15.9 ± 2.7	12.57 ± 0.09	-309.3 ± 6.2	~ 19.8	12.73 ± 2.25	~ 1.00
		-272.5 ± 1.9	19.8 ± 2.0	13.82 ± 0.13	-273.3 ± 2.4	18.0 ± 3.7	13.78 ± 0.38	
		-220.3 ± 3.7	36.7 ± 9.0	14.40 ± 0.11	-231.1 ± 14.2	~ 31.9	~ 14.14	
		-187.5 ± 2.7	~ 2.0	13.09 ± 0.79	-187.5 ± 37.8	~ 47.5	14.32 ± 9.13	
		-165.2 ± 3.4	25.0 ± 12.1	13.99 ± 0.33	-157.9 ± 10.0	~ 25.1	~ 13.47	
		-129.2 ± 4.6	20.3 ± 3.3	13.86 ± 0.20	-127.7 ± 4.7	19.4 ± 18.2	13.73 ± 1.75	
		-70.2 ± 7.7	24.9 ± 7.2	13.88 ± 0.40	-75.8 ± 2.0	21.1 ± 10.1	13.62 ± 0.63	
		-37.8 ± 3.7	18.5 ± 11.1	13.54 ± 0.47	-41.0 ± 3.5	34.3 ± 14.5	13.99 ± 0.24	
		-25.9 ± 128.7	44.7 ± 43.1	13.29 ± 2.25	-10.2 ± 1.3	13.6 ± 3.7	13.16 ± 0.34	
		-12.2 ± 6.0	15.8 ± 4.2	13.45 ± 0.45	22.2 ± 10.6	~ 30.2	12.21 ± 2.60	
rbs563a	2[cd]	-268.9 ± 2.6	~ 2.0	12.11 ± 0.10	-268.3 ± 1.6	~ 3.0	12.60 ± 0.71	0.39 ± 0.26
		-235.3 ± 1.1	~ 2.0	12.59 ± 0.06	-234.4 ± 1.2	3.4 ± 0.8	15.24 ± 3.61	
rbs563a	3[cd]	-135.0 ± 3.6	26.9 ± 5.2	12.73 ± 0.06	-135.2 ± 1.9	20.7 ± 12.1	13.96 ± 1.16	0.13 ± 0.09
rbs799a	0	-1453.5 ± 3.4	29.8 ± 0.8	13.32 ± 0.04	-1437.0 ± 1.6	49.6 ± 0.7	14.04 ± 0.03	0.49 ± 0.01
		-1407.2 ± 4.0	28.5 ± 0.8	13.19 ± 0.06	-1324.7 ± 0.1	~ 79.4	12.01 ± 0.24	
rxj0053a	0	183.0 ± 1.4	29.2 ± 1.9	13.19 ± 0.03	231.7 ± 1.3	116.6 ± 1.5	13.72 ± 0.03	0.91 ± 0.01
		258.5 ± 0.5	22.4 ± 0.2	14.44 ± 0.02	257.2 ± 0.8	19.8 ± 0.2	14.68 ± 0.04	
rxj0503a	0[cd]	-561.0 ± 3.3	41.2 ± 5.7	13.18 ± 0.04	-561.0 ± 1.8	41.2 ± 5.7	13.18 ± 0.04	~ 1.00
rxj1503a	0	-1848.8 ± 2.4	24.4 ± 1.1	13.45 ± 0.04	-1850.0 ± 1.8	~ 30.0	13.45 ± 0.04	~ 1.00
		-1751.9 ± 1.7	22.2 ± 0.3	17.38 ± 0.15	-1741.7 ± 1.4	26.3 ± 0.4	17.46 ± 0.14	
		-1654.2 ± 3.8	21.0 ± 1.8	15.70 ± 0.30	-1654.2 ± 4.0	26.3 ± 2.2	15.60 ± 0.84	
		-1587.3 ± 2.6	27.5 ± 0.4	14.52 ± 0.09	-1585.9 ± 1.7	29.8 ± 0.5	14.41 ± 0.10	
		-1518.1 ± 6.3	~ 21.0	12.80 ± 0.09	-1512.0 ± 3.4	~ 36.7	12.72 ± 0.11	
rxj1503a	1	-1136.3 ± 2.7	50.2 ± 1.0	13.57 ± 0.03	-1134.7 ± 1.4	33.8 ± 0.7	13.55 ± 0.03	0.99 ± 0.02
rxj1503a	2[d]	-574.6 ± 2.1	27.4 ± 0.6	13.10 ± 0.04	-574.6 ± 1.6	34.5 ± 0.5	13.16 ± 0.04	0.94 ± 0.02
rxj1503a	3[cd]	-176.9 ± 1.2	19.8 ± 2.0	13.25 ± 0.02	-176.9 ± 1.1	19.8 ± 2.0	13.25 ± 0.02	~ 1.00
		-39.7 ± 0.5	22.6 ± 2.2	15.20 ± 0.32	-39.7 ± 0.7	22.6 ± 2.2	15.20 ± 0.32	
s091728b	0[cd]	-230.7 ± 0.8	28.8 ± 1.2	13.77 ± 0.01	-230.7 ± 0.9	28.8 ± 1.2	13.77 ± 0.01	~ 1.00
s091728b	1[cd]	-36.3 ± 4.4	26.6 ± 4.6	13.45 ± 0.10	-36.8 ± 2.1	26.1 ± 4.6	13.44 ± 0.10	1.00 ± 0.01
		75.6 ± 1.6	59.2 ± 2.4	14.87 ± 0.04	75.4 ± 1.2	58.7 ± 2.5	14.89 ± 0.05	
s121930a	0[cd]	-579.1 ± 4.2	29.0 ± 6.6	12.83 ± 0.06	-579.1 ± 2.0	29.0 ± 6.6	12.83 ± 0.06	~ 1.00
s121930a	1[cd]	-229.4 ± 35.1	45.3 ± 31.3	12.96 ± 0.40	-224.9 ± 6.3	46.6 ± 33.3	13.30 ± 0.47	0.55 ± 0.17
		-169.6 ± 4.8	30.4 ± 4.4	13.47 ± 0.12	-169.8 ± 1.9	25.5 ± 6.7	13.93 ± 0.42	
s135712a	0	-914.7 ± 2.8	94.2 ± 3.3	14.05 ± 0.01	-916.8 ± 1.9	90.0 ± 4.3	14.26 ± 0.10	0.75 ± 0.09
sbs1624a	0[cd]	-1397.8 ± 4.1	59.1 ± 6.2	13.38 ± 0.03	-1397.9 ± 2.0	55.5 ± 18.3	13.80 ± 1.28	~ 0.45
ton1187a	0[cd]	-488.8 ± 2.9	14.8 ± 5.0	12.51 ± 0.07	-488.9 ± 1.7	13.4 ± 5.0	13.39 ± 0.15	0.19 ± 0.03
		-329.7 ± 2.3	17.4 ± 3.8	12.77 ± 0.05	-328.1 ± 1.6	~ 7.8	15.44 ± 7.16	
		-196.3 ± 1.8	11.5 ± 3.4	12.68 ± 0.05	-196.4 ± 1.5	~ 7.2	14.54 ± 8.99	

Table 4.6 (cont'd)

Target[a]	Sys.	Vel. (Full Cov.) (km s^{-1})	b (Full Cov.) (km s^{-1})	log N (Full Cov.) (log N [cm^{-2}])	Vel. (PC) (km s^{-1})	b (PC) (km s^{-1})	log $N_{\rm max}$ (PC) (log N [cm^{-2}])	C (PC)
		-40.4 ± 6.0	32.6 ± 9.2	12.71 ± 0.08	-40.0 ± 2.5	30.0 ± 8.6	13.53 ± 0.11	
		71.8 ± 3.0	~ 2.0	12.19 ± 0.15	71.8 ± 2.7	~ 2.6	13.67 ± 10.29	
tons210a	0	-1468.7 ± 19.6	99.0 ± 37.3	12.91 ± 0.07	-1467.3 ± 4.2	95.1 ± 35.8	13.38 ± 0.75	~ 0.36
		-1442.9 ± 2.0	26.6 ± 4.6	12.81 ± 0.11	-1443.2 ± 1.4	24.7 ± 7.8	13.37 ± 1.03	
uks0242a	0[cd]	-422.0 ± 9.6	66.3 ± 15.6	12.95 ± 0.07	-417.8 ± 2.8	~ 27.7	16.28 ± 11.55	0.08 ± 0.01
vpc0798a	0[cd]	-697.9 ± 10.2	26.9 ± 16.7	12.66 ± 0.18	-629.9 ± 6.4	86.9 ± 21.7	13.71 ± 0.76	0.41 ± 0.02
		-608.7 ± 2.6	41.5 ± 4.0	13.50 ± 0.03	-608.5 ± 1.6	~ 11.8	16.27 ± 14.96	
vpc0798a	1[cd]	-144.1 ± 5.7	54.7 ± 3.0	14.97 ± 0.09	-144.1 ± 2.4	54.7 ± 3.0	14.97 ± 0.09	~ 1.00
		-51.5 ± 9.5	36.4 ± 5.1	14.07 ± 0.18	-51.5 ± 3.1	36.4 ± 5.1	14.07 ± 0.18	

[a]Column (1) gives the short target name from Table 4.1 and Column (2) gives the absorption system ID number. Columns (3)-(5) give the component velocity in the AGN restframe, the Doppler b parameter, and column density for a fit assuming total coverage of the background light. Columns (6)-(9) give the component velocity in the AGN restframe, the Doppler b parameter, the maximum column density, and the covering factor for a fit assuming a simple step-function partial covering model without velocity dependence. Values marked with a $\sim$ are poorly constrained or pinned at the limits of the fitting range, and thus should be treated as rough estimates only.

[b]This absorber is a BAL, as defined in the text, and all measurements should be treated as unreliable.

[c]Only one transition is available for this absorber, so partial covering models are unreliable unless the maximum column density in the beam is heavily saturated.

[d]Absorption identified as associated based only on low velocity offset from AGN systemic redshift.

Table 4.7. CIV Line Fits

Target[a]	Sys.	Vel. (Full Cov.) (km s^{-1})	b (Full Cov.) (km s^{-1})	log N (Full Cov.) (log N [cm^{-2}])	Vel. (PC) (km s^{-1})	b (PC) (km s^{-1})	log $N_{\rm max}$ (PC) (log N [cm^{-2}])	C (PC)
1h1613a	0[d]	-610.7 ± 2.0	25.7 ± 0.4	13.46 ± 0.03	-611.3 ± 1.5	31.5 ± 0.6	13.50 ± 0.03	0.99 ± 0.01
hs0033a	0[b]	105.8 ± 63.0	117.4 ± 36.7	14.35 ± 0.34	128.7 ± 3.4	~ 125.0	14.51 ± 0.05	0.96 ± 0.02
		273.2 ± 19.8	110.9 ± 22.6	14.77 ± 0.14	248.0 ± 2.9	69.5 ± 12.8	14.53 ± 0.15	
		396.7 ± 2.6	17.6 ± 5.3	13.75 ± 0.12	371.7 ± 5.6	~ 125.0	14.67 ± 0.06	
		489.2 ± 2.0	46.3 ± 2.8	14.49 ± 0.03	495.0 ± 1.5	33.7 ± 4.1	14.38 ± 0.07	
		676.0 ± 21.2	~ 150.0	14.11 ± 0.04	631.0 ± 5.2	~ 125.0	14.01 ± 0.06	
i22456a	0	-1673.8 ± 0.5	18.8 ± 0.1	13.79 ± 0.01	-1673.9 ± 0.7	12.8 ± 0.2	14.23 ± 0.03	0.67 ± 0.01
i22456a	1	-921.0 ± 1.8	32.6 ± 2.7	13.39 ± 0.03	-922.0 ± 1.3	25.3 ± 2.4	13.35 ± 0.03	0.99 ± 0.01
		-732.3 ± 0.4	28.9 ± 0.8	14.37 ± 0.01	-838.8 ± 1.7	22.7 ± 4.6	12.98 ± 0.05	
		-674.7 ± 3.3	~ 3.1	12.52 ± 0.16	-731.7 ± 0.6	28.9 ± 0.7	14.39 ± 0.02	
		-649.8 ± 1.0	9.9 ± 1.8	13.44 ± 0.03	-651.0 ± 0.8	13.2 ± 1.2	13.46 ± 0.02	
		-566.4 ± 0.2	24.0 ± 0.3	14.45 ± 0.01	-566.4 ± 0.5	23.8 ± 0.4	14.47 ± 0.01	
		-437.4 ± 0.7	26.2 ± 1.0	13.72 ± 0.01	-437.6 ± 0.8	26.6 ± 1.0	13.73 ± 0.01	
		-245.1 ± 0.2	35.2 ± 0.5	15.19 ± 0.03	-244.9 ± 0.5	32.6 ± 0.6	15.36 ± 0.04	
		-148.7 ± 0.3	12.4 ± 0.5	13.92 ± 0.01	-149.0 ± 0.6	13.0 ± 0.5	13.94 ± 0.01	
i23443a	0[b]	$-2335, 1493$						
kaz238a	0[b]	-43.0 ± 8.5	90.6 ± 9.9	14.99 ± 0.07	-43.0 ± 2.9	90.6 ± 9.9	14.99 ± 0.07	~ 1.00
mr2251a	0	-365.2 ± 1.9	36.5 ± 2.6	13.48 ± 0.04	-368.1 ± 1.6	30.8 ± 3.0	13.60 ± 0.04	0.80 ± 0.03
		-240.9 ± 2.8	36.2 ± 6.9	13.55 ± 0.21	-324.4 ± 1.8	15.9 ± 5.3	13.01 ± 0.17	
		-218.9 ± 7.8	89.9 ± 13.3	14.14 ± 0.04	-234.5 ± 1.0	54.8 ± 2.0	14.28 ± 0.03	
		-154.5 ± 1.3	~ 2.0	12.78 ± 0.10	-156.3 ± 1.2	14.6 ± 3.0	13.21 ± 0.09	
		-67.6 ± 10.9	58.4 ± 8.9	13.43 ± 0.14	-98.0 ± 2.4	77.2 ± 6.4	13.81 ± 0.04	
mrk1253a	0	-199.6 ± 3.4	12.3 ± 5.4	12.98 ± 0.11	-199.6 ± 1.8	12.3 ± 5.4	13.01 ± 0.11	0.94 ± 0.02
		-133.1 ± 1.9	16.7 ± 2.8	13.43 ± 0.05	-133.0 ± 1.4	16.6 ± 2.8	13.47 ± 0.05	
		-1.7 ± 0.8	35.2 ± 1.2	14.44 ± 0.02	-1.6 ± 0.9	33.3 ± 1.3	14.55 ± 0.04	
mrk1392a	0	-411.5 ± 2.1	27.1 ± 0.4	13.24 ± 0.05	-408.7 ± 3.0	134.1 ± 3.8	13.76 ± 0.04	0.92 ± 0.01
		-320.8 ± 0.5	28.0 ± 0.2	14.43 ± 0.01	-320.5 ± 0.7	28.9 ± 0.3	14.49 ± 0.02	
mrk1513a	0	-1529.0 ± 1.0	40.4 ± 1.9	14.14 ± 0.03	-1529.2 ± 1.0	36.7 ± 1.8	14.33 ± 0.04	0.81 ± 0.02
		-1497.6 ± 9.4	99.1 ± 9.8	13.77 ± 0.08	-1500.3 ± 2.8	95.4 ± 8.6	13.92 ± 0.07	
mrk1513a	5	-27.4 ± 3.2	37.1 ± 4.6	13.18 ± 0.04	-27.4 ± 1.8	37.1 ± 4.6	13.18 ± 0.04	~ 1.00
mrk279a	0	-467.5 ± 1.8	57.8 ± 2.3	14.48 ± 0.01	-467.7 ± 1.0	39.1 ± 3.3	15.14 ± 0.13	0.73 ± 0.01
		-354.6 ± 3.8	35.5 ± 5.2	14.14 ± 0.07	-353.8 ± 1.2	39.1 ± 5.7	14.63 ± 0.09	
		-269.8 ± 4.7	52.1 ± 4.7	14.34 ± 0.04	-271.2 ± 1.3	36.3 ± 3.0	14.83 ± 0.10	
		-137.5 ± 3.8	9.6 ± 7.3	12.94 ± 0.12	-138.0 ± 1.1	37.9 ± 4.3	13.40 ± 0.12	
mrk304a	0[b]	$-1597, -294$						
mrk509a	0[b]	-410.2 ± 0.7	11.1 ± 0.9	13.31 ± 0.05	-409.9 ± 0.8	11.4 ± 1.2	13.37 ± 0.08	0.92 ± 0.01
		-381.0 ± 2.6	21.6 ± 4.8	13.19 ± 0.09	-377.4 ± 1.6	25.7 ± 9.9	13.31 ± 0.15	
		-331.2 ± 0.9	2.8 ± 1.2	14.58 ± 0.51	-325.0 ± 0.8	10.4 ± 1.1	14.23 ± 0.06	
		-317.0 ± 0.9	4.7 ± 1.1	13.60 ± 0.05	-300.0 ± 3.4	26.5 ± 7.8	14.15 ± 0.19	
		-302.3 ± 0.7	33.1 ± 1.0	14.13 ± 0.01	-267.9 ± 8.3	~ 19.2	12.64 ± 10.53	
		-243.5 ± 0.9	21.0 ± 0.9	13.50 ± 0.02	-243.1 ± 3.9	21.1 ± 6.3	13.60 ± 0.54	
		-64.8 ± 0.2	3.6 ± 0.2	13.88 ± 0.06	-74.7 ± 4.4	13.4 ± 10.4	12.99 ± 0.83	

Table 4.7 (cont'd)

Target[a]	Sys.	Vel. (Full Cov.) (km s^{-1})	b (Full Cov.) (km s^{-1})	$\log N$ (Full Cov.) ($\log N$ [cm^{-2}])	Vel. (PC) (km s^{-1})	b (PC) (km s^{-1})	$\log N_{\rm max}$ (PC) ($\log N$ [cm^{-2}])	C (PC)
		-28.0 ± 0.3	36.9 ± 0.4	14.16 ± 0.00	-61.8 ± 0.9	8.1 ± 1.0	13.87 ± 0.11	
		-20.3 ± 0.1	5.4 ± 0.6	14.89 ± 0.32	-22.0 ± 0.4	16.4 ± 0.2	14.47 ± 0.01	
		36.1 ± 0.3	11.4 ± 0.6	13.31 ± 0.01	31.4 ± 0.5	19.2 ± 0.6	13.58 ± 0.01	
		88.0 ± 2.7	24.7 ± 3.5	13.32 ± 0.06	84.7 ± 1.1	15.6 ± 1.8	13.20 ± 0.04	
		120.9 ± 0.8	13.9 ± 1.1	13.34 ± 0.05	118.7 ± 0.8	15.3 ± 0.9	13.47 ± 0.02	
		198.5 ± 1.2	39.3 ± 2.4	13.33 ± 0.02	182.0 ± 1.4	~ 2.0	12.45 ± 0.12	
		269.8 ± 1.5	15.8 ± 2.2	12.73 ± 0.04	210.4 ± 1.6	59.5 ± 3.1	13.37 ± 0.02	
mrk509b	0[b]	-398.0 ± 0.6	14.2 ± 1.9	13.41 ± 0.06	-398.4 ± 0.8	12.7 ± 1.6	13.47 ± 0.04	0.92 ± 0.01
		-318.7 ± 0.5	4.7 ± 1.7	14.68 ± 0.77	-317.5 ± 0.9	6.0 ± 2.6	14.84 ± 0.91	
		-301.5 ± 31.5	68.7 ± 24.3	13.62 ± 0.34	-303.1 ± 5.5	68.2 ± 21.7	13.67 ± 0.29	
		-297.4 ± 3.3	21.6 ± 5.1	13.89 ± 0.17	-294.2 ± 2.2	21.6 ± 7.1	13.96 ± 0.21	
		-249.4 ± 6.3	36.5 ± 8.3	13.66 ± 0.23	-248.1 ± 3.1	36.3 ± 10.9	13.69 ± 0.28	
		-51.9 ± 0.5	12.6 ± 0.7	13.81 ± 0.01	-55.1 ± 0.8	8.6 ± 0.8	13.83 ± 0.03	
		-22.1 ± 1.0	3.5 ± 0.5	15.04 ± 0.30	-15.2 ± 1.2	15.7 ± 1.8	14.32 ± 0.04	
		-6.5 ± 4.4	13.6 ± 3.9	13.89 ± 0.15	8.7 ± 9.0	~ 2.3	~ 11.45	
		39.6 ± 1.4	21.4 ± 2.0	13.52 ± 0.03	37.9 ± 1.4	25.7 ± 2.4	13.61 ± 0.03	
		125.8 ± 0.7	22.8 ± 1.2	13.53 ± 0.01	126.6 ± 0.8	19.3 ± 1.1	13.55 ± 0.01	
		240.8 ± 5.3	32.3 ± 8.0	12.99 ± 0.07	256.7 ± 1.7	14.4 ± 5.1	12.83 ± 0.07	
mrk509c	0[b]	-401.7 ± 0.1	2.5 ± 0.0	15.47 ± 0.18	-401.6 ± 0.4	2.4 ± 0.2	14.95 ± 0.48	0.92 ± 0.01
		-392.8 ± 2.4	30.2 ± 3.7	13.39 ± 0.03	-375.6 ± 2.7	48.9 ± 7.7	13.51 ± 0.05	
		-321.9 ± 0.4	3.3 ± 0.1	16.48 ± 0.05	-321.9 ± 1.0	4.2 ± 1.8	15.13 ± 1.42	
		-304.7 ± 1.6	26.9 ± 1.8	14.13 ± 0.02	-301.1 ± 1.6	19.3 ± 3.6	14.14 ± 0.08	
		-271.7 ± 1.0	~ 2.0	13.19 ± 0.23	-271.6 ± 1.2	2.3 ± 1.0	13.62 ± 0.40	
		-238.7 ± 2.2	31.3 ± 2.4	13.67 ± 0.03	-241.8 ± 1.5	32.9 ± 2.4	13.77 ± 0.03	
		-54.1 ± 0.5	9.8 ± 0.8	13.74 ± 0.02	-54.7 ± 0.7	9.5 ± 0.8	13.80 ± 0.02	
		-13.8 ± 0.4	15.5 ± 0.7	14.24 ± 0.02	-13.3 ± 0.6	16.3 ± 0.8	14.41 ± 0.03	
		37.1 ± 1.9	28.1 ± 2.8	13.50 ± 0.03	38.6 ± 1.1	17.2 ± 2.6	13.36 ± 0.06	
		125.3 ± 1.0	16.2 ± 1.8	13.39 ± 0.03	125.1 ± 1.0	9.0 ± 2.3	13.21 ± 0.05	
		207.8 ± 6.2	48.3 ± 7.8	13.31 ± 0.07	139.2 ± 3.5	94.8 ± 14.3	13.57 ± 0.06	
mrk841a	2	-639.0 ± 6.1	99.5 ± 1.8	13.70 ± 0.05	-684.0 ± 2.4	~ 31.2	13.11 ± 0.08	1.00 ± 0.02
		-618.7 ± 1.3	~ 9.7	13.64 ± 0.06	-619.9 ± 1.4	29.0 ± 0.5	13.79 ± 0.03	
mrk876a	0	-3763.3 ± 5.4	88.3 ± 7.7	13.46 ± 0.03	-3763.3 ± 2.3	88.1 ± 10.2	13.51 ± 1.66	~ 0.90
ngc985a	0[b]	-658.4 ± 1.9	33.8 ± 3.2	13.80 ± 0.05	-658.6 ± 1.4	33.3 ± 3.0	14.04 ± 0.04	0.75 ± 0.01
		-508.3 ± 6.0	104.6 ± 12.7	14.37 ± 0.05	-505.1 ± 2.4	99.2 ± 11.1	14.57 ± 0.04	
		-390.8 ± 1.9	42.1 ± 3.9	14.03 ± 0.07	-389.9 ± 1.3	35.4 ± 3.4	14.40 ± 0.06	
		-245.4 ± 1.1	60.7 ± 1.8	14.27 ± 0.01	-245.3 ± 1.1	54.8 ± 1.8	14.51 ± 0.02	
		129.6 ± 1.0	21.1 ± 1.4	13.82 ± 0.02	130.4 ± 1.1	18.1 ± 1.5	14.14 ± 0.04	
ngc985b	0[b]	-679.3 ± 2.4	26.9 ± 3.8	13.15 ± 0.04	-679.3 ± 1.6	26.8 ± 3.8	13.24 ± 0.04	0.83 ± 0.03
		-519.4 ± 6.6	81.5 ± 11.3	13.51 ± 0.05	-519.4 ± 2.6	80.9 ± 11.2	13.60 ± 0.05	
		-391.8 ± 2.1	39.1 ± 3.0	13.56 ± 0.03	-391.6 ± 1.4	38.7 ± 2.9	13.67 ± 0.04	
		-267.9 ± 1.4	30.0 ± 2.2	13.42 ± 0.02	-268.0 ± 1.2	29.8 ± 2.2	13.52 ± 0.03	
		81.3 ± 14.5	62.9 ± 14.8	13.28 ± 0.12	74.9 ± 3.8	58.6 ± 16.0	13.32 ± 0.12	

Table 4.7 (cont'd)

Target[a]	Sys.	Vel. (Full Cov.) (km s^{-1})	b (Full Cov.) (km s^{-1})	log N (Full Cov.) (log N [cm^{-2}])	Vel. (PC) (km s^{-1})	b (PC) (km s^{-1})	log $N_{\rm max}$ (PC) (log N [cm^{-2}])	C (PC)
		130.4 ± 0.4	10.9 ± 0.9	13.83 ± 0.02	130.2 ± 0.7	11.6 ± 0.9	14.05 ± 0.05	
		249.9 ± 12.2	88.5 ± 16.6	13.32 ± 0.07	248.8 ± 3.1	88.7 ± 14.4	13.42 ± 0.06	
pg0804a	1	557.4 ± 1.0	16.2 ± 1.7	13.21 ± 0.02	556.4 ± 0.9	13.5 ± 1.6	13.28 ± 0.03	0.83 ± 0.02
		601.3 ± 0.3	9.7 ± 0.5	13.88 ± 0.02	602.0 ± 0.6	11.0 ± 0.5	14.12 ± 0.04	
		624.4 ± 0.3	~ 2.0	13.61 ± 0.11	626.5 ± 0.8	~ 2.0	13.49 ± 0.12	
pg1448a	1	-256.4 ± 2.8	46.5 ± 2.7	14.90 ± 0.04	-266.0 ± 1.6	25.2 ± 5.8	15.31 ± 0.46	0.98 ± 0.01
		-129.2 ± 4.2	75.8 ± 4.1	14.88 ± 0.03	-169.6 ± 2.0	106.5 ± 2.7	15.06 ± 0.03	
		126.2 ± 1.6	4.7 ± 1.3	17.90 ± 0.25	133.9 ± 1.0	33.1 ± 1.5	14.57 ± 0.03	
		156.8 ± 22.8	44.6 ± 17.0	13.97 ± 0.37	424.7 ± 1.8	16.4 ± 5.2	13.76 ± 0.10	
q0045a	0	320.8 ± 0.7	18.0 ± 1.2	14.19 ± 0.04	320.7 ± 0.8	16.8 ± 1.2	14.35 ± 0.05	0.92 ± 0.01
		333.1 ± 5.3	41.0 ± 5.9	13.62 ± 0.14	332.4 ± 2.1	39.3 ± 5.1	13.71 ± 0.13	
q1230a	0[b]	-3555.9 ± 1.5	26.3 ± 2.3	13.64 ± 0.04	-3551.8 ± 1.6	25.7 ± 5.6	14.00 ± 0.16	0.68 ± 0.01
		-3462.1 ± 1.8	68.9 ± 3.3	14.23 ± 0.02	-3468.3 ± 1.8	27.6 ± 6.1	14.18 ± 0.16	
		-3285.8 ± 14.3	~ 150.0	13.89 ± 0.02	-3448.9 ± 4.3	83.0 ± 9.4	14.48 ± 0.14	
		-3005.5 ± 16.4	~ 150.0	13.66 ± 0.04	-3206.5 ± 2.5	~ 125.0	14.09 ± 0.02	
		-2686.8 ± 7.4	63.8 ± 10.3	13.24 ± 0.06	-2421.6 ± 1.2	18.4 ± 2.8	13.73 ± 0.06	
		-2411.5 ± 1.6	57.4 ± 2.2	13.89 ± 0.02	-2402.5 ± 1.8	81.8 ± 4.6	14.06 ± 0.03	
		-1912.8 ± 8.8	110.3 ± 12.3	13.48 ± 0.04	-1926.9 ± 4.0	118.7 ± 22.2	13.48 ± 0.07	
q1230a	2	-325.5 ± 0.6	9.9 ± 1.2	13.33 ± 0.04	-325.4 ± 0.8	9.8 ± 1.2	13.50 ± 0.09	0.84 ± 0.07
		-313.6 ± 4.0	75.6 ± 7.3	13.87 ± 0.02	-313.0 ± 2.0	75.3 ± 7.2	13.97 ± 0.05	
		-235.1 ± 0.7	17.6 ± 1.5	13.50 ± 0.04	-235.2 ± 0.8	17.0 ± 1.5	13.61 ± 0.07	
		-145.3 ± 2.7	35.2 ± 4.6	13.26 ± 0.04	-145.4 ± 1.7	35.0 ± 4.7	13.35 ± 0.06	
rbs1763a	0	-201.4 ± 0.2	22.5 ± 0.1	14.34 ± 0.01	-201.4 ± 0.5	23.4 ± 0.2	14.37 ± 0.01	0.96 ± 0.01
rbs542a	1	-213.3 ± 0.2	34.7 ± 0.2	14.64 ± 0.00	-239.5 ± 1.0	17.4 ± 0.7	14.14 ± 0.04	0.95 ± 0.01
		-145.7 ± 0.2	12.9 ± 0.5	13.89 ± 0.03	-203.3 ± 1.0	22.8 ± 0.8	14.54 ± 0.02	
		-120.6 ± 1.9	~ 2.0	11.97 ± 0.30	-170.7 ± 2.2	77.7 ± 6.1	13.85 ± 0.06	
		-112.7 ± 12.3	35.7 ± 13.9	13.19 ± 0.21	-146.5 ± 0.5	13.2 ± 0.4	13.93 ± 0.02	
		-32.3 ± 0.4	27.2 ± 0.5	13.87 ± 0.01	-32.0 ± 0.5	26.6 ± 0.4	13.89 ± 0.01	
rxj0053a	0	253.7 ± 2.4	25.0 ± 0.8	14.08 ± 0.06	252.0 ± 1.7	32.4 ± 0.9	14.10 ± 0.06	0.99 ± 0.03

[a]Column (1) gives the short target name from Table 4.1 and Column (2) gives the absorption system ID number. Columns (3)-(5) give the component velocity in the AGN restframe, the Doppler b parameter, and column density for a fit assuming total coverage of the background light. Columns (6)-(9) give the component velocity in the AGN restframe, the Doppler b parameter, the maximum column density, and the covering factor for a fit assuming a simple step-function partial covering model without velocity dependence. Values marked with a $\sim$ are poorly constrained or pinned at the limits of the fitting range, and thus should be treated as rough estimates only.

[b]This absorber is a BAL, as defined in the text, and all measurements should be treated as unreliable.

[c]Only one transition is available for this absorber, so partial covering models are unreliable unless the maximum column density in the beam is heavily saturated.

[d]Absorption identified as associated based only on low velocity offset from AGN systemic redshift.

Table 4.8. OVI Line Fits

Target[a]	Sys.	Vel. (Full Cov.) (km s^{-1})	b (Full Cov.) (km s^{-1})	$\log N$ (Full Cov.) ($\log N$ [cm^{-2}])	Vel. (PC) (km s^{-1})	b (PC) (km s^{-1})	$\log N_{\rm max}$ (PC) ($\log N$ [cm^{-2}])	C (PC)
he2258a	0	-3030.8 ± 3.0	25.8 ± 0.6	14.03 ± 0.04	-3032.1 ± 1.9	28.4 ± 0.9	14.03 ± 0.04	1.00 ± 0.01
		-2967.5 ± 4.1	23.8 ± 0.6	13.79 ± 0.05	-2966.6 ± 2.3	30.9 ± 1.0	13.82 ± 0.05	
		-2886.9 ± 4.3	26.0 ± 0.5	13.72 ± 0.05	-2878.5 ± 2.4	32.8 ± 0.7	13.72 ± 0.06	
he2258a	1[d]	-1851.8 ± 1.9	25.0 ± 0.9	14.11 ± 0.03	-1850.7 ± 1.5	30.0 ± 1.2	14.12 ± 0.03	0.98 ± 0.01
he2258a	2	-725.8 ± 2.6	23.8 ± 0.3	14.44 ± 0.07	-673.4 ± 0.8	30.3 ± 0.3	16.53 ± 0.06	0.99 ± 0.01
		-655.9 ± 1.3	25.8 ± 0.3	16.48 ± 0.11	-569.5 ± 1.8	29.9 ± 0.7	14.44 ± 0.04	
		-499.5 ± 0.6	23.3 ± 0.2	18.67 ± 0.05	-486.8 ± 1.1	37.3 ± 0.3	15.75 ± 0.05	
he2332a	2	-36.2 ± 0.9	24.8 ± 2.3	14.01 ± 0.05	-29.8 ± 1.4	30.0 ± 1.9	14.00 ± 0.06	~ 1.00
hs0033a	0[b]	48.1 ± 0.1	~ 145.2	~ 10.62	-8.7 ± 0.9	13.7 ± 1.6	13.93 ± 0.21	0.96 ± 0.01
		117.4 ± 0.1	~ 40.1	~ 10.61	169.9 ± 2.0	39.5 ± 1.2	19.76 ± 0.11	
		297.5 ± 2.4	193.9 ± 2.6	16.21 ± 0.02	425.6 ± 2.2	33.7 ± 1.3	19.75 ± 0.08	
		470.4 ± 0.1	~ 57.6	~ 9.00	617.3 ± 2.1	30.1 ± 4.9	14.24 ± 0.10	
i22456a	0[bc]	-1694.7 ± 1.5	20.6 ± 2.5	13.94 ± 0.03	-1695.2 ± 1.2	~ 10.3	16.20 ± 11.60	0.28 ± 0.03
i22456a	1[b]	$-1395, -33$						
mrk876a	0	-3801.1 ± 1.0	26.3 ± 0.5	14.16 ± 0.02	-3805.3 ± 1.3	~ 31.6	14.03 ± 0.04	0.93 ± 0.01
		-3754.3 ± 1.3	25.1 ± 0.2	14.10 ± 0.02	-3765.5 ± 1.3	~ 34.8	14.28 ± 0.02	
		-3693.2 ± 2.3	25.8 ± 0.2	13.56 ± 0.03	-3697.3 ± 1.8	33.4 ± 0.6	13.63 ± 0.03	
		-3515.5 ± 0.6	~ 24.8	14.16 ± 0.01	-3515.0 ± 0.8	28.2 ± 0.4	14.20 ± 0.01	
		-3440.5 ± 3.2	~ 26.2	13.34 ± 0.03	-3431.7 ± 2.0	~ 30.6	13.35 ± 0.03	
mrk877a	0	-623.6 ± 1.5	34.7 ± 0.7	14.58 ± 0.02	-626.4 ± 1.3	34.6 ± 0.6	14.55 ± 0.02	~ 1.00
		-506.2 ± 3.1	41.2 ± 1.0	14.30 ± 0.04	-508.5 ± 1.8	60.5 ± 1.6	14.36 ± 0.03	
pg0804a	1	548.6 ± 1.7	25.9 ± 0.4	13.72 ± 0.03	546.7 ± 1.3	28.5 ± 0.5	13.66 ± 0.03	0.99 ± 0.01
		600.9 ± 1.2	25.1 ± 0.2	13.96 ± 0.02	599.1 ± 1.2	30.5 ± 0.4	13.99 ± 0.02	
q0045b	0	305.8 ± 0.3	29.8 ± 0.1	15.08 ± 0.01	305.8 ± 0.6	30.1 ± 0.1	15.08 ± 0.01	1.00 ± 0.01
q0045c	0	312.8 ± 0.9	36.1 ± 0.4	15.02 ± 0.02	312.7 ± 0.9	33.0 ± 0.3	15.08 ± 0.03	1.00 ± 0.01
q1230a	0	-3516.9 ± 2.4	78.3 ± 1.9	15.18 ± 0.02	-4486.6 ± 1.9	26.0 ± 6.1	14.08 ± 0.07	0.95 ± 0.01
		-3511.7 ± 0.1	4.1 ± 0.0	16.75 ± 0.02	-3524.7 ± 1.7	73.6 ± 2.5	15.16 ± 0.03	
		-3337.6 ± 2.7	103.2 ± 6.4	15.17 ± 0.02	-3349.7 ± 2.2	128.6 ± 9.4	15.31 ± 0.03	
		-3328.6 ± 0.1	2.6 ± 0.2	15.37 ± 0.22	-3136.2 ± 1.2	61.1 ± 1.8	15.08 ± 0.02	
		-3138.2 ± 1.5	67.6 ± 1.5	15.04 ± 0.01	-2983.2 ± 2.5	36.1 ± 9.7	13.50 ± 0.08	
		-2730.2 ± 2.2	27.7 ± 4.5	13.98 ± 0.06	-2839.6 ± 1.4	9.0 ± 4.8	13.56 ± 0.07	
		-2669.7 ± 9.4	160.3 ± 9.2	14.91 ± 0.02	-2720.8 ± 1.3	68.4 ± 3.1	14.74 ± 0.01	
		-2490.0 ± 0.1	3.5 ± 0.0	16.46 ± 0.09	-2612.2 ± 1.4	29.0 ± 3.2	14.22 ± 0.04	
		-2403.1 ± 1.9	126.6 ± 1.4	15.49 ± 0.01	-2411.7 ± 0.9	124.2 ± 1.1	15.63 ± 0.01	
q1230a	2	-437.1 ± 2.1	~ 25.9	13.25 ± 0.04	-468.3 ± 2.2	26.6 ± 0.4	12.68 ± 0.06	0.99 ± 0.01
		-375.8 ± 0.5	21.4 ± 0.8	14.69 ± 0.02	-374.2 ± 0.9	32.5 ± 0.4	14.48 ± 0.03	
		-325.4 ± 0.6	26.7 ± 0.2	15.13 ± 0.02	-335.7 ± 0.8	34.7 ± 0.2	15.23 ± 0.02	
		-243.5 ± 0.3	24.6 ± 0.1	14.99 ± 0.01	-244.8 ± 0.6	26.3 ± 0.2	14.92 ± 0.01	
		-135.3 ± 0.2	25.8 ± 0.1	15.63 ± 0.01	-136.2 ± 0.5	39.5 ± 0.2	15.05 ± 0.01	
rbs2023a	0[c]	-686.2 ± 15.9	160.1 ± 14.4	15.18 ± 0.05	-683.8 ± 4.9	163.5 ± 19.7	15.18 ± 0.08	~ 1.00
		-608.5 ± 5.0	20.7 ± 10.2	14.94 ± 0.32	-596.4 ± 2.4	44.2 ± 9.6	14.87 ± 0.10	
		-535.2 ± 14.3	34.9 ± 22.1	14.37 ± 0.25	-503.8 ± 2.5	~ 3.2	~ 15.86	

Table 4.8 (cont'd)

Target[a]	Sys.	Vel. (Full Cov.) (km s^{-1})	b (Full Cov.) (km s^{-1})	log N (Full Cov.) (log N [cm^{-2}])	Vel. (PC) (km s^{-1})	b (PC) (km s^{-1})	log $N_{\rm max}$ (PC) (log N [cm^{-2}])	C (PC)
rbs542a	1	-271.3 ± 0.6	20.3 ± 0.1	14.34 ± 0.02	-307.3 ± 0.8	26.5 ± 0.4	13.88 ± 0.01	0.98 ± 0.01
		-204.1 ± 0.3	21.4 ± 0.1	19.06 ± 0.01	-208.1 ± 0.4	26.6 ± 0.1	18.23 ± 0.02	
		-61.8 ± 0.2	28.7 ± 0.1	14.71 ± 0.00	-65.5 ± 0.4	34.3 ± 0.1	14.80 ± 0.00	
rbs799a	0	-1532.2 ± 0.1	~ 123.4	~ 9.40	-1669.5 ± 2.4	28.8 ± 0.9	17.64 ± 0.34	0.40 ± 0.01
		-1436.6 ± 5.1	89.1 ± 1.1	14.26 ± 0.03	-1436.0 ± 1.5	23.5 ± 0.4	15.66 ± 0.10	
rxj0053a	0	226.0 ± 1.2	53.3 ± 1.0	14.25 ± 0.02	216.8 ± 1.5	114.9 ± 46.4	14.68 ± 1.33	0.61 ± 0.48
rxj1503a	0[c]	-1803.5 ± 40.8	75.5 ± 51.1	14.23 ± 0.27	-1799.2 ± 6.7	78.1 ± 51.9	14.27 ± 0.29	0.96 ± 0.07
		-1717.5 ± 2.0	22.2 ± 5.1	15.02 ± 0.16	-1717.3 ± 1.4	19.3 ± 10.3	15.26 ± 0.89	
s135712a	0[c]	-915.7 ± 2.4	64.4 ± 3.5	14.53 ± 0.02	-915.7 ± 1.6	64.4 ± 3.5	14.53 ± 0.02	~ 1.00

[a]Column (1) gives the short target name from Table 4.1 and Column (2) gives the absorption system ID number. Columns (3)-(5) give the component velocity in the AGN restframe, the Doppler b parameter, and column density for a fit assuming total coverage of the background light. Columns (6)-(9) give the component velocity in the AGN restframe, the Doppler b parameter, the maximum column density, and the covering factor for a fit assuming a simple step-function partial covering model without velocity dependence. Values marked with a $\sim$ are poorly constrained or pinned at the limits of the fitting range, and thus should be treated as rough estimates only.

[b]This absorber is a BAL, as defined in the text, and all measurements should be treated as unreliable.

[c]Only one transition is available for this absorber, so partial covering models are unreliable unless the maximum column density in the beam is heavily saturated.

[d]Absorption identified as associated based only on low velocity offset from AGN systemic redshift.

Table 4.9. Power-Law Inhomogeneous HI Line Measurements

Target[a]	Sys.	Velocity (km s^{-1})	log N (Int.) (log N [cm^{-2}])	Vel. (km s^{-1})	b (km s^{-1})	log $N_{\rm max}$ (log N [cm^{-2}])	a
1h1613a	0[c]			-631.5 ± 3.6	20.5 ± 5.2	15.17 ± 0.65	0.97 ± 0.46
				-582.5 ± 39.9	39.5 ± 24.3	13.74 ± 0.54	
				-520.3 ± 2.6	~ 5.5	13.20 ± 0.35	
1h1613a	1[cd]			-191.7 ± 0.6	32.1 ± 0.9	13.88 ± 0.01	~ 0.00
fair9a	0[cd]			-230.5 ± 2.1	~ 3.8	14.26 ± 2.45	28.91 ± 28.89
				-168.5 ± 3.4	32.2 ± 10.8	15.04 ± 1.42	
				-39.2 ± 1.8	11.2 ± 6.0	14.26 ± 1.17	
h1118a	0[cd]			-817.3 ± 9.5	66.5 ± 23.6	14.29 ± 1.56	~ 13.22
h1118a	1[cd]			-585.7 ± 9.3	95.3 ± 36.9	13.83 ± 2.99	~ 3.22
h1118a	2[cd]			~ -505.3	~ 2.0	~ 13.74	3.42 ± 1.24
				-351.2 ± 2.1	3.3 ± 0.9	18.22 ± 0.18	
				-305.0 ± 4.9	34.8 ± 3.6	15.42 ± 0.60	
				~ -187.7	~ 2.0	~ 9.00	
h1118a	3[cd]			26.2 ± 0.4	14.1 ± 0.5	13.92 ± 0.07	0.36 ± 0.11
				159.7 ± 0.4	20.9 ± 1.3	15.26 ± 0.22	
he0003a	0[cd]			-809.5 ± 4.3	23.0 ± 13.5	17.61 ± 3.98	109.83 ± 105.57
he0003a	1[bc]			~ -292.7	~ 32.9	~ 10.23	6.23 ± 1.19
				-264.2 ± 151.3	37.3 ± 35.2	13.89 ± 1.87	
				-196.3 ± 9.8	24.8 ± 3.9	14.75 ± 0.36	
				-176.5 ± 0.0	79.7 ± 5.6	15.10 ± 0.17	
				62.4 ± 3.3	68.5 ± 5.1	14.43 ± 0.11	
				~ 172.9	~ 16.7	15.65 ± 3.44	
				~ 173.0	~ 15.1	~ 16.35	
				~ 173.1	~ 15.0	16.48 ± 14.90	
he0429a	0[cd]			-634.2 ± 4.2	~ 6.2	13.75 ± 6.45	~ 0.00
				-599.0 ± 1.9	10.6 ± 2.0	13.15 ± 1.88	
he0429a	1[cd]			-189.0 ± 0.5	21.5 ± 1.1	14.18 ± 0.03	~ 0.00
				-99.4 ± 0.4	33.5 ± 1.1	14.77 ± 0.04	
				150.1 ± 0.9	35.4 ± 1.7	15.91 ± 0.18	
				239.3 ± 7.6	32.9 ± 6.4	13.37 ± 0.12	
he0429a	2[cd]			647.2 ± 0.4	37.2 ± 1.0	17.32 ± 0.16	~ 0.00
he2258a	0[d]	$-3231, -2990$	~ 14.58	-3095.7 ± 2.4	24.5 ± 0.4	13.50 ± 0.04	0.58 ± 0.13
				-3032.1 ± 0.8	24.4 ± 0.3	14.31 ± 0.06	
he2258a	1[d]	$-1901, -1767$	~ 14.42	-1828.8 ± 10.5	79.4 ± 1.2	14.76 ± 0.08	12.21 ± 1.78
he2258a	2	$-883, -341$	~ 16.48	-660.7 ± 0.5	21.4 ± 0.1	18.31 ± 0.03	1.78 ± 0.06
				-473.5 ± 0.5	31.7 ± 0.2	16.31 ± 0.05	
				~ -386.2	~ 49.3	~ 9.00	
he2332a	0[cd]			-1971.5 ± 27.6	89.1 ± 16.5	14.38 ± 0.31	3.55 ± 1.08
				-1841.0 ± 8.7	63.7 ± 8.7	15.26 ± 0.23	
				-1667.3 ± 6.8	64.8 ± 6.1	14.93 ± 0.22	
				-1564.2 ± 29.7	136.2 ± 10.3	14.77 ± 0.25	
he2332a	1[cd]			-499.1 ± 5.4	~ 20.6	15.77 ± 13.06	~ 76.95
he2332a	2[cd]			-86.1 ± 0.9	32.3 ± 0.9	13.76 ± 0.03	0.22 ± 0.07

Table 4.9 (cont'd)

Target[a]	Sys.	Velocity (km s^{-1})	log N (Int.) (log N [cm^{-2}])	Vel. (km s^{-1})	b (km s^{-1})	log $N_{\rm max}$ (log N [cm^{-2}])	a
				-18.6 ± 0.4	27.6 ± 0.9	14.31 ± 0.05	
hs0033a	0[b]	$-61, 713$		~ -12.7	~ 15.4	~ 11.38	7.36 ± 0.26
				150.9 ± 1.7	43.7 ± 0.5	19.78 ± 0.10	
				333.6 ± 3.7	38.6 ± 0.9	19.99 ± 0.22	
				502.1 ± 2.5	23.3 ± 0.5	19.90 ± 0.08	
i06229a	0[d]	$-729, -531$	~ 14.50	-647.4 ± 3.7	46.6 ± 9.0	14.61 ± 0.55	14.92 ± 9.71
i06229b	1[d]	$-770, -565$	~ 14.00	-656.1 ± 3.8	43.5 ± 9.3	14.79 ± 0.68	18.49 ± 12.86
i19169a	0[c]			-657.0 ± 38.9	35.4 ± 19.8	13.71 ± 0.79	1.80 ± 0.15
				-631.9 ± 0.5	14.9 ± 0.7	16.86 ± 0.34	
i22456a	0[c]			-1669.7 ± 0.1	20.2 ± 0.4	14.37 ± 0.05	~ 0.00
i22456a	1[c]			-915.3 ± 0.8	33.3 ± 0.8	14.55 ± 0.04	2.07 ± 0.09
				-762.0 ± 24.7	105.8 ± 9.2	14.56 ± 0.33	
				-708.2 ± 1.5	26.6 ± 1.2	17.85 ± 0.36	
				~ -671.0	~ 147.8	~ 9.08	
				-561.3 ± 0.7	21.6 ± 0.6	17.23 ± 0.25	
				-441.9 ± 1.9	32.4 ± 0.9	14.83 ± 0.05	
				-281.5 ± 0.6	10.7 ± 0.2	18.41 ± 0.02	
				-205.8 ± 2.0	37.6 ± 0.5	16.60 ± 0.16	
izw1a	0[c]			-1955.3 ± 9.0	53.9 ± 12.4	13.16 ± 1.18	~ 0.00
				-1816.8 ± 4.7	71.6 ± 10.2	13.63 ± 1.25	
izw1a	2[c]			-246.0 ± 7.8	~ 21.9	13.19 ± 13.05	~ 2.69
				-154.8 ± 10.7	~ 3.2	~ 13.45	
izw1a	4[cd]			232.5 ± 5.7	17.0 ± 5.0	18.57 ± 0.98	72.18 ± 16.98
izw1b	0[c]			-1972.6 ± 6.8	34.3 ± 13.4	14.90 ± 0.69	18.64 ± 9.53
				-1828.2 ± 4.3	42.9 ± 9.1	16.64 ± 1.42	
izw1b	1[cd]			-1180.0 ± 2.5	36.5 ± 7.6	13.20 ± 4.30	~ 0.86
izw1b	2[cd]			-240.0 ± 2.8	27.9 ± 10.2	15.35 ± 1.20	28.75 ± 18.61
				-156.3 ± 3.0	13.8 ± 3.5	14.76 ± 1.02	
izw1b	3[cd]			26.3 ± 8.9	23.2 ± 17.0	13.17 ± 9.39	~ 5.55
				67.6 ± 3.4	~ 7.0	13.37 ± 11.69	
				~ 126.8	~ 9.9	~ 10.36	
izw1b	4[cd]			233.1 ± 2.0	50.2 ± 4.0	13.43 ± 1.60	~ 0.88
kaz238a	0[bc]			-345.3 ± 10.8	133.1 ± 9.1	14.37 ± 0.04	~ 0.00
				-64.4 ± 26.5	139.3 ± 16.3	14.83 ± 0.10	
				70.7 ± 15.1	84.8 ± 4.2	14.97 ± 0.21	
mr2251a	0[c]			-697.0 ± 3.7	65.9 ± 3.2	13.31 ± 0.04	~ 0.05
				-606.3 ± 2.0	32.4 ± 2.5	13.12 ± 0.04	
				-530.9 ± 0.5	44.6 ± 1.1	13.86 ± 0.04	
				-374.1 ± 4.3	103.4 ± 1.5	13.96 ± 0.03	
				-245.1 ± 2.1	98.5 ± 0.9	14.38 ± 0.06	
				-110.7 ± 2.2	84.9 ± 1.1	14.06 ± 0.04	
				14.0 ± 1.0	61.0 ± 1.0	13.73 ± 0.04	
				119.0 ± 2.0	32.6 ± 2.6	12.95 ± 0.05	

Table 4.9 (cont'd)

Target[a]	Sys.	Velocity (km s^{-1})	log N (Int.) (log N [cm^{-2}])	Vel. (km s^{-1})	b (km s^{-1})	log $N_{\rm max}$ (log N [cm^{-2}])	a
				230.2 ± 2.3	18.1 ± 3.6	12.40 ± 0.08	
mr2251a	1[c]			445.3 ± 2.1	12.6 ± 3.5	14.32 ± 0.64	29.96 ± 21.11
				527.5 ± 1.0	17.3 ± 5.6	16.55 ± 2.18	
				627.4 ± 1.9	15.8 ± 5.2	14.46 ± 0.80	
				724.7 ± 1.2	9.5 ± 3.9	15.08 ± 1.41	
mrk106a	3	$-1143, -996$	~ 14.64	-1077.5 ± 2.9	10.8 ± 2.2	18.22 ± 0.59	80.87 ± 13.30
mrk1253a	0[c]			-219.7 ± 0.6	16.9 ± 1.0	13.60 ± 0.04	~ 0.00
				-146.2 ± 0.5	25.3 ± 0.9	13.85 ± 0.03	
				-20.8 ± 0.4	34.3 ± 1.3	14.79 ± 0.08	
mrk1392a	0[c]			-440.1 ± 5.0	27.3 ± 4.7	13.02 ± 0.10	1.34 ± 0.13
				-321.7 ± 0.4	33.8 ± 1.6	15.70 ± 0.19	
				-198.0 ± 35.1	~ 3.2	12.10 ± 10.51	
mrk1392a	1[c]			18.3 ± 0.8	34.2 ± 3.6	13.90 ± 0.25	~ 1.05
				91.1 ± 0.8	~ 4.1	13.57 ± 0.43	
mrk1501a	0[cd]			-409.6 ± 4.3	36.2 ± 6.9	14.83 ± 0.27	~ 0.00
				-310.2 ± 5.8	39.2 ± 5.9	14.17 ± 0.07	
mrk1501a	1[c]			-47.5 ± 1.1	17.3 ± 10.5	16.71 ± 3.88	~ 3.37
mrk1513a	0[c]			-1519.8 ± 0.6	56.3 ± 1.8	14.57 ± 0.07	0.75 ± 0.17
				-1412.5 ± 4.3	20.6 ± 4.4	12.93 ± 0.10	
mrk1513a	2[c]			-788.9 ± 6.6	35.3 ± 29.4	16.01 ± 4.88	~ 89.24
mrk1513a	3[c]			-647.2 ± 4.6	15.9 ± 3.9	13.46 ± 0.95	~ 8.67
				-559.3 ± 4.0	~ 10.0	13.17 ± 0.95	
				-478.8 ± 10.9	41.7 ± 15.8	13.84 ± 0.87	
				-410.8 ± 5.2	18.3 ± 7.1	13.86 ± 1.25	
mrk1513a	4[cd]			-254.6 ± 3.6	30.3 ± 6.0	12.49 ± 3.15	~ 0.00
mrk1513a	5[c]			~ -187.2	~ 2.0	~ 13.86	2.66 ± 1.35
				-23.0 ± 0.7	23.5 ± 3.9	14.80 ± 0.55	
				11.9 ± 7.8	82.2 ± 6.4	14.10 ± 0.22	
				172.6 ± 1.6	23.9 ± 1.9	13.40 ± 0.17	
mrk279a	0[c]			-560.8 ± 6.9	24.5 ± 7.1	14.19 ± 0.44	5.20 ± 0.33
				-470.4 ± 3.3	31.9 ± 2.2	18.26 ± 0.27	
				-361.4 ± 3.5	17.7 ± 1.7	15.33 ± 0.20	
				-314.6 ± 7.1	~ 3.1	14.14 ± 4.58	
				-255.1 ± 6.9	49.3 ± 6.1	14.65 ± 0.05	
mrk279a	1[c]			101.9 ± 0.5	32.5 ± 1.9	15.38 ± 0.21	1.56 ± 0.22
mrk304a	1[cd]			-165.9 ± 8.3	51.6 ± 4.1	13.75 ± 0.13	0.21 ± 0.14
				-134.7 ± 0.6	20.4 ± 4.8	14.57 ± 0.47	
mrk304b	1[cd]			-131.8 ± 2.3	52.6 ± 4.6	14.13 ± 0.17	0.49 ± 0.32
				-125.1 ± 0.8	18.8 ± 6.6	14.73 ± 0.86	
mrk304b	2[cd]			279.1 ± 4.7	42.0 ± 10.2	13.77 ± 1.95	~ 1.93
mrk421a	0[cd]			-1389.8 ± 8.3	~ 24.6	~ 16.81	~ 130.36
mrk421b	0[cd]			-1411.7 ± 3.9	~ 2.0	18.25 ± 0.51	64.11 ± 18.61
mrk478a	0[c]			-2762.6 ± 2.1	44.7 ± 4.9	13.79 ± 0.53	~ 0.32

Table 4.9 (cont'd)

Target[a]	Sys.	Velocity (km s^{-1})	log N (Int.) (log N [cm^{-2}])	Vel. (km s^{-1})	b (km s^{-1})	log $N_{\rm max}$ (log N [cm^{-2}])	a
				-2673.8 ± 4.5	9.1 ± 8.4	12.65 ± 0.53	
mrk478a	1[c]			-2275.8 ± 3.5	~ 13.5	13.75 ± 1.26	~ 2.36
				-2234.5 ± 11.0	44.5 ± 10.1	14.21 ± 1.40	
mrk478a	2[cd]			-1110.6 ± 26.8	55.9 ± 30.0	13.13 ± 2.60	~ 0.97
				-1032.5 ± 8.6	35.8 ± 7.6	13.32 ± 2.88	
mrk478a	3[cd]			-402.4 ± 0.4	11.4 ± 3.8	15.54 ± 1.70	2.36 ± 1.90
				-278.7 ± 2.8	~ 2.0	13.30 ± 0.49	
mrk478a	4[c]			-89.4 ± 3.1	29.9 ± 4.8	12.91 ± 0.06	~ 0.00
mrk486a	0[bc]			-961.0 ± 4.5	196.4 ± 8.1	14.56 ± 0.01	~ 0.00
				-602.8 ± 6.3	~ 200.0	15.24 ± 0.04	
				-201.0 ± 22.6	183.6 ± 40.3	15.35 ± 0.11	
				161.6 ± 15.0	185.9 ± 14.4	15.23 ± 0.06	
				456.8 ± 5.2	172.0 ± 6.0	14.56 ± 0.02	
mrk504a	0[cd]			-1050.2 ± 37.3	62.0 ± 25.2	13.39 ± 0.28	0.56 ± 0.21
				-990.1 ± 0.8	19.2 ± 2.7	14.89 ± 0.31	
mrk504a	1[cd]			-728.0 ± 6.7	~ 21.3	16.86 ± 9.41	~ 38.52
mrk504a	2[cd]			-432.7 ± 1.6	24.1 ± 3.0	13.92 ± 0.41	~ 0.14
mrk504a	3[cd]			-134.0 ± 5.9	36.9 ± 7.3	13.98 ± 0.40	2.28 ± 1.91
				-120.7 ± 0.9	12.1 ± 5.6	16.13 ± 2.41	
mrk509a	0[bc]			-387.2 ± 0.6	38.2 ± 0.5	14.16 ± 0.01	1.12 ± 0.02
				-312.0 ± 0.4	28.8 ± 0.4	15.03 ± 0.02	
				-245.6 ± 0.6	33.0 ± 0.4	14.42 ± 0.02	
				-39.7 ± 0.5	39.0 ± 0.3	15.05 ± 0.02	
				82.6 ± 1.5	62.3 ± 0.9	15.14 ± 0.02	
				182.9 ± 3.6	45.2 ± 1.2	14.33 ± 0.04	
				221.8 ± 0.6	30.3 ± 0.5	14.33 ± 0.06	
mrk509b	0[bc]			-391.3 ± 2.5	40.1 ± 2.2	14.13 ± 0.03	1.14 ± 0.05
				-307.1 ± 1.6	33.1 ± 1.2	15.00 ± 0.06	
				-235.1 ± 2.7	29.3 ± 1.9	14.18 ± 0.04	
				-55.4 ± 1.6	31.0 ± 0.9	14.80 ± 0.04	
				32.5 ± 3.1	43.3 ± 2.0	14.99 ± 0.05	
				134.4 ± 3.3	38.6 ± 2.3	14.87 ± 0.06	
				217.1 ± 2.4	30.2 ± 1.5	14.67 ± 0.04	
mrk509c	0[bc]			-427.5 ± 2.0	14.4 ± 1.0	13.34 ± 0.09	0.90 ± 0.07
				-391.2 ± 2.7	21.8 ± 2.3	13.77 ± 0.06	
				-316.7 ± 1.8	37.5 ± 1.7	14.76 ± 0.06	
				-245.0 ± 2.7	41.4 ± 1.5	14.33 ± 0.05	
				-79.2 ± 0.7	17.0 ± 1.4	13.85 ± 0.03	
				-13.6 ± 2.0	54.0 ± 1.1	14.89 ± 0.06	
				117.6 ± 3.0	61.9 ± 1.8	14.89 ± 0.05	
				216.9 ± 2.8	35.7 ± 1.2	14.38 ± 0.04	
				243.2 ± 2.2	~ 11.2	13.28 ± 0.14	
				291.5 ± 3.0	~ 2.9	12.44 ± 0.58	

Table 4.9 (cont'd)

Target[a]	Sys.	Velocity (km s^{-1})	log N (Int.) (log N [cm^{-2}])	Vel. (km s^{-1})	b (km s^{-1})	log $N_{\rm max}$ (log N [cm^{-2}])	a
mrk817a	0[c]			-1037.6 ± 2.8	36.3 ± 7.2	14.28 ± 0.52	8.36 ± 6.96
				-925.5 ± 9.0	65.6 ± 11.7	13.93 ± 0.39	
mrk817b	0[cd]			-1039.7 ± 2.5	~ 5.5	14.18 ± 1.98	~ 14.42
				-1016.8 ± 5.4	43.5 ± 11.3	14.33 ± 1.04	
mrk817b	1[c]			-510.5 ± 2.2	~ 8.4	16.10 ± 8.70	~ 40.00
mrk841a	0[cd]			-1684.8 ± 1.5	42.7 ± 1.4	14.19 ± 0.03	~ 0.00
				-1660.2 ± 3.4	16.8 ± 4.5	14.06 ± 0.25	
mrk841a	1[cd]			-1050.3 ± 12.5	57.1 ± 7.0	13.98 ± 0.77	~ 1.70
				-1003.8 ± 2.4	27.2 ± 7.0	13.88 ± 0.80	
mrk841a	2[cd]			-688.9 ± 15.5	84.5 ± 6.0	13.89 ± 0.13	~ 0.00
				-685.5 ± 1.4	22.7 ± 2.0	13.67 ± 0.09	
				-617.3 ± 0.7	23.8 ± 2.2	14.43 ± 0.14	
				-516.6 ± 7.3	49.0 ± 9.9	13.23 ± 0.10	
mrk841a	3[cd]			273.4 ± 2.1	~ 3.3	~ 13.81	~ 0.50
				290.5 ± 19.8	~ 19.3	12.61 ± 9.31	
mrk876a	0	$-3883, -3355$	14.75 ± 0.14	-3773.9 ± 1.1	59.0 ± 3.2	13.94 ± 0.35	~ 2.06
				-3519.5 ± 2.1	60.0 ± 2.6	13.81 ± 0.33	
				-3406.6 ± 2.5	27.9 ± 2.3	13.18 ± 0.32	
mrk876a	1[cd]			-1554.6 ± 1.0	9.2 ± 2.6	16.75 ± 1.69	35.55 ± 15.90
				-1451.9 ± 4.3	29.6 ± 12.3	14.24 ± 0.32	
				-1307.1 ± 7.1	35.3 ± 7.6	14.06 ± 0.29	
				-1225.6 ± 1.6	14.0 ± 3.3	15.65 ± 1.07	
mrk876a	2[d]	$-591, -499$	~ 13.53	-562.2 ± 1.0	7.0 ± 1.3	13.59 ± 0.29	6.23 ± 2.86
				-548.9 ± 1.4	30.2 ± 2.7	14.02 ± 0.27	
				-535.8 ± 1.4	~ 2.8	13.14 ± 0.45	
mrk877a	0	$-827, -409$	16.37 ± 0.08	-655.2 ± 1.5	19.0 ± 0.2	16.92 ± 0.15	1.35 ± 0.14
				-617.4 ± 2.1	21.6 ± 0.3	16.98 ± 0.19	
				-528.4 ± 1.2	21.1 ± 0.3	14.25 ± 0.05	
ngc985a	0[bc]			-879.4 ± 19.5	70.6 ± 16.8	14.43 ± 0.15	7.31 ± 0.36
				-727.9 ± 7.4	53.7 ± 3.6	15.85 ± 0.23	
				-552.4 ± 4.2	59.6 ± 2.5	18.40 ± 0.31	
				-517.5 ± 6.6	28.8 ± 3.9	14.88 ± 0.21	
				-311.0 ± 6.0	72.4 ± 2.6	17.21 ± 0.16	
				113.0 ± 0.6	11.1 ± 0.6	17.72 ± 0.14	
ngc985b	0[bc]			-921.9 ± 16.5	95.8 ± 11.9	13.11 ± 0.11	~ 0.00
				-824.3 ± 3.6	50.8 ± 9.7	13.11 ± 0.13	
				-659.3 ± 1.3	92.2 ± 1.6	14.03 ± 0.06	
				-514.4 ± 1.4	70.0 ± 1.6	14.07 ± 0.08	
				-409.8 ± 1.0	57.2 ± 1.1	14.00 ± 0.07	
				-272.4 ± 1.8	69.0 ± 2.9	13.98 ± 0.07	
				-180.9 ± 3.1	46.0 ± 2.9	13.32 ± 0.08	
				110.2 ± 0.5	27.5 ± 0.7	13.84 ± 0.13	
				~ 115.1	~ 39.5	~ 11.23	

Table 4.9 (cont'd)

Target[a]	Sys.	Velocity (km s^{-1})	log N (Int.) (log N [cm^{-2}])	Vel. (km s^{-1})	b (km s^{-1})	log $N_{\rm max}$ (log N [cm^{-2}])	a
pg0804a	1[c]			557.3 ± 0.8	15.8 ± 0.7	13.88 ± 0.07	0.24 ± 0.11
				602.4 ± 1.5	17.3 ± 2.9	14.42 ± 0.29	
				613.6 ± 7.9	24.1 ± 3.6	13.96 ± 0.36	
pg0838a	1[d]	335, 576	~ 14.23	400.7 ± 1.8	31.4 ± 3.1	13.69 ± 0.72	~ 2.04
				508.8 ± 3.6	45.8 ± 5.6	13.56 ± 0.66	
pg0844a	0[cd]			-1471.0 ± 9.4	146.4 ± 21.6	13.68 ± 2.71	~ 0.79
pg0844a	1[cd]			-1180.0 ± 1.0	50.9 ± 2.3	13.95 ± 0.26	~ 0.40
pg0844a	2[c]			-142.5 ± 5.4	20.2 ± 12.6	12.34 ± 0.12	~ 0.00
				73.6 ± 0.3	39.9 ± 0.8	15.55 ± 0.06	
				305.9 ± 5.0	36.6 ± 6.6	12.74 ± 0.06	
pg1011a	0[cd]			-1033.5 ± 4.5	11.2 ± 8.8	15.43 ± 3.87	~ 45.16
				-861.9 ± 6.8	22.9 ± 14.8	14.90 ± 2.54	
				-751.6 ± 3.1	19.1 ± 17.4	16.39 ± 5.68	
pg1011a	3[cd]			71.6 ± 2.7	17.0 ± 11.2	15.76 ± 3.40	~ 25.01
pg1126a	0[c]			-4970.6 ± 10.8	144.6 ± 7.7	14.19 ± 0.04	~ 0.00
				-4744.1 ± 8.6	128.6 ± 12.0	14.22 ± 0.04	
				-4493.5 ± 4.9	77.5 ± 6.5	13.80 ± 0.03	
pg1126a	1[c]			-3420.6 ± 2.4	~ 2.0	19.38 ± 0.06	3.38 ± 0.22
				-3251.6 ± 2.5	19.7 ± 2.1	15.33 ± 0.16	
pg1126a	2[c]			-2771.9 ± 28.5	119.8 ± 4.5	14.73 ± 0.36	~ 0.10
				-2682.0 ± 41.0	132.5 ± 6.3	14.54 ± 0.31	
				-2346.0 ± 1.8	53.4 ± 2.2	14.18 ± 0.07	
				-2238.4 ± 3.7	60.2 ± 3.5	13.92 ± 0.06	
pg1126a	3[c]			-1761.1 ± 0.8	48.5 ± 2.0	14.78 ± 0.09	0.85 ± 0.14
				-1640.0 ± 6.0	32.7 ± 7.8	13.17 ± 0.09	
				-1483.3 ± 1.1	81.5 ± 2.6	14.51 ± 0.04	
pg1126a	4[c]			-985.7 ± 0.5	22.8 ± 1.7	15.21 ± 0.25	1.46 ± 0.28
pg1126a	5[c]			-673.5 ± 4.6	39.9 ± 3.6	13.83 ± 0.11	1.13 ± 0.17
				-659.2 ± 0.7	17.7 ± 1.3	14.57 ± 0.18	
				-543.3 ± 7.3	~ 29.5	12.92 ± 0.09	
				-443.9 ± 0.7	30.3 ± 2.0	14.99 ± 0.15	
pg1126b	0[c]			-4936.6 ± 20.1	48.2 ± 13.6	16.49 ± 0.29	12.75 ± 0.90
				-4745.9 ± 10.1	29.1 ± 7.4	~ 20.00	
				-4476.9 ± 4.8	42.1 ± 6.1	16.00 ± 0.26	
pg1126b	1[c]			-3488.4 ± 34.8	113.2 ± 24.6	14.10 ± 0.18	~ 0.00
				~ -3401.1	~ 2.2	~ 9.00	
				-3283.7 ± 3.4	~ 15.3	15.17 ± 6.18	
				-3203.7 ± 11.2	~ 6.5	14.57 ± 12.54	
pg1126b	2[c]			-2819.7 ± 7.2	75.9 ± 7.0	14.63 ± 0.04	~ 0.00
				-2664.4 ± 7.7	73.6 ± 6.7	14.62 ± 0.04	
				-2505.7 ± 3.7	~ 6.0	13.77 ± 4.85	
				-2346.4 ± 2.7	22.4 ± 12.9	15.29 ± 1.97	
				-2226.3 ± 3.6	34.9 ± 5.5	13.97 ± 0.05	

Table 4.9 (cont'd)

Target[a]	Sys.	Velocity (km s^{-1})	log N (Int.) (log N [cm^{-2}])	Vel. (km s^{-1})	b (km s^{-1})	log $N_{\rm max}$ (log N [cm^{-2}])	a
pg1126b	3[c]			-1759.1 ± 0.8	50.3 ± 2.1	14.35 ± 0.05	0.18 ± 0.11
				-1638.7 ± 8.6	35.1 ± 13.3	12.88 ± 0.16	
				-1486.8 ± 1.2	86.5 ± 1.5	14.18 ± 0.03	
pg1126b	4[c]			-984.8 ± 0.3	18.6 ± 2.2	16.02 ± 0.60	2.08 ± 0.55
pg1126b	5[c]			-662.6 ± 1.7	28.3 ± 2.3	14.70 ± 0.16	3.91 ± 0.13
				-655.2 ± 0.7	10.0 ± 0.6	17.28 ± 0.20	
				-449.3 ± 2.1	16.4 ± 0.8	17.82 ± 0.07	
				-412.1 ± 4.2	18.1 ± 6.0	14.13 ± 0.50	
pg1126c	0[c]			-4973.0 ± 5.4	~ 15.6	14.28 ± 3.81	~ 0.05
				-4783.1 ± 11.5	131.3 ± 49.6	14.28 ± 0.78	
				-4500.6 ± 14.3	73.9 ± 19.2	13.80 ± 0.75	
pg1126c	1[c]			-3520.9 ± 278.8	~ 150.0	14.12 ± 2.12	~ 0.00
				~ -3424.5	~ 137.3	~ 9.04	
pg1126c	2[c]			-2753.8 ± 1.7	115.5 ± 8.0	15.44 ± 0.14	0.55 ± 0.08
				-2514.5 ± 7.7	~ 3.5	15.35 ± 12.14	
				-2358.9 ± 2.9	~ 18.3	16.44 ± 6.36	
				-2239.7 ± 4.3	36.3 ± 6.3	14.25 ± 0.06	
pg1126c	3[c]			-1770.3 ± 1.4	53.3 ± 3.5	14.41 ± 0.11	0.27 ± 0.20
				-1651.0 ± 11.9	35.5 ± 14.1	12.90 ± 0.17	
				-1494.9 ± 1.5	87.1 ± 2.0	14.25 ± 0.06	
pg1126c	4[c]			-992.3 ± 0.5	28.8 ± 1.1	14.38 ± 0.08	0.28 ± 0.11
pg1126c	5[c]			-666.3 ± 0.4	25.1 ± 0.9	14.02 ± 0.06	~ 0.00
				-453.2 ± 0.4	36.7 ± 1.0	14.25 ± 0.07	
pg1126d	0[c]			-4901.8 ± 23.8	94.0 ± 19.2	14.59 ± 0.31	2.17 ± 1.32
				-4734.4 ± 10.4	70.0 ± 17.9	14.82 ± 0.37	
				-4507.2 ± 7.9	92.7 ± 9.0	14.34 ± 0.23	
				-4245.9 ± 7.4	22.4 ± 12.5	13.38 ± 0.21	
pg1126d	1[bc]			-3716.3 ± 6.1	12.6 ± 8.6	13.00 ± 0.13	~ 0.00
				-3492.7 ± 7.1	102.8 ± 9.8	14.06 ± 0.05	
				-3244.3 ± 2.5	15.6 ± 8.9	14.32 ± 1.10	
pg1126d	2[c]			-2756.1 ± 7.3	91.5 ± 8.5	15.26 ± 0.23	1.10 ± 0.18
				~ -2716.9	150.0 ± 24.7	15.00 ± 0.20	
				-2342.9 ± 2.9	45.3 ± 3.7	14.63 ± 0.09	
				-2226.6 ± 3.0	37.6 ± 3.9	14.29 ± 0.06	
pg1126d	3[c]			-1768.8 ± 4.5	26.5 ± 7.2	15.87 ± 1.33	1.98 ± 1.28
				-1727.1 ± 55.8	57.1 ± 34.2	14.20 ± 0.72	
				-1491.3 ± 1.6	67.1 ± 8.6	14.73 ± 0.35	
pg1126d	4[c]			-989.5 ± 0.4	15.8 ± 2.3	16.59 ± 0.93	2.43 ± 0.64
pg1126d	5[c]			-664.2 ± 1.3	34.7 ± 3.4	14.21 ± 0.09	1.16 ± 0.12
				-660.7 ± 1.3	13.5 ± 2.0	14.71 ± 0.24	
				-550.0 ± 8.8	~ 3.0	12.68 ± 3.35	
				-448.9 ± 0.4	30.6 ± 1.3	15.08 ± 0.10	
pg1229a	0[cd]			-660.0 ± 1.9	16.2 ± 7.6	14.74 ± 1.76	~ 8.92

Table 4.9 (cont'd)

Target[a]	Sys.	Velocity (km s^{-1})	log N (Int.) (log N [cm^{-2}])	Vel. (km s^{-1})	b (km s^{-1})	log $N_{\rm max}$ (log N [cm^{-2}])	a
pg1351a	0[bc]			-2088.7 ± 21.8	120.1 ± 14.9	13.68 ± 0.11	0.70 ± 0.14
				-1949.9 ± 7.8	87.4 ± 11.4	14.12 ± 0.05	
				-1778.0 ± 9.3	90.5 ± 8.3	14.50 ± 0.07	
				-1624.5 ± 10.0	77.5 ± 5.6	14.35 ± 0.08	
				-1468.6 ± 6.8	70.1 ± 13.9	13.84 ± 0.06	
				-1283.4 ± 3.7	103.8 ± 5.0	14.47 ± 0.05	
				-999.5 ± 13.0	123.0 ± 4.4	14.95 ± 0.12	
				-812.5 ± 22.4	113.2 ± 8.2	14.63 ± 0.07	
				-653.6 ± 34.4	137.9 ± 12.2	14.09 ± 0.14	
pg1351a	1[cd]			79.1 ± 4.1	26.4 ± 6.8	13.00 ± 7.01	~ 0.08
pg1411a	1[cd]			-66.8 ± 0.8	22.7 ± 5.7	15.32 ± 0.81	0.16 ± 0.06
				~ 4.3	85.9 ± 4.5	14.04 ± 0.05	
				67.7 ± 0.7	29.0 ± 2.1	14.45 ± 0.07	
pg1411b	1[cd]			-51.8 ± 0.4	32.0 ± 1.3	14.70 ± 0.07	~ 0.00
				71.4 ± 0.4	34.6 ± 0.8	14.53 ± 0.02	
pg1411c	1[cd]			-63.8 ± 0.8	20.4 ± 3.1	16.00 ± 0.67	~ 0.00
				41.1 ± 10.1	55.1 ± 5.4	13.90 ± 0.10	
				67.8 ± 1.0	22.9 ± 4.0	15.05 ± 0.46	
pg1435a	0[d]	$-801, -561$	~ 13.61	-669.3 ± 3.1	62.6 ± 6.4	14.18 ± 0.48	~ 3.04
pg1448a	1[c]			-298.9 ± 3.3	43.9 ± 2.5	14.82 ± 0.09	0.49 ± 0.05
				-188.4 ± 7.6	83.2 ± 6.5	15.00 ± 0.08	
				-14.4 ± 3.5	27.6 ± 4.0	14.02 ± 0.06	
				125.2 ± 1.3	55.5 ± 3.3	15.46 ± 0.13	
pg1626a	0[d]	$-543, -124$	~ 15.04	-439.0 ± 0.3	30.4 ± 0.5	14.39 ± 0.02	0.26 ± 0.03
				-276.2 ± 3.5	27.6 ± 4.1	13.85 ± 0.11	
				-252.8 ± 3.6	68.4 ± 6.8	13.89 ± 0.14	
				-224.1 ± 1.0	22.6 ± 0.6	14.24 ± 0.04	
q0045b	0	$9,445$	~ 15.02	298.3 ± 1.8	17.4 ± 0.9	14.54 ± 0.06	0.34 ± 0.05
				326.4 ± 4.7	19.5 ± 1.6	13.99 ± 0.16	
q0045c	0	$239, 436$	~ 14.84	314.1 ± 0.5	25.0 ± 0.6	14.84 ± 0.05	0.90 ± 0.07
				400.0 ± 4.1	24.7 ± 10.8	13.10 ± 0.08	
q1230a	0[bc]			-3555.5 ± 1.0	34.6 ± 2.4	13.45 ± 0.04	~ 0.00
				-3465.0 ± 2.0	85.4 ± 1.4	14.11 ± 0.01	
				-3293.9 ± 5.0	88.2 ± 5.4	13.52 ± 0.02	
				-3164.1 ± 2.2	58.8 ± 2.8	13.52 ± 0.02	
				-3007.8 ± 10.4	94.3 ± 10.8	12.96 ± 0.06	
				-2759.3 ± 3.9	28.5 ± 6.8	12.59 ± 0.07	
				-2667.3 ± 7.1	63.7 ± 9.0	12.91 ± 0.04	
				-2421.0 ± 0.7	27.7 ± 1.9	13.49 ± 0.01	
				-2410.0 ± 2.2	109.3 ± 3.1	13.78 ± 0.01	
				-2191.1 ± 15.1	79.8 ± 20.9	12.59 ± 0.08	
q1230a	1[cd]			-587.2 ± 8.0	13.7 ± 8.1	13.12 ± 5.19	~ 1.39
				-556.9 ± 10.6	24.9 ± 8.8	12.85 ± 4.84	

Table 4.9 (cont'd)

Target[a]	Sys.	Velocity (km s^{-1})	log N (Int.) (log N [cm^{-2}])	Vel. (km s^{-1})	b (km s^{-1})	log $N_{\rm max}$ (log N [cm^{-2}])	a
q1230a	2[c]			-367.2 ± 15.5	26.4 ± 6.8	14.76 ± 0.28	12.36 ± 0.71
				-350.2 ± 19.4	101.4 ± 11.0	14.81 ± 0.15	
				-330.4 ± 1.4	11.1 ± 1.8	15.81 ± 0.99	
				-228.1 ± 13.5	59.3 ± 16.1	14.14 ± 0.33	
				-140.3 ± 0.6	10.6 ± 0.5	17.71 ± 0.50	
				-111.9 ± 14.5	42.8 ± 10.8	14.28 ± 0.39	
rbs144a	0[cd]			-774.6 ± 5.2	19.1 ± 14.6	14.47 ± 2.11	~ 19.35
				-663.1 ± 4.3	19.0 ± 14.3	14.62 ± 2.53	
rbs144a	1[cd]			-448.3 ± 3.1	22.5 ± 7.7	13.85 ± 1.18	~ 5.47
				-353.7 ± 2.9	14.6 ± 7.7	13.70 ± 1.23	
				-239.8 ± 4.4	29.7 ± 7.4	13.75 ± 0.95	
rbs144a	2[cd]			-18.0 ± 1.6	9.3 ± 1.2	18.14 ± 0.23	33.45 ± 3.38
rbs1483a	0[cd]			-57.8 ± 3.3	15.7 ± 6.7	14.55 ± 1.87	~ 3.31
				-31.0 ± 17.1	21.7 ± 4.5	14.18 ± 1.79	
rbs1503a	0[cd]			8.4 ± 0.6	20.2 ± 0.5	13.54 ± 0.02	~ 0.00
rbs1763a	0[c]			-213.9 ± 0.3	20.3 ± 0.8	16.05 ± 0.20	1.09 ± 0.08
rbs2023a	0[c]			-829.6 ± 4.9	33.9 ± 8.0	13.45 ± 0.11	1.53 ± 0.57
				-747.6 ± 1.6	13.6 ± 1.9	14.34 ± 0.28	
				-690.7 ± 2.1	25.3 ± 4.8	14.28 ± 0.20	
				-602.8 ± 3.2	23.1 ± 5.0	15.75 ± 0.87	
				-534.5 ± 15.2	36.0 ± 10.5	14.11 ± 0.25	
rbs2023a	1[c]			-206.9 ± 0.7	18.2 ± 2.5	14.96 ± 0.42	1.14 ± 0.42
rbs2055a	0[c]			-1343.0 ± 1.2	8.4 ± 2.4	13.82 ± 0.08	4.47 ± 0.40
				-1260.9 ± 0.3	5.9 ± 0.5	17.04 ± 0.20	
rbs2055a	1[c]			-676.4 ± 1.1	32.4 ± 5.8	14.41 ± 0.59	7.61 ± 6.36
rbs390a	0[c]			-283.7 ± 1.3	28.7 ± 3.6	14.23 ± 0.33	1.09 ± 0.98
rbs390a	1[c]			-96.9 ± 35.7	26.0 ± 10.5	14.89 ± 1.84	9.44 ± 9.23
				-63.5 ± 2.0	12.2 ± 4.2	16.62 ± 2.40	
rbs542a	0[cd]			-628.7 ± 0.7	4.3 ± 1.1	13.14 ± 0.16	4.16 ± 1.09
				-571.4 ± 0.4	8.0 ± 1.5	13.66 ± 0.15	
				-528.1 ± 6.5	31.8 ± 3.2	13.66 ± 0.15	
				-477.9 ± 2.3	27.7 ± 2.5	14.15 ± 0.15	
rbs542a	1[c]			-306.7 ± 7.4	24.9 ± 4.8	12.91 ± 0.20	0.46 ± 0.07
				-262.5 ± 2.4	23.3 ± 0.9	14.37 ± 0.09	
				-222.4 ± 5.0	17.1 ± 3.6	14.32 ± 0.29	
				-195.1 ± 16.8	24.7 ± 3.8	14.22 ± 0.82	
				-166.3 ± 34.0	24.9 ± 5.1	14.19 ± 0.53	
				-130.3 ± 6.5	20.1 ± 1.5	14.12 ± 0.29	
				-68.4 ± 0.9	24.9 ± 4.0	14.15 ± 0.05	
				-25.7 ± 2.0	24.5 ± 3.0	13.99 ± 0.09	
				~ -12.2	38.5 ± 4.4	13.14 ± 0.64	
				-6.3 ± 1.0	~ 2.0	12.91 ± 1.96	
rbs563a	2[cd]			-268.9 ± 3.2	~ 2.0	12.46 ± 10.88	~ 1.09

Table 4.9 (cont'd)

Target[a]	Sys.	Velocity (km s^{-1})	log N (Int.) (log N [cm^{-2}])	Vel. (km s^{-1})	b (km s^{-1})	log $N_{\rm max}$ (log N [cm^{-2}])	a
				-235.3 ± 2.2	~ 2.0	~ 13.04	
rbs563a	3[cd]			-135.0 ± 4.6	~ 22.5	14.23 ± 3.35	~ 16.12
rbs799a	0	$-1590, -1282$	~ 15.21	-1438.9 ± 2.3	26.3 ± 0.3	15.22 ± 0.09	7.47 ± 0.72
				-1375.2 ± 7.8	~ 26.0	13.68 ± 0.12	
rxj0053a	0	$94, 353$		189.0 ± 1.8	38.2 ± 0.7	13.82 ± 0.04	2.13 ± 0.13
				259.3 ± 0.6	20.7 ± 0.2	15.55 ± 0.07	
rxj0503a	0[cd]			-561.0 ± 3.4	41.3 ± 4.2	13.18 ± 0.04	~ 0.00
rxj1503a	0	$-1920, -1462$	~ 16.46	-1851.1 ± 4.2	35.1 ± 1.4	13.43 ± 0.06	~ 0.00
				-1749.7 ± 2.2	23.6 ± 0.4	17.54 ± 0.16	
				-1650.5 ± 6.8	18.5 ± 1.0	16.35 ± 0.60	
				-1584.2 ± 2.6	27.9 ± 0.5	14.41 ± 0.09	
				-1511.0 ± 7.9	21.9 ± 9.1	12.69 ± 0.10	
rxj1503a	1	$-1223, -1038$	~ 14.49	-1134.0 ± 2.1	26.4 ± 0.8	14.98 ± 0.11	5.69 ± 0.65
rxj1503a	2[d]	$-673, -473$	~ 14.78	-575.9 ± 2.8	22.8 ± 0.4	17.14 ± 0.14	41.65 ± 3.71
rxj1503a	3[cd]			-176.9 ± 1.7	19.4 ± 1.5	13.25 ± 0.03	~ 0.00
				-39.7 ± 0.5	23.1 ± 1.9	15.12 ± 0.23	
s091728b	0[cd]			-230.7 ± 0.9	28.8 ± 0.7	13.77 ± 0.01	~ 0.00
s091728b	1[cd]			-36.8 ± 4.6	26.1 ± 2.9	13.50 ± 0.13	0.16 ± 0.03
				75.4 ± 2.0	58.7 ± 3.4	14.96 ± 0.06	
s121930a	0[cd]			-578.2 ± 3.4	~ 2.0	17.98 ± 0.41	34.28 ± 9.97
s121930a	1[cd]			-225.0 ± 59.8	45.6 ± 33.6	13.69 ± 0.80	~ 3.23
				-168.9 ± 6.2	25.0 ± 8.0	14.33 ± 0.90	
s135712a	0	$-1004, -755$	~ 14.21	-917.1 ± 3.2	87.0 ± 2.7	14.61 ± 0.11	1.66 ± 0.42
sbs1624a	0[cd]			-1397.6 ± 5.1	58.0 ± 12.5	13.75 ± 2.57	~ 1.21
ton1187a	0[cd]			-489.0 ± 3.0	8.8 ± 3.2	15.64 ± 0.86	45.21 ± 12.41
				-328.7 ± 2.4	8.4 ± 3.1	17.03 ± 1.17	
				-196.2 ± 2.4	5.2 ± 3.4	17.38 ± 0.66	
				-39.4 ± 6.2	20.2 ± 6.1	15.37 ± 0.57	
				71.9 ± 9.1	~ 4.2	14.92 ± 5.15	
tons210a	0	$-1553, -1359$	~ 14.87	-1460.9 ± 8.4	78.7 ± 16.8	13.88 ± 0.94	~ 6.98
				-1442.5 ± 3.1	21.9 ± 8.0	13.74 ± 1.21	
uks0242a	0[cd]			-419.1 ± 9.4	~ 32.6	16.80 ± 9.64	~ 80.86
vpc0798a	0[cd]			-640.3 ± 25.9	99.2 ± 41.9	13.64 ± 1.05	~ 1.57
				-607.5 ± 3.8	32.5 ± 10.2	13.80 ± 1.35	
vpc0798a	1[cd]			-145.6 ± 4.3	53.9 ± 2.6	14.96 ± 0.08	~ 0.00
				-54.0 ± 8.7	37.8 ± 4.1	14.12 ± 0.13	

[a]Column (1) gives the short target name from Table 4.1 and Column (2) gives the absorption system ID number. Column (3) gives the velocity range in the restframe of the AGN overwhich the absorption was integrated, and Column (4) gives the column density as measured with the velocity dependent power-law inhomogeneous absorber model. Columns () give the component velocity in the AGN restframe, the Doppler b parameter, and column density for a fit assuming a power law inhomogeneous absorber. Values marked with a $\sim$ are poorly constrained or pinned at the limits of the fitting range, and thus should be treated as rough estimates only.

[b]This absorber is a BAL, as defined in the text, and all measurements should be treated as unreliable.

[c]Only one transition is available for this absorber, so the power-law inhomogeneous absorption fit is unreliable, as it is only weakly sensitive to line-profile shape.

[d]Absorption identified as associated based only on low velocity offset from AGN systemic redshift.

Table 4.10. Power-Law Inhomogeneous CIV Line Measurements

Target[a]	Sys.	Velocity (km s^{-1})	log N (Int.) (log N [cm^{-2}])	Vel. (km s^{-1})	b (km s^{-1})	log $N_{\rm max}$ (log N [cm^{-2}])	a
1h1613a	0[d]	$-661, -547$	~ 14.27	-609.9 ± 2.0	26.0 ± 0.6	13.78 ± 0.09	0.94 ± 0.50
hs0033a	0[b]	$-204, 725$	~ 16.38	134.1 ± 16.2	126.2 ± 9.3	14.85 ± 0.10	0.90 ± 0.17
				244.5 ± 7.4	62.8 ± 8.4	14.83 ± 0.13	
				369.8 ± 15.9	98.6 ± 13.3	14.96 ± 0.11	
				495.9 ± 2.3	33.6 ± 3.6	14.77 ± 0.09	
				618.5 ± 13.6	83.8 ± 17.4	14.18 ± 0.09	
i22456a	0	$-1724, -1634$	14.44 ± 0.29	-1674.1 ± 0.6	22.1 ± 0.2	13.93 ± 0.05	0.37 ± 0.16
i22456a	1	$-1006, -82$	~ 16.36	-924.5 ± 1.6	22.4 ± 2.5	14.04 ± 0.03	3.01 ± 0.06
				-731.8 ± 0.5	10.3 ± 0.3	18.54 ± 0.17	
				~ -689.0	~ 84.1	~ 11.96	
				-650.3 ± 0.7	~ 2.0	16.15 ± 0.25	
				-566.6 ± 0.3	8.8 ± 0.2	18.35 ± 0.05	
				-437.7 ± 0.9	22.3 ± 0.7	14.42 ± 0.02	
				-245.4 ± 0.3	20.7 ± 0.3	18.48 ± 0.08	
				-149.7 ± 0.4	9.5 ± 0.6	15.17 ± 0.07	
kaz238a	0[b]	$-176, 152$	~ 15.97	-43.2 ± 8.2	88.8 ± 7.9	14.99 ± 0.07	~ 0.00
mr2251a	0	$-448, 48$	~ 14.77	-370.0 ± 1.5	26.2 ± 2.4	13.99 ± 0.12	3.25 ± 0.45
				-281.7 ± 16.4	83.4 ± 5.8	14.49 ± 0.12	
				-240.3 ± 1.6	33.1 ± 2.8	14.34 ± 0.10	
				-180.6 ± 7.2	71.7 ± 3.9	14.71 ± 0.06	
				-54.2 ± 3.4	43.4 ± 4.1	13.96 ± 0.07	
mrk1253a	0	$-236, 102$	~ 14.61	-199.4 ± 3.7	12.3 ± 5.6	13.18 ± 0.12	0.62 ± 0.13
				-133.0 ± 1.9	16.4 ± 1.9	13.66 ± 0.06	
				-1.6 ± 0.8	33.0 ± 1.4	14.75 ± 0.07	
mrk1392a	0	$-455, -247$	~ 14.89	-406.6 ± 2.1	~ 25.7	13.55 ± 0.04	0.99 ± 0.09
				-320.6 ± 0.5	26.5 ± 0.2	14.91 ± 0.04	
mrk1513a	0	$-1675, -1328$	~ 15.00	-1530.1 ± 1.0	33.9 ± 1.5	14.83 ± 0.07	2.17 ± 0.33
				-1501.6 ± 6.1	89.1 ± 6.1	14.39 ± 0.09	
mrk1513a	5	$-146, 166$	~ 14.15	-27.7 ± 3.3	35.7 ± 5.7	13.53 ± 2.06	~ 1.18
mrk279a	0	$-622, -71$	~ 15.64	-468.5 ± 0.8	44.8 ± 2.3	15.47 ± 0.11	2.24 ± 0.22
				-356.7 ± 1.2	33.7 ± 3.6	14.93 ± 0.09	
				-268.1 ± 1.2	40.0 ± 2.7	15.20 ± 0.10	
				-139.6 ± 0.9	32.3 ± 4.5	13.79 ± 0.11	
mrk509a	0[b]	$-454, 240$	15.69 ± 0.04	-402.9 ± 0.3	21.3 ± 0.5	13.97 ± 0.02	1.47 ± 0.08
				-325.1 ± 0.6	6.9 ± 0.7	14.72 ± 0.19	
				-312.6 ± 39.8	~ 13.0	12.89 ± 1.29	
				-304.1 ± 1.9	39.0 ± 1.4	14.52 ± 0.04	
				-301.4 ± 5.2	18.7 ± 2.4	14.03 ± 0.16	
				-242.4 ± 1.2	21.0 ± 0.9	14.01 ± 0.05	
				-62.7 ± 0.2	8.2 ± 0.4	14.32 ± 0.02	
				-47.9 ± 5.1	33.0 ± 0.8	13.90 ± 0.19	
				-20.9 ± 0.4	13.9 ± 0.5	15.08 ± 0.02	
				31.0 ± 0.4	18.6 ± 0.5	14.00 ± 0.02	

Table 4.10 (cont'd)

Target[a]	Sys.	Velocity (km s^{-1})	log N (Int.) (log N [cm^{-2}])	Vel. (km s^{-1})	b (km s^{-1})	log $N_{\rm max}$ (log N [cm^{-2}])	a
				86.5 ± 0.8	15.1 ± 0.8	13.60 ± 0.02	
				120.3 ± 0.4	12.9 ± 0.9	13.85 ± 0.02	
				179.3 ± 4.4	31.6 ± 3.1	13.44 ± 0.09	
				218.0 ± 2.8	15.4 ± 3.1	13.22 ± 0.11	
mrk509b	0[b]	$-439, 171$	~ 15.71	-395.8 ± 0.6	16.9 ± 0.7	13.81 ± 0.04	0.91 ± 0.16
				-317.4 ± 0.7	6.6 ± 1.5	14.43 ± 0.14	
				-305.6 ± 12.9	26.2 ± 4.0	14.10 ± 0.76	
				-289.9 ± 19.3	30.1 ± 6.7	14.17 ± 0.64	
				-239.0 ± 4.6	30.7 ± 3.5	13.89 ± 0.10	
				-55.2 ± 0.7	8.8 ± 0.8	14.10 ± 0.05	
				-15.3 ± 1.3	14.2 ± 2.2	14.49 ± 0.16	
				~ -10.0	29.0 ± 8.9	13.95 ± 0.46	
				42.4 ± 3.3	18.2 ± 2.8	13.76 ± 0.09	
				126.8 ± 0.8	23.1 ± 1.1	13.83 ± 0.04	
				250.4 ± 4.8	21.7 ± 6.2	13.12 ± 0.08	
mrk509c	0[b]	$-474, 169$	~ 15.75	-396.0 ± 1.3	25.4 ± 3.1	13.87 ± 0.03	1.36 ± 0.12
				-357.4 ± 3.2	2.3 ± 0.9	12.98 ± 0.21	
				-319.9 ± 1.1	6.1 ± 2.2	14.62 ± 0.20	
				-300.9 ± 3.7	25.8 ± 1.8	14.51 ± 0.18	
				-289.0 ± 10.8	27.0 ± 5.7	13.97 ± 0.51	
				-236.7 ± 3.8	29.4 ± 1.8	14.07 ± 0.06	
				-37.9 ± 1.9	25.6 ± 1.6	14.53 ± 0.05	
				-7.4 ± 0.6	10.9 ± 0.6	14.64 ± 0.09	
				36.6 ± 1.7	24.4 ± 1.9	13.88 ± 0.04	
				120.2 ± 4.2	25.1 ± 3.9	13.78 ± 0.11	
				139.0 ± 24.2	55.5 ± 18.5	13.56 ± 0.20	
mrk841a	2	$-713, -590$	~ 14.59	-686.0 ± 4.8	~ 24.9	13.55 ± 0.09	1.58 ± 0.47
				-619.7 ± 1.7	25.2 ± 0.4	14.28 ± 0.09	
mrk876a	0	$-3936, -3611$	~ 14.55	-3763.1 ± 5.4	88.0 ± 7.1	13.46 ± 0.03	~ 0.00
ngc985a	0[b]	$-723, 211$	~ 15.92	-659.5 ± 1.7	32.5 ± 2.5	14.41 ± 0.05	1.97 ± 0.18
				-503.0 ± 5.5	97.7 ± 5.9	14.99 ± 0.05	
				-387.3 ± 1.6	37.0 ± 2.4	14.64 ± 0.07	
				-246.3 ± 1.0	49.8 ± 1.8	14.94 ± 0.05	
				130.4 ± 1.3	17.3 ± 1.5	14.45 ± 0.06	
ngc985b	0[b]	$-852, 385$	~ 15.81	-679.4 ± 2.4	26.5 ± 2.9	13.77 ± 0.15	2.79 ± 1.29
				-520.3 ± 5.8	78.4 ± 7.0	14.12 ± 0.15	
				-391.3 ± 1.9	36.8 ± 3.1	14.25 ± 0.18	
				-267.8 ± 1.4	28.4 ± 1.7	14.08 ± 0.17	
				71.8 ± 10.3	54.0 ± 10.9	13.77 ± 0.14	
				130.4 ± 0.5	9.5 ± 1.3	14.98 ± 0.56	
				244.7 ± 10.4	101.6 ± 12.8	13.94 ± 0.14	
pg0804a	1	$497, 697$	14.74 ± 0.34	556.1 ± 0.8	12.2 ± 1.1	13.97 ± 0.10	3.53 ± 0.71
				598.1 ± 1.1	8.2 ± 0.7	14.76 ± 0.67	

Table 4.10 (cont'd)

Target[a]	Sys.	Velocity (km s^{-1})	log N (Int.) (log N [cm^{-2}])	Vel. (km s^{-1})	b (km s^{-1})	log $N_{\rm max}$ (log N [cm^{-2}])	a
				611.0 ± 6.5	13.8 ± 2.1	14.63 ± 0.37	
pg1448a	1	$-427, 316$	~ 16.33	-268.8 ± 3.6	16.7 ± 1.6	19.12 ± 0.15	4.51 ± 0.17
				-151.1 ± 5.0	34.7 ± 1.9	19.70 ± 0.11	
				126.7 ± 2.9	10.0 ± 1.2	18.77 ± 0.13	
				171.1 ± 12.5	17.9 ± 10.1	14.61 ± 0.54	
q0045a	0	$210, 408$	~ 15.18	320.1 ± 0.8	15.5 ± 0.7	14.91 ± 0.14	1.48 ± 0.24
				334.2 ± 4.6	36.8 ± 3.9	14.09 ± 0.13	
q1230a	0[b]	$-3602, -2061$	~ 15.77	-3556.7 ± 1.6	21.4 ± 2.0	14.21 ± 0.09	2.87 ± 0.30
				-3465.5 ± 2.4	20.4 ± 2.8	14.01 ± 0.13	
				-3464.8 ± 2.9	73.1 ± 2.9	15.12 ± 0.06	
				-3230.3 ± 9.4	~ 150.0	14.54 ± 0.04	
				-2694.5 ± 12.2	100.2 ± 15.9	13.92 ± 0.06	
				-2413.3 ± 1.5	56.4 ± 1.8	14.69 ± 0.05	
				-1898.6 ± 24.1	149.3 ± 37.5	13.86 ± 0.09	
q1230a	2	$-417, -102$	~ 14.36	-325.5 ± 0.7	9.9 ± 1.1	13.75 ± 0.16	1.35 ± 0.69
				-320.6 ± 3.5	65.0 ± 4.1	14.22 ± 0.12	
				-236.3 ± 0.7	15.3 ± 0.9	13.90 ± 0.15	
				-125.3 ± 29.1	145.8 ± 14.4	14.10 ± 0.12	
rbs1763a	0	$-283, -124$	~ 14.50	-201.3 ± 0.3	22.8 ± 0.1	14.63 ± 0.03	0.65 ± 0.06
rbs542a	1	$-335, 23$	~ 15.37	-213.8 ± 0.2	26.5 ± 0.3	15.49 ± 0.03	1.31 ± 0.03
				-145.9 ± 0.2	12.3 ± 0.3	14.46 ± 0.02	
				-128.6 ± 12.9	149.3 ± 7.7	13.99 ± 0.08	
				-122.6 ± 14.5	44.2 ± 8.0	13.28 ± 0.17	
				-32.0 ± 0.3	22.9 ± 0.6	14.27 ± 0.02	
rxj0053a	0	$150, 321$	~ 14.89	254.5 ± 2.6	24.4 ± 1.1	14.31 ± 0.27	~ 0.53

[a]Column (1) gives the short target name from Table 4.1 and Column (2) gives the absorption system ID number. Column (3) gives the velocity range in the restframe of the AGN overwhich the absorption was integrated, and Column (4) gives the column density as measured with the velocity dependent power-law inhomogeneous absorber model. Columns () give the component velocity in the AGN restframe, the Doppler b parameter, and column density for a fit assuming a power law inhomogeneous absorber. Values marked with a $\sim$ are poorly constrained or pinned at the limits of the fitting range, and thus should be treated as rough estimates only.

[b]This absorber is a BAL, as defined in the text, and all measurements should be treated as unreliable.

[c]Only one transition is available for this absorber, so the power-law inhomogeneous absorption fit is unreliable, as it is only weakly sensitive to line-profile shape.

[d]Absorption identified as associated based only on low velocity offset from AGN systemic redshift.

Table 4.11. Power-Law Inhomogeneous OVI Line Measurements

Target[a]	Sys.	Velocity (km s^{-1})	log N (Int.) (log N [cm^{-2}])	Vel. (km s^{-1})	b (km s^{-1})	log $N_{\rm max}$ (log N [cm^{-2}])	a
he2258a	0	$-3108, -2799$	~ 14.97	-3031.2 ± 3.1	25.4 ± 0.7	14.19 ± 0.07	0.45 ± 0.23
				-2969.0 ± 4.2	23.0 ± 0.5	13.95 ± 0.07	
				-2887.2 ± 4.4	27.8 ± 0.9	13.91 ± 0.07	
he2258a	1[d]	$-1929, -1769$	~ 15.23	-1851.2 ± 1.6	~ 2.2	18.59 ± 0.12	5.90 ± 0.90
he2258a	2	$-772, -349$	~ 16.54	~ -756.7	~ 17.3	~ 9.95	0.07 ± 0.03
				-665.5 ± 0.7	51.3 ± 0.4	15.48 ± 0.03	
				-494.3 ± 0.6	44.9 ± 0.3	15.65 ± 0.03	
he2332a	2	$-103, 19$	~ 15.07	-32.9 ± 0.9	25.8 ± 0.6	14.01 ± 0.21	~ 0.00
hs0033a	0[b]	$-92, 666$	~ 16.94	140.8 ± 3.7	77.1 ± 2.1	17.44 ± 0.21	3.45 ± 0.30
				~ 238.0	~ 14.0	~ 10.92	
				274.3 ± 6.2	96.0 ± 2.5	18.46 ± 0.30	
				502.2 ± 8.1	83.2 ± 1.6	16.96 ± 0.20	
i22456a	0[bc]			-1694.9 ± 1.5	11.9 ± 11.7	16.75 ± 3.94	~ 17.85
mrk876a	0	$-3865, -3398$	~ 15.68	-3800.9 ± 1.0	24.6 ± 0.2	14.63 ± 0.03	1.35 ± 0.07
				-3752.7 ± 1.2	25.0 ± 0.5	14.56 ± 0.03	
				-3689.3 ± 2.4	24.0 ± 0.3	13.88 ± 0.03	
				-3515.2 ± 0.7	~ 24.4	14.62 ± 0.02	
				-3441.2 ± 4.0	~ 26.0	13.61 ± 0.04	
mrk877a	0	$-682, -475$	~ 14.62	-622.9 ± 1.3	31.4 ± 0.6	14.59 ± 0.02	~ 0.00
				-511.4 ± 1.8	21.8 ± 0.7	14.27 ± 0.05	
pg0804a	1	$524, 632$	~ 15.23	550.3 ± 1.9	24.5 ± 0.4	13.86 ± 0.04	0.38 ± 0.18
				601.0 ± 1.4	25.9 ± 0.5	14.09 ± 0.05	
q0045b	0	$221, 390$	15.80 ± 0.03	305.8 ± 0.3	30.0 ± 0.1	15.07 ± 0.01	~ 0.00
q0045c	0	$202, 396$	~ 15.82	312.4 ± 0.8	29.5 ± 0.3	15.49 ± 0.07	0.58 ± 0.10
q1230a	0	$-3695, -2111$	~ 16.56	-4025.5 ± 3.3	17.2 ± 5.3	17.00 ± 0.99	2.12 ± 0.10
				~ -3635.5	~ 63.6	~ 9.00	
				-3524.5 ± 2.9	56.6 ± 2.0	16.24 ± 0.06	
				-3350.2 ± 4.9	82.9 ± 4.2	15.85 ± 0.08	
				-3251.3 ± 19.2	189.0 ± 11.3	15.47 ± 0.12	
				-3138.8 ± 1.5	46.0 ± 1.2	15.87 ± 0.05	
				-2757.9 ± 5.0	79.8 ± 2.8	15.09 ± 0.07	
				-2538.1 ± 14.9	152.6 ± 5.6	15.79 ± 0.06	
				-2382.8 ± 1.7	88.4 ± 1.4	16.50 ± 0.06	
q1230a	2	$-436, -28$	15.79 ± 0.28	-451.2 ± 1.7	~ 24.3	13.27 ± 0.05	0.69 ± 0.02
				-374.0 ± 0.7	24.1 ± 0.2	15.06 ± 0.02	
				-325.4 ± 0.8	23.9 ± 0.2	15.60 ± 0.04	
				-245.0 ± 0.3	22.6 ± 0.1	15.40 ± 0.02	
				-136.3 ± 0.2	34.3 ± 0.1	15.49 ± 0.01	
rbs2023a	0[c]			-685.5 ± 22.5	153.6 ± 26.2	15.54 ± 0.99	~ 1.01
				-610.3 ± 11.0	~ 16.8	15.57 ± 4.88	
				-543.1 ± 46.8	~ 41.8	14.76 ± 0.84	
rbs542a	1	$-339, 6$	~ 16.70	-267.2 ± 0.5	25.6 ± 0.1	15.45 ± 0.03	2.57 ± 0.02
				-202.3 ± 0.3	25.4 ± 0.1	19.41 ± 0.02	

Table 4.11 (cont'd)

Target[a]	Sys.	Velocity (km s^{-1})	log N (Int.) (log N [cm^{-2}])	Vel. (km s^{-1})	b (km s^{-1})	log $N_{\rm max}$ (log N [cm^{-2}])	a
				-64.7 ± 0.2	20.7 ± 0.1	16.13 ± 0.02	
rbs799a	0	$-1584, -1309$	~ 15.56	~ -1669.5	~ 25.0	~ 14.00	10.72 ± 0.92
				-1431.2 ± 2.9	32.0 ± 0.6	16.29 ± 0.09	
rxj0053a	0	$106, 338$	~ 15.18	218.1 ± 1.7	92.1 ± 1.4	15.24 ± 0.08	3.98 ± 0.66
rxj1503a	0[c]			-1798.0 ± 50.3	77.8 ± 39.6	14.62 ± 0.52	~ 1.17
				-1717.2 ± 2.0	17.0 ± 14.6	15.98 ± 2.69	
s135712a	0[c]			-915.7 ± 2.4	64.5 ± 2.9	14.53 ± 0.02	~ 0.00

[a]Column (1) gives the short target name from Table 4.1 and Column (2) gives the absorption system ID number. Column (3) gives the velocity range in the restframe of the AGN overwhich the absorption was integrated, and Column (4) gives the column density as measured with the velocity dependent power-law inhomogeneous absorber model. Columns () give the component velocity in the AGN restframe, the Doppler b parameter, and column density for a fit assuming a power law inhomogeneous absorber. Values marked with a $\sim$ are poorly constrained or pinned at the limits of the fitting range, and thus should be treated as rough estimates only.

[b]This absorber is a BAL, as defined in the text, and all measurements should be treated as unreliable.

[c]Only one transition is available for this absorber, so the power-law inhomogeneous absorption fit is unreliable, as it is only weakly sensitive to line-profile shape.

[d]Absorption identified as associated based only on low velocity offset from AGN systemic redshift.

In general, the power-law inhomogeneous absorption measurements are more poorly constrained than the step function partial covering models. Although those models share the same number of parameters, the power-law models are, in a sense, more complex in that they can produce a larger range of different line profiles and absorption ratios, as both free parameters are unbounded. This can potentially make disentangling the relative merits of the models more complex than simply observing a species with more than two transitions, as was undertaken by Arav et al. (2008). It also has the effect of making many of our power-law measurements highly uncertain. For the remainder of this preliminary report with its limited sample, we focus primarily on the standard partial covering model. It is worth noting, however, that the 384 partial-covering component fits in our sample typically provide better fits to the data than power-law component fits to the same data points with the same number of components. The power-law models result in a lower χ^2 statistic only 19% of the time, and the two provide equally good fits 34% of the time (usually when the absorber is consistent with full coverage and the parameters are near $a = 0$ and $C = 1$). This suggests that the use of power-law covering models is not presently required by the data.

Table 4.12. Detection Frequencies by AGN Type

AGN Type	$\mathcal{N}_{\rm abs,HI}$	$\mathcal{N}_{\rm targ,HI}$	$\mathcal{N}_{\rm abs,CIV}$	$\mathcal{N}_{\rm targ,CIV}$	$\mathcal{N}_{\rm abs,OVI}$	$\mathcal{N}_{\rm targ,OVI}$
AGN	$2^{+2.6}_{-1.3}$	2	$1^{+2.3}_{-0.8}$	2	$1^{+2.3}_{-0.8}$	1
BLLac	$2^{+2.6}_{-1.3}$	4	$0^{+1.8}_{-0.0}$	2	$0^{+1.8}_{-0.0}$	1
NLSy1	$7^{+3.8}_{-2.6}$	8	$2^{+2.6}_{-1.3}$	2	$2^{+2.6}_{-1.3}$	3
Sy1	$20^{+5.5}_{-4.4}$	26	$5^{+3.4}_{-2.2}$	15	$7^{+3.8}_{-2.6}$	10
Sy1.0	$23^{+5.9}_{-4.8}$	23	$4^{+3.2}_{-1.9}$	10	$3^{+2.9}_{-1.6}$	13
Sy1.2	$6^{+3.6}_{-2.4}$	7	$0^{+1.8}_{-0.0}$	4	$0^{+1.8}_{-0.0}$	2
Sy1.5	$18^{+5.3}_{-4.2}$	18	$11^{+4.4}_{-3.3}$	15	$3^{+2.9}_{-1.6}$	4
Sy1.8	$1^{+2.3}_{-0.8}$	1	$1^{+2.3}_{-0.8}$	1	$0^{+0.0}_{-0.0}$	0
Sy2	$1^{+2.3}_{-0.8}$	1	$1^{+2.3}_{-0.8}$	1	$0^{+0.0}_{-0.0}$	0
All	$80^{+10.0}_{-8.9}$	90	$25^{+6.1}_{-5.0}$	52	$16^{+5.1}_{-4.0}$	34

4.4 Discussion

4.4.1 Detection Rates and the Global Covering Fraction

The final catalog contains 80, 25, and 16 candidate H I, C IV, and O VI absorbers, respectively. These detection totals are given for the full sample, as well as by AGN activity type, in Table 4.12, along with the asymmetric Poisson confidence limits (Gehrels, 1986). Normalizing these detection totals by the number of AGN sightlines with at least $\Delta v = 1500$ km s^{-1} of velocity coverage for the absorption transition in question, we can obtain the detection fractions, $F_{\rm ion}$: $0.89^{+0.11}_{-0.10}$ for H I, $0.48^{+0.12}_{-0.10}$ for C IV, and $0.47^{+0.15}_{-0.12}$ for O VI. These C IV and O VI detection rates are in line with previous measurements of associated absorber frequency. George et al. (2000), for example, find evidence for intrinsic H I absorption in $F_{\rm HI} = 15/24 = 0.63$ of their X-ray observations of radio-quiet quasars, although the rate drops to $F_{\rm HI} = 8/24 = 0.33$ if one only considers absorption detected at $> 90\%$ confidence. Laor & Brandt (2002) find $F_{\rm CIV} = 28/56 = 0.5$ in their FOS and *IUE* observations of soft-X-ray-weak quasars. Vestergaard (2003) studied C IV absorbers at $1.5 < z_{\rm abs} < 3.6$ and found $F_{\rm CIV} = 59/114 = 0.52$, while Ganguly et al. (2001a) find $F_{\rm CIV} = 15/59 = 0.25$ using early *HST* spectra with relatively low S/N. Misawa et al. (2007) find $F_{\rm CIV} = 0.24 - 0.32$ at $2 < z_{\rm AGN} < 4$. At the higher end, Culliton et al. (2012) find $F_{\rm CIV} = 49/73 = 0.67$ at $1.5 < z_{\rm AGN} < 5$, though their full methodology is not published. Finally, the Lyβ and O VI *FUSE* sample from Dunn et al. (2008) gives $F_{{\rm Ly}\beta,{\rm OVI}} = 35/72 = 0.49$.

Our H I detection rate appears, at first glance, to be unrealistically high. However, because

we included absorption candidates in our absorber list for which the only evidence of association is velocity offset, there are likely many contaminating IGM and CGM features in the H I sample. This effect is not likely to substantially affect absorbers identified through O VI or C IV, which are both rarer in the IGM and usually provide more conclusive evidence of association. Using the H I absorber frequency distribution from Danforth et al. (2016), we estimate that ~ 40 cosmologically intervening Lyα absorbers contaminate the sample, which brings the occurence rate, $F_{\rm HI} \sim 0.44$, more in line with the metal ions.

Using our occurence rates, we can calculate an approximate global covering fraction for associated absorbers. We assume that the partial covering model is a sufficient approximation to the physical behavior of the absorbing gas. The average measured covering factor of the absorbersis $\langle C_{\rm ion} \rangle$ multiplied by the occurence rate of the absorbers then gives the fraction of the background AGN light source (including both emission line regions and continuum regions) that the associated absorber covers averaged over all of the AGN sightlines in the sample. This quantity C_g was first introduced by Crenshaw et al. (1999):

$$C_g = F_{\rm ion} \langle C_{\rm ion} \rangle, \tag{4.12}$$

For our sample, $\langle C_{\rm CIV} \rangle = 0.89$ and $\langle C_{\rm OVI} \rangle = 0.89$, so $C_g = 0.42^{+0.10}_{-0.09}$ for C IV, and $C_g = 0.42^{+0.13}_{-0.11}$ for O VI. This quantity also implicitly assumes that the sightlines in the sample are sufficiently sampling different angluar lines of sight toward the AGNs. Its usefulness thus depends on an understanding of the selection effects that defined the AGN sample, which is not well-studied for this limited preliminary sample. It is nonetheless suggestive of a geometric distribution of absorbers that covers a substantial solid angle from the point of view of the AGN. Many AGN host associated absorbers that frequently cover most of the line of sight, rather than, for example, absorbers being found only in a very narrow or collimated solid angle range.

4.4.2 Trends with Luminosity

One of the most common suggestions for an acceleration mechanism of BAL and NAL outflows is some variant of radiative acceleration, most likely due to resonant line scattering. Radiation driving is an appealing model, both for its relative simplicity and the obvious existence of the energy source that powers it, in contrast to more exotic models that often require unobserved phenomena, such as a population of ultrarelativistic neutrons (Begelman et al., 1991). Models have shown that radiative acceleration can plausibly explain the extent of BAL outflows (Arav et al., 1994, 1995), but what observational support exists has been mostly limited to BALs (Weymann et al., 1991; Korista et al., 1993; Arav & Begelman, 1994; Vilkoviskij & Irwin, 2001; Srianand et al., 2002; North et al., 2006; Nestor et al., 2007; Cottis et al., 2010; Bowler et al., 2014).

It has long been predicted that if radiation pressure is driving the outflows probed by BALs or NALs, then their outflow velocities should be correlated with host AGN luminosities (e.g., Stocke et al., 1992). To test this idea within our sample, we calculate the monochromatic luminosity λL_λ at restframe 1350 Å for all of the objects in our sample. To do so, we correct the observed flux for Galactic extinction assuming a Fitzpatrick (1999) reddening law with values derived from the Schlafly & Finkbeiner (2011) recalibration of the Schlegel et al. (1998) dust maps. We follow Schlegel et al. (1998) and adopt 1σ uncertainties of 16% in the selective extinction, $E(B-V)$. We assume a mean value $R_V = 3.13$ for the ratio of total-to-selective extinction and adopt a 1σ uncertainty of 0.52, following the distribution of Galactic sightlines from Geminale & Popowski (2004). A simple Monte Carlo calculation is used to determine the uncertainty in the luminosities, accounting for uncertainties in the extinction correction, COS wavelength calibration, $z_{\rm AGN}$, and statistics of the data.

For each sightline with useable data at this rest wavelength, we plot these luminosities against the most-negative velocity detection in each sightline in Figure 4.4. Though low velocity absorbers persist at all AGN luminosities, the spread to higher blueshifted velocities increases with increasing luminosity (i.e., the envelope of the distribution moves to higher outflow velocities), perhaps

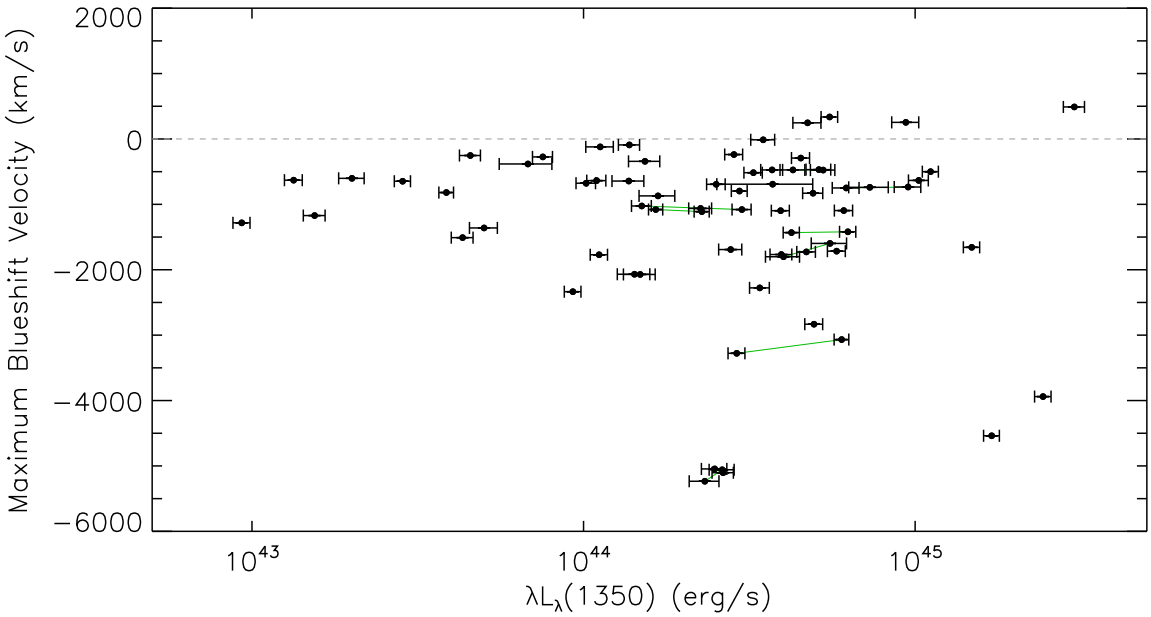

Figure 4.4 Plot of the most negative absorption velocity detected in each sightline versus the monochromatic luminosity λL_λ at 1350 Å in the AGN rest frame. Data points connected by green lines are multiple observational epochs of the same target.

suggesting a radiative effect. This trend is qualitatively consistent with the trends seen in the *FUSE*-only sample of Dunn et al. (2008) and the FOS and *IUE* observations of the soft-X-ray-weak quasar sample from Laor & Brandt (2002). However, it is worth noting that in most samples, including the COS archive, luminosity is highly correlated with redshift; the two cannot be statistically disentangled without a larger or less biased sample. Further searches for evidence of radiative acceleration will be possible in the larger, expanded form of this catalog, including a statistical search for component structures that exhibit "line-locking," in which absorption features tend to cluster at the spacing of multiplet or doublet features (e.g., Weymann et al., 1981).

Laor & Brandt (2002) also detected a highly significant trend between C IV EWs and luminosity (Spearman rank-order coefficient $\rho = -0.93$ with significance 1.1×10^{-4}) in their soft-X-ray-weak quasar sample. As found in the *FUSE*-only sample of Dunn et al. (2008), we also do not significantly detect this trend (Spearman rank-order coefficient $\rho = -0.32$ with significance 0.10). We plot this distribution in Figure 4.5. As both the *FUSE* and COS spectra typically have much higher S/N and resolving power than the IUE spectra used in Laor & Brandt (2002), it is possible

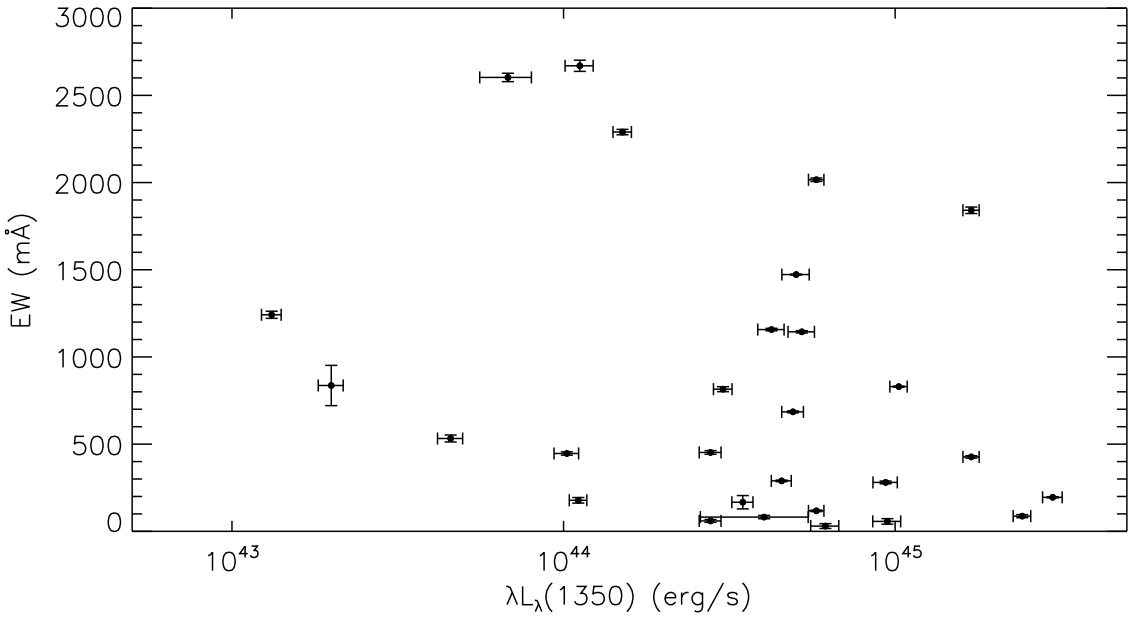

Figure 4.5 Plot of C IV EWs versus the monochromatic luminosity λL_λ at 1350 Å of the AGN in its rest frame. No significant correlation is found.

that a systematic effect was influencing that result.

4.4.3 Possible Strong Covering-Fraction Velocity Dependence in a Single Transition

Two absorbers, toward RBS542 and IRAS F22456-5125, show gradients in saturation of the troughs of Lyα in the normalized spectra that are not present in their other absorption lines (Figure 4.6). These trends could be explained by a strong velocity dependence of the the covering factor. This hypothesis is somewhat supported by their position on the steepest parts of the blue side of the Lyα AGN emission lines. As this velocity dependence correlates with the changing ratio of emission-line flux to accretion disk continuum flux, this dependence could occur if there is a differential covering of the broad-line region compared to the accretion disk by a portion of the absorbing material. However, with this data alone, we cannot rule out other explanations, such as a more complicated physical absorption structure from gas at a range of different velocities. However, even if gas dynamics are creating this effect, it may offer a means for disentangling the

relative importance of different driving mechanism. Shocked continuum-driven flows, for example, are predicted to form absorption profiles with a gradient in the opposite direction (Williams, 2000); these absorption systems are inconsistent with these models. In any case, the identification of more such absorbers may offer a route toward disentangling the underlying causes of velocity-dependent partial covering solutions.

4.5 Summary and Conculsions

In this chapter, we have presented preliminary results from a survey of the associated absorbers in the COS archive of medium-resolution spectra of AGN. This preliminary sample identifies absorption systems towards 76 AGNs in 93 observational epochs, representing all available COS data for AGN at redshifts $0.03 < z_{\rm AGN} < 0.16$, and all detectable C IV absorbers. Column densities derived through six methods common in the literature, EWs, and velocities are presented for all absorbers. Though firm conclusions should wait for the full sample of associated absorbers in the COS archive, we tentatively find:

- Associated absorbers occur in $\sim 50\%$ of AGN.
- The occurence rate combined with the average absorber covering fractions implies a global AGN covering fraction of associated absorbers $C_g \approx 0.42$.
- The maximum outflow velocity in a sightline hosting associated absorbers is correlated with the AGN's UV luminosity, perhaps suggesting a radiation-driven acceleration method, but luminosity is highly correlated with redshift in our sample.
- No significant correlation is seen between absorber EWs and AGN luminosity.
- Absorbers toward RBS542 and IRAS F22456-5125 may show strong velocity dependence in their partical covering, which may help constrain partial covering models in the future.
- Though many of our power-law inhomogeneous absorption model measurements are poorly constrained, there is weak evidence that the standard partial-covering model can better

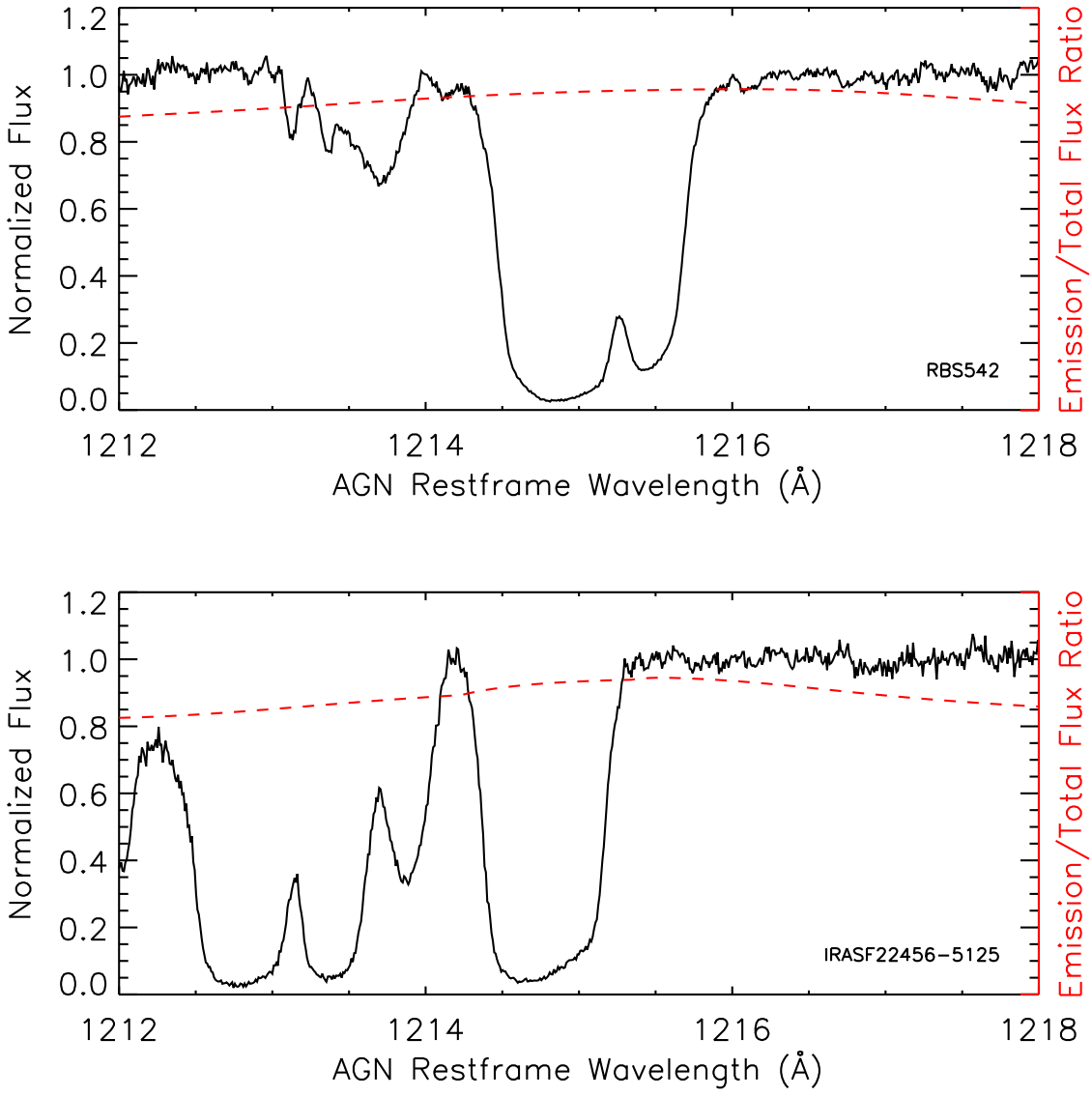

Figure 4.6 Lyα absorption toward RBS542 and IRAS F22456-5125. The black line is the normalized COS spectrum, and the red line is the ratio of emission-line flux to power-law continuum flux.

reproduce the data.

Until these results have been compared against photoionization modeling, it is not possible to constrain the quantities, such as kinetic luminosity $\dot{E}_k$, relevant to place these absorbers in direct context with feedback models. Dunn et al. (2010) compiled kinetic luminosities ranging from $10^{41} < \dot{E}_k < 10^{45.7}$, though most of these values were derived from BALs rather than the NALs that dominate our sample. The one target that has an absorber similar to the ones in the present sample is 3C 191 (Hamann et al., 2001), which has an estimated kinetic luminosity $\dot{E}_k \approx 10^{44}$ erg s^{-1}, or about $0.25 - 2.5\%$ of its bolometric luminosity (Perry & Dyson, 1990). However, kinetic luminosity is directly proportional to the assumed global covering fraction; our tentative estimate of the global covering fraction suggests a slightly higher value of $0.6 - 6\%$ the bolometric luminosity. Similarly, (Arav et al., 2013), who assume a covering fraction in agreement with our findings, find that the outflow in HE0238-1904 is roughly 1% that object's bolometric luminosity. As models of AGN feedback typically require $\sim 5\%$ or less of the bolometric luminosity of the AGN (Di Matteo et al., 2005; Hopkins et al., 2005a; Hopkins & Elvis, 2010), these findings and others (e.g., Crenshaw & Kraemer, 2012; Crenshaw et al., 2015) suggest that associated absorber outflows may be a significant contributor to AGN feedback, and that further, more detailed investigations into the energetics of these absorbers is warranted.

The full sample and subsequent followup work will extend these results, as discussed in Chapter 5.

Chapter 5

Summary and Future Work

5.1 Summary

In this thesis, I have explored several physical environments via the analysis of the UV spectra of AGNs. In particular, I have addressed:

- The metal abundance of the IGM by comparing observations of carbon, silicon, and oxygen to numerical photoionization models. Our basic findings are:
  - Using mass densities of adjacent ionization states of carbon and silicon from the Danforth et al. (2014, 2016) IGM surveys, we statistically calculate the mean mass abundance ratios of these species, C III/C IV= $0.70^{+0.43}_{-0.20}$ and Si III/Si IV= $0.67^{+0.35}_{-0.19}$. Combined with photoionization models, these values imply correction factors for the unseen ionization states and suggest an enhancement to Si/C abundance to approximately three times the solar ratios by mass.
  - We can express the total metals mass densities as a fractional contribution to closure density, $\Omega_{\rm Z} \equiv \rho_{\rm Z}/\rho_{\rm crit}$ where $\rho_{\rm crit} \equiv 3H_0^2/8\pi G = 9.205 \times 10^{-30} h_{70}^2$ g cm^{-3} = $(1.36 \times 10^{11}$ M$_\odot$ Mpc$^{-3})h_{70}^2$ and $H_0 = (70$ km s^{-1} Mpc$^{-1})h_{70}$. Expressed in this form, the photoionized gas accounts for a total metal abundance of $\Omega_{\rm Z} = (4.0 \pm 0.5) \times 10^{-6}$, while the more highly ionized gas traced by O VI accounts for $\Omega_{\rm Z} = (6.7 \pm 0.8) \times 10^{-6}$. Combined, this represents a mass density of $\rho_{\rm Z} = (1.45 \pm 0.92) \times 10^6$ M$_\odot$ Mpc^{-3} assuming $h_{70} = 1$, or $\sim 10 \pm 5\%$ of the expected cosmic heavy elements.

  - Our photoionization models are roughly consistent with a UVB with a unidirectional hydrogen ionizing flux of $\Phi_0 = 10^4$ cm^{-2} s^{-1}, a value higher than that recommended by the recent study of the UVB by Haardt & Madau (2012). This value is consistent with other values in the literature (Shull et al., 1999; Haardt & Madau, 2001; Kollmeier et al., 2014; Shull et al., 2015; Khaire & Srianand, 2015). However, all of the UVB SEDs investigated show some tension with the observational constraints, suggesting that more work is required if calculations of the UVB are to fully match observations.
  - The combination of observations and photoionization models requires an ionization parameter $\log U \approx -1.5 \pm 0.4$ and baryon overdensities $\Delta_b \approx 200 \pm 50$. At the mean redshift of the observations, $\langle z_{\rm abs} \rangle = 0.14$, the overdensity corresponds to a hydrogen density typical of extended halo gas, $n_{\rm H} \approx 10^{-4.25 \pm 0.10}$ cm^{-3}.

- The typical EUV spectrum of AGNs. Our basic findings are:
  - Compared to previous AGN composite spectra, $F_\nu \propto \nu^{-1.41 \pm 0.15}$ between 700 Å $< \lambda <$ 900 Å, the 450 Å $< \lambda <$ 770 Å region of AGN spectra exhibits a hardening spectral slope, $F_\nu \propto \nu^{-0.72 \pm 0.26}$. Similar hardening can be seen in the composites from Telfer et al. (2002) and Stevans et al. (2014). Though this hardening may represent curvature of the continuum slope, it could represent a failure of the power-law model to separate continuum from a pseudo-continuum of EUV emission-line flux.
  - The EUV spectral band contains a variety of prominent broad emission lines from ions of O, Ne, N, Mg, and other elements that are difficult to disentangle and identify. Possible identifications based upon `Cloudy` models were presented in Section 3.5.2 along with measurements of the strength of emission in different spectral regions. Improvements to photoionization codes and observations targeting AGNs with narrower emission lines are required to fully disentangle these features.
  - The He I 504 Å absorption edge predicted by some accretion disk models is not detected. Our composite spectra limit the typical He I optical depth just below the

edge to $\tau_{\rm HeI} < 0.047$ ($N_{\rm HeI} < 10^{15.8}$ cm^{-2}).

- A preliminary accounting of the associated absorbers seen in the COS archive of AGN spectra. We surveyed 76 AGNs (three BL Lac objects, one Type II AGN, and 72 Type I AGNs) in 93 total observational epochs and fit a total of 384 absorption complexes of H I, C IV, and O VI. Our basic findings are:
  - Associated absorbers occur in $\sim 50\%$ of Type I AGNs.
  - The occurence rate combined with the average absorber covering fractions implies a global AGN covering fraction of associated absorbers $C_g \approx 0.42$.
  - The maximum outflow velocity in a sightline hosting associated absorbers is correlated with the AGN's UV luminosity, perhaps suggesting a radiation-driven acceleration method. However, luminosity is highly correlated with redshift in our sample, so we cannot rule out an evolutionary effect. No significant correlation is seen between absorber EWs and AGN luminosity.
  - Absorbers toward RBS542 and IRAS F22456-5125 may show strong velocity dependence in their partial covering, which may help to constrain partial covering models in the future.
  - There is weak evidence that the standard partial-covering model can better reproduce the data than power-law distributed inhomogeous absorption models.

5.2 Future Work

In this section, to conclude this thesis, I sketch some future directions that the presented research could take.

5.2.1 IGM Absorption Lines

- **The low-z evolution of the IGM.** The catalog of absorbers that we presented in Danforth et al. (2016) and used in Chapter 2 represents identifications of absorbers in only 82

of the highest S/N COS G130M and G160M medium-resolution sightlines. Hundreds of lower-S/N sightlines have been and continue to be observed. Though surveys of absorbers in these sightlines will not substantially improve the statistics of the absorber frequency distribution as a function of column density, they could significantly improve the constraints on the redshift evolution of higher column density IGM asborbers at low redshift. This redshift evolution, parameterized as a power law $f(N, z) \propto (1+z)^{\gamma}$, remains quite uncertain in the Danforth et al. (2016) survey.

- **The weak end of the absorber distribution.** Similarly, the Danforth et al. (2016) study does not optimally constrain the statistics of the lowest column-density absorbers owing to its focus on firm absorber detections detected at high significance level. The absorber frequency distributions become highly uncertain at low equivalent widths ($\log N_{\rm HI} < 12.8$, $\log N_{\rm OVI} < 13.4$). A more statistical approach that searches for marginal detections in context with a careful characterization of the noise properties of the spectra and the detection rates of absorbers could better determine the absorber frequency distribution at these low column densities. For the high-ionization metal species in particular, these low column density absorbers may be tracing inter-group or true intergalactic gas, in contrast to the higher column density absorbers, which are more likely tracing circumgalactic gas (e.g., Tumlinson et al., 2011; Stocke et al., 2014)

- **The intermdiate-z absorber distribution.** Though the IGM absorber distribution is well studied at low redshifts (Tilton et al., 2012; Danforth et al., 2016) and high redshifts (Rudie et al., 2013), the intermediate redshift range ($0.5 < z < 2$) remains highly uncertain. Though several studies, most notably Janknecht et al. (2006a), have attempted to measure this distribution with Lyα absorption in NUV data, they are limited by both small samples and insufficient methodological choices. As I showed in Chapter 3, there is broad disagreement about both the H I column-density distribution as well as its evolution in redshift, and a portion of this uncertainty is due to incorrect column density measurements based

on optically-thick Lyman α lines alone. Measurements of the intermediate-redshift IGM distribution should be improved via a reanalysis of existing NUV spectra. New observations with *HST*/COS and STIS could help to expand the sample. The sample should use a combination of COS and STIS space-based NUV data with publicly available data from the UVES instrument on the Very Large Telescope (VLT). Though many of the high column density ($\log N_{\rm HI} > 14$) absorber measurements will be limited to a single optically-thick transition, a full exploration of the posterior probability distribution of each absorption component's parameters combined with an appropriate treatment of those uncertainties in the determination of the absorber distribution can robustly constrain the absorber frequency distribution. This absorber distribution is a primary uncertainty in studies such as Chapter 3, and it also will determine the redshift evolution of the IGM.

- **FUV priors on X-ray WHIM absorption.** X-ray observations of WHIM-like absorbers due to species such as O VII and O VIII (e.g., Rasmussen et al., 2007; Fang et al., 2010; Nicastro et al., 2010; Nicastro, 2014, 2016, among many others) are frequently of low statistical significance and often disputed (e.g., Yao et al., 2012). It is unlikely that a large sample of high-significance X-ray absorbers will be detected in the near future. More robust statistical constraints on the baryon content of warm-hot gas can be achieved by correlating FUV O VI surveys, numerical simulations, and galaxy surveys (e.g. Cen, 2012; Nevalainen et al., 2015, 2016) which can serve as priors on the X-ray detections. Though this approach has been attempted in a very limited sense (e.g. Bonamente et al., 2016), there has not been a robust survey, which may be an important step toward a unified census of IGM baryons. Such an approach may be especially useful if combined with targeted observations of galaxy clusters (e.g., the X Comae sightline toward the Coma cluster), which are expected to show FUV absorption (Emerick et al., 2015).

5.2.2 The EUV spectra of AGNs.

- **Biases in luminosity.** One of the primary limitations of the work presented in Chapter 3 is the sample of $z_{\rm AGN} \gtrsim 1.5$ AGNs. Because the AGNs were selected primarily on the basis of high UV flux, they sample only the high end of the AGN luminosity function. Though this facilitates observations, it also potentially introduces biases. EUV slope and relative flux may correlate with AGN luminosity (e.g., Koratkar & Blaes, 1999; Romano & Peterson, 1999; Trèvese & Vagnetti, 2002), so it is necessary to sample fainter portions of the AGN luminosity function. Though the observational cost is high, it is worth obtaining additional UV spectra of fainter AGNs at $z_{\rm AGN} \gtrsim 1.5$. This is a crucial observation to make while we have extant UV facilities, as the EUV spectral energy distribution propagates to many other calculations via the UVB.

- **EUV emission lines.** In the long term, understanding the AGN broad-line region will require an improved understanding of the EUV emission lines. Presently, the emission lines are heavily blended, and photoionization models break down due to high gas densities and uncertain atomic parameters (but see Moloney & Shull, 2014). Disentangling the flux of these emission lines will require a combination of targeted observations of AGNs with narrower emission lines than the Tilton et al. (2016) sample and improvements to photoionization codes.

5.2.3 The UVB.

- **Improving predictions of the UVB.** As pointed out by Faucher-Giguère et al. (2009) over eight years ago, "the ionizing background spectrum is not yet uniquely determined." Nonetheless, approaches to determining the UVB have primarily proceeded with the same basic methodology as was employed nearly three decades ago (Miralda-Escudé & Ostriker, 1990), and the ability of these spectra to reproduce observations has not substantially changed in nearly two decades (Shull et al., 1999). Present models are based on radiative

transfer calculations that choose single values of highly uncertain and degenerate parameters such as the redshift evolution of Lyman limit systems, the spectra of high redshift galaxies, the Lyman-continuum escape fraction from galaxies, and AGN luminosity functions, among others. As computational resources grow, UVB determinations must begin to exploit these resources. In the short term, radiative transfer calculations must better treat their uncertainties and degeneracies and fully sample the posterior probability distribution of the UVB spectral energy distribution as a function of wavelength. A major step toward this goal would be the development of a fully extensible and open-source radiative transfer code for this purpose, perhaps based on existing code (e.g., Mirocha, 2014; Mirocha et al., 2017). In the future, as computational resources continue to improve, ensembles of cosmological simulations, perhaps even with several frequency bands of radiative transfer, may offer a way forward, attempting to reproduce multiple observables from differing input background spectra.

5.2.4 Associated Absorbers

The preliminary work presented in Chapter 4 represents only the first step toward obtaining a more general, statistical understanding of associated absorbers. In particular, future work will need to address the following issues:

- **A larger sample.** The primary goal of the work begun in Chapter 4 is to produce a large, homogeneously-measured sample of the basic properties of associated absorbers with which a variety of statistical analyses can be performed. Though great progress has been made with detailed studies of individual absorbers, that approach has not yet answered many of the outstanding questions about associated absorbers, especially the NALs. The next step, currently underway, is to complete the identification and characterization of the absorption lines present in the full extent of COS archive of medium-resolution observations, which contains observations of more than 300 AGNs at $z_{\rm AGN} < 2$ with S/N > 5 and will approximately triple the number of absorbers compared to the preliminary sample of

Chapter 4.

- **Radio and X-ray properties.** It is essential to assemble a uniform catalog of X-ray and radio luminosities and X-ray warm absorber properties for the targets observer in the UV. It is well-established that X-ray and UV absorbers show correlations that suggest a physical connection (e.g., Crenshaw et al., 1999; Brandt et al., 2000; Kriss, 2002). However, photoionization models of some sightlines suggest that the same gas cannot produce both the X-ray and UV absorption lines (e.g., Kraemer et al., 2003). Further, there have long been suggestions that BALs may be correlated with radio properties (e.g., Stocke et al., 1992), and recently there have been suggestions that radio properties may predict NAL presence (Culliton et al., 2017).

- **Photoionization state.** Previously, photoionization modeling of NAL systems has occured primarily on a case-by-case basis, with varying methodologies and photoionization codes, but it is now computationally feasible to produce large grids of numerical photoionization models to fit to an entire catalog of absorbers in a semi-automated fashion. By constructing a grid of photoionization models with software such as `Cloudy` (Ferland et al., 2013) and `XSTAR` (Bautista & Kallman, 2001), one could fit each absorber's column density measurements to ionization parameters. These ionization parameters depend on the gas density and distance to the AGN. In most cases, this will yield limits only, as the number density of the gas remains unknown. A subset of the absorbers, however, show transitions from collisionally populated metastable states from species such as C II, C III, Si II, and Si III. In combination with collisional modeling using a database such as `Chianti` (Dere et al., 1997; Del Zanna et al., 2015), one can derive number densities and thus distances. Additionally, the subset of absorbers with multi-epoch observations imply distance constraints, and thus density constraints, based on variability arguments. Constraints on density and distance translate directly to constraints on the mass outflow rates and kinetic luminosities that are of interest for estimating contributions to AGN feedback. Further, predictions of

strengths of X-ray lines from the photoionization models will test the connection between X-ray warm absorbers and UV associated absorbers.

- **AGN inclination.** The geometric distribution of associated absorbers relative to the AGN remains mostly unknown, especially with respect to AGN inclination. Their angular position relative to the AGN disk is especially important to constrain if we wish to determine if the associated absorbers are related to disk winds, because some classes of magnetohydrodynamic disk-wind models (Emmering et al., 1992; Chajet & Hall, 2013, 2017) predict different angular distributions than line-driven disk winds (Proga & Kallman, 2004), which prefer more equatorial distributions. For large samples of absorbers, the equivalent-width distributions of the AGN emission lines can be used to statistically determine the angular frequency of absorbers with respect to AGN inclination (Boroson, 2011) as has recently been done for a sample of the strongest BAL systems in the Sloan Digital Sky Survey (Matthews et al., 2017). Recent advances in the determination of AGN inclination via narrow emission lines (Fischer et al., 2013) provide more precise determinations of inclination for a growing subset of low-redshift AGNs, which have been shown to be highly reliable (Marin, 2016). Combined with the associated absorber catalog, these measurements will provide a complete geometric picture of these absorbers relative to the AGN, placing them in context with AGN unification models.

- **Variability.** Many objects in the COS catalog have been observed at multiple epochs, either by other spectrographs (*IUE*, *Hopkins Ultraviolet Telescope*, *FUSE*, Faint Object Spectrograph [FOS], Space Telescope Imaging Spectrograph [STIS], Goddard High Resolution Spectrograph [GHRS]) or by previous visits with COS. These observations allow all of these investigations to be conducted as a function of time for a subset of the absorbers, with the goal of understanding the variability of these absorbers. These measurements will test whether the variability of these absorbers is more plausibly explained by changes in ionization state, as has been suggested for some absorbers (e.g., Barlow et al., 1992;

Capellupo et al., 2012; Filiz Ak et al., 2013; Arav et al., 2012, 2015), or by transverse motion, which has been suggested for others (e.g., Boroson et al., 1991; Capellupo et al., 2012). If NAL variations can be modeled by a random-walk statistical model that has timescales consistent with large samples of BALs as presented by Filiz Ak et al. (2013), it may provide evidence that these populations are related. New observations with COS could improve constraints on typical NAL variability timescales by targeting sightlines with existing single epochs of observations for follow-up observations.

Many of these types of measurements and calculations have been demonstrated in detailed studies of single or small numbers of objects, but larger, homogeneous samples are required to fully address the underlying physical questions.

Bibliography

Abazajian, K., et al. 2004, AJ, 128, 502

Adelman-McCarthy, J. K., et al. 2006, ApJS, 162, 38

—. 2007, ApJS, 172, 634

Akaike, H. 1974, IEEE Transactions on Automatic Control, 19, 716

Akerman, C. J., Carigi, L., Nissen, P. E., Pettini, M., & Asplund, M. 2004, A&A, 414, 931

Alam, S., et al. 2015, ApJS, 219, 12

Allen, D. A., Longmore, A. J., Hawarden, T. G., Cannon, R. D., & Allen, C. J. 1978, MNRAS, 184, 303

Alloin, D., Barvainis, R., Gordon, M. A., & Antonucci, R. R. J. 1992, A&A, 265, 429

Anderson, K. S., & Kraft, R. P. 1969, ApJ, 158, 859

Antonucci, R. R. J., & Miller, J. S. 1985, ApJ, 297, 621

Aoki, K., Iwata, I., Ohta, K., Ando, M., Akiyama, M., & Tamura, N. 2006, ApJ, 651, 84

Arav, N. 1997, in Astronomical Society of the Pacific Conference Series, Vol. 128, Mass Ejection from Active Galactic Nuclei, ed. N. Arav, I. Shlosman, & R. J. Weymann, 208

Arav, N. 2002, in X-ray Spectroscopy of AGN with Chandra and XMM-Newton, ed. T. Boller, S. Komossa, S. Kahn, H. Kunieda, & L. Gallo, 153

Arav, N., Barlow, T. A., Laor, A., & Blandford, R. D. 1997, MNRAS, 288, 1015

Arav, N., & Begelman, M. C. 1994, ApJ, 434, 479

Arav, N., Borguet, B., Chamberlain, C., Edmonds, D., & Danforth, C. 2013, MNRAS, 436, 3286

Arav, N., Kaastra, J., Kriss, G. A., Korista, K. T., Gabel, J., & Proga, D. 2005, ApJ, 620, 665

Arav, N., Korista, K. T., Barlow, T. A., & Begelman. 1995, Nature, 376, 576

Arav, N., Korista, K. T., de Kool, M., Junkkarinen, V. T., & Begelman, M. C. 1999, ApJ, 516, 27

Arav, N., Li, Z.-Y., & Begelman, M. C. 1994, ApJ, 432, 62

Arav, N., Moe, M., Costantini, E., Korista, K. T., Benn, C., & Ellison, S. 2008, ApJ, 681, 954

Arav, N., et al. 2007, ApJ, 658, 829

—. 2012, A&A, 544, A33

—. 2015, A&A, 577, A37

Armstrong, B. 1967, J. Quant. Spec. Radiat. Transf., 7, 61

Baade, W., & Minkowski, R. 1954, ApJ, 119, 206

Bachev, R., Strigachev, A., Semkov, E., & Mihov, B. 2008, A&A, 488, 887

Bade, N., Fink, H. H., Engels, D., Voges, W., Hagen, H.-J., Wisotzki, L., & Reimers, D. 1995, A&AS, 110, 469

Bahcall, J. N., & Goldsmith, S. 1971, ApJ, 170, 17

Bahcall, J. N., & Spitzer, Jr., L. 1969, ApJ, 156, L63

Baldwin, J., Ferland, G., Korista, K., & Verner, D. 1995, ApJ, 455, L119

Barlow, T. A., Hamann, F., & Sargent, W. L. W. 1997, in Astronomical Society of the Pacific Conference Series, Vol. 128, Mass Ejection from Active Galactic Nuclei, ed. N. Arav, I. Shlosman, & R. J. Weymann, 13

Barlow, T. A., Junkkarinen, V. T., & Burbidge, E. M. 1989, ApJ, 347, 674

Barlow, T. A., Junkkarinen, V. T., Burbidge, E. M., Weymann, R. J., Morris, S. L., & Korista, K. T. 1992, ApJ, 397, 81

Bautista, M. A., & Kallman, T. R. 2001, ApJS, 134, 139

Begelman, M., de Kool, M., & Sikora, M. 1991, ApJ, 382, 416

Bianchi, L., Conti, A., & Shiao, B. 2014, Advances in Space Research, 53, 900

Binette, L., & Krongold, Y. 2008a, A&A, 477, 413

—. 2008b, A&A, 478, 739

Bolton, J. G. 1948, Nature, 162, 141

—. 1982, Proceedings of the Astronomical Society of Australia, 4, 349

Bolton, J. G., Stanley, G. J., & Slee, O. B. 1949, Nature, 164, 101

Bonamente, M., & Dixon, W. V. D. 2004, ApJ, 609, 597

Bonamente, M., Nevalainen, J., Tilton, E., Liivamägi, J., Tempel, E., Heinämäki, P., & Fang, T. 2016, MNRAS, 457, 4236

Borguet, B. C. J., Edmonds, D., Arav, N., Dunn, J., & Kriss, G. A. 2012, ApJ, 751, 107

Boroson, T. A. 2011, ApJ, 735, L14

Boroson, T. A., & Green, R. F. 1992, ApJS, 80, 109

Boroson, T. A., Meyers, K. A., Morris, S. L., & Persson, S. E. 1991, ApJ, 370, L19

Bouwens, R. J., et al. 2011, ApJ, 737, 90

Bowler, R. A. A., Hewett, P. C., Allen, J. T., & Ferland, G. J. 2014, MNRAS, 445, 359

Brandt, W. N., Laor, A., & Wills, B. J. 2000, ApJ, 528, 637

Bregman, J. N. 2007, ARA&A, 45, 221

Brotherton, M. S., Tran, H. D., Becker, R. H., Gregg, M. D., Laurent-Muehleisen, S. A., & White, R. L. 2001, ApJ, 546, 775

Bryan, G. L., et al. 2014, ApJS, 211, 19

Burnham, K. P., & Anderson, D. R. 2003, Model Selection and Multimodel Inference: A Practical Information-Theoretic Approach (Springer Science & Business Media)

—. 2004, Sociological Methods & Research, 33, 261

Caffau, E., Ludwig, H.-G., Steffen, M., Freytag, B., & Bonifacio, P. 2011, Sol. Phys., 268, 255

Canalizo, G., & Stockton, A. 2001, ApJ, 555, 719

Capellupo, D. M., Hamann, F., Shields, J. C., Rodríguez Hidalgo, P., & Barlow, T. A. 2012, MNRAS, 422, 3249

Carballo, R., González-Serrano, J. I., Benn, C. R., Sánchez, S. F., & Vigotti, M. 1999, MNRAS, 306, 137

Carilli, C. L., Wrobel, J. M., & Ulvestad, J. S. 1998, AJ, 115, 928

Castelló-Mor, N., et al. 2017, MNRAS

Cen, R. 2012, ApJ, 753, 17

Cen, R., & Fang, T. 2006, ApJ, 650, 573

Cen, R., & Ostriker, J. P. 1999, ApJ, 519, L109

Chajet, L. S., & Hall, P. B. 2013, MNRAS, 429, 3214

—. 2017, MNRAS, 465, 1741

Chartas, G., Brandt, W. N., & Gallagher, S. C. 2003, ApJ, 595, 85

Cirasuolo, M., Celotti, A., Magliocchetti, M., & Danese, L. 2003, MNRAS, 346, 447

Colless, M., et al. 2003, ArXiv Astrophysics e-prints, arXiv:astro-ph/0306581

Comerford, J. M., & Greene, J. E. 2014, ApJ, 789, 112

Corwin, Jr., H. G., Buta, R. J., & de Vaucouleurs, G. 1994, AJ, 108, 2128

Costantini, E., et al. 2007, A&A, 461, 121

Cottis, C. E., Goad, M. R., Knigge, C., & Scaringi, S. 2010, MNRAS, 406, 2094

Cowley, A. P., Crampton, D., Hutchings, J. B., Helfand, D. J., Hamilton, T. T., Thorstensen, J. R., & Charles, P. A. 1984, ApJ, 286, 196

Crenshaw, D. M., Fischer, T. C., Kraemer, S. B., & Schmitt, H. R. 2015, ApJ, 799, 83

Crenshaw, D. M., & Kraemer, S. B. 2001, ApJ, 562, L29

—. 2012, ApJ, 753, 75

Crenshaw, D. M., Kraemer, S. B., Boggess, A., Maran, S. P., Mushotzky, R. F., & Wu, C.-C. 1999, ApJ, 516, 750

Crenshaw, D. M., Kraemer, S. B., & George, I. M. 2003, ARA&A, 41, 117

Culliton, C., Eracleous, M., Charlton, J., & Misawa, T. 2012, in Astronomical Society of the Pacific Conference Series, Vol. 460, AGN Winds in Charleston, ed. G. Chartas, F. Hamann, & K. M. Leighly, 109

Culliton, C. S., Charlton, J. C., Eracleous, M., Roberts, A., Ganguly, R., Misawa, T., & Muzahid, S. 2017, in American Astronomical Society Meeting Abstracts, Vol. 229, American Astronomical Society Meeting Abstracts, 302.07

Danforth, C. W., & Shull, J. M. 2005, ApJ, 624, 555

—. 2008, ApJ, 679, 194

Danforth, C. W., Shull, J. M., Rosenberg, J. L., & Stocke, J. T. 2006, ApJ, 640, 716

Danforth, C. W., Stocke, J. T., & Shull, J. M. 2010, ApJ, 710, 613

Danforth, C. W., et al. 2014, ArXiv e-prints, arXiv:1402.2655v1

—. 2016, ApJ, 817, 111

Davé, R., Hernquist, L., Katz, N., & Weinberg, D. H. 1999, ApJ, 511, 521

Davé, R., et al. 2001, ApJ, 552, 473

Davies, R. I., et al. 2017, MNRAS

Davis, S. W., & Laor, A. 2011, ApJ, 728, 98

de Kool, M., Arav, N., Becker, R. H., Gregg, M. D., White, R. L., Laurent-Muehleisen, S. A., Price, T., & Korista, K. T. 2001, ApJ, 548, 609

de Kool, M., Korista, K. T., & Arav, N. 2002, ApJ, 580, 54

Del Zanna, G., Dere, K. P., Young, P. R., Landi, E., & Mason, H. E. 2015, A&A, 582, A56

Dere, K. P., Landi, E., Mason, H. E., Monsignori Fossi, B. C., & Young, P. R. 1997, A&AS, 125

Di Matteo, T., Springel, V., & Hernquist, L. 2005, Nature, 433, 604

Done, C., & Davis, S. W. 2008, ApJ, 683, 389

Done, C., Davis, S. W., Jin, C., Blaes, O., & Ward, M. 2012, MNRAS, 420, 1848

Dressler, A., & Shectman, S. A. 1988, AJ, 95, 284

Dunn, J. P., Crenshaw, D. M., Kraemer, S. B., & Gabel, J. R. 2007, AJ, 134, 1061

Dunn, J. P., Crenshaw, D. M., Kraemer, S. B., & Trippe, M. L. 2008, AJ, 136, 1201

Dunn, J. P., et al. 2010, ApJ, 709, 611

Ebrero, J., Costantini, E., Kaastra, J. S., Detmers, R. G., Arav, N., Kriss, G. A., Korista, K. T., & Steenbrugge, K. C. 2010, A&A, 520, A36

Ebrero, J., Kriss, G. A., Kaastra, J. S., & Ely, J. C. 2016, A&A, 586, A72

Edge, D. O., Shakeshaft, J. R., McAdam, W. B., Baldwin, J. E., & Archer, S. 1959, MmRAS, 68, 37

Edmonds, D., et al. 2011, ApJ, 739, 7

Elvis, M. 2006, Mem. Soc. Astron. Italiana, 77, 573

Emerick, A., Bryan, G., & Putman, M. E. 2015, MNRAS, 453, 4051

Emmering, R. T., Blandford, R. D., & Shlosman, I. 1992, ApJ, 385, 460

Engels, D., Hagen, H.-J., Cordis, L., Koehler, S., Wisotzki, L., & Reimers, D. 1998, A&AS, 128, 507

Fabian, A. C. 2004, Coevolution of Black Holes and Galaxies, 446

Fabian, A. C., Lohfink, A., Belmont, R., Malzac, J., & Coppi, P. 2017, MNRAS, 467, 2566

Falco, E. E., et al. 1999, PASP, 111, 438

Falomo, R., Maraschi, L., Treves, A., & Tanzi, E. G. 1987, ApJ, 318, L39

Falomo, R., Pesce, J. E., & Treves, A. 1993, ApJ, 411, L63

Falomo, R., Pian, E., & Treves, A. 2014, A&A Rev., 22, 73

Fanaroff, B. L., & Riley, J. M. 1974, MNRAS, 167, 31P

Fang, T., Buote, D. A., Humphrey, P. J., Canizares, C. R., Zappacosta, L., Maiolino, R., Tagliaferri, G., & Gastaldello, F. 2010, ApJ, 714, 1715

Fath, E. A. 1909, Lick Observatory Bulletin, 5, 71

Faucher-Giguère, C.-A., Lidz, A., Zaldarriaga, M., & Hernquist, L. 2009, ApJ, 703, 1416

Federer, C. A., editor. 1960, "First True Radio Star," Sky and Telescope, March, 21, 148

Ferland, G. J., et al. 2013, Rev. Mexicana Astron. Astrofis., 49, 137

Fields, D. L., Mathur, S., Krongold, Y., Williams, R., & Nicastro, F. 2007, ApJ, 666, 828

Filiz Ak, N., et al. 2013, ApJ, 777, 168

Fischer, T. C., Crenshaw, D. M., Kraemer, S. B., & Schmitt, H. R. 2013, ApJS, 209, 1

Fitzpatrick, E. L. 1999, PASP, 111, 63

Foreman-Mackey, D., Hogg, D. W., Lang, D., & Goodman, J. 2013, PASP, 125, 306

Fox, A. J., et al. 2017, Cosmic Origins Spectrograph Instrument Handbook, Version 9.0 (Baltimore, MD: STScI)

Francis, P. J., Hewett, P. C., Foltz, C. B., Chaffee, F. H., Weymann, R. J., & Morris, S. L. 1991, ApJ, 373, 465

Fukugita, M., Hogan, C. J., & Peebles, P. J. E. 1998, ApJ, 503, 518

Fumagalli, M., Haardt, F., Theuns, T., Morris, S. L., Cantalupo, S., Madau, P., & Fossati, M. 2017, ArXiv e-prints

Gabel, J. R., et al. 2005, ApJ, 623, 85

Gaikwad, P., Khaire, V., Choudhury, T. R., & Srianand, R. 2017a, MNRAS, 466, 838

Gaikwad, P., Srianand, R., Choudhury, T. R., & Khaire, V. 2017b, MNRAS, 467, 3172

Gallazzi, A., Brinchmann, J., Charlot, S., & White, S. D. M. 2008, MNRAS, 383, 1439

Ganguly, R., Bond, N. A., Charlton, J. C., Eracleous, M., Brandt, W. N., & Churchill, C. W. 2001a, ApJ, 549, 133

Ganguly, R., Charlton, J. C., & Eracleous, M. 2001b, ApJ, 556, L7

Ganguly, R., Masiero, J., Charlton, J. C., & Sembach, K. R. 2003, ApJ, 598, 922

Ganguly, R., et al. 2007, AJ, 133, 479

—. 2013, MNRAS, 435, 1233

Gaskell, C. M. 1982, ApJ, 263, 79

—. 2009, New A Rev., 53, 140

Gehrels, N. 1986, ApJ, 303, 336

Geminale, A., & Popowski, P. 2004, Acta Astron., 54, 375

George, I. M., Turner, T. J., Yaqoob, T., Netzer, H., Laor, A., Mushotzky, R. F., Nandra, K., & Takahashi, T. 2000, ApJ, 531, 52

Ghavamian, P., et al. 2009, Preliminary Characterization of the Post- Launch Line Spread Function of COS, Tech. rep.

Gibson, R. R., Marshall, H. L., Canizares, C. R., & Lee, J. C. 2005, ApJ, 627, 83

Giustini, M., et al. 2011, A&A, 536, A49

Gofford, J., et al. 2011, MNRAS, 414, 3307

Goodman, J., & Weare, J. 2010, Communications in applied mathematics and computational science, 5, 65

Grazian, A., Cristiani, S., D'Odorico, V., Omizzolo, A., & Pizzella, A. 2000, AJ, 119, 2540

Green, J. C., et al. 2012, ApJ, 744, 60

Greenstein, J. L. 1963, Nature, 197, 1041

Grupe, D., Beuermann, K., Mannheim, K., & Thomas, H.-C. 1999, A&A, 350, 805

Grupe, D., Beuermann, K., Thomas, H.-C., Mannheim, K., & Fink, H. H. 1998, A&A, 330, 25

Gunn, J. E., & Peterson, B. A. 1965, ApJ, 142, 1633

Haardt, F., & Madau, P. 2001, in Clusters of Galaxies and the High Redshift Universe Observed in X-rays, ed. D. M. Neumann & J. T. V. Tran

Haardt, F., & Madau, P. 2012, ApJ, 746, 125

Hagen, H.-J., Engels, D., & Reimers, D. 1999, A&AS, 134, 483

Hall, P. B. 2007, AJ, 133, 1271

Hamann, F. 1997, ApJS, 109, 279

Hamann, F. W., Barlow, T. A., Chaffee, F. C., Foltz, C. B., & Weymann, R. J. 2001, ApJ, 550, 142

Hasinger, G. 1994, in Astrophysics and Space Science Library, Vol. 187, Frontiers of Space and Ground-Based Astronomy, ed. W. Wamsteker, M. S. Longair, & Y. Kondo, 381

Hasinger, G. 1996, A&AS, 120, C607

Hazard, C. 1962, MNRAS, 124, 343

Hazard, C., Mackey, M. B., & Shimmins, A. J. 1963, Nature, 197, 1037

Heckman, T. M., & Best, P. N. 2014, ARA&A, 52, 589

Hewett, P. C., & Wild, V. 2010, MNRAS, 405, 2302

Ho, L. C. 2008, ARA&A, 46, 475

Hopkins, P. F., & Elvis, M. 2010, MNRAS, 401, 7

Hopkins, P. F., Hernquist, L., Cox, T. J., Di Matteo, T., Martini, P., Robertson, B., & Springel, V. 2005a, ApJ, 630, 705

Hopkins, P. F., Hernquist, L., Cox, T. J., Di Matteo, T., Robertson, B., & Springel, V. 2005b, ApJ, 630, 716

Hopkins, P. F., Hernquist, L., Cox, T. J., & Kereš, D. 2008, ApJS, 175, 356

Hopkins, P. F., Murray, N., & Thompson, T. A. 2009, MNRAS, 398, 303

Hopkins, P. F., Somerville, R. S., Hernquist, L., Cox, T. J., Robertson, B., & Li, Y. 2006, ApJ, 652, 864

Hubeny, I., & Hubeny, V. 1997, ApJ, 484, L37

Hubeny, I., & Lanz, T. 1995, ApJ, 439, 875

—. 2011, TLUSTY: Stellar Atmospheres, Accretion Disks, and Spectroscopic Diagnostics, Astrophysics Source Code Library

Huchra, J., Latham, D. W., da Costa, L. N., Pellegrini, P. S., & Willmer, C. N. A. 1993, AJ, 105, 1637

Huchra, J. P., Vogeley, M. S., & Geller, M. J. 1999, ApJS, 121, 287

Hutchings, J. B., Crenshaw, D. M., Kraemer, S. B., Gabel, J. R., Kaiser, M. E., Weistrop, D., & Gull, T. R. 2002, AJ, 124, 2543

Janknecht, E., Reimers, D., Lopez, S., & Tytler, D. 2006a, A&A, 458, 427

—. 2006b, VizieR Online Data Catalog, 345, 80427

Jones, D. H., et al. 2009, MNRAS, 399, 683

Kaastra, J. S., et al. 2004, A&A, 428, 57

Kaspi, S., Netzer, H., Chelouche, D., George, I. M., Nandra, K., & Turner, T. J. 2004, ApJ, 611, 68

Kazarian, M. A. 1987, Astrofizika, 27, 399

Keeney, B. A., Danforth, C. W., Stocke, J. T., France, K., & Green, J. C. 2012, PASP, 124, 830

Kellermann, K. I. 2013, Bulletin of the Astronomical Society of India, 41, 1

Kellermann, K. I., Sramek, R., Schmidt, M., Shaffer, D. B., & Green, R. 1989, AJ, 98, 1195

Khachikian, É. Y., & Weedman, D. W. 1971, Astrophysics, 7, 231

Khachikian, E. Y., & Weedman, D. W. 1974, ApJ, 192, 581

Khaire, V., & Srianand, R. 2015, MNRAS, 451, L30

Kim, T.-S., Carswell, R. F., Cristiani, S., D'Odorico, S., & Giallongo, E. 2002, MNRAS, 335, 555

Kollmeier, J. A., et al. 2014, ApJ, 789, L32

Kolykhalov, P. I., & Sunyaev, R. A. 1984, Advances in Space Research, 3, 249

Komossa, S., & Meerschweinchen, J. 2000, A&A, 354, 411

Koratkar, A., & Blaes, O. 1999, PASP, 111, 1

Korista, K. T., Voit, G. M., Morris, S. L., & Weymann, R. J. 1993, ApJS, 88, 357

Kraemer, S. B., Crenshaw, D. M., Yaqoob, T., McKernan, B., Gabel, J. R., George, I. M., Turner, T. J., & Dunn, J. P. 2003, ApJ, 582, 125

Kriss, G. A. 2002, in Astronomical Society of the Pacific Conference Series, Vol. 255, Mass Outflow in Active Galactic Nuclei: New Perspectives, ed. D. M. Crenshaw, S. B. Kraemer, & I. M. George, 69

Kriss, G. A. 2011, Improved Medium Resolution Line Spread Functions for COS FUV Spectra, Tech. rep.

Kriss, G. A., et al. 2011, A&A, 534, A41

Krolik, J. H. 1999, Active galactic nuclei : from the central black hole to the galactic environment

Krongold, Y., Binette, L., & Hernández-Ibarra, F. 2010, ApJ, 724, L203

Laor, A., & Brandt, W. N. 2002, ApJ, 569, 641

Laor, A., & Davis, S. W. 2014, MNRAS, 438, 3024

Lauberts, A., & Valentijn, E. A. 1989, The Messenger, 56, 31

Lawrence, A. 2012, MNRAS, 423, 451

Lehner, N., Savage, B. D., Richter, P., Sembach, K. R., Tripp, T. M., & Wakker, B. P. 2007, ApJ, 658, 680

Lehner, N., et al. 2013, ApJ, 770, 138

Liddle, A. R. 2007, MNRAS, 377, L74

Liu, W., Hu, J. Y., Li, Z. Y., & Cao, L. 1999, ApJS, 122, 257

Lusso, E., Worseck, G., Hennawi, J. F., Prochaska, J. X., Vignali, C., Stern, J., & O'Meara, J. M. 2015, MNRAS, 449, 4204

Lynds, R. 1971, ApJ, 164, L73

Madau, P., & Dickinson, M. 2014, ARA&A, 52, 415

Madau, P., & Haardt, F. 2015, ApJ, 813, L8

Marconi, A., Risaliti, G., Gilli, R., Hunt, L. K., Maiolino, R., & Salvati, M. 2004, MNRAS, 351, 169

Marin, F. 2016, MNRAS, 460, 3679

Markwardt, C. B. 2009, in Astronomical Society of the Pacific Conference Series, Vol. 411, Astronomical Data Analysis Software and Systems XVIII, ed. D. A. Bohlender, D. Durand, & P. Dowler, 251

Marr, G. V., & West, J. B. 1976, Atomic Data and Nuclear Data Tables, 18, 497

Marziani, P., Sulentic, J. W., Dultzin-Hacyan, D., Calvani, M., & Moles, M. 1996, ApJS, 104, 37

Mathews, W. G., & Ferland, G. J. 1987, ApJ, 323, 456

Matthews, J. H., Knigge, C., & Long, K. S. 2017, MNRAS

Matthews, T. A., Bolton, J. G., Greenstein, J. L., Munch, G., & Sandage, A. R. 1960, paper presented at the 107th meeting of the AAS, December 1960. See also Sky and Telescope, 21, 148

Matthews, T. A., & Sandage, A. R. 1963, ApJ, 138, 30

Mikulski Archive for Space Telescopes. 2017, `https://archive.stsci.edu/` Accessed 2015 − 2017.

Minkowski, R. 1960, ApJ, 132, 908

Miralda-Escudé, J., & Ostriker, J. P. 1990, ApJ, 350, 1

Mirocha, J. 2014, MNRAS, 443, 1211

Mirocha, J., Furlanetto, S. R., & Sun, G. 2017, MNRAS, 464, 1365

Misawa, T., Charlton, J. C., Eracleous, M., Ganguly, R., Tytler, D., Kirkman, D., Suzuki, N., & Lubin, D. 2007, ApJS, 171, 1

Moloney, J., & Shull, J. M. 2014, ApJ, 793, 100

Monier, E. M., Mathur, S., Wilkes, B., & Elvis, M. 2001, ApJ, 559, 675

Moré, J. J. 1978, in Numerical analysis (Springer), 105–116

Morton, D. C. 2003, ApJS, 149, 205

Murray, N., Quataert, E., & Thompson, T. A. 2005, ApJ, 618, 569

Muzahid, S., Srianand, R., Arav, N., Savage, B. D., & Narayanan, A. 2013, MNRAS, 431, 2885

Muzahid, S., Srianand, R., Charlton, J., & Eracleous, M. 2016, MNRAS, 457, 2665

NASA/IPAC Extragalactic Database. 2017, `http://nedwww.ipac.caltech.edu/` Accessed 2015 − 2017.

Nestor, D. B., Hamann, F., & Rodriquez Hidalgo, P. 2007, in Astronomical Society of the Pacific Conference Series, Vol. 373, The Central Engine of Active Galactic Nuclei, ed. L. C. Ho & J.-W. Wang, 295

Netzer, H. 1990, in Active Galactic Nuclei, ed. R. D. Blandford, H. Netzer, L. Woltjer, T. J.-L. Courvoisier, & M. Mayor, 57–160

Netzer, H. 2015, ARA&A, 53, 365

Netzer, H., & Laor, A. 1993, ApJ, 404, L51

Nevalainen, J., et al. 2015, A&A, 583, A142

Nevalainen, J., et al. 2016, in IAU Symposium, Vol. 308, The Zeldovich Universe: Genesis and Growth of the Cosmic Web, ed. R. van de Weygaert, S. Shandarin, E. Saar, & J. Einasto, 368–371

Nicastro, F. 2014, in The X-ray Universe 2014, 11

Nicastro, F. 2016, in XMM-Newton: The Next Decade, 27

Nicastro, F., Krongold, Y., Fields, D., Conciatore, M. L., Zappacosta, L., Elvis, M., Mathur, S., & Papadakis, I. 2010, ApJ, 715, 854

North, M., Knigge, C., & Goad, M. 2006, MNRAS, 365, 1057

Oke, J. B. 1963, Nature, 197, 1040

Oke, J. B., & Gunn, J. E. 1974, ApJ, 189, L5

Oppenheimer, B. D., & Davé, R. 2008, MNRAS, 387, 577

—. 2009, MNRAS, 395, 1875

Osterbrock, D. E. 1989, Astrophysics of gaseous nebulae and active galactic nuclei

Penton, S. V., Shull, J. M., & Stocke, J. T. 2000, ApJ, 544, 150

Perry, J. J., & Dyson, J. E. 1990, ApJ, 361, 362

Peterson, B. M. 1993, PASP, 105, 247

Peterson, B. M. 1997, An Introduction to Active Galactic Nuclei (Cambridge University Press)

Peterson, B. M. 2006, in Lecture Notes in Physics, Berlin Springer Verlag, Vol. 693, Physics of Active Galactic Nuclei at all Scales, ed. D. Alloin, 77

Peterson, B. M., et al. 2004, ApJ, 613, 682

Pettini, M. 1999, in Chemical Evolution from Zero to High Redshift, ed. J. R. Walsh & M. R. Rosa, 233

Pettini, M., Zych, B. J., Steidel, C. C., & Chaffee, F. H. 2008, MNRAS, 385, 2011

Pieri, M. M., et al. 2014, MNRAS, 441, 1718

Pietsch, W., Bischoff, K., Boller, T., Doebereiner, S., Kollatschny, W., & Zimmermann, H.-U. 1998, A&A, 333, 48

Planck Collaboration et al. 2016, A&A, 594, A13

Pounds, K. A., King, A. R., Page, K. L., & O'Brien, P. T. 2003, MNRAS, 346, 1025

Pringle, J. E. 1981, ARA&A, 19, 137

Proga, D. 2007, in Astronomical Society of the Pacific Conference Series, Vol. 373, The Central Engine of Active Galactic Nuclei, ed. L. C. Ho & J.-W. Wang, 267

Proga, D., & Kallman, T. R. 2004, ApJ, 616, 688

Ramírez, J. M., Komossa, S., Burwitz, V., & Mathur, S. 2008, ApJ, 681, 965

Rasmussen, A. P., Kahn, S. M., Paerels, F., Herder, J. W. d., Kaastra, J., & de Vries, C. 2007, ApJ, 656, 129

Reeves, J. N., Porquet, D., Braito, V., Gofford, J., Nardini, E., Turner, T. J., Crenshaw, D. M., & Kraemer, S. B. 2013, ApJ, 776, 99

Remillard, R. A., Bradt, H. V., Buckley, D. A. H., Roberts, W., Schwartz, D. A., Tuohy, I. R., & Wood, K. 1986, ApJ, 301, 742

Renzini, A., & Daddi, E. 2008, in Astronomical Society of the Pacific Conference Series, Vol. 399, Panoramic Views of Galaxy Formation and Evolution, ed. T. Kodama, T. Yamada, & K. Aoki, 399

Romano, P., & Peterson, B. M. 1999, in Astronomical Society of the Pacific Conference Series, Vol. 175, Structure and Kinematics of Quasar Broad Line Regions, ed. C. M. Gaskell, W. N. Brandt, M. Dietrich, D. Dultzin-Hacyan, & M. Eracleous, 55

Rudie, G. C., Steidel, C. C., Shapley, A. E., & Pettini, M. 2013, ApJ, 769, 146

Savage, B. D., Kim, T.-S., Wakker, B. P., Keeney, B., Shull, J. M., Stocke, J. T., & Green, J. C. 2014, ApJS, 212, 8

Savage, B. D., & Sembach, K. R. 1991, ApJ, 379, 245

Schlafly, E. F., & Finkbeiner, D. P. 2011, ApJ, 737, 103

Schlegel, D. J., Finkbeiner, D. P., & Davis, M. 1998, ApJ, 500, 525

Schmachtenberger, B. R., Gabel, J., Crenshaw, D. M., & Kraemer, S. B. 2015, in American Astronomical Society Meeting Abstracts, Vol. 225, American Astronomical Society Meeting Abstracts, 432.03

Schmidt, M. 1963, Nature, 197, 1040

Schmidt, M. 2013, in Fifty Years of Quasars: A Symposium in Honor of Maarten Schmidt, retrieved from `http://www.astro.caltech.edu/q50/pdfs/Schmidt.pdf`

Schmidt, M., & Green, R. F. 1983, ApJ, 269, 352

Schneider, D. P., et al. 2010, AJ, 139, 2360

Schwarz, G. 1978, The Annals of Statistics, 6, 461

Schwope, A., et al. 2000, Astronomische Nachrichten, 321, 1

Scott, J., Arav, N., Borguet, B., Danforth, C., Froning, C., & Winter, L. 2012, in Astronomical Society of the Pacific Conference Series, Vol. 460, AGN Winds in Charleston, ed. G. Chartas, F. Hamann, & K. M. Leighly, 128

Scott, J. E., Arav, N., Gabel, J. R., Kriss, G. A., Quijano, J. K., Kaastra, J. S., Costantini, E., & Korista, K. 2009, ApJ, 694, 438

Scott, J. E., Kriss, G. A., Brotherton, M., Green, R. F., Hutchings, J., Shull, J. M., & Zheng, W. 2004a, ApJ, 615, 135

Scott, J. E., et al. 2004b, ApJS, 152, 1

Selsing, J., Fynbo, J. P. U., Christensen, L., & Krogager, J.-K. 2015, ArXiv e-prints

Seyfert, C. K. 1941, PASP, 53, 231

—. 1943, Contributions from the Mount Wilson Observatory / Carnegie Institution of Washington, 671, 1

Seyfert, C. K. 1946, in Publications of the American Astronomical Society, Vol. 10, Publications of the American Astronomical Society, 317

Shakura, N. I. 1973, Soviet Ast., 16, 756

Shakura, N. I., & Sunyaev, R. A. 1973, A&A, 24, 337

Shakura, N. I., Sunyaev, R. A., & Zilitinkevich, S. S. 1978, A&A, 62, 179

Shull, J. M. 2003, in Astrophysics and Space Science Library, Vol. 281, The IGM/Galaxy Connection. The Distribution of Baryons at z=0, ed. J. L. Rosenberg & M. E. Putman, 1

Shull, J. M., Danforth, C. W., & Tilton, E. M. 2014, ApJ, 796, 49

Shull, J. M., Moloney, J., Danforth, C. W., & Tilton, E. M. 2015, ApJ, 811, 3

Shull, J. M., Roberts, D., Giroux, M. L., Penton, S. V., & Fardal, M. A. 1999, AJ, 118, 1450

Shull, J. M., Smith, B. D., & Danforth, C. W. 2012a, ApJ, 759, 23

Shull, J. M., Stevans, M., & Danforth, C. W. 2012b, ApJ, 752, 162

Shull, J. M., Tumlinson, J., Giroux, M. L., Kriss, G. A., & Reimers, D. 2004, ApJ, 600, 570

Silk, J., & Norman, C. 2009, ApJ, 700, 262

Silk, J., & Rees, M. J. 1998, A&A, 331, L1

Sincell, M. W., & Krolik, J. H. 1997, ApJ, 476, 605

Slipher, V. M. 1917, Lowell Observatory Bulletin, 3, 59

Slone, O., & Netzer, H. 2012, MNRAS, 426, 656

Smith, B. D., Hallman, E. J., Shull, J. M., & O'Shea, B. W. 2011, ApJ, 731, 6

Spitzer, Jr., L. 1956, ApJ, 124, 20

Springel, V. 2005, MNRAS, 364, 1105

Srianand, R., & Petitjean, P. 2000, A&A, 357, 414

Srianand, R., Petitjean, P., Ledoux, C., & Hazard, C. 2002, MNRAS, 336, 753

Steidel, C. C., Adelberger, K. L., Giavalisco, M., Dickinson, M., & Pettini, M. 1999, ApJ, 519, 1

Stengler-Larrea, E. A., et al. 1995, ApJ, 444, 64

Stevans, M. L., Shull, J. M., Danforth, C. W., & Tilton, E. M. 2014, ApJ, 794, 75

Stocke, J., Keeney, B., Danforth, C., Oppenheimer, B., Pratt, C., & Berlind, A. 2017, ArXiv e-prints, arXiv:1702.08554

Stocke, J. T., Keeney, B. A., Danforth, C. W., Shull, J. M., Froning, C. S., Green, J. C., Penton, S. V., & Savage, B. D. 2013, ApJ, 763, 148

Stocke, J. T., Morris, S. L., Weymann, R. J., & Foltz, C. B. 1992, ApJ, 396, 487

Stocke, J. T., et al. 2014, ApJ, 791, 128

Storrie-Lombardi, L. J., McMahon, R. G., Irwin, M. J., & Hazard, C. 1994, ApJ, 427, L13

Strauss, M. A., & Huchra, J. 1988, AJ, 95, 1602

Tang, B., Shang, Z., Gu, Q., Brotherton, M. S., & Runnoe, J. C. 2012, ApJS, 201, 38

Tarenghi, M., Garilli, B., & Maccagni, D. 1994, AJ, 107, 1629

Telfer, R. C., Kriss, G. A., Zheng, W., Davidsen, A. F., & Green, R. F. 1998, ApJ, 509, 132

Telfer, R. C., Zheng, W., Kriss, G. A., & Davidsen, A. F. 2002, ApJ, 565, 773

Thom, C., & Chen, H.-W. 2008, ApJS, 179, 37

Tilton, E. M., Danforth, C. W., Shull, J. M., & Ross, T. L. 2012, ApJ, 759, 112

Tilton, E. M., & Shull, J. M. 2013, ApJ, 774, 67

Tilton, E. M., Stevans, M. L., Shull, J. M., & Danforth, C. W. 2016, ApJ, 817, 56

Tofany, B. W., Winter, L. M., Borguet, B., Edmonds, D., Danforth, C., Green, J., & Arav, N. 2014, MNRAS, 439, 3649

Trèvese, D., & Vagnetti, F. 2002, ApJ, 564, 624

Tripp, T. M., Sembach, K. R., Bowen, D. V., Savage, B. D., Jenkins, E. B., Lehner, N., & Richter, P. 2008, ApJS, 177, 39

Tumlinson, J., et al. 2011, Science, 334, 948

—. 2013, ApJ, 777, 59

Türler, M., et al. 1999, A&AS, 134, 89

Ulrich, M. H., & Boisson, C. 1983, ApJ, 267, 515

Urry, C. M., & Padovani, P. 1995, PASP, 107, 803

Urry, M. 1999, in Astronomical Society of the Pacific Conference Series, Vol. 159, BL Lac Phenomenon, ed. L. O. Takalo & A. Sillanpää, 3

Vanden Berk, D. E., et al. 2001, AJ, 122, 549

Véron-Cetty, M.-P., & Véron, P. 2001, A&A, 374, 92

Vestergaard, M. 2003, ApJ, 599, 116

Vestergaard, M., & Peterson, B. M. 2006, ApJ, 641, 689

Vilkoviskij, E. Y., & Irwin, M. J. 2001, MNRAS, 321, 4

Wagner, G., & Kohl, A. T. 2012, Visual Resources Association: statement on the fair use of images for teaching, research and study

Wallerstein, G. 1962, ApJS, 6, 407

Wang, T., & Wang, J. 1999, Publications of the Purple Mountain Observatory, 18, 248

Wang, T. G., Brinkmann, W., Wamsteker, W., Yuan, W., & Wang, J. X. 1999a, MNRAS, 307, 821

Wang, T. G., Wang, J. X., Brinkmann, W., & Matsuoka, M. 1999b, ApJ, 519, L35

Wei, J. Y., Xu, D. W., Dong, X. Y., & Hu, J. Y. 1999, A&AS, 139, 575

Werk, J. K., Prochaska, J. X., Thom, C., Tumlinson, J., Tripp, T. M., O'Meara, J. M., & Peeples, M. S. 2013, ApJS, 204, 17

Werk, J. K., et al. 2014, ApJ, 792, 8

Weymann, R. J., Carswell, R. F., & Smith, M. G. 1981, ARA&A, 19, 41

Weymann, R. J., Morris, S. L., Foltz, C. B., & Hewett, P. C. 1991, ApJ, 373, 23

White, R. L., et al. 2000, ApJS, 126, 133

Wilkes, B. J., Kuraszkiewicz, J., Green, P. J., Mathur, S., & McDowell, J. C. 1999, ApJ, 513, 76

Williams, R. J. R. 2000, MNRAS, 316, 803

Wise, J. H., Eracleous, M., Charlton, J. C., & Ganguly, R. 2004, ApJ, 613, 129

Wisotzki, L., Christlieb, N., Bade, N., Beckmann, V., Köhler, T., Vanelle, C., & Reimers, D. 2000, A&A, 358, 77

Wolfe, A. M., Gawiser, E., & Prochaska, J. X. 2003, ApJ, 593, 235

Xie, X., Shen, S., Shao, Z., & Yin, J. 2015, ApJ, 802, L16

Yao, Y., Shull, J. M., Wang, Q. D., & Cash, W. 2012, ApJ, 746, 166

Zheng, W., Kriss, G. A., Telfer, R. C., Grimes, J. P., & Davidsen, A. F. 1997, ApJ, 475, 469

Zheng, W., et al. 2001, ApJ, 562, 152

Appendix A

Notes on Individual Sightlines

In this section, we provide notes on several sightlines discussed in Chapter 4 that have unique features or complicating factors not apparent from the measurements reported in the data tables alone, and we also direct the reader to other sightline-specific studies in the literature.

A.1 H 1118-429

Dunn et al. (2007, 2008) analyzed the *FUSE* data for this sightline.

A.2 HE 0429-5343

Dunn et al. (2007) analyzed the *FUSE* data for this sightline, but detected no absorbers. Our System ID 0 identification is uncertain. The system is near Galactic Si II and C I lines, and it has no unambiguous metal detections. System IDs 1 and 2 are firmly detected in both H I and Si III, but are undetected in N V. O VI and C IV are not covered by the COS observations for any of the detected absorption systems.

A.3 HE 1228+0131

The absorbers in this sightline have been observed at higher spectral resolution with STIS/E140M as well as with *FUSE* (Dunn et al., 2007, 2008; Ganguly et al., 2003, 2013)

A.4 HE 2332-3556

System ID 0 in this sightline is identified only through Lyα, which is located atop an unusually curved portion of the AGN spectrum. The unabsorbed continuum model is systematically uncertain beyond the reported error bars. It is possible that the strength of this absorber is systematically in error, or even that the feature is entirely misidentified. However, we include it in the catalog to maintain homogeneity, as it meets all of our inclusion criteria.

A.5 IRAS 23443-4502

The broad absorber in this sightline does not appear to have been discussed previously. We do not attempt to measure column densities or covering fractions for this absorber because it meets our definition of a BAL and the C IV lines heavily overlap each other. The Lyα line, however, appears to be black in its center, suggesting nearly full coverage.

A.6 IRASF22456-5125

Our System ID 1 in this sightline was studied in great detail using both COS and *FUSE* data by Dunn et al. (2010) and Borguet et al. (2012), and we refer the reader to those articles for a more comprehensive discussion. System ID 0, not discussed in those studies, is firmly detected via H I, Si III, O VI, and C IV. Curiously, N V seems to be weak or absent. The O VI measurement, observed only via the λ1038 line, is highly uncertain due to proximity to the blue end of the COS spectrum and blending with System ID 1.

A.7 Kaz 238

Though the S/N is quite low in the region of C IV for this sightline, the one absorber in this sightline is firmly detected in H I, C IV, and Si III. However, the low S/N makes the determination of the covering factor difficult. It is consistent with full coverage, but highly uncertain. Though there is a suggestive qualitative depression in the spectrum in the region of the N V lines, it is not

statistically significant. Deeper observations are required to confirm the presence of N V.

A.8 MR 2251-178

MR 2251-178 hosts an absorber covering -750 km s^{-1} to 150 km s^{-1} (System ID 0) that has been observed to be variable. It has been studied in the UV with *FUSE*, *IUE*, and STIS (Crenshaw & Kraemer, 2001; Ganguly et al., 2001b; Monier et al., 2001; Wise et al., 2004; Dunn et al., 2007, 2008) as well as in the X-ray (Kaspi et al., 2004; Gibson et al., 2005; Ramírez et al., 2008; Gofford et al., 2011; Reeves et al., 2013). We also list a second absorption line (System ID 1) that is weak and seen only in Lyα, but it is near the position of Galactic S I, so it is possibly a misidentification.

A.9 Mrk 279

This sightline is host to one of the most intensively studied associated absorbers (Arav et al., 2005; Kaastra et al., 2004; Gabel et al., 2005; Costantini et al., 2007; Fields et al., 2007; Scott et al., 2004b, 2009; Ebrero et al., 2010, among others). We refer the reader to the discussions and references in the literature for detail discussions of the *FUSE*, STIS, and X-ray data that exists for this target. A conference abstract (Schmachtenberger et al., 2015) further suggests a forthcoming detailed variability study that incorporates the COS data presented here.

The primary absorption system (System ID 0) extends from -600 km s^{-1} to -155 km s^{-1} with at least five components, all of which are detectable in multiple high ionization species. The Lyα absorber in this system likely has minor contamination from Galactic S II. An additional component at $v_{\rm abs} = 101$ km s^{-1} (System ID 1) appears to have a much different ionization structure, as the H I is quite strong but the only metal species apparent in the COS spectrum is Si III. The Lyα line in this system is blended with the three Galactic S II λ1253 lines. They are heavily blended in the COS data but well-resolved in the STIS/E140M observations, so we use fixed column densities from that data to separate them from the H I in the COS data.

A.10 Mrk 304

Kriss (2002) used *FUSE* data to identify our System ID 0 as a broad intrinsic absorber, though Dunn et al. (2007) rejected this identification as having insufficient evidence. We confirm that this is an intrinsic absorber, with clear detections in H I, Si III, and N V.

A.11 Mrk 478

Crenshaw et al. (1999) studied this sightline with FOS but failed to detect the absorbers, probably owing to the low spectral resolution. Kriss (2002) identified our System ID 0 via O VI absorption in the *FUSE* data. Our System IDs 1 and 4, previously undetected, are clearly identified via both H I and N V. System IDs 2 and 3 are firmly detected in Lyα, but are not seen in any metal lines (however, this target lacks G160M observations, rendering C IV inaccessible). They may thus be contaminating, cosmologically-intervening systems.

A.12 Mrk 486

This sightline has a single, broad absorber. The Lyα line is likely heavily contaminated by Galactic S II, Si II, and C I, but the absorber is also firmly detected in Si III and N V.

A.13 Mrk 509

This target has been extensively studied with *FUSE*, *IUE*, FOS, GHRS, STIS, and COS in the UV as well as the *Chandra* X-ray telescope (Kriss et al., 2011; Dunn et al., 2007, 2008, and references therein).

A.14 Mrk 841

Crenshaw & Kraemer (2001) searched the *IUE* data of this sightline for associated absorbers but found none, likely due to insufficient spectral resolution.

A.15 Mrk 876

The *FUSE* data for this sightline were studied by Dunn et al. (2007, 2008) and the primary absorber (System ID 0) was also identified in the COS data used here by Scott et al. (2012). The two Lyα components of our System ID 1 are suspiciously close to matching the component structure and wavelength position of S I absorption for System ID 0. However, the lack of other low-ionization species and slight differences in the velocity offsets of the components lead us to favor the H I interpretation. Nonetheless, the identification is uncertain.

A.16 Mrk 1513

This target, which has two major absorbers (System IDs 0 and 5), has historical data from STIS, the Goddard High Resolution Spectrograph (GHRS), *IUE*, and *FUSE*, which have been studied in detail (Dunn et al., 2008; Tofany et al., 2014). All major absorption lines are isolated and in regions of well-behaved continuum, making these absorbers some of the easiest and most reliable to measure.

A.17 NGC 985

The variability of the single absorber in this sightline has been studied extensively with *IUE*, *FUSE*, STIS, COS, and multiple X-ray telescopes (Arav, 2002; Ebrero et al., 2016). Lyα may have minor contamination from Galactic Si II.

A.18 PG0804+761

See Dunn et al. (2007, 2008) for an analysis of the *FUSE* data for this sightline.

A.19 PG0844+349

The primary absorber toward PG0844+349 (System ID 2) at $v_{\rm abs} \approx 100$ km s^{-1} is at a much different velocity offset than the known X-ray absorber in that sightline (Pounds et al., 2003). The

absorber also has been identified in *FUSE* data (Kriss, 2002; Dunn et al., 2007, 2008).

A.20 PG1126-041

Though the absorbers in this sightline were identified in early *IUE* data, it has been more comprehensively studied in the X-ray regime (Wang & Wang, 1999; Wang et al., 1999a; Giustini et al., 2011; Komossa & Meerschweinchen, 2000). The *FUSE* data appears not to have been analyzed in the context of associated absorbers.

A.21 PG1351+640

The broad absorber (Sytem ID 0) toward PG1351+640 has also been studied using *IUE*, *FUSE*, FOS, and STIS (Zheng et al., 2001; Wise et al., 2004; Dunn et al., 2007, 2008).

A.22 PG1411+442

Laor & Brandt (2002) identified the System ID 0 BAL in low-resolution spectra, and Dunn et al. (2007, 2008) identified the narrow System ID 1 in *FUSE* data. It was also discussed by Wang et al. (1999b). As there are already multiple epochs of observations with several instruments, the BAL in this sightline is a promising target for future variability studies.

A.23 PG1626+554

This sightline contains an H I absorber (System ID 0; $\log N_{\rm HI} \approx 14.64$) that is detected through both Lyα and Lyβ covering approximately -550 km s^{-1} to -170 km s^{-1}. The covering factor is consistent with full coverage. Interestingly, it is not detected in any metal lines, which is perhaps why the Lyβ line was not identified in the Dunn et al. (2007) *FUSE* survey.

A.24 QSO 0045+3926

The single absorption system in this sightline is redshifted relative to $z_{\rm AGN}$, and was also identified in the *FUSE* data by Dunn et al. (2007, 2008).

A.25 RBS542

This sightline has been studied in detail by Edmonds et al. (2011). The spectrum is dominated by an outflow that extends from approximately -350 km s^{-1} to 90 km s^{-1} (System ID 1) which shows strong absorption from H I, C II, C IV, O VI, N V, Si III, Si IV, S IV, and many others. The system mostly shows a three-component structure, with the strongest being the most negative velocity component, which is present in all transitions. The two other components are weaker and seen only in the high-ionization transitions. The most redward component of H I, which lies on the steepest portion of the blue side of the Lyα emission line, has a substantial skew to its absorption trough shape, suggesting a strong velocity-dependent trend in its partial covering. This trend may suggest differential partial coverage of the BLR and the continuum source, as it is present only in the Lyα absorption that lies on the protion of the spectrum with the most rapidly changing ratio of emission-line flux to continuum flux. Because of this complication, our reported component fits, which require more than three components for H I, likely over-fit the number of components because the assumed model is likely an insufficient approximation. This feature may make this absorption system important to future studies of different partial-covering and inhomogeneous-absorption models of absorption. The O VI λ1038 line may suffer some minor contamination from Galactic Fe II absorption, and both O VI lines may suffer from enhanced uncertainty in the unabsorbed spectrum determination because of their close proximity to the blue end of the COS spectrum.

We additionally report a possible absorption system covering approximately -675 km s^{-1} to -410 km s^{-1} (System ID 0). This absorption is seen only in H I Lyα, and it is coincident with a cluster of Galactic lines from C II and P III. A portion of the absorption is certainly due to these contaminating features, but it is difficult to explain the full complex of absorption components with these lines alone. We therefore report this as an associated absorber in our data tables, but we caution that this feature may be incorrectly identified.

This sightline was also observed with *FUSE* approximately four years prior to the COS

observations; no substantial variation in the absorption or continuum flux is apparent over this time period.

A.26 RBS1763

This sightline has been observed with *FUSE*, which was studied by Bonamente & Dixon (2004), who identified the single absorber as intrinsic, but suggested that the absorber could alternatively be associated with a nearby galaxy cluster. The C IV and N V show marginal evidence of partial coverage, so we prefer the AGN-associated interpretation.

A.27 RBS2055

The identifications of both systems in this sightline are uncertain. System ID 0 is blended with Galactic S II, and System ID 1 is blended with Galactic Si II and C I. Neither system is detected in metal lines. If the Galactic ISM lines have unusually complex component structure, they may be able to account for all of the absorption.

A.28 SDSS J091728.56+271951.0

The strong System ID 1 H I absorber, which is consistent with full coverage, is also firmly detected in N V; wavelength coverage for O VI and C IV is not available. The additional COS exposures from 30 November 2015 are not used, as they have no useable counts owing to a guide star acquisition failure.

A.29 SDSS J135712.61+170444.1

The single absorber in this sightline does not appear to have been identified previously. It is clearly detected in Lyα and O VI λ1032, although Lyα may have some contamination from Galactic Si IV. However, it is a relatively broad, shallow absober, and Lyβ is not detected. Further, O VI λ1038 is unmeasureable due to heavy blending with Galactic S III and Si II. It is undetected in

C IV and N V, and marginally detected in Si III. It is thus difficult to ascertain the covering properties and column densities of this absorber.

A.30 VPC 0798

The column density of the System ID 1 H I absorber is likely unreliable, as it is heavily saturated and only Lyα is available. This absorber, which does not appear to have been previously identified, is clearly identified in H I and Si III, but is not present in N V. Unfortunately, the wavelengths that would host O VI and C IV have not been observed.